Simulation adaptative des grandes échelles d'écoulements turbulents fondée sur une méthode Galerkine discontinue

Fabio Naddei

université PARIS-SACLAY

ÉCOLE POLYTECHNIQUE
UNIVERSITÉ PARIS-SACLAY

NNT : 2019SACLX060

Thèse de doctorat

Adaptive Large Eddy Simulations based on discontinuous Galerkin methods

Thèse de doctorat de l'Université Paris-Saclay
préparée à École Polytechnique

Ecole doctorale n°574 Ecole doctorale de mathématiques Hadamard (EDMH)
Spécialité de doctorat : Mathématiques appliquées

Thèse présentée et soutenue à Palaiseau, le 8/10/2019, par

NADDEI FABIO

Composition du Jury :

Georges Gerolymos Professeur des Universités, Université Pierre-et-Marie-Curie	Président
Claus-Dieter Munz Professeur des Universités, Universität Stuttgart	Rapporteur
Antonella Abbà Professeur associé, Politecnico di Milano	Rapporteur
Christophe Chalons Professeur des Universités, Université Versailles Saint-Quentin-en-Yvelines	Examinateur
Eusebio Valero Professeur des Universités, Universitad Politécnica de Madrid	Examinateur
Frédéric Coquel Directeur de recherce, École Polytechnique	Directeur de thèse
Marta de la Llave Plata Ingénieur de Recherce, ONERA	Co-encadrant
Vincent Couaillier Chef d'unité de recherche, ONERA	Co-encadrant

RÉSUMÉ

L'objectif principal de ce travail est d'améliorer la précision et l'efficacité des modèles LES au moyen des méthodes Galerkine discontinues (DG). Deux thématiques principales ont été étudiées: les stratégies d'adaptation spatiale et les modèles LES pour les méthodes d'ordre élevé.

Concernant le premier thème, dans le cadre des méthodes DG la résolution spatiale peut être efficacement adaptée en modifiant localement soit le maillage (adaptation-*h*) soit le degré polynômial de la solution (adaptation-*p*). L'adaptation automatique de la résolution nécessite l'estimation des erreurs pour analyser la qualité de la solution locale et les exigences de résolution.

L'efficacité de différentes stratégies de la littérature est comparée en effectuant des simulations *h*- et *p*-adaptatives. Sur la base de cette étude comparative, des algorithmes dynamiques et statiques *p*-adaptatifs pour la simulation des écoulements instationnaires sont ensuite développés et analysés. Les simulations numériques réalisées montrent que les algorithmes proposés peuvent réduire le coût de calcul des simulations des écoulements transitoires et statistiquement stationnaires.

Un nouvel estimateur d'erreur est ensuite proposé. Il est local, car n'exige que des informations de l'élément et de ses voisins directs, et peut être calculé en cours de simulation pour un coût limité. Il est démontré que l'algorithme statique *p*-adaptatif basé sur cet estimateur d'erreur peut être utilisé pour améliorer la précision des simulations LES sur des écoulements turbulents statistiquement stationnaires.

Concernant le second thème, une nouvelle méthode, consistante avec la discrétisation DG, est développée pour l'analyse *a priori* des modèles DG-LES à partir des données DNS. Elle permet d'identifier le transfert d'énergie idéal entre les échelles résolues et non résolues. Cette méthode est appliquée à l'analyse de l'approche Variotional Multiscale (VMS). Il est démontré que pour les résolutions fines, l'approche DG-VMS est capable de reproduire le transfert d'énergie idéal. Cependant, pour les résolutions grossières, typique de la LES à nombres de Reynolds élevés, un meilleur accord peut être obtenu en utilisant un modèle mixte Smagorinsky-VMS.

ABSTRACT

The main goal of this work is to improve the accuracy and computational efficiency of Large Eddy Simulations (LES) by means of discontinuous Galerkin (DG) methods. To this end, two main research topics have been investigated: resolution adaptation strategies and LES models for high-order methods.

As regards the first topic, in the framework of DG methods the spatial resolution can be efficiently adapted by modifying either the local mesh size (h-adaptation) or the degree of the polynomial representation of the solution (p-adaptation). The automatic resolution adaptation requires the definition of an error estimation strategy to analyse the local solution quality and resolution requirements. The efficiency of several strategies derived from the literature are compared by performing p- and h-adaptive simulations. Based on this comparative study a suitable error indicator for the adaptive scale-resolving simulations is selected.

Both static and dynamic p-adaptive algorithms for the simulation of unsteady flows are then developed and analysed. It is demonstrated by numerical simulations that the proposed algorithms can provide a reduction of the computational cost for the simulation of both transient and statistically steady flows.

A novel error estimation strategy is then introduced. It is local, requiring only information from the element and direct neighbours, and can be computed at run-time with limited overhead. It is shown that the static p-adaptive algorithm based on this error estimator can be employed to improve the accuracy for LES of statistically steady turbulent flows.

As regards the second topic, a novel framework consistent with the DG discretization is developed for the *a priori* analysis of DG-LES models from DNS databases. It allows to identify the ideal energy transfer mechanism between resolved and unresolved scales.

This approach is applied for the analysis of the DG Variational Multiscale (VMS) approach. It is shown that, for fine resolutions, the DG-VMS approach is able to replicate the ideal energy transfer mechanism. However, for coarse resolutions, typical of LES at high Reynolds numbers, a more accurate agreement is obtained by a mixed Smagorinsky-VMS model.

AWARDS, SECONDMENTS AND PUBLICATIONS

This thesis has been awarded the

- *Prix des doctorants ONERA 2019* in the category «*Simulation Numérique Avancée*».

Part of the work presented in this thesis has been carried out in the framework of two secondments

- one month within the research group of Pr. S. Sherwin at *Imperial College London*, July 2017.
- 2018 Summer Program, 4 weeks program at the *Center for Turbulence Research, Stanford University*, July 2018.

PUBLICATIONS

Some ideas and figures have appeared previously in the following publications and conferences.

Publications on international journals

- F. Naddei, M. de la Llave Plata, V. Couaillier, and F. Coquel. «A comparison of refinement indicators for p-adaptive simulations of steady and unsteady flows using discontinuous Galerkin methods.» in *J. Comput. Phys.* (2019).
- F. Naddei, M. de la Llave Plata and E. Lamballais. «Spectral and modal energy transfer analyses of the discontinuous Galerkin Variational Multiscale approach.» Submitted May 2019 to *J. Comput. Phys*.
- M. de la Llave Plata, E. Lamballais, and F. Naddei. «On the performance of a high-order multiscale DG approach to LES at increasing Reynolds numbers.» in *Comput. Fluids* (2019).

Proceedings of international conferences and collaborations

- F. Naddei, M. de la Llave Plata and V. Couaillier. «A comparison of refinement indicators for p-adaptive discontinuous Galerkin methods for the Euler and Navier-Stokes equations. » In *Proceedings of the 2018 AIAA Aerospace Sciences Meeting* (2018).

- M. de la Llave Plata, F. Naddei and V. Couaillier. «LES of the flow past a circular cylinder using a multiscale discontinuous Galerkin method.» In *Proceedings of the 5th international conference on Turbulence and Interactions TI 2018*, Springer (2018).
- F. Naddei, M. de la Llave Plata et al. «Large-scale space definition for the DG-VMS method based on energy transfer analyses.» In *Proceedings of the 2018 Summer Program*, Center for Turbulence Research, Stanford (2018).
- K. Bando, F. Naddei, M. de la Llave Plata et al. «Variational multiscale SGS modeling for LES using a high-order discontinuous Galerkin method.» In *2018 Annual Research Briefs*, Center for Turbulence Research, Stanford (2018).
- Book chapter: «Development of hp-adaptive discontinuous Galerkin methods for scale-resolving simulations.» to be published in the book *TILDA: Towards Industrial LES/DNS in Aeronautics - Paving the Way for Future Accurate CFD - Results of the H2020 Research Project TILDA, Funded by the European Union, 2015 -2018*, Springer

Other international conferences

- F. Naddei, M. de la Llave Plata and V. Couaillier. «Development of a p-adaptive discontinuous Galerkin method based on various refinement indicators», *Eurogen 2017*, Madrid (2017).
- F. Naddei, M. de la Llave Plata and V. Couaillier, «On the use of instantaneous versus average quantities for error-based p-adaptive simulation of turbulent flows», *7th ECCFD*, Glasgow (2018).
- J. Marcon, F. Naddei, J. Peiró et al., «Error-driven high-order mesh r-adaptation», *7th ECCFD*, Glasgow (2018).
- F. Naddei, M. de la Llave Plata and E. Lamballais, «Development of a scale-partition adaptive DG-VMS method for large-eddy simulation of turbulence», *1st HiFiLeD Symposium on Industrial LES & DNS*, Brussels (2018).
- M. de la Llave Plata, F. Naddei and V. Couaillier, «Assessment of high-order hp-adaptive methods for the simulation of turbulent flows», *1st HiFiLeD Symposium on Industrial LES & DNS*, Brussels (2018).
- F. Naddei, M. de la Llave Plata and V. Couaillier, «High-order p-adaptive simulations of turbulent flows using discontinuous Galerkin methods», *Airbus DiPart 2018*, Filton (2018).
- F. Naddei, M. de la Llave Plata and V. Couaillier, «p-adaptive LES of transitional flows using discontinuous Galerkin methods», *ADMOS 2019*, Alicante (2019).

- M. de la Llave Plata, F. Naddei and E. Lamballais, «A dynamic model adaptation strategy for the high-order discontinuous Galerkin VMS approach to LES», *ADMOS 2019*, Alicante (2019)

ACKNOWLEDGEMENTS

At the end of this long journey that is a PhD thesis, I need to thank all the people that have contributed to this work and have been part of my life throughout this project.

First of all I need to thank my supervisors Marta de la Llave Plata and Vincent Couaillier for guiding and supporting me and my decisions throughout this process. I am extremely grateful for our engaging discussions and the way they have always motivated me to improve my work. I also need to thank Pr. Frédéric Coquel for directing this thesis and Pr. Eric Lamballais for our stimulating collaboration, as well as all the members of the jury who have expressed their interest and dedicated precious time to this research.

My sincere gratitude goes to all the people at ONERA, and in particular Emeric Martin, Florent Renac and Marie Claire Le Pape for their help in answering my countless questions. A special mention goes to Mathieu Lorteau for our endless discussions and the innumerable times he has been able to guide me in understanding Aghora. Without his help finishing this work would have taken much longer.

I need then to thank my friends here in Paris, Rocco, Javier, Fabrizio, Pratik, Francesca and many others. Their friendship has made this journey far less stressful, less serious, and much more fun. And I cannot forget my friends of a lifetime, Alessandro, Marco, Gaetano and Davide. Despite the distance I know I can always count on their support and their willingness to hear my unintelligible rants.

Obviously none of this would have been possible without the European Commission financing this thesis and the SSeMID project. The amazing collaborations that have been promoted and the results obtained are a clear indication of what the European Union means and can achieve. I am thankful for all the experiences and all the friends I have met thanks to this project. I am sure all of them will move on to do great things.

Finally my deepest gratitude goes to my family. The distance and my habit of immersing myself in the work have not always been easy to deal with for them. However, to them I own all my achievements, for their unending support and all the opportunities they have provided for me.

CONTENTS

LIST OF FIGURES

LIST OF TABLES

ACRONYMS

CFD	Computational Fluid Dynamics
DG	discontinuous Galerkin
DE	Discretization error
DNS	Direct Numerical Simulation
dofs	Degrees of freedom
FD	Finite Difference
FE	Finite Element
FV	Finite Volume
HiOCFD	International Workshop on High-Order CFD Methods
HPC	High performance computing
ILES	Implicit Large Eddy Simulation
LSB	Laminar separation bubble
MGS	Modified Gram-Schmidt
MPI	Message passing interface
NCF	Non-conformity
NS	Navier-Stokes
LES	Large Eddy Simulation
RANS	Reynolds Averaged Navier-Stokes
RE	Residual error
SGS	Subgrid-scale
SIP	Symmetric interior penalty
SSED	Small-scale energy density
SSL	Small-scale Lifted
SSP	Strong Stability Preserving
TE	Truncation Error
TGV	Taylor-Green Vortex
VMS	Variational Multiscale

CHAPTER 1

INTRODUCTION

RÉSUMÉ DU CHAPITRE EN FRANÇAIS

Ce chapitre est dédié à l'introduction et à la définition des objectifs de ce travail de recherche et à la description du document de thèse.

L'un des défis les plus importants pour l'application de la mécanique des fluides numérique (CFD) aux applications industrielles est le coût de calcul exigé par la simulation des écoulements turbulents avec résolution d'échelles. Plusieurs approches sont brièvement décrites dans ce chapitre illustrant l'intérêt pour le développement des techniques de simulation des grandes échelles (LES).

Afin de promouvoir l'application des simulations LES sur des configurations avancées, de nouvelles méthodes numériques qui réduisent les erreurs de dissipation et de dispersion et permettent d'obtenir une efficacité parallèle élevée sur des architectures de mémoire distribuée sont nécessaires. Une méthode qui présente des propriétés intéressantes pour le développement d'approches LES est la méthode Galerkine discontinue (DG). Les principaux avantages de la méthode DG et les principaux défis ouverts sont ainsi décrits dans la Sec. 1.1.

Le travail de thèse porte sur l'amélioration de la précision et de l'efficacité des méthodes DG-LES. Deux axes de recherche sont analysés à cette fin : le développement de stratégies de résolution adaptatives et l'analyse de modèles LES pour les méthodes de DG de haut niveau. Celles-ci sont présentées dans la Sec. 1.2.

Le cadre de recherche et les outils utilisés sont ensuite décrits dans la Sec. 1.3. En particulier, nous décrivons le solveur DG ainsi que la plate-forme de calcul à haute performance utilisés dans les travaux réalisés. De plus, les collaborations établies dans le cadre de cette étude sont présentées.

Enfin, les chapitres décrivant les travaux réalisés sont résumés dans la Sec. 1.4.

1.1 INTRODUCTION

Computational Fluid Dynamics (CFD) is nowadays a fundamental tool for the prediction and analysis of flows in both industrial and academic applications.

In the scientific community, CFD is employed for the analysis of the physical mechanisms governing the motion of fluids. The main objective is to improve the understanding of these mechanisms to be able to model and control them. In this context CFD must accurately reproduce complex phenomena on relatively simplified configurations.

In industry, particularly in the aerospace and automotive fields, CFD is used throughout the development cycle of products, starting from the preliminary design phases, to the optimization and the analysis of the performance of the final product. For this type of applications, CFD must thus provide reliable results on complex configurations and within short turn-around times.

Despite the rapid improvement of these techniques and the maturity of advanced simulation tools available, there are still several challenges that limit the range of applications of CFD. This implies that experimental results are still required to verify the accuracy of numerical predictions. One of these challenges is the prohibitive computational cost required for the accurate simulation of turbulent flows, which are characterized by a chaotic three-dimensional mixing behaviour and exhibit a wide range of spatial and temporal scales.

The accurate simulation of such flows without any modelling assumptions requires the resolution of all the turbulent scales. This approach is commonly referred to as Direct Numerical Simulation (DNS) and presents a prohibitive computational cost for most industrial applications, which are characterized by high Reynolds numbers and complex geometries. The most commonly employed approach to reduce this computational cost consists in modelling all the turbulent scales and only resolving the mean flow. This strategy is known as Reynolds-Averaged Navier-Stokes (RANS) and is nowadays the standard industrial approach. Several works have shown, however, that RANS type approaches present serious limitations. They often require the ad-hoc choice of the RANS model and the tuning of the model parameters. Furthermore, this approach is often unable to predict unsteady large-scale phenomena and separated flows. These phenomena are typically encountered in critical off-design conditions in many aeronautical applications.

An intermediate approach between DNS and RANS is called Large Eddy Simulation (LES) and consists in resolving the largest energy-containing turbulent scales and modelling only the smallest turbulent scales. This approach is justified by the universal character of the smallest scales of turbulence, which, in principle, allows for a reduction of the modelling assumptions and a more general description of the behaviour of these flows.

Despite the reduction of the computational cost of LES with respect to DNS and the large number of works demonstrating improved results compared to RANS approaches, LES is seldom applied in the industrial context. This is due to the high computational cost for the accurate simulation of the largest three-dimensional unsteady turbulent scales. In order to promote the application of LES to industrial problems,

new numerical methods must be developed with low dispersion and dissipation errors and which can take full advantage of recent progress in high performance computing (HPC) to provide accurate results in reasonable times.

The Finite Volume (FV) method is currently the most employed numerical method for the simulation of flows in industrial applications. This is due to their robustness and relatively simple formulation for any polyhedral elements in structured and unstructured approaches and therefore their capability of handling complex geometries. Typical FV methods are however of first or second order, *i. e.* the error of the solution is proportional to the characteristic mesh size or to its square. In order to obtain sufficiently low dissipation and dispersion errors for LES, second-order methods require very fine meshes and therefore a prohibitively large number of degrees of freedom. Despite recent developments in higher-order FV methods, they still require the use of large stencils which can increase the computational cost and decrease their robustness in the case of stiff unstructured meshes and reduces the parallel efficiency of the algorithm.

For this reason, academic research focusing on the analysis of turbulent flows has made extensive use of alternative high-order methods such as high-order finite difference (FD), spectral and pseudo-spectral methods. These approaches allow for a large reduction of the dissipation and dispersion errors but rely on the use of structured meshes and are often limited to the analysis of simplified geometries.

Recent years have seen therefore a growing interest and rapid progress in the development of various methods which combine high-order accuracy with the flexibility of FV methods for the analysis of complex industrial configurations. Examples of these approaches are the discontinuous Galerkin (DG) method [46], the Spectral Element method (SEM) [101], the Spectral Difference (SD) method [123], and the Flux Reconstruction (FR) method [97].

Among these, the DG method, based on the variational formulation of the set of equations to be solved, combines features of FV and Finite Element (FE) methods and presents a number of advantages for LES of industrial applications. In the DG method, the solution is represented by a linear combination of polynomials within each element similarly to FE approaches. However, similarly to FV approaches, the solution is assumed to be discontinuous across element interfaces, requiring the definition of numerical fluxes.

By modifying the polynomial degree of the representation of the solution, the DG method can achieve arbitrary order of accuracy while employing unstructured and non-conforming meshes. In contrast to high-order FV methods, the order of accuracy is also preserved near physical boundaries. Additionally, the spatial resolution can be efficiently adapted by modifying the local mesh size (h-adaptation) or the local polynomial degree of the representation of the solution within each element (p-adaptation). These properties allow for the analysis of complex geometrical configurations typical of industrial applications.

High-order DG methods are also particularly suited for modern HPC architectures, achieving high parallel efficiency on distributed memory machines. This is due to the compact stencil of the scheme, as the evaluation of numerical fluxes only requires the knowledge of the solution inside the element and at the interface with its direct neighbours.

Finally, if hierarchical bases are employed, the variational formulation on which these methods rely allows for the natural application of multilevel LES models such as the Variational Multiscale approach, which has shown promising results in a number of applications [50].

There are, however, still a number of challenges that hinder the application of high-order DG methods to industrial applications. One of these limitations is the reduction of the local order of accuracy in the presence of geometrical or physical discontinuities, such as shock waves. These introduce numerical oscillations and require shock-capturing techniques in order to obtain stable solutions [151].

It is also important to take into account the lack of significant experience for the generation of curvilinear meshes for industrial applications using high-order methods. This is due to the limited number of advanced high-order mesh generators available and the relatively recent application of high-order methods to industrial problems [196].

The development of adaptive spatial resolution techniques represents a solution to these challenges and can considerably reduce the computational cost of simulations. On the one hand, by measuring the local regularity of the solution, adaptive resolution strategies can reduce the local mesh size in the presence of discontinuities, thereby isolating them and reducing the generation of numerical oscillations and errors. Similarly, the local order of the method can be increased in regions characterized by smooth solutions, thus efficiently improving the accuracy of simulations. On the other hand, adaptive resolution strategies reduce the amount of expertise required by the user, as error estimation techniques are used to measure the local quality of the solution and identify the local resolution requirements. The development of error estimation and resolution adaptive strategies is thus particularly relevant in the framework of LES. This is due to the high computational cost of simulations and the difficulties in assessing their quality.

Another relevant research subject is the development of accurate LES models in the context of high-order schemes. In the framework of DG methods two main strategies are employed for performing LES. One possible approach, referred to as implicit LES (ILES), consists in taking advantage of the dissipation properties of the numerical scheme or specific stabilization techniques in order to mimic the dissipative effect of the unresolved scales, see *e.g.* [74, 142, 188]. A second strategy consists in the discretization of LES models developed in the continuous framework without taking into account the effect of the numerical discretization [205].

Only a limited number of works have recently started to develop LES models specifically tailored for high-order FE-type methods, *e. g.* [41, 42]. The analysis of the influence of the parameters of the *hp*-discretization, such as the local polynomial degree and the discretization of the numerical fluxes, on these models represents therefore an important research topic to promote the use of DG-LES approaches.

1.2 OBJECTIVE OF THE THESIS

The main objective of the present work is to improve the accuracy and the computational efficiency of DG-LES methods. To this end, two main lines of research are analysed: the development of adaptive resolution strategies and the analysis of LES models in the context of high-order DG methods.

As regards the first topic, resolution adaptation strategies analyse the local solution quality and the resolution requirements. They allow for the optimization of the spatial discretization to improve the accuracy of simulations for a fixed computational cost or reduce the computational cost for a fixed level of accuracy. One of the most important factors determining the efficiency of a resolution adaptation algorithm is the choice of the error estimation strategy. The first part of this thesis is therefore dedicated to the analysis of various error estimation strategies derived from the literature. Discretization-error and residual-error based indicators are compared for the purpose of identifying advantages and drawbacks of these indicators for the development of both *p*- and *h*-adaptation strategies.

In the case of large scale computations, high parallel efficiency on distributed memory architectures must be preserved for the adaptive computations to reduce the total computational time. This requires the development of load balancing techniques which can take into account the computational load dependency on the local polynomial degree (for *p*-adaptation) and on the number of interfaces (for *h*-adaptation) of each element in the computational grid.

In the second part of this work, we then study *p*-adaptation strategies for the simulation of unsteady flows and, in particular, for LES of turbulent flows. The focus on *p*-adaptation is due to the potentially higher efficiency of this technique, as regards the reduction of dissipation and dispersion errors, for scale-resolving simulations of turbulent flows at relatively low Mach numbers.

Both static and dynamic *p*-adaptation strategies are studied. Static adaptation allows for the reduction of the computational cost of the LES of statistically steady flows, for which the resolution requirements remain approximately unchanged over time. Dynamic adaptation, on the other hand, presents higher complexity but can provide a further reduction of the computational cost for unsteady problems, in particular for transient flows presenting significant variation over time of the resolution requirements.

The computational gain provided by the algorithms developed in this thesis is analysed through several numerical experiments. We measure, in particular, the reduction of the number of degrees of freedom and of the computational time required to achieve a target level of accuracy.

The second research topic considered in this work is the analysis of LES models for high-order DG methods. For this purpose, a novel framework is developed for the *a-priori* analysis of DG-LES models taking into account the effect of the numerical discretization. This analysis aims at improving the current understanding of the influence of the *hp*-discretization on the resolution properties of the scheme in the context of scale-resolving simulations and in defining the separation between resolved and unresolved scales. The proposed methodology is applied for the analysis of the Variational Multiscale approach [93], which has been shown to provide improved predictions of turbulent flows as compared to classical LES models. Various open questions, however, hinder its systematic application for configurations of industrial interest. The developed framework is therefore used to study the accuracy of the VMS approach in combination with the DG discretization and suggest guidelines for the selection of the model parameters.

1.3 CONTEXT OF THE THESIS

This research is carried out in the framework of the development of the high-order DG solver *Aghora* at ONERA. The *Aghora* solver is implemented in Fortran90 and uses the *message passing interface* (MPI) to perform parallel computations on distributed memory machines. Based on both the modal and the nodal DG formulations on unstructured meshes, it is designed for the simulation of compressible flows with a variety of mathematical, numerical, and physical models. The verification of the solver and the analysis of its accuracy and performance has already been the subject of several publications [42, 43, 125, 205] and collaborations, namely in the framework of European projects [110, 162].

The computations carried out in this research project have been performed on two supercomputing platforms: *Sator* and *Occigen*.

Sator is a supercomputer produced by *NEC corporation* and has been acquired by ONERA in 2017. At the time of writing, it is composed of two types of nodes. A first group comprises 620 nodes each equipped with two Intel Xeon «Broadwell» E5-2680v4 processors with 14 cores at 2.4 GHz and 35 MB cache and a total of 128 GB of RAM. A second group of 160 nodes is composed of two Intel Xeon «Skylake-6152» processors with 22 cores at 2.1 GHz and 30.25 MB cache and presents 192 GB of RAM. Inter-node connection is based on the low latency Intel Omnipath Architecture fabrics running at 100 Gbps.

Thanks to two grants offered by GENCI (Grand Equipement National de Calcul Intensif) under projects A0022A10129 and A0032A10309, some of the computations pre-

sented in this thesis have been performed on the HPC platform called *Occigen*, owned by GENCI and operated by CINES (Centre Informatique National de l'Enseignement Superieur). Produced by Atos-Bull, it is currently ranked as the 70^{th} supercomputer in the *Top*500 world ranking of June 2018. Occigen is equipped with 2016 nodes each composed of two Intel Xeon «Haswell» E5-2690v3 processors with 12 cores at 2.6 GHz, and 1260 nodes composed of two Intel Xeon «Broadwell» E5-2690v4 processors with 14 cores at 2.6 GHz. Each node is equipped with 128 GB (Haswell) or 64 GB of RAM (Broadwell) and inter-node communication is provided by Intel Infiniband fabrics running at 56 Gbps.

This PhD thesis has been fully supported by the Marie Skłodowska-Curie Innovative Training Network (ITN) *Stability and Sensitivity Methods for Industrial Design* (SSeMID) [168] funded by the European Union's Horizon 2020 research and innovation programme. As such, over the course of the project, several collaborations have been established within the framework of this ITN. These include two joint research projects with J. Marcon and the research group of Pr. J. Peiro and Pr. S. Sherwin at Imperial College London, and with A. Rueda Ramirez, in the research group of Pr. E. Valero, at the Universidad Politécnica de Madrid.

Finally, part of the research work presented in Chap. 10 has been carried out in the framework of the 2018 Summer Program at the Center for Turbulence Research, at Stanford University. This study has been part of a collaboration with Pr. E. Lamballais from the Université de Poitiers, Pr. M. Massot from École Polytechnique, and K. Bando and the research group of Pr. M. Ihme from Stanford University.

1.4 OUTLINE OF THE THESIS

This dissertation is organized as follows.

In Chap. 2 we present an overview of the physical models employed throughout this work. After a brief description of the Navier-Stokes equations governing the motion of compressible flows, we discuss the different approaches for scale-resolving simulations to justify the interest in the development of LES techniques. Two different approaches for deriving the LES equations are then introduced, the classical approach based on spatial filters and the variational approach based on the projection on a discrete solution space.

Chap. 3 focuses on the description of the DG numerical discretization employed throughout the present work. Following a brief presentation of the history of the development of DG methods, the relevant formulation of the spatial and temporal discretization of these methods is introduced.

Chap. 4 presents an overview of resolution adaptation strategies. Adaptation techniques based on *h*- and *p*-adaptation are described highlighting the advantages and drawbacks of the different approaches. The resolution adaptation

algorithm for steady problems is then described and various error estimation and marking strategies are outlined. In particular, in Sec. 4.4.6 we present a novel error estimation strategy developed over the course of this work. Different strategies for the application of adaptive approaches to unsteady problems are then discussed. Finally, the difficulties associated with the development of refinement indicators for LES are presented.

Chap. 5 provides a comparison of different refinement indicators for the development of *p*-adaptive simulations. The efficiency of different refinement indicators is initially analysed by performing numerical simulations of inviscid and viscous steady flows. The convergence history of a number of relevant quantities of interest and the distribution of the local polynomial degree obtained from the use of the considered indicators are studied. The applicability of the results obtained to unsteady flow simulations is then demonstrated. Finally, a comparison of the computational cost and potential implementation issues associated with the different refinement indicators is presented.

In Chap. 6 we analyse the suitability of the considered error estimation strategies for the development of an *h*-adaptive algorithm based on element splitting. For this purpose, the comparison presented in Chap. 5 is extended by performing *h*-adaptive simulations.

In Chap. 7 we discuss the development of a load balancing algorithm for *h*- and *p*-adaptive simulations. At first, the graph partitioning algorithm is briefly described highlighting the requirement to obtain accurate estimates of the non-uniform distribution of the computational load for *h*/*p*-adaptive simulations. An approach to calibrate the load balancing algorithm from direct performance measurements is then introduced. The effectiveness of the developed strategy in providing well-balanced partitionings is demonstrated by performing numerical experiments on configurations using non-uniform polynomial degree.

Chap. 8 discusses the development of a dynamic *p*-adaptation algorithm. After a brief description of the proposed algorithm, dynamically *p*-adaptive simulations of three different configurations are performed: the transport of a vortex by a uniform inviscid flow, the collision of a dipole with a no-slip boundary, and the Taylor-Green Vortex at Re = 500. The considered configurations allow for the analysis of the performance of the dynamic algorithm and of the influence of various parameters on the accuracy and the computational cost of the simulations.

In Chap. 9 we present a static *p*-adaptation algorithm for scale-resolving simulations. At first, different strategies to define refinement indicators for the static adaptation of unsteady problems are presented. These are initially compared by performing statically *p*-adaptive simulations of the periodic laminar flow

past a cylinder. The applicability of the results obtained to the static adaptation of statistically steady turbulent flows is analysed by studying the flow over periodic hills. Finally, adaptive LES of the transitional flow past a NACA0012 airfoil are performed. It is shown that the novel error estimation strategy developed in this work can be employed to efficiently improve the accuracy of LES.

Chap. 10 discusses the *a-priori* analysis of DG-LES models. We propose a novel framework to carry out energy transfer analyses of DG-LES models from DNS databases. *A-priori* analyses of the DG-VMS approach are then presented. Its accuracy in reproducing the ideal energy transfer mechanism between resolved and unresolved scales is analysed. The influence of various formulations and model parameters are discussed and guidelines for further developments are presented.

Chap. 11 presents the main conclusions of this research, alongside possible perspectives for future research.

CHAPTER 2

THE PHYSICAL MODEL

RÉSUMÉ DU CHAPITRE EN FRANÇAIS

Ce chapitre est dédié à la description des équations de modélisation physique utilisées dans cette étude.

Après avoir brièvement présenté les équations de Navier-Stokes (NS), qui régissent le mouvement d'un fluide compressible, dans la Sec. 2.3 nous nous concentrons sur la description des différentes approches de modélisation physique qui peuvent être utilisées pour la simulation des écoulements turbulents. Celles-ci vont de la simulation numérique directe (DNS), qui résout toutes les échelles turbulentes, à l'approche Reynolds Averaged Navier-Stokes (RANS), qui décrit l'évolution de la moyenne d'ensemble des écoulements en modélisant toutes les échelles turbulentes. Dans ce contexte, la simulation des grandes échelles (LES pour Large Eddy Simulation) représente une approche intermédiaire. Dans cette approche, une fraction limitée des échelles turbulentes est résolue, correspondant aux grandes échelles, alors que l'effet des échelles non résolues sur les échelles résolues est modélisé.

Le reste de ce chapitre est dédié à la formulation des équations LES et à la présentation des modèles de sous-mailles LES utilisés dans cette étude. Deux approches pour la dérivation des équations du LES sont présentées. La première approche, classique, est décrite dans la Sec. 2.4. Elle consiste à dériver les équations LES en filtrant les équations NS à l'aide d'un filtre de convolution. Le deuxième approche consiste à projeter les équations NS sur un espace fonctionnel associé à la discrétisation spatiale. Cette approche, fondée sur une formulation variationnelle des équations LES, est présentée dans la Sec. 2.5.

La formulation variationnelle des équations LES est employée dans la Sec. 2.6 pour introduire l'approche Variational Multiscale (VMS). Elle consiste à séparer les échelles résolues en deux composantes: une composante à grande échelle, supposée sans interaction avec les échelles non résolues, et une composante à petite échelle. En limitant l'effet du modèle de sous-maille aux petites échelles résolues, il a été démontré que l'approche VMS améliore la prédiction des simulations LES en réduisant l'excès de dissipation introduit par les modèles LES standard mono-échelle sur les plus grandes échelles résolues.

2.1 INTRODUCTION AND OUTLINE OF THE CHAPTER

In this chapter we introduce the physical modelling equations employed throughout the present work. In Sec. 2.2 we present the Navier-Stokes equations describing the motion of a compressible fluid. Then in Sec. 2.3 we discuss the difficulties encountered in the simulation of turbulent flows and the need for modelling turbulent scales by means of Large Eddy Simulations (LES). Two approaches for deriving the LES equations are outlined. At first, we present in Sec. 2.4 the classical approach applying a spatial filter to the Navier-Stokes equations. Three models used in this work for representing the effect of the unresolved turbulent scales are also introduced. The variational approach to derive the LES equations is then outlined in Sec. 2.5.

Finally, we present in Sec. 2.6 the Variational Multiscale approach. The combination of this model with the discontinuous Galerkin (DG) formulation presents several remarkable properties which are discussed in this section. Several questions regarding the model parameters remain, however, open and are therefore the subject of Chap. 10.

2.2 THE COMPRESSIBLE NAVIER-STOKES EQUATIONS

The motion of a compressible fluid in a three-dimensional domain $\Omega \in \mathbb{R}^3$ is described by the compressible Navier-Stokes (NS) equations, which take the form

$$\partial_t \mathbf{u} + \nabla \cdot \boldsymbol{\mathcal{F}}_c(\mathbf{u}) - \nabla \cdot \boldsymbol{\mathcal{F}}_v(\mathbf{u}, \nabla \mathbf{u}) = 0 \quad , \quad \forall \mathbf{x} \in \Omega, t > 0 \tag{1}$$

$$\mathbf{u}(\mathbf{x}, 0) = \mathbf{u}_0(\mathbf{x}) \quad , \quad \forall \mathbf{x} \in \Omega \tag{2}$$

with appropriate boundary conditions prescribed on $\partial\Omega$. The vector $\mathbf{u} = (\rho, \rho\mathbf{v}, \rho E)^T$ represents the conservative state variables, with ρ being the density, $\mathbf{v} = (U_1, U_2, U_3)^T$ the velocity vector and $E = \frac{p}{(\gamma-1)\rho} + \frac{\mathbf{v}\cdot\mathbf{v}}{2}$ the specific total energy. Here, p is the static pressure and $\gamma = \frac{C_p}{C_v} > 1$ is the ratio of specific heats. The nonlinear convective and diffusive fluxes in Eq. (1) are defined, respectively, as:

$$\boldsymbol{\mathcal{F}}_c(\mathbf{u}) = \begin{bmatrix} \rho\mathbf{v}^T \\ \rho\mathbf{v} \otimes \mathbf{v} + p\mathbf{I} \\ \rho E\mathbf{v}^T + p\mathbf{v}^T \end{bmatrix} \quad \text{and} \quad \boldsymbol{\mathcal{F}}_v(\mathbf{u}, \nabla\mathbf{u}) = \begin{bmatrix} 0 \\ \boldsymbol{\tau} \\ \boldsymbol{\tau}\cdot\mathbf{v} - \mathbf{q}^T \end{bmatrix} \tag{3}$$

with

$$\boldsymbol{\tau} = 2\mu \mathbf{S}^D = \mu\left(\boldsymbol{\nabla}\mathbf{v} + (\boldsymbol{\nabla}\mathbf{v})^T - \frac{2}{3}\boldsymbol{\nabla}\cdot\mathbf{v}\mathbf{I}\right) \tag{4}$$

$$\mathbf{q} = -\lambda \boldsymbol{\nabla} T \tag{5}$$

$$p = \rho R T \tag{6}$$

where μ is the dynamic viscosity, $\boldsymbol{S}^D$ is the deviatoric component of the strain-rate tensor $\boldsymbol{S} = \frac{1}{2}(\boldsymbol{\nabla}\mathbf{v} + (\boldsymbol{\nabla}\mathbf{v})^T)$, T denotes the temperature, and R is the specific gas constant. The thermal conductivity is given by $\lambda = \mu\frac{C_p}{\mathrm{Pr}}$ with Pr the Prandtl number, set in this work to 0.7.

The NS equations can be adimensionalized by defining a characteristic length L_{ref}, velocity U_{ref}, density ρ_{ref} and temperature T_{ref}. These lead to the definition of the Reynolds number

$$\mathrm{Re} = \frac{\rho_{ref} U_{ref} L_{ref}}{\mu_{ref}} \ ,$$

measuring the relative importance of convective and viscous effects, and the reference Mach number

$$\mathrm{M}_{ref} = \frac{U_{ref}}{c_{ref}}$$

measuring the importance of compressibility effects, where $c(T) = \sqrt{\gamma RT}$ is the speed of sound and $c_{ref} = c(T_{ref})$.

2.3 SCALE-RESOLVING SIMULATIONS

For relatively high values of the Reynolds number, the inertial forces lead to a chaotic three-dimensional motion which we identify as turbulence. A physical mechanism can be identified by which the energy is transferred through an *energy cascade* from the largest vortices to smaller and smaller vortices until the energy is ultimately dissipated by the viscous effects. One of the fundamental obstacles that still hinder the systematic application of CFD to engineering problems is the high computational cost associated with the simulation of the broad range of scales which characterizes turbulent flows.

At least from the conceptual point of view, the deterministic simulation of turbulent flows does not present any additional complexity. The motion of fluid particles in the continuum assumption is ultimately controlled by the NS equations. Therefore, the same numerical tools designed for the prediction of laminar flows can be directly employed for the simulation of turbulent configurations, provided that dissipation and dispersion errors are sufficiently reduced.

This type of approach is referred to as *Direct Numerical Simulation (DNS)* as no particular modelling is employed to represent the turbulent scales of the flow. In DNS the full energy cascade must be resolved from the largest inertial to the smallest dissipative scales. An estimate of the computational cost of DNS can be derived following the dimensional analysis of Kolmogorov for homogeneous isotropic turbulence [182], which links the smallest scales of motion to the Reynolds number. From

the Kolmogorov analysis it can be shown that the smallest turbulent scale η, in the case of homogeneous isotropic turbulence, can be estimated as

$$\frac{\eta}{L_{ref}} = \mathcal{O}(\mathrm{Re}^{-\frac{3}{4}}) \ .$$

The numerical discretization requires a characteristic mesh size smaller than the smallest dissipative scale and, as turbulence is an inherently three-dimensional phenomenon, it can be inferred that the required number of degrees of freedom to simulate a box of volume L_{ref}^3 is $\mathcal{O}(\mathrm{Re}^{\frac{9}{4}})$. If explicit time-integration is employed, the time-step is proportional to the mesh size and therefore the computational cost of DNS is $\mathcal{O}(\mathrm{Re}^3)$. Additionally, it has been shown by Choi and Moin [44] that for wall-bounded flows the complexity increases to $\mathcal{O}(\mathrm{Re}^{3.5})$, due to the more stringent resolution requirements for turbulent boundary layers. The computational cost of DNS is therefore prohibitively high for practical industrial applications for which typical values of the Reynolds number are in the range 10^5-10^8.

The solution routinely employed for industrial problems is therefore to employ the *Reynolds-Averaged Navier-Stokes (RANS)* equations. The RANS equations are obtained by performing time or ensemble averaging of the NS equations and introducing a turbulent model to represent the effect of turbulent fluctuations on the base flow. The result is a system of equations that describes only the evolution of the average flow and the turbulent scales are completely modelled, thus largely reducing the complexity of the simulations.

RANS models have been successfully applied to a variety of configurations. However, they are known to present several limitations. In particular no general RANS model valid for all types of flows has been proposed and often ad-hoc modifications and calibrations of the model coefficients are required. Additionally, despite several improvements in recent years, they often fail in the prediction of transitional and fully unsteady separated flows, for which the largest turbulent scales do not satisfy the equilibrium hypotheses on which some of the RANS models are based.

An intermediate approach is provided by *Large Eddy Simulation (LES)* [72, 170]. LES consists in resolving only a limited amount of turbulent scales and modelling the effect of unresolved ones by means of a subgrid-scale (SGS) model. A critical advantage of LES, as compared to RANS, is that based on the Kolmogorov hypothesis the smallest turbulent scales are isotropic and universal. Therefore in theory a universal SGS model could be derived, which can accurately predict the energy transfer mechanism for all types of flows controlled by large-scale dynamics. This is in contrast with RANS, which requires modelling even the large turbulent scales, which can be anisotropic and strongly depend on the flow configuration. Additionally, LES provides a methodology to control the amount of turbulent scales that are resolved and therefore a more accurate prediction of the large-scale flow features for the given available computational resources.

2.4 THE CLASSICAL FORMULATION OF THE LES EQUATIONS

Several approaches have been employed in the literature to derive the LES equations. The most common and classical approach is to derive the LES formulation by filtering the NS equations by means of a spatial filter denoted by $\overline{(\cdot)}$ characterized by a filter length Δ. It is assumed that the filter is conservative (preserves the average) and commutes with differentiation. The application of the filter corresponds to the decomposition of the state variables in $\mathbf{u} = \overline{\mathbf{u}} + \mathbf{u}'$ where $\overline{\mathbf{u}}$ is the resolved component of the state vector and $\mathbf{u}'$ is the subfilter or subgrid component of which we want to model the effect on the resolved scales. In the case of compressible flow problems, such as the ones considered in the present work, it is common to introduce the concept of a Favre filtering operator $\tilde{(\cdot)}$, such that for any function f we define a Favre filtered quantity as

$$\tilde{f} = \frac{\overline{\rho f}}{\overline{\rho}} \ . \tag{7}$$

By applying the spatial filter to the compressible NS equations, we obtain the following set of equations

$$\partial_t \overline{\mathbf{u}} + \nabla \cdot \overline{\boldsymbol{\mathcal{F}}_c}\,(\mathbf{u}) - \nabla \cdot \overline{\boldsymbol{\mathcal{F}}_v}\,(\mathbf{u}, \nabla \mathbf{u}) = 0 \ , \tag{8}$$

where $\overline{\mathbf{u}} = (\overline{\rho}, \overline{\rho}\tilde{\mathbf{v}}, \overline{\rho}\tilde{E})^T$ is the vector of Favre filtered variables. The filtered fluxes take the form

$$\overline{\boldsymbol{\mathcal{F}}_c} = \begin{bmatrix} \overline{\rho}\tilde{\mathbf{v}}^T \\ \overline{\rho}\tilde{\mathbf{v}} \otimes \tilde{\mathbf{v}} + \overline{p}\mathbf{I} + (\overline{\rho \mathbf{v} \otimes \mathbf{v}} - \overline{\rho}\tilde{\mathbf{v}} \otimes \tilde{\mathbf{v}}) \\ \overline{\rho}\tilde{E}\tilde{\mathbf{v}}^T + \overline{p}\tilde{\mathbf{v}}^T + (\overline{(\rho E + p)\mathbf{v}^T} - (\overline{\rho}\tilde{E} + \overline{p})\tilde{\mathbf{v}}^T) \end{bmatrix} \ , \tag{9}$$

and

$$\overline{\boldsymbol{\mathcal{F}}_v} = \begin{bmatrix} 0 \\ \overline{\boldsymbol{\tau}} \\ \overline{\boldsymbol{\tau} \cdot \mathbf{v}} - \overline{\lambda \nabla^T T} \end{bmatrix} \ . \tag{10}$$

We have isolated in the Eq. (9) the terms only depending on the resolved variables and those which represent the effect of the unresolved scales on the resolved ones. One such term in Eq. (9) is defined as the *subgrid-stress tensor*:

$$\boldsymbol{\tau}_{sgs} = -\overline{\rho \mathbf{v} \otimes \mathbf{v}} + \overline{\rho}\tilde{\mathbf{v}} \otimes \tilde{\mathbf{v}} \ . \tag{11}$$

This term is decomposed into a deviatoric $\boldsymbol{\tau}^D_{sgs}$ and a spherical component $\boldsymbol{\tau}^S_{sgs}$ as

$$\boldsymbol{\tau}_{sgs} = \underbrace{\boldsymbol{\tau}_{sgs} - \frac{1}{3}\mathrm{tr}(\boldsymbol{\tau}_{sgs})\mathbf{I}}_{\boldsymbol{\tau}^D_{sgs}} + \underbrace{\frac{1}{3}\mathrm{tr}(\boldsymbol{\tau}_{sgs})\mathbf{I}}_{\boldsymbol{\tau}^S_{sgs}} \ . \tag{12}$$

The spherical component is then combined with the pressure term to define the macropressure,

$$P\mathbf{I} = \overline{p}\mathbf{I} - \boldsymbol{\tau}_{sgs}^{S} \ . \tag{13}$$

Following the work of Lesieur *et al.* [120], the total energy density is expressed as

$$\begin{aligned} \overline{\rho}\tilde{E} =& \overline{\rho}C_v\tilde{T} + \frac{1}{2}\overline{\rho}\tilde{\mathbf{v}}\cdot\tilde{\mathbf{v}} - \frac{1}{2}\mathrm{tr}(\boldsymbol{\tau}_{sgs}) = \\ =& \overline{\rho}C_v\left(\tilde{T} - \frac{1}{2\overline{\rho}C_v}\mathrm{tr}(\boldsymbol{\tau}_{sgs})\right) + \frac{1}{2}\overline{\rho}\tilde{\mathbf{v}}\cdot\tilde{\mathbf{v}} \ , \end{aligned} \tag{14}$$

where we introduce the macrotemperature as $\Theta = \tilde{T} - \frac{1}{2\overline{\rho}C_v}\mathrm{tr}(\boldsymbol{\tau}_{sgs})$, and the equation of state is manipulated to obtain

$$P = \overline{\rho}R\Theta + \frac{3\gamma - 5}{6}\mathrm{tr}(\boldsymbol{\tau}_{sgs}) \ . \tag{15}$$

Lesieur *et al.* [120] have proposed to neglect the second term in Eq. (15) such that the equation of state becomes

$$P = \overline{\rho}R\Theta \ . \tag{16}$$

The expression of the filtered viscous flux can also be rearranged in order to isolate terms depending only on the resolved quantities. Vreman *et al.* [192], however, have demonstrated that the resulting subgrid terms are negligible as compared to those obtained from the convective flux. The filtered variables are therefore assumed to satisfy the equation

$$\frac{\partial\overline{\mathbf{u}}}{\partial t} + \boldsymbol{\nabla}\cdot\left[\boldsymbol{\mathcal{F}}_c(\overline{\mathbf{u}}) - \boldsymbol{\mathcal{F}}_v(\overline{\mathbf{u}}, \boldsymbol{\nabla}\overline{\mathbf{u}}) - \boldsymbol{\mathcal{F}}_{sgs}(\overline{\mathbf{u}}, \mathbf{u})\right] = 0 \ , \tag{17}$$

where the convective, viscous and subgrid fluxes take the form

$$\boldsymbol{\mathcal{F}}_c(\overline{\mathbf{u}}) = \begin{bmatrix} \overline{\rho}\tilde{\mathbf{v}}^T \\ \overline{\rho}\tilde{\mathbf{v}}\otimes\tilde{\mathbf{v}} + P\mathbf{I} \\ \overline{\rho}\tilde{E}\tilde{\mathbf{v}}^T + P\tilde{\mathbf{v}}^T \end{bmatrix} \ , \qquad \mathcal{F}_v(\overline{\mathbf{u}}, \boldsymbol{\nabla}\overline{\mathbf{u}}) = \begin{bmatrix} 0 \\ \mu(\Theta)\tilde{\mathbf{S}}^D \\ \mu(\Theta)\tilde{\mathbf{S}}^D\cdot\tilde{\mathbf{v}} - \frac{C_p\mu(\Theta)}{\mathrm{Pr}}\nabla^T\Theta \end{bmatrix} \ ,$$

and

$$\boldsymbol{\mathcal{F}}_{sgs}(\overline{\mathbf{u}}, \mathbf{u}) = \begin{bmatrix} 0 \\ \boldsymbol{\tau}_{sgs}^{D} \\ \mathbf{q}_{sgs} \end{bmatrix} \ .$$

where $\mathbf{q}_{sgs} = -\overline{(\rho E + p)\mathbf{v}^T} + (\overline{\rho}\tilde{E} + \overline{p})\tilde{\mathbf{v}}^T$ is the subgrid scale heat flux.

By employing the presented derivation, Eq. (17) combined with Eq. (16) describes the evolution of the resolved component of the vector of state and presents the same structure as the NS equations. It is expressed however in terms of the Favre filtered variables, the macropressure and macrotemperature, and includes an additional subgrid flux representing the effect of the unresolved scales on the motion of the resolved scales.

2.4.1 *Subgrid-scale models*

The subgrid flux in Eq. (17) must be approximated by a suitable model that only depends on the resolved scales in order to obtain a closed system of equations. One of the most common approaches is to approximate the deviatoric component of the subgrid stress tensor as a viscous dissipation term by introducing the concept of a subgrid eddy-viscosity ν_{sgs}. Under this assumption the subgrid-stress tensor takes the form

$$\boldsymbol{\tau}_{sgs}^{D} \approx \overline{\rho}\nu_{sgs}\tilde{\boldsymbol{S}}^{D} \ . \tag{18}$$

The subgrid heat flux can then be modelled with a similar eddy-viscosity approach, leading to

$$\mathbf{q}_{sgs} \approx \frac{1}{\mathrm{Pr}_t}\overline{\rho}\nu_{sgs}\boldsymbol{\nabla}\Theta \ ,$$

where Pr_t is the turbulent Prandtl number, which is assumed constant and takes values between 0.7 and 1 [103]. In this work it is considered to be equal to 0.9.

Three eddy-viscosity models employed in the present work, namely, the Smagorinsky, the WALE and the Vreman models, are described in what follows.

2.4.1.1 *The Smagorinsky model*

The Smagorinsky model [174] is one of the most commonly employed LES models. It is derived from dimensional analysis assuming that the eddy viscosity is proportional to a characteristic length scale and a characteristic turbulent velocity. This leads to the definition of the model eddy viscosity as

$$\nu_{sgs} = (C_S\Delta)^2|\tilde{\boldsymbol{S}}| \ , \quad \text{with} \quad |\tilde{\boldsymbol{S}}| = \sqrt{2\tilde{\boldsymbol{S}}\colon\tilde{\boldsymbol{S}}} \ , \tag{19}$$

where Δ is the LES filter width and C_S is the so-called Smagorinsky coefficient. The value of C_S can be obtained by following the procedure outlined by Lilly [122] which leads to $C_S = 0.18$. Several works have shown that the optimal value for C_S is between 0.1 and 0.2 but depends on the turbulent flow and can vary in space and time for inhomogeneous flows. This model presents several drawbacks:

- The value of C_S is fixed *a-priori*;
- It is too dissipative on the largest resolved scales;
- The turbulent eddy viscosity does not tend to zero in laminar flows with non-zero mean shear, and near walls;
- As most eddy-viscosity models, the physical process of back-scatter, consisting in energy being transferred from the unresolved to the resolved scales, is not modelled.

Despite these drawbacks, the Smagorinsky model is numerically cheap, robust and easy to implement. These are the main reasons why it is still widely employed. Several turbulence models, however, have been proposed to reduce the above mentioned drawbacks.

2.4.1.2 *The WALE model*

The WALE (Wall-Adapting Local-Eddy viscosity) model was derived by Nicoud *et al.* [145] with the objective of obtaining an LES model capable of providing the proper scaling of the turbulent viscosity near the wall, $\nu_{sgs} = \mathcal{O}(y^3)$ with y being the distance in the wall-normal direction. The eddy-viscosity is expressed as

$$\nu_{sgs} = (C_W \Delta)^2 \frac{(\boldsymbol{S}^d : \boldsymbol{S}^d)^{\frac{3}{2}}}{(\tilde{\boldsymbol{S}} : \tilde{\boldsymbol{S}})^{\frac{5}{2}} + (\boldsymbol{S}^d : \boldsymbol{S}^d)^{\frac{5}{4}}} \ , \tag{20}$$

where $\boldsymbol{S}^d$ is the traceless symmetric part of the square of the gradient velocity tensor

$$\boldsymbol{S}^d_{ij} = \frac{1}{2}(\overline{g}^2_{ij} + \overline{g}^2_{ji}) - \frac{1}{2}\delta_{ij}\overline{g}^2_{kk} \ , \tag{21}$$

with $\overline{g}^2_{ij} = \frac{\partial \tilde{U}_i}{\partial x_k}\frac{\partial \tilde{U}_k}{\partial x_j}$. The calibration of the model constant C_W has been obtained by assuming that the WALE model should provide the same ensemble-averaged SGS dissipation as the Smagorinsky model for homogeneous isotropic turbulence. This leads to $C^2_W \approx 10.6 C^2_S$. Compared to the Smagorinsky model, the WALE model provides the theoretical near-wall scaling and leads to a zero eddy-viscosity in cases of pure shear, which is a fundamental property for the simulation of transitional flows.

2.4.1.3 *The Vreman model*

Vreman [190] has proposed an eddy-viscosity model which takes the form

$$\nu_{sgs} = C_V \sqrt{\frac{B_\beta}{\alpha_{ij}\alpha_{ij}}} \tag{22}$$

with

$$\alpha_{ij} = \frac{\partial \tilde{U}_j}{\partial x_i} \quad , \quad \beta_{ij} = \Delta_m^2 \alpha_{mi} \alpha_{mj} \ ,$$

$$B_\beta = \beta_{11}\beta_{22} - \beta_{12}^2 + \beta_{11}\beta_{33} - \beta_{13}^2 + \beta_{22}\beta_{33} - \beta_{23}^2 \ ,$$

with $C_V \approx 2.5 C_S^2$ and Δ_m being the filter length in the m-th direction, here assumed to be the same in the three-spatial directions and equal to Δ.

Similarly to the WALE and Smagorinsky models, the Vreman model only requires knowledge of the local filter width and the first-order derivatives of the velocity filed, therefore presenting a limited computational cost. It provides an eddy viscosity which is zero for several types of laminar flows and has demonstrated improved results with respect to the standard Smagorinsky model on transitional flows. However, it does not reproduce the correct near-wall scaling, as it leads to $\nu_{sgs} = \mathcal{O}(y)$.

In regions with low gradients the evaluation of B_β is sensitive to numerical errors. It was therefore suggested by Vreman [190] to set the eddy-viscosity to $\nu_{sgs} = 0$ for small values of B_β ($e.g. B_\beta < 10^{-8}$) which allows us to recover the correct value of the eddy viscosity in the limit of $\|\alpha\| \to 0$.

2.5 VARIATIONAL DERIVATION OF THE LES EQUATIONS

The classical derivation of the LES equations presented in Sec. 2.4 is based on the definition of a low-pass filter that separates the resolved from the unresolved components of the solution. The obtained set of continuous equations is then discretized by means of a numerical method. The derivation of the LES equations and their numerical discretization are therefore considered as two fundamentally different problems. This is in stark contrast with practical LES for which the LES filter is implicitly introduced by the numerical discretization itself. Additionally, the use of meshes with variable cell size implies a variation of the LES filter width, which leads to the loss of the commutative property between filtering and derivation, employed to obtain Eq. (8).

Several authors have therefore proposed to derive the LES equations by projection on the finite solution space introduced by the numerical discretization. This approach has been proposed by Pope [153], known as LES by projection onto local basis functions, and by Hughes *et al.* [93] in the formulation of the Variational Multiscale approach and later extended by Collis [49] and van der Bos *et al.* [27].

Following their approach we write the weak form of Eq. (1) as

$$\mathcal{B}(\mathbf{u}, \mathbf{w}) = 0 \quad , \quad \forall \mathbf{w} \in \mathcal{V} \ . \tag{23}$$

The solution space $\mathcal{V}$ is then decomposed into a finite dimensional space of resolved scales $\overline{\mathcal{V}}$ and an infinite dimensional space of unresolved scales $\mathcal{V}'$

$$\mathcal{V} = \overline{\mathcal{V}} \oplus \mathcal{V}' \ .$$

The solution is therefore expressed as the superposition of the resolved $\overline{\mathbf{u}}$ and unresolved scale $\mathbf{u}'$ components which can be obtained by projecting $\mathbf{u}$ onto the resolved and unresolved solution spaces, $\mathbf{u} = \overline{\mathbf{u}} + \mathbf{u}'$.

The variational form Eq. (23) is thus rewritten as

$$\mathcal{B}(\overline{\mathbf{u}} + \mathbf{u}', \mathbf{w}) = \mathcal{B}(\overline{\mathbf{u}}, \mathbf{w}) + \mathcal{B}^{sgs}(\overline{\mathbf{u}}, \mathbf{u}', \mathbf{w}) = 0 \ , \tag{24}$$

where we have isolated a term depending only on the resolved scales and a subgrid term depending on both the resolved and the unresolved scales.

The specific form of Eq. (24) depends on the numerical method for which the LES equations are to be derived. Thus, without loss of generality, we indicate as $\mathcal{V}_h$ the discretization space. Assuming that $\mathbf{w} \in \mathcal{V}_h$, we obtain

$$\mathcal{B}_h(\overline{\mathbf{u}}, \mathbf{w}_h) + \mathcal{B}_h^{sgs}(\overline{\mathbf{u}}, \mathbf{u}', \mathbf{w}_h) = 0 \ . \tag{25}$$

The resolved solution space is therefore defined by the discretization space, which corresponds to the practical approach of equating the LES filter with the spatial discretization.

In order to close the system of LES equations the subgrid-stress term $\mathcal{B}_h^{sgs}(\overline{\mathbf{u}}, \mathbf{u}', \mathbf{w}_h)$ is then approximated by a model term $\mathcal{M}_h^{sgs}(\overline{\mathbf{u}}, \mathbf{w}_h)$, which depends on the resolved scales only

$$\mathcal{B}_h(\overline{\mathbf{u}}, \mathbf{w}_h) + \mathcal{M}_h^{sgs}(\overline{\mathbf{u}}, \mathbf{w}_h) = 0 \ . \tag{26}$$

Compared to the classical LES approach, the above equation Eq. (26) has the critical advantage that, at least in theory, no numerical errors are introduced by the discretization [153]. This is because the resolved scales are perfectly represented on the considered discretization space. Only modelling errors appear due to the discrepancy between the employed model and the exact subgrid-stress. We point out however that from Eq. (25) the subgrid-stress term is itself defined by the employed numerical discretization. Turbulence models should therefore be derived which can take this feature into account [153]. Further discussion on this topic is presented in Chap. 10.

2.6 THE VARIATIONAL MULTISCALE MODEL

The variational formulation of the LES equations, described in the previous section, has been employed by Hughes *et al.* [93] to derive a turbulence model referred to as the Variational Multiscale (VMS) approach. The VMS model has been originally proposed to reduce one of the most common drawbacks of classical LES models, namely the excessive dissipation introduced on the largest resolved scales.

To illustrate this approach, let us consider a further decomposition of the resolved solution space into a large and a small-scale component

$$\mathcal{V} = \mathcal{V}^L \oplus \mathcal{V}^S \oplus \mathcal{V}' \ ,$$

where $\mathcal{V}^L$ and $\mathcal{V}^S$ are the finite dimensional spaces of the large and small resolved scales, respectively. Based on this decomposition, Eq. (24) can be rewritten as

$$\mathcal{B}_h(\mathbf{u}^L, \mathbf{w}^L) + \mathcal{B}_h^1(\mathbf{u}^L, \mathbf{u}^S, \mathbf{w}^L) + \mathcal{B}_h^{sgs}(\overline{\mathbf{u}}, \mathbf{u}', \mathbf{w}^L) = 0 \quad , \quad \forall \mathbf{w}^L \in \mathcal{V}^L \ , \tag{27}$$

$$\mathcal{B}_h(\mathbf{u}^S, \mathbf{w}^S) + \mathcal{B}_h^1(\mathbf{u}^L, \mathbf{u}^S, \mathbf{w}^S) + \mathcal{B}_h^{sgs}(\overline{\mathbf{u}}, \mathbf{u}', \mathbf{w}^S) = 0 \quad , \quad \forall \mathbf{w}^S \in \mathcal{V}^S \ , \tag{28}$$

where Eqs. (27) and (28) govern the evolution of the large and small resolved scales, respectively. The term $\mathcal{B}_h^1$ represents the interaction between large and small scales, whereas $\mathcal{B}_h^{sgs}$ identifies the interaction between the resolved and the unresolved scales.

The main assumption of the VMS approach consists then in neglecting the effect of the unresolved scales on the large resolved scales, *i. e.* $\mathcal{B}_h^{sgs}(\overline{\mathbf{u}}, \mathbf{u}', \mathbf{w}^L) \approx 0$, and modelling $\mathcal{B}_h^{sgs}(\overline{\mathbf{u}}, \mathbf{u}', \mathbf{w}^S)$, leading to the following set of equations

$$\mathcal{B}_h(\mathbf{u}^L, \mathbf{w}^L) + \mathcal{B}_h^1(\mathbf{u}^L, \mathbf{u}^S, \mathbf{w}^L) = 0 \ , \tag{29}$$

$$\mathcal{B}_h(\mathbf{u}^S, \mathbf{w}^S) + \mathcal{B}_h^1(\mathbf{u}^L, \mathbf{u}^S, \mathbf{w}^S) = -\mathcal{M}_h^{sgs}(\overline{\mathbf{u}}, \mathbf{w}_h) \ . \tag{30}$$

The subgrid model therefore acts only on the small resolved scales and takes often the form of an eddy-viscosity model, such as the Smagorinsky or the WALE models presented in Sec. 2.4.1.

Several variants of the VMS approach have been proposed in the literature. We refer to the works of Gravemeier [81], Ahmed *et al.* [4] and Rasthofer and Gravemeier [159] for an overview of the VMS approach and its application using various numerical discretization techniques.

In Chap. 10 we analyse the accuracy of the VMS approach in modelling the exact subgrid-stress term in the context of the discontinuous Galerkin method.

CHAPTER 3

THE DISCONTINUOUS GALERKIN METHOD

RÉSUMÉ DU CHAPITRE EN FRANÇAIS

Dans ce chapitre, nous fournissons une brève description de la discrétisation numérique et de la formulation de la méthode Galerkine discontinue utilisée dans ce travail.

En particulier, dans les Sec. 3.2 et 3.3, nous présentons la discrétisation spatiale, la formulation des flux numériques et la discrétisation temporelle considérées dans cette étude. Dans la Sec. 3.4, nous discutons ensuite de la nécessité des maillages d'ordre élevé et de l'intégration numérique. Enfin, la Sec. 3.5 décrit la base functionelle utilisée dans ce travail. La description présentée a pour objectif d'introduire la notation employée et d'illustrer les détails de formulation et de mise en œuvre qui seront pertinents pour l'analyse des résultats dans la suite de ce travail.

Une analyse plus détaillée des propriétés numériques et de la dérivation de la méthode Galerkine discontinue peut être trouvée dans plusieurs monographies dédiées [46, 57, 89].

3.1 INTRODUCTION AND OUTLINE OF THE CHAPTER

The discontinuous Galerkin method was originally introduced by Reed and Hill [160] for the solution of the neutron transport equations. The method was later extended to hyperbolic problems by Cockburn and Shu [48], who combined the DG method with explicit time integration by means of Runge-Kutta type methods. Several approaches have also been developed for the solution of parabolic and elliptic problems, which propose different ways of dealing with the discretization of the diffusive fluxes [9]. The first application of this approach to the compressible NS equations is due to Bassi and Rebay [14]. Since then the DG method has been gaining a growing amount of interest as demonstrated by the large number of related research, dedicated monographs [46, 57, 89], joint research projects [110, 111] and the series of *International Workshops on High-Order CFD Methods (HiOCFD)* [196].

An overview of the many interesting properties of the DG method has already been presented in Chap. 1. In this chapter a brief description is provided of the numerical discretization and the specific formulation employed in the present work. In particular, in Sec. 3.2 and 3.3 we present the spatial discretization, the formulation of the numerical fluxes and the time discretization considered in this research. In Sec. 3.4 we then discuss the requirement of high-order meshes and numerical integration. Finally in Sec. 3.5 the expansion basis selected in this work is described.

For a more detailed analysis of the numerical properties and the derivation of the DG method, we refer to the works cited above.

3.2 THE SPATIAL DISCRETIZATION

Let us consider Ω_h to be a shape-regular partitioning of the domain $\Omega \subset \mathbb{R}^d$ into N non-overlapping and non-empty elements K of characteristic size h_K. We further define the sets $\mathcal{E}_i$ and $\mathcal{E}_b$ of interior and boundary faces in Ω_h such that $\mathcal{E}_h = \mathcal{E}_i \cup \mathcal{E}_b$.

Let $S_h^p = \left\{\phi \in L^2(\Omega_h) : \phi|_K \in \mathcal{P}^p(K), \forall K \in \Omega_h\right\}$ be the functional space formed by piecewise polynomials of partial degree at most p defined in the element, and $(\phi_K^1, \dots \phi_K^{N_p}) \in \mathcal{P}^p(K)$ a basis of $\mathcal{P}^p(K)$ of dimension $N_p = (p+1)^d$.

The solution in each element is thus expressed as

$$\mathbf{u}_h(\mathbf{x}, t) = \sum_{l=1}^{N_p} \phi_K^l(\mathbf{x}) \mathbf{u}_K^l(t), \qquad \forall \mathbf{x} \in K, K \in \Omega_h, \forall t > 0 \ , \tag{31}$$

in which the polynomial coefficients $(\mathbf{u}_K^l)_{1 \le l \le N_p}$ represent the degrees of freedom (dofs) of the discrete problem in element K. The semi-discrete variational form of the NS equations Eq. (1) therefore reads: find $\mathbf{u}_h$ in S_h^p such that $\forall \phi_h \in S_h^p$

$$\int_{\Omega_h} \phi_h \partial_t \mathbf{u}_h \mathrm{d}V + \mathcal{L}_c(\mathbf{u}_h, \phi_h) + \mathcal{L}_v(\mathbf{u}_h, \phi_h) = 0 \ . \tag{32}$$

In Eq. (32) $\mathcal{L}_c$ and $\mathcal{L}_v$ represent the variational projection of the convective and the viscous terms onto the functional space S_h^p. Their formulation is described in the following sections. For this purpose, we introduce the following notation. For any internal face e in $\mathcal{E}_i$, we define u^+ and u^- to be the traces of a variable u onto the interface e taken from the interior of element K^+ and the interior of element K^- (see Fig. 1). That is

$$u^{\pm}(\mathbf{x}_e) = \lim_{\mathbf{x} \to \mathbf{x}_e, \mathbf{x} \in K^{\pm}} u(\mathbf{x}) \ , \qquad \forall \mathbf{x}_e \in e \ , \tag{33}$$

where K^+ and K^- such that the normal $\mathbf{n}$ to e points outwards from K^+ to K^-, as shown in Fig. 1. We additionally define the average and jump operators as

$$\{\!\{u\}\!\} = \left(u^+ + u^-\right)/2 \quad , \qquad [\![u]\!] = u^+ - u^- \ , \tag{34}$$

$$\{\!\{\mathbf{u}\}\!\} = \left(\mathbf{u}^+ + \mathbf{u}^-\right)/2 \quad \text{and} \quad [\![\mathbf{u}]\!] = \left(\mathbf{u}^+ - \mathbf{u}^-\right) \otimes \mathbf{n} \ . \tag{35}$$

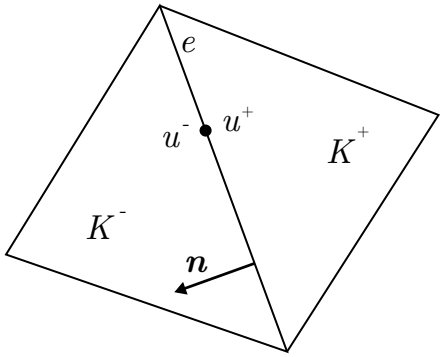

Figure 1 – Inner and exterior elements K^+ and K^-, definition of traces $u^{\pm}$, and of the outward unit normal vector $\mathbf{n}$.

3.2.1 *Discretization of the inviscid operator*

The discrete variational form of the inviscid term reads

$$\mathcal{L}_c(\mathbf{u}_h, \phi_h) = -\int_{\Omega_h} \boldsymbol{\mathcal{F}}_c(\mathbf{u}_h) \cdot \boldsymbol{\nabla}\phi_h \mathrm{d}V + \int_{\mathcal{E}_i} [\![\phi_h]\!] \mathbf{h}_c(\mathbf{u}_h^+, \mathbf{u}_h^-, \mathbf{n}) \mathrm{d}S + \int_{\mathcal{E}_b} \phi_h^+ \boldsymbol{\mathcal{F}}_c(\mathbf{u}_b) \cdot \mathbf{n} \mathrm{d}S \ . \tag{36}$$

The boundary values $\mathbf{u}_b = \mathbf{u}_b(\mathbf{u}_h^+, \mathbf{u}_{\text{ext}}, \mathbf{n})$, with $\mathbf{u}_{\text{ext}}$ a reference external state, are computed so as to impose the appropriate natural boundary condition on each physical boundary.

The function $\mathbf{h}_c$ in Eq. (36) is a numerical flux that approximates the convective flux on an element face. The numerical flux must satisfy two conditions

- conservativity : $\mathbf{h}_c(\mathbf{u}_h^+, \mathbf{u}_h^-, \mathbf{n}) = -\mathbf{h}_c(\mathbf{u}_h^-, \mathbf{u}_h^+, -\mathbf{n})$,
- consistency: $\mathbf{h}_c(\mathbf{u}, \mathbf{u}, \mathbf{n}) = \boldsymbol{\mathcal{F}}_c(\mathbf{u}) \cdot \mathbf{n}$.

In this work we employ two different numerical fluxes:

- the Roe flux [82, 164]:

$$\mathbf{h}_c^{\text{Roe}}(\mathbf{u}_h^+, \mathbf{u}_h^-, \mathbf{n}) := \{\!\{\boldsymbol{\mathcal{F}}_c(\mathbf{u}_h)\}\!\} \cdot \mathbf{n} + \frac{1}{2} \tilde{\boldsymbol{\mathcal{R}}} \, |\tilde{\lambda}| \, \tilde{\boldsymbol{\mathcal{R}}}^{-1} \left(\mathbf{u}_h^+ - \mathbf{u}_h^-\right) \ , \tag{37}$$

  where $\boldsymbol{\mathcal{R}}$ is the matrix of the right eigenvectors of $\boldsymbol{\mathcal{A}}$, $\boldsymbol{\mathcal{A}} := \partial(\boldsymbol{\mathcal{F}}_c(\mathbf{u}) \cdot \mathbf{n})/\partial \mathbf{u}$ is the Jacobian matrix of the inviscid fluxes in the direction of $\mathbf{n}$, $|\lambda|$ is the diagonal matrix formed by the absolute value of the eigenvalues λ_i of $\boldsymbol{\mathcal{A}}$, and the symbol $\tilde{(\cdot)}$ indicates that the matrices are computed using Roe averages [164]. The Harten fix is employed to capture the correct entropy solution [82].

- the Local Lax Friedrichs (LLF) flux:

$$\mathbf{h}_c^{\text{LLF}}(\mathbf{u}_h^+, \mathbf{u}_h^-, \mathbf{n}) := \{\!\{\boldsymbol{\mathcal{F}}_c(\mathbf{u}_h)\}\!\} \cdot \mathbf{n} + \frac{1}{2} \alpha \left(\mathbf{u}_h^+ - \mathbf{u}_h^-\right) \ , \tag{38}$$

where $\alpha = \max\left\{\rho_s(\boldsymbol{\mathcal{A}}(\mathbf{u})) : \mathbf{u} = \mathbf{u}_h^{\pm}\right\}$ and ρ_s is the spectral radius.

Later in this work we also consider a modified version of both the Roe and LLF fluxes where the upwind component is scaled by a parameter $k \in [0, 1]$. The parameter k can therefore be employed to control the amount of numerical dissipation introduced by the discretization of the inviscid term.

3.2.2 *Discretization of the viscous operator*

Three approaches are employed in the present work for the discretization of the viscous terms in Eq. (32): the *symmetric interior penalty (SIP)* method by Hartmann and Houston [85], and the *BR*1 and *BR*2 methods of Bassi *et al.* [12–14]. These are briefly outlined below.

3.2.2.1 *The symmetric interior penalty method*

Using the SIP method, the discrete variational form of the viscous term reads:

$$\begin{aligned}\mathcal{L}_v(\mathbf{u}_h, \phi_h) = \quad & \int_{\Omega_h} \boldsymbol{\mathcal{F}}_v(\mathbf{u}_h, \boldsymbol{\nabla}\mathbf{u}_h) \cdot \boldsymbol{\nabla}\phi_h \mathrm{d}V \\ & - \int_{\mathcal{E}_i} [\![\phi_h]\!] \{\!\{\boldsymbol{\mathcal{F}}_v(\mathbf{u}_h, \boldsymbol{\nabla}\mathbf{u}_h)\}\!\} \cdot \mathbf{n} \mathrm{d}S - \int_{\mathcal{E}_b} \phi_h^+ \boldsymbol{\mathcal{F}}_v(\mathbf{u}_b, \boldsymbol{\nabla}\mathbf{u}_b) \cdot \mathbf{n} \mathrm{d}S \\ & - \int_{\mathcal{E}_i} [\![\mathbf{u}_h]\!] \{\!\{\mathcal{G}^T(\mathbf{u}_h)\boldsymbol{\nabla}\phi_h\}\!\} \cdot \mathbf{n} \mathrm{d}S - \int_{\mathcal{E}_b} (\mathbf{u}_h^+ - \mathbf{u}_b) \{\!\{\mathcal{G}^T(\mathbf{u}_h)\boldsymbol{\nabla}\phi_h\}\!\} \cdot \mathbf{n} \mathrm{d}S \\ & + \int_{\mathcal{E}_i} \delta_{IP}(\mathbf{u}_h) [\![\phi_h]\!] \mathrm{d}S + \int_{\mathcal{E}_b} \delta_{IP}(\mathbf{u}_h, \mathbf{u}_b) \phi_h^+ \mathrm{d}S \ ,\end{aligned} \tag{39}$$

where $\mathcal{G} \coloneqq \partial\boldsymbol{\mathcal{F}}_v / \partial(\boldsymbol{\nabla}\mathbf{u}_h)$ is the so-called homogeneity tensor, and δ_{IP} is the penalty function defined as

$$\delta_{IP}(\mathbf{u}_h) = \eta_{IP} \frac{p^2}{h_e} \{\!\{G(\mathbf{u}_h)\}\!\} [\![\mathbf{u}_h]\!] \quad \text{, with} \quad h_e = \frac{\min(|K^+|, |K^-|)}{|e|} \ , \tag{40}$$

and a similar expression consistent with the boundary conditions is derived for the boundary faces. The penalty parameter η_{IP} has to be chosen sufficiently large to ensure numerical stability [85].

3.2.2.2 *The BR1 and BR2 methods*

An alternative formulation has been presented by Bassi and Rebay in [14]. This approach consists in formulating the NS equations as a system of first-order partial

differential equations by introducing an auxiliary variable $\boldsymbol{\sigma}_h$ representing the gradient of the state vector. The auxiliary variable then satisfies the following discrete equation

$$\int_{\Omega_h} \phi \boldsymbol{\sigma}_h \mathrm{d}V = \int_{\Omega_h} \phi \boldsymbol{\nabla} \mathbf{u}_h \mathrm{d}V - \int_{\mathcal{E}_i} \{\!\{\phi\}\!\} [\![\mathbf{u}_h]\!] \mathrm{d}S - \int_{\mathcal{E}_b} \frac{\phi^+}{2} \left[\mathbf{u}_h^+ - \mathbf{u}_b\right] \otimes \mathbf{n} \mathrm{d}S \ . \tag{41}$$

This equation can be rewritten by introducing the so called lifting operator $\boldsymbol{L}_h$ such that

$$\boldsymbol{\sigma}_h = \boldsymbol{\nabla} \mathbf{u}_h + \boldsymbol{L}_h \ , \tag{42}$$

and $\boldsymbol{L}_h$ satisfies the following condition

$$\int_{\Omega_h} \phi \boldsymbol{L}_h \mathrm{d}V = - \int_{\mathcal{E}_i} \{\!\{\phi\}\!\} [\![\mathbf{u}_h]\!] \mathrm{d}S - \int_{\mathcal{E}_b} \frac{\phi^+}{2} \left[\mathbf{u}_h^+ - \mathbf{u}_b\right] \otimes \mathbf{n} \mathrm{d}S \ . \tag{43}$$

The discrete variational form of the viscous term takes therefore the form

$$\begin{aligned} \mathcal{L}_v(\mathbf{u}_h, \phi_h) = & \int_{\Omega_h} \boldsymbol{\mathcal{F}}_v(\mathbf{u}_h, \boldsymbol{\nabla} \mathbf{u}_h + \boldsymbol{L}_h) \cdot \boldsymbol{\nabla} \phi_h \mathrm{d}V \\ & - \int_{\mathcal{E}_i} [\![\phi_h]\!] \{\!\{\boldsymbol{\mathcal{F}}_v(\mathbf{u}_h, \boldsymbol{\nabla} \mathbf{u}_h + \boldsymbol{L}_h)\}\!\} \cdot \mathbf{n} \mathrm{d}S - \int_{\mathcal{E}_b} \phi_h^+ \boldsymbol{\mathcal{F}}_v(\mathbf{u}_b, \boldsymbol{\nabla} \mathbf{u}_b + \boldsymbol{L}_h) \cdot \mathbf{n} \mathrm{d}S \ . \end{aligned} \tag{44}$$

The resulting scheme, commonly known as the $BR1$ scheme, is of order $p+1$ for both the solution and its gradient, however it presents some drawbacks pointed out by the authors in [12] and [13]. First, the scheme is not compact as the computation of the surface terms in Eq. (44) for each element requires the knowledge of the lifting operator in the neighbouring elements. This in turn requires knowledge of the trace of the solution at the interface with each of its neighbouring elements resulting in an extended stencil. Additionally the scheme is only marginally stable [9] and does not introduce sufficient dissipation at wavenumbers close to the grid cut-off, as shown *e. g.* in [7].

Bassi *et al.* [12, 13] have proposed to overcome these drawbacks by introducing the concept of local and global lifting operators. The local lifting operator $\boldsymbol{l}_h^e$ is defined for each internal face $\mathcal{E}_i$ as an auxiliary variable satisfying the following equation

$$\int_{K^+ \cup K^-} \phi \boldsymbol{l}_h^e \mathrm{d}V = - \int_{\partial K^+ \cap \partial K^-} [\![\phi]\!] [\![\mathbf{u}_h]\!] \mathrm{d}S \ . \tag{45}$$

A similar expression consistent with the boundary conditions is derived for the boundary faces $\mathcal{E}_b$. The global lifting operator is defined by Eq. (43), as in the $BR1$ method, and can be evaluated in each element K as $\boldsymbol{L}_h = \sum_{e \in \partial K} \boldsymbol{l}_h^e$.

The discrete variational form of the viscous term is then expressed as

$$\begin{aligned}\mathcal{L}_v(\mathbf{u}_h, \phi_h) = &\int_{\Omega_h} \boldsymbol{\mathcal{F}}_v(\mathbf{u}_h, \boldsymbol{\nabla}\mathbf{u}_h + \boldsymbol{L}_h) \cdot \boldsymbol{\nabla}\phi_h \mathrm{d}V \\ &- \int_{\mathcal{E}_i} [\![\phi_h]\!] \{\!\{ \boldsymbol{\mathcal{F}}_v(\mathbf{u}_h, \boldsymbol{\nabla}\mathbf{u}_h + \eta_{BR2}\boldsymbol{l}_h^e) \}\!\} \cdot \mathbf{n} \mathrm{d}S \\ &- \int_{\mathcal{E}_b} \phi_h^+ \boldsymbol{\mathcal{F}}_v(\mathbf{u}_b, \boldsymbol{\nabla}\mathbf{u}_b + \eta_{BR2}\boldsymbol{l}_h^e) \cdot \mathbf{n} \mathrm{d}S \ ,\end{aligned} \tag{46}$$

where η_{BR2} is a numerical parameter that ensures the stability of the method.

3.3 DISCRETIZATION OF TIME DERIVATIVES

A non-linear system of equations can be obtained for the polynomial coefficients of the solution by considering as test functions in Eq. (32) the basis functions ϕ_K^i. The time derivative term can thus be written in the form

$$\int_{\Omega_h} \phi_K^i \partial_t \mathbf{u}_h \mathrm{d}V = \sum_{j=1}^{N_p} \partial_t \mathbf{u}_K^i \int_K \phi_K^i \phi_K^j \mathrm{d}V \ , \qquad \forall K \in \Omega_h, i = 1, \ldots, N_p \ . \tag{47}$$

Using this relation, Eq. (32) can be expressed formally as

$$M\partial_t \mathbf{U} = \mathcal{R}(\mathbf{U}) \ , \tag{48}$$

in which $\mathbf{U}$ is the vector of degrees of freedom $\mathbf{u}_K^i(t)$, $\mathcal{R}$ is the residual vector composed of the convective and diffusive terms $\mathcal{L}_c$ and $\mathcal{L}_v$, and M is a block-diagonal matrix of which the K-th block is the mass matrix of element K, with components

$$M_{ij}^K = \int_K \phi_K^i \phi_K^j \mathrm{d}V \ . \tag{49}$$

Equation (48) constitutes a system of ordinary differential equations for the evolution of the dofs $\mathbf{u}_K^i(t)$. It can be solved with any discretization scheme starting from the initial condition $\mathbf{u}_h(\mathbf{x}, 0) = \sum_K \sum_i \mathbf{u}_K^i(0)\phi_K^i$ with $\mathbf{u}_h(\mathbf{x}, 0)$ being the projection of the initial condition $\mathbf{u}_0(\mathbf{x})$ on the discretization space.

In the present work two types of temporal discretization schemes are employed. For steady problems the implicit Euler method is used to advance the solution in time starting from a fictitious initial condition until the steady state solution is achieved. The GMRES method with ILU(0) preconditioning is employed to solve the resulting non-linear system of equations. Unsteady flow simulations are carried out using Runge-Kutta (RK) type schemes. In particular, we employ the second-order two-stage Strong Stability Preserving (SSP) scheme, also referred to as the Heun scheme, and the third-order four-stage SSP scheme by Spiteri and Ruuth [175].

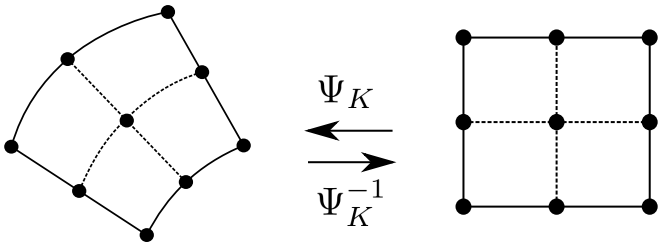

Figure 2 – Example of second-order curvilinear element and mapping between reference and physical element.

3.4 HIGH-ORDER ELEMENTS AND NUMERICAL INTEGRATION

As discussed in Sec. 3.2, the discretization of the considered set of equations requires the partitioning of the computational domain Ω into a set Ω_h composed of elements K referred to as the computational mesh. High-order meshes are required to achieve the nominal order of accuracy of high-order methods such as DG, SEM and FR, in the presence of curved boundaries. Unlike linear meshes, which are characterized by edges corresponding to straight lines and faces that are planes, high-order meshes are characterized by curved elements. An example of curved element is shown in Fig. 2. Each curvilinear element is described by a function Ψ_K mapping each point of a reference element K_{ref} in a reference system of coordinates $\boldsymbol{\xi}$ to the coordinates $\mathbf{x}$ of the element in the physical frame. The mapping function is a polynomial of a given degree which defines the order of the mesh.

To evaluate the volume integrals in Eq. (32) the mapping between the reference and physical element is used such that for any function $f(\mathbf{x})$

$$\int_K f(\mathbf{x})\mathrm{d}\mathbf{x} = \int_{K_{ref}} f(\Psi(\boldsymbol{\xi}))J_K(\boldsymbol{\xi})\mathrm{d}\boldsymbol{\xi} \ , \tag{50}$$

where $J_K(\boldsymbol{\xi}) \equiv \det(\boldsymbol{\nabla}\Psi_K)$ is the determinant of the Jacobian of the transformation. A similar operation is performed to evaluate surface integrals. Integration is then performed by numerical quadrature.

In this work, each element is mapped to a reference cube (surfaces are mapped to a reference square) and the integrals are evaluated by Gaussian quadrature with q integration points per space direction. We recall that this quadrature formula is exact for the integration of polynomials of maximum partial degree lower than or equal to $2q-1$.

The number of integration points can be locally adapted, for example depending on the local polynomial degree of the approximation of the solution and/or on the level of distortion of the element (see App. A).

3.5 THE EXPANSION BASIS

The expansion basis employed influences the numerical efficiency, conditioning, as well as the approximation properties of the DG method. Commonly used bases are the Legendre polynomials, which are often employed in reference frame formulations, or the Lagrange polynomials, also referred to as nodal basis [101]. In the present work we employ hierarchical orthonormal basis functions following the procedure outlined by Bassi *et al.* [17].

In order to describe the algorithm for the generation of this basis, we indicate with $\Phi_K^p = \{\phi_K^1, \dots, \phi_K^{N_p}\}$ the generic basis of the polynomial space $\mathcal{P}^p(K)$, and $\Phi^p = \{\Phi_K^p\}_{K\in\Omega_h}$ the corresponding basis of the broken Sobolev space S_h^p. Additionally, we recall that Φ_K^p, and by extension Φ^p, is a hierarchical basis if it is contained in the higher-order basis, that is $\Phi_K^p \subset \Phi_K^{p+1}$.

Let us denote by $\hat{\Phi}_K^p = \{\hat{\phi}_K^i\}_{i=1,\dots,N_p}$ an initial set of linearly independent basis functions. In the present work, we consider the initial basis $\hat{\Phi}_K^p$ as the set of normalized monomials of maximum partial degree p, namely,

$$\Phi_K^p = \left\{ \frac{\prod_{i=1}^{d} \chi_i^{\alpha_i}}{\left\| \prod_{i=1}^{d} \chi_i^{a_i} \right\|_K} \right\}_{\mathbf{a}\in\mathbb{N}^d, \|\mathbf{a}\|_\infty \le p} \tag{51}$$

where $\{\chi_i\}_{i=1,\dots,d}$ are the coordinates in a physical frame which is centered on the centroid of K and is aligned with the principal axes of K.

A new set of orthonormal basis functions can be obtained from $\hat{\Phi}_K^p$ by applying the modified Gram-Schmidt (MGS) orthonormalization algorithm. The procedure is presented in Alg. 1, where $(\cdot,\cdot)_K$ refers to the L^2-product on element K, *i.e.* $(u,v)_K = \int_K uv\mathrm{d}V$.

Algorithm 1 : The modified Gram-Schmidt algorithm.

```
for i = 1 to N_p do
    for j = 1 to i − 1 do
        r_ij^K = (φ̂_K^i, φ_K^j)_K
        φ̂_K^i = φ̂_K^i − r_ij^K φ_K^j
    end
    r_ii^K = sqrt((φ̂_K^i, φ̂_K^i)_K)
    φ_K^i = φ̂_K^i / r_ii^K
end
```

The resulting basis is orthonormal as the steps at line 4 and line 7 lead to $(\phi_K^i, \phi_K^j) = \delta_{ij}$. Additionally, it can produce a hierarchical basis as the set Φ_K^{p+1} can be obtained from Φ_K^p by introducing $N_{p+1} - N_p$ additional functions which can be orthonormalized by the MGS algorithm while keeping unchanged the first N_p functions.

We note that the application of Alg. 1 is performed numerically and therefore requires the evaluation of the coefficients r_{ij}^K by numerical integration and the computation of the steps at line 4 and line 7 at the quadrature points. This procedure, however, presents two shortcomings. First, the exact evaluation of the coefficients r_{ij}^K might require an extremely large number of quadrature points (see App. A). As a result, in practice, this is performed using the same quadrature rule as that employed for the evaluation of the volume integrals of Eq. (32). The basis is therefore only numerically orthonormal with respect to the employed quadrature formula. The second shortcoming is that the basis functions are specific to the element and are only available at the quadrature points. Thus, in terms of implementation, three possible choices are available:

1. The initial basis is generated and the MGS algorithm is applied each time the local basis needs to be employed;
2. The coefficients r_{ij}^K are evaluated only once and stored in memory for each element. The initial basis and the MGS algorithm, skipping line 3 and 6, are evaluated each time the local basis is required;
3. The generated orthonormal basis (and the corresponding derivatives) are computed only once and stored in memory.

In the present work the last approach is employed, which leads to the highest memory requirement but the lowest computational cost. The second option provides an intermediate approach as it largely reduces the memory requirement whilst allowing a reduction of the computational cost as compared to option 1. This approach is particularly useful when the basis or the quadrature points need to be frequently updated during the simulation. This is the case when performing dynamic p-adaptive simulations as described in Chap. 8.

CHAPTER 4

RESOLUTION ADAPTATION STRATEGIES

RÉSUMÉ DU CHAPITRE EN FRANÇAIS

L'objectif de ce chapitre est de présenter les stratégies et d'adaptation de résolution spatiale employées dans le cadre de cette étude.

Une des propriétés les plus intéressantes de la méthode DG est la possibilité d'adapter localement le degré polynomial local de la solution (adaptation-*p*), et donc sa précision formelle, en plus de la résolution spatiale associée au raffinement de maillage local (adaptation-*h*). Grâce au taux de convergence exponentielle de la méthode DG par rapport au degré polynomial, on peut utiliser l'adaptation-p pour obtenir la réduction la plus rapide des erreurs de dissipation et de dispersion pour des problèmes lisses. En présence de discontinuités physiques ou géométriques, l'adaptation-h est nécessaire en raison de la réduction du taux de convergence et de l'apparition d'oscillations numériques dues au phénomène de Gibbs. Trois catégories de techniques d'adaptation-h peuvent être identifiées : la division/agglomération d'éléments, la déformation du maillage sans changement de topologie (adaptation-*r*), et le remaillage. Une vue d'ensemble décrivant les avantages et les inconvénients des différentes techniques d'adaptation-*h* et -*p* est présentée dans la Sec. 4.2.

L'algorithme d'adaptation pour les problèmes stationnaires est décrit dans la Sec. 4.3. La précision et l'efficacité de l'algorithme adaptatif sont principalement déterminées par la technique d'estimation d'erreur employée. Un aperçu des diverses stratégies d'estimation des erreurs utilisées dans la littérature est fourni dans la Sec. 4.4. Il est suivi par une description détaillée des estimateurs d'erreur utilisés dans le reste de ce travail. En particulier, dans la Sec. 4.4.6 nous présentons un nouvel estimateur d'erreur qui a été développé dans le cadre de cette étude.

Une fois la distribution de l'estimateur d'erreur locale obtenue, une procédure de marquage est utilisée pour identifier les éléments qui nécessitent un raffinement ou un déraffinement. Un aperçu des diverses stratégies de marquage développées dans la littérature est présenté dans la Sec. 4.5.

L'extension de l'algorithme adaptatif présenté à l'analyse des problèmes instationnaires peut être obtenue par deux approches différentes: l'adaptation dynamique et statique. La première stratégie consiste à adapter la résolution spatiale au cours de la

simulation pour suivre l'évolution des exigences de résolution. La deuxième stratégie est formellement similaire à l'adaptation de problèmes stables et consiste à identifier une résolution fixe dans le temps qui peut être utilisée pour améliorer la qualité de la solution au cours de la simulation complète. Les avantages et les points faibles des deux stratégies sont décrits dans la Sec. 4.6.

Enfin, dans la Sec. 4.7, nous présentons les défis spécifiques rencontrés dans le développement de stratégies d'adaptation pour les simulations LES. Ils sont liées à l'interaction de la modélisation et des erreurs numériques, à l'utilisation de la discrétisation numérique comme filtre implicite et au concept controversé de convergence de grille pour les simulations LES.

4.1 INTRODUCTION AND OUTLINE OF THE CHAPTER

In Chap. 1 we have outlined the importance of adaptation in improving the accuracy and reducing the computational cost for the simulation of flows on complex configurations. The objective of this chapter is therefore to provide an overview of resolution adaptation strategies and techniques employed in the present work.

For this purpose, in Sec. 4.2 we present various adaptation techniques which can be employed to modify the spatial resolution in the framework of DG methods. The general adaptation algorithm for steady flow computations is then discussed in Sec. 4.3. The efficiency of the algorithm is influenced by the specific choice of error estimation and marking strategy employed. Their role and several approaches used throughout this work are therefore presented in Secs. 4.4 and 4.5. In particular, a novel error indicator that we have developed over the course of this research is presented in Sec. 4.4.6

Thereafter in Sec. 4.6 we discuss two possible strategies for the extension of the adaptation algorithm for steady flows to the simulation of unsteady flows: *dynamic* and *static* adaptation. Finally Sec. 4.7 presents the specific challenges encountered in the development of adaptation strategies for LES of turbulent flows.

4.2 ADAPTATION TECHNIQUES

Several techniques have been developed to adapt the local spatial resolution to improve the accuracy and reduce the computational cost of CFD simulations. The DG method allows for the optimization of the local spatial resolution by either adapting the local mesh size (h-adaptation) or by modifying the local polynomial degree for the representation of the solution within element (p-adaptation). Three main h-adaptation techniques of can be distinguished:

- *element splitting/agglomeration* is one of the most commonly employed techniques for methods such as FV and DG which allow the use of non-conforming quadrilateral or hexahedral elements [8, 84, 177, 194]. In

this framework, a quadrilateral or hexahedral element which is identified as requiring refinement is divided into 2^d smaller child elements. Conversely, coarsening is performed by reverting a refinement step, *i. e.* agglomerating child elements into the original parent element. The described methodology is especially useful and commonly employed in dynamic adaptation strategies based on multi-resolution analysis. This is often combined with octree-based data-structures to keep track of the adaptive process. Despite its apparent simplicity, the implementation of *h*-adaptation by element splitting/agglomeration, especially in the case of dynamic anisotropic adaptation on distributed memory architectures, presents several difficulties due to the need of complex data-structures.

Albeit more common in the context of non-conforming hexahedral meshes, similar strategies have also been developed for simplicial and conforming meshes by employing edge splitting, collapse and swap [23, 53].

- A second approach, commonly referred to as *r-adaptation*, consists in the optimal distribution of the local resolution by deformation of the computational grid [34, 92, 127, 201]. Two main strategies are employed for this purpose. A first possibility consists in deforming the mesh by solving an optimization problem, often based on the elastic analogy, to distribute the nodes of the mesh based on the local resolution requirements, mesh quality or shock-fitting. In this case, *r*-adaptation can be considered as an off-line phase, separate from the flow simulation process, and requires the interpolation of the solution from the original to the *r*-adapted grid. A second strategy consists in the use of a moving grid which is deformed over the course of the simulation. In this case, the Arbitrary Lagrangian Eulerian (ALE) framework is employed which can take into account the movement of the mesh and is especially suited for the simulation of flows with moving boundaries. No additional interpolation is required, however, the method presents in general a higher computational cost as the fluid and mesh motion are coupled and must be solved at the same time. Additionally, specific techniques need to be employed to avoid mesh tangling.

  One of the main advantages of *r*-adaptation is the preservation of the mesh topology. This implies that for distributed memory machines the computational load remains well balanced throughout the simulation and does not require complex dynamic load balancing techniques. Nonetheless, *r*-adaptation presents a limited flexibility as the optimal resolution is fundamentally limited by the initial number of nodes and connectivity of the grid. Moreover the improvement of the resolution distribution might come at the cost of a reduction in mesh quality. This limitation can be mitigated by employing a mixed r-adaptive/element splitting/agglomeration approach.
- Finally a third approach to *h*-adaptation consists in *remeshing*. A complete regeneration of the computational grid is thus performed based on the definition

of a metric from a error estimate based on the available solution [67, 69, 161]. Remeshing provides the highest degree of flexibility. However, it can present a relatively high computational cost especially when dealing with complex three-dimensional configurations. Furthermore, at each adaptive iteration the solution needs to be interpolated on the new mesh over the entire computational domain, thus increasing the computational cost and possibly introducing interpolation errors.

As an alternative to *h*-adaptation, *p*-adaptation provides the fastest convergence rate for smooth problems. Indeed, it has been shown that, if the solution is sufficiently regular, the error converges as $\mathcal{O}(h^{p+1})$ [47, 48]. Additionally, *p*-adaptation is straightforward to implement in the framework of the DG method as it only requires the modification of the local basis functions set at each adaptation step. As a consequence, it does not require complex data-structures. Nonetheless, this strategy presents a lower flexibility as compared to other approaches. Indeed, *p*-adaptation is fundamentally limited by the underlying computational grid employed. Additionally, in practice, for some specific implementations of the DG method the maximum affordable local polynomial degree might be limited by the rapid increase of the computational cost with increasing *p*. Finally, the presence of geometrical or physical singularities, such as shock-waves, reduces the convergence rate of the method and introduces numerical oscillations when high polynomial degree representations are employed.

The optimal adaptive strategy would therefore consist in employing both *h*- and *p*-adaptation. *h*-adaptation increases the flexibility of the algorithm and allows for a more efficient adaptation of the solution near geometrical and physical discontinuities. Conversely, *p*-adaptation increases the convergence rate and the efficiency of the adaptive algorithm in smooth regions. The choice of either *h*- or *p*-adaptation is controlled by an *hp*-decision strategy. These are usually based on smoothness or regularity indicators, as described *e. g.* by Mitchell and McClain [139]. Their applicability to scale resolving simulations is however still an open subject for research and are not considered here.

Over the course of the present work *p*-adaptation and *h*-adaptation by element splitting/agglomeration are separately investigated. Most of the results to be presented focus on the analysis of the former strategy. Indeed the minimization of dissipation and dispersion errors by means of *p*-adaptation can provide the largest computational gain for turbulent flows at relatively low Mach numbers that are considered in this research.

4.3 THE ADAPTIVE ALGORITHM FOR STEADY PROBLEMS

A generic adaptive algorithm for steady problems is described by the graph in Fig. 3. A large number of variants can be derived depending on the specific type of

problem or adaptation technique employed. The process, outlined in Fig. 3, corresponds to the specific case of element splitting/agglomeration, from here on referred to as simply *h*-adaptation, and *p*-adaptation.

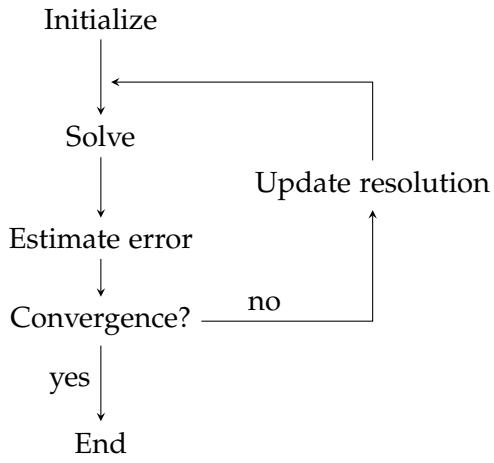

Figure 3 – Adaptive algorithm loop.

The adaptive simulation is *initialized* from a starting discretization defined by an initial computational grid and a given distribution of the local polynomial degree. The solution is then computed on the employed discretization during the *solve* phase. The quality of the solution and the spatial resolution is therefore assessed by computing a local *error estimator*, also called *refinement indicator*. Next, a *convergence* criterion is used to determine whether the considered discretization satisfies the specified user-defined requirement. Suitable convergence criteria include a global error indicator η_{glob} satisfying a user defined threshold, and the specification of a maximum number of dofs or of a maximum number of iterations of the adaptive algorithm.

If the convergence criterion is satisfied, the algorithm is stopped and the final solution is obtained. Otherwise the spatial discretization can be improved, at least in some regions of the computational domain. In this case, the spatial resolution is updated following the specific adaptation technique employed. In the case of *p*-adaptation and *h*-adaptation by element splitting/agglomeration, this phase is further divided in two successive steps: *marking* and *refinement/coarsening*.

The *marking* phase consists in the process by which the local error estimator is used to identify the elements that require increased resolution (marked for refinement) and those for which the local spatial resolution can be reduced without a significant loss of accuracy (marked for coarsening). The marking strategy significantly influences the robustness and efficiency, in terms of computational and accuracy gain, of the adaptive algorithm. Several marking strategies are described in Sec. 4.5.

Once the marking procedure is completed, the specific adaptation technique is applied by either splitting/agglomerating elements in the case of *h*-adaptation, or

by increasing/decreasing the polynomial degree in marked elements in the case of *p*-adaptation.

The newly adapted discretization is then employed to obtain an updated solution and the process is repeated.

In most practical applications, two additional steps are performed after the update of the resolution: *(re-)initialization* of the solution and, for distributed memory computations, *load balancing*. The former consists in starting the new simulation from the L^2-projection of the available solution on the newly adapted discretization space. For the considered *h/p*-adaptation strategies this operation is local and limited to marked elements. The second step consists in obtaining a partitioning of the computational grid such that the computational load is evenly distributed between the processes used for the parallel computation. For *hp*-adaptive simulations, the load balancing process presents specific difficulties as it requires the estimation of the local computational load associated with each element. Further discussion on this topic is provided in Chap. 7.

4.4 ERROR ESTIMATOR STRATEGIES

Considerable efforts have been dedicated to the development of robust *a-posteriori* error estimators for partial differential equations [91, 139, 165]. The large variety of refinement indicators reported in the literature can be classified in three main groups:

(i) *Feature based indicators* are often derived from physical or theoretical properties of the problem to be solved or from the observation that some phenomena must be fully resolved in order to obtain an accurate representation of the flow field. Examples include methods for vortex detection [140], boundary layer detection, or interface detection for two-phase flows [194]. These methods are often inefficient, lack of robustness and do not take into account error propagation. However, they are often inexpensive, simple to implement, and can provide reasonably good results when employed by expert users.

(ii) *Discretization-Error (DE) based indicators* identify for refinement regions characterized by high values of the error between the numerical and the exact solution. The most common strategy to estimate DE is to perform two simulations on successively refined discretization spaces and compare the two numerical solutions [148]. Other possible approaches include the computation of estimates of higher-order solutions [59], estimates of the truncation error from the decay rate of the Legendre expansion coefficients [130] or the exploitation of superconvergent phenomena [52]. A possible drawback of these methods is that the DE is produced in regions of insufficient spatial resolution and then diffused and convected as a scalar quantity [11, 165]. An adaptation process which is driven by local values of the DE would thus also refine regions where the error is transported and not produced, thus exhibiting sub-optimal performance. For

this reason, Residual-Error (RE) and Truncation-Error (TE) based methods are often employed in the FE and FV frameworks, respectively. This is justified by the fact that the TE and the RE appear as production terms in the discretization error transport equations [11, 84, 105, 165, 167, 178]. In the FE framework, RE-based methods can often be classified as DE-based estimators since RE estimates can provide DE bounds provided that suitable norms are employed.

(iii) *Goal oriented indicators* evaluate the contribution of the numerical error to the error in the evaluation of a target functional (e.g. the drag or the lift coefficient). Their derivation requires the computation of element-wise residuals which are weighted by the solution of a dual problem derived from the discretization employed and the target quantity. These methods capture the inherent mechanism of error propagation in hyperbolic and nearly-hyperbolic problems. Thanks to this property, they have been shown to provide the lowest computational cost to achieve a prescribed level of accuracy when a target functional is the goal of a simulation [62, 66, 83, 84]. However, the solution of the adjoint problem must be performed in a refined discretization space [66] and requires the backward integration in time for unsteady problems, thus requiring the numerical solution to be known at each previous time step. This can lead to prohibitively high computational and memory requirements. Furthermore, the adjoint problem for chaotic systems, such as scale resolving simulations of turbulent flows, produce intractably high and inaccurate sensitivities. This issue, often described as the 'butterfly effect', is due to the sensitivity of chaotic systems to the initial condition and leads to the divergence of sensitivity derivatives for time averaged quantities [116]. Despite the introduction of alternative techniques, such as ensemble averaging of short-time adjoints [117] or Least Square Shadowing [195], the computational cost of these methods currently limits their application to relatively simple chaotic systems and low Reynolds number flows, see *e. g.* [144].

In the present work, we focus our analysis on DE- and RE-based refinement indicators. Goal oriented/adjoint-based methods are not considered. Despite the fact that a vast number of authors have demonstrated their superiority with respect to DE methods for steady problems, the outlined limitations prohibit their application to turbulent flow configurations of industrial interest. Conversely, DE- and feature-based refinement indicators have already been successfully applied to LES, as discussed later in Sec. 4.7, and are of interest thanks to the very limited computational overhead required [3, 8, 140, 185].

In the remainder of this section, the error estimators/refinement indicators considered in this research are introduced. First, three refinement indicators that can be classified as DE- or feature-based indicators are presented: the *small-scale energy density*, the *spectral decay* and the *non-conformity error* indicators. Second, two additional indicators are introduced: the *residual-based* and the *residuum-non-conformity* indicator.

These can be described as RE-based indicators. Finally, in Sec. 4.4.6 a novel DE-based *small-scale lifted indicator* introduced in the present work is described.

4.4.1 *The SSED indicator*

The first refinement indicator that we consider in this work has been developed by Kuru *et al.* [113] in the context of the variational multiscale simulation (VMS) approach [93] and is defined as

$$\eta_K := \left(\int_K \left\| (\rho \mathbf{v})_{h,p} - (\rho \mathbf{v})_{h,p-1} \right\|^2 \mathrm{d}V \right)^{\frac{1}{2}} = \left\| (\rho \mathbf{v})_{h,p} - (\rho \mathbf{v})_{h,p-1} \right\|_{L^2(K)} \tag{52}$$

where $(\rho \mathbf{v})_{h,p-1}$ is the projection of the discrete momentum density on the reduced-order space S_h^{p-1}. This refinement indicator acts as a DE estimate for $\mathbf{u}_{h,p}$ based on a lower-order solution. It can also be interpreted as a feature-based refinement indicator, measuring the 'kinetic energy' associated with the highest-order modes.

While in the original work [113] this indicator has been referred to as VMS indicator, this error estimator is not directly related to the VMS approach. Therefore, in order to avoid confusion, we reckon it would be more appropriate to refer to it as the *small-scale energy density* (SSED) indicator.

This estimator bears strong similarities with the refinement indicator proposed by Mavriplis [129, 130] for which an additional term, that depends on the decay rate of the modal coefficients, is also included. The corresponding DE estimate developed, however, has been shown to produce relatively poor estimates of the exact DE for two- and three-dimensional problems [128]. For this reason, this indicator is not considered here.

As regards the original version of the SSED indicator, we have observed that poor results can be obtained from the use of this indicator when a mesh with large variation in element size in the domain is employed. In this work a normalized version of the SSED indicator is therefore considered, namely,

$$\eta_K^{SSED} := \frac{\left\| (\rho \mathbf{v})_{h,p} - (\rho \mathbf{v})_{h,p-1} \right\|_{L^2(K)}}{|K|^{\frac{1}{2}}} \ , \tag{53}$$

where $|K|$ is the volume of the element.

4.4.2 *The spectral decay indicator*

The so-called spectral decay indicator has been first introduced as a discontinuity sensor by Persson and Peraire [151] for shock-capturing to stabilize numerical simu-

lations in the presence of discontinuities. The spectral decay indicator, also known as smoothness indicator, is defined as

$$S_e := \frac{\left\| f(\mathbf{u}_{h,p}) - f(\mathbf{u}_{h,p-1}) \right\|_{L^2(K)}}{\left\| f(\mathbf{u}_{h,p}) \right\|_{L^2(K)}} \,, \tag{54}$$

where $\mathbf{u}_{h,p-1}$ represents the projection of the numerical solution on S_h^{p-1} and f is a function that depends on the solution. In [151], the authors have employed this smoothness indicator as a shock-capturing parameter based on either the entropy or the enthalpy for $f(\mathbf{u})$. In successive works, Gassner *et al.* [73] have considered Eq. (54) based on the momentum density in one direction as a refinement indicator. Finally, Tumolo *et al.* [3, 185–187] have used this refinement indicator for the adaptive simulation of various CFD configurations. Following their approach, we define the spectral decay indicator as

$$\eta_K^{SD} := \frac{\left\| (\rho\mathbf{v})_{h,p} - (\rho\mathbf{v})_{h,p-1} \right\|_{L^2(K)}}{\left\| (\rho\mathbf{v})_{h,p} \right\|_{L^2(K)}} \,. \tag{55}$$

Note that Eq. (55) corresponds to the SSED indicator in Eq. (52) normalized by the total 'energy' in the cell defined by $\left\| (\rho\mathbf{v})_{h,p} \right\|_{L^2(K)}$.

4.4.3 *The non-conformity error indicator*

The third refinement indicator considered in this work is the so-called non-conformity (NCF) error. This indicator is based on the assumption that, unless a physical discontinuity is present, the exact solution is continuous across element faces. This implies that a jump in the numerical solution can be considered as a measure of the error. For this reason, Krivodonova *et al.* [108, 109] have introduced the following discontinuity sensor

$$\eta_K := \max_{\mathcal{E}\in\partial K} \max_j \left| \frac{[\![u_h(\mathbf{x}_j)]\!]}{2\{\!\{ u_h(\mathbf{x}_j) \}\!\}} \right| \,, \tag{56}$$

where u_h is a variable, such as the density or the pressure, and $\mathbf{x}_j$ are the positions of the quadrature points on the element faces. This error estimator can also be considered as a local DE estimator. This is thanks to the superconvergent phenomena at outflow boundaries exhibited by some particular formulations of the DG method [108, 109]. Gassner and Altmann [73] and Blaise and St-Cyr [24] have employed this quantity as a refinement indicator. Following their approach, we indicate as non-conformity error indicator

$$\eta_K^{NCF} := \max_{\mathcal{E}\in\partial K} \max_j \frac{\left\| (\rho\mathbf{v}_h)^+(\mathbf{x}_j) - (\rho\mathbf{v}_h)^-(\mathbf{x}_j) \right\|}{2\left\| \{\!\{ (\rho\mathbf{v}_h)(\mathbf{x}_j) \}\!\} \right\|} \,. \tag{57}$$

4.4.4 *The residual-based indicator*

The residual-based refinement indicator described here follows from the classical derivation of residual-based error estimators for FE methods [5] and that by Hartmann and Houston [86]. Let us write the semidiscrete form of Eq. (32) as

$$\mathcal{N}_h(\mathbf{u}_h, \mathbf{w}) = 0 \qquad \forall \mathbf{w} \in [S_h^p]^{d+2} \tag{58}$$

and let $J(\mathbf{u})$ be a non-linear target functional. Provided that the target functional satisfies a compatibility condition [86], it is possible to show that

$$J(\mathbf{u}) - J(\mathbf{u}_h) = -\mathcal{N}_h(\mathbf{u}_h, \mathbf{z}) \ , \tag{59}$$

where $\mathbf{z}$ is the solution of an adjoint problem derived from the target functional $J(\mathbf{u})$. The derivation of this result corresponds to the general derivation of duality-based *a-posteriori* error estimators. Manipulating the semi-discrete operator Eq. (58), we obtain

$$\mathcal{N}_h(\mathbf{u}_h, \mathbf{w}) = \sum_{K \in \Omega_h} \left[\int_K \mathbf{R}(\mathbf{u}_h) \mathbf{w} \mathrm{d}V \ + \int_{\partial K \cap \mathcal{E}_i} \mathbf{r}(\mathbf{u}_h) \mathbf{w}^+ \mathrm{d}S \ + \int_{\partial K \cap \mathcal{E}_b} \mathbf{r}_b(\mathbf{u}_h) \mathbf{w}^+ \mathrm{d}S \right] \ , \tag{60}$$

in which the terms on the right-hand side are defined as

$$\mathbf{R}(\mathbf{u}_h) = \frac{\partial \mathbf{u}_h}{\partial t} + \nabla \cdot \mathcal{F}_c(\mathbf{u}_h) - \nabla \cdot \mathcal{F}_v(\mathbf{u}_h, \nabla_h \mathbf{u}_h + \boldsymbol{L}_h) \ , \tag{61}$$

$$\begin{aligned} \mathbf{r}(\mathbf{u}_h) = & \left[H_c(\mathbf{u}_h^+, \mathbf{u}_h^-, \mathbf{n}) - \mathcal{F}_c(\mathbf{u}_h^+) \cdot \mathbf{n} \right] \\ & - \left[\{\!\{ \mathcal{F}_v(\mathbf{u}_h, \nabla_h \mathbf{u}_h + \eta_{BR2} \boldsymbol{l}_h^e) \}\!\} - \mathcal{F}_v(\mathbf{u}_h^+, \nabla_h \mathbf{u}_h^+ + \boldsymbol{L}_h) \right] \cdot \mathbf{n} \ , \end{aligned} \tag{62}$$

$$\begin{aligned} \mathbf{r}_b(\mathbf{u}_h) = & \left[\mathcal{F}_c(\mathbf{u}_b) - \mathcal{F}_c(\mathbf{u}_h^+) \right] \cdot \mathbf{n} \\ & - \left[\mathcal{F}_v(\mathbf{u}_b, \nabla_h \mathbf{u}_b + \eta_{BR2} \boldsymbol{l}_h^e) - \mathcal{F}_v(\mathbf{u}_h^+, \nabla_h \mathbf{u}_h^+ + \boldsymbol{L}_h) \right] \cdot \mathbf{n} \ . \end{aligned} \tag{63}$$

In Eqs. (61) to (63), $\mathbf{R}(\mathbf{u}_h)$ measures how accurately the numerical solution within an element satisfies the (continuous) mathematical model, the inter-element residual $\mathbf{r}(\mathbf{u}_h)$ measures the jump in the convective and viscous fluxes at the internal faces, and the boundary residual $\mathbf{r}_b(\mathbf{u}_h)$ measures the error in the imposition of the specified natural boundary conditions.

Provided that the adjoint solution is $\mathbf{z}|_K \in [H^s(K)]^{d+2}$ with $2 \leq s \leq p+1, \forall K \in \Omega_h$, it can be shown [84] that the error in the target functional is bounded by

$$|J(\mathbf{u}) - J(\mathbf{u}_h)| \leq C_{\text{int}} \left(\sum_{K \in \Omega_h} \eta_K^2 \right)^{\frac{1}{2}} \tag{64}$$

with C_{int} a positive constant which depends on the regularity of the mesh, the polynomial degree p and the regularity of the dual solution, and

$$\eta_K := h_K^s \|\mathbf{R}(\mathbf{u}_h)\|_{L^2(K)} + h_K^{s-\frac{1}{2}} \|\mathbf{r}(\mathbf{u}_h)\|_{L^2(\partial K \cap \mathcal{E}_i)} + h_K^{s-\frac{1}{2}} \|\mathbf{r}_b(\mathbf{u}_h)\|_{L^2(\partial K \cap \mathcal{E}_b)} \ . \tag{65}$$

On the basis of numerical experiments, Hartmann and Houston have actually employed the following residual-based indicator:

$$\eta_K^{RB} := h_K \|\mathbf{R}(\mathbf{u}_h)\|_{L^2(K)} + h_K^{\frac{1}{2}} \|\mathbf{r}(\mathbf{u}_h)\|_{L^2(\partial K \cap \mathcal{E}_i)} + h_K^{\frac{1}{2}} \|\mathbf{r}_b(\mathbf{u}_h)\|_{L^2(\partial K \cap \mathcal{E}_b)} \ , \tag{66}$$

with

$$\eta_{\text{glob}} := \left(\sum_{K \in \Omega_h} \eta_K^2 \right)^{\frac{1}{2}} \ . \tag{67}$$

In the present work, a normalized variant of this indicator is also considered

$$\eta_K^{RBN} := \|\mathbf{R}(\mathbf{u}_h)\|_{L^2(K)} + h_K^{-\frac{1}{2}} \|\mathbf{r}(\mathbf{u}_h)\|_{L^2(\partial K \cap \mathcal{E}_i)} + h_K^{-\frac{1}{2}} \|\mathbf{r}_b(\mathbf{u}_h)\|_{L^2(\partial K \cap \mathcal{E}_b)} \ . \tag{68}$$

We remark that Eqs. (66) and (68) corresponds to assuming $s = 1$ and 0, respectively. This violates the assumption of regularity of the adjoint solution used to derive Eqs. (64) and (65). In alternative these two indicators can be assumed to be derived from Eq. (65) by assuming $s = 2$ and normalizing by h_K and h_K^2, respectively.

4.4.5 *The residuum-NCF based indicator*

In [56] Dolejší has proposed a refinement indicator based on the following global error definition

$$E := \left(R(\mathbf{u}_h)^2 + \text{NCF}(\mathbf{u}_h)^2 \right)^{\frac{1}{2}} \ , \tag{69}$$

where $R(\mathbf{u}_h)$ is called residuum error and $\text{NCF}(\mathbf{u}_h)$ is a measure of the non-conformity error in the sense of Sec. 4.4.3.

Denoting by $X := \left\{ \mathbf{w} : \mathbf{w}|_K \in [H^2(K)]^{d+2}, \forall K \in \Omega_h \right\}$ the broken Sobolev space of vector valued functions, these quantities are defined as

$$R(\mathbf{u}_h) := \|\mathcal{N}_h(\mathbf{u}_h, \cdot)\|_X = \sup_{\mathbf{w} \in X \setminus \{0\}} \frac{|\mathcal{N}_h(\mathbf{u}_h, \mathbf{w})|}{\|\mathbf{w}\|_X} \ , \tag{70}$$

and

$$\text{NCF}(\mathbf{u}_h) := \left(\sum_{K \in \Omega_h} \text{NCF}_K^2(\mathbf{u}_h) \right)^{\frac{1}{2}}, \tag{71}$$

with

$$\text{NCF}_K(\mathbf{u}_h) := \int_{\partial K \in \mathcal{E}_i} h_{\partial K}^{-1} [\![\mathbf{u}_h]\!]^2 \mathrm{d}S + \int_{\partial K \in \mathcal{E}_b} h_{\partial K}^{-1} (\mathbf{u}_h - \mathbf{u}_b)^2 \mathrm{d}S \ . \tag{72}$$

For the analytical solution we have that $\mathcal{N}_h(\mathbf{u}, \mathbf{w}) = 0, \forall \mathbf{w} \in X$, while for the numerical solution this is only true for $\mathbf{w} \in \mathbf{S}_h^p$, where $\mathbf{S}_h^p := [S_h^p]^{d+2}$. Thus the residuum error is a measure of the residual in the weak form of Eq. (1) .

Using Eq. (59) and Eq. (70), it can be readily shown that

$$|J(\mathbf{u}) - J(\mathbf{u}_h)| = |\mathcal{N}_h(\mathbf{u}_h, \mathbf{z})| \leq R(\mathbf{u}_h)\|\mathbf{z}\|_X \ . \tag{73}$$

Therefore, limiting the residuum error has a similar effect to limiting the residual-based indicator defined in Eq. (65) in the evaluation of the error in a target functional.

The residuum error Eq. (70) cannot be exactly computed, as it is defined on an infinite-dimensional space. Thus, the global and local residuum error estimators are used in practice and are defined as

$$\rho_h(\mathbf{u}_h) := \sup_{\mathbf{w} \in \mathbf{S}_h^{p+1} \setminus \{0\}} \frac{|\mathcal{N}_h(\mathbf{u}_h, \phi)|}{\|\mathbf{w}\|_X} \ , \tag{74}$$

$$\rho_{h,K}(\mathbf{u}_h) := \sup_{\mathbf{w} \in \mathbf{S}_K^{p+1} \setminus \{0\}} \frac{|\mathcal{N}_h(\mathbf{u}_h, \phi)|}{\|\mathbf{w}\|_X} \ . \tag{75}$$

The space S_h^{p+1} and S_K^{p+1} correspond, respectively, to the space of vector valued functions of which each component is a piecewise polynomial of maximum degree $p+1$ and its restriction to the considered element K for the evaluation of the local residuum error estimator, defined by

$$\mathbf{S}_K^{p+1} := \left\{ \mathbf{w} \in L^2(K) : \mathbf{w}|_K \in [\mathcal{P}^{p+1}(K)]^{d+2}, \mathbf{w}|_{K'} = 0, \forall K, K' \in \Omega_h, K \neq K' \right\} \ . \tag{76}$$

As regards the norm $\|\cdot\|_X$ employed in this work, following Dolejší [56], we use the definition

$$\|\cdot\|_X := \left(\|\cdot\|^2_{L^2(\Omega)} + \frac{1}{\mathrm{Re}} |\cdot|^2_{H^1(\Omega_h)} \right)^{\frac{1}{2}} \ , \tag{77}$$

where Re is the Reynolds number and $|\cdot|_{H^1}$ is the broken Sobolev seminorm. Other norms have also been employed in the literature [55, 58]. It can be shown (see [58]) that, based on this choice, the residuum error estimator can be directly computed from the element-wise values, namely,

$$\rho_h(\mathbf{u}_h)^2 = \sum_{K \in \Omega_h} \rho_{h,K}(\mathbf{u}_h)^2 \ . \tag{78}$$

The residuum-NCF refinement indicator therefore takes the final form:

$$\eta_K^{RNCF} := \left(\rho_{h,K}(\mathbf{u}_h)^2 + \mathrm{NCF}_K(\mathbf{u}_h)^2 \right)^{\frac{1}{2}} \ , \tag{79}$$

with

$$\eta_{\text{glob}} := \left(\sum_{K \in \Omega_h} \eta_k^2 \right)^{\frac{1}{2}} = \left(\rho_h(\mathbf{u}_h)^2 + \text{NCF}(\mathbf{u}_h)^2 \right)^{\frac{1}{2}} \quad . \tag{80}$$

In order to evaluate the indicator Eq. (79), the local residuum estimator $\rho_{h,K}(\mathbf{u}_h)$ is computed by seeking a solution of the form $\mathbf{w} = \sum_{i=1}^{N_{p+1}} \boldsymbol{\xi}_i \phi_i$, where $\{\phi_i\}_{1 \leq i \leq N_{p+1}}$ is a basis for S_K^{p+1} and $\boldsymbol{\xi}_i$ are the unknown coefficients, such that $|\mathcal{N}_h(\mathbf{u}_h, \mathbf{w})|$ is maximum and $\|\mathbf{w}\|_X = 1$. This leads to a constrained optimisation problem which can be solved via the Lagrange multipliers technique, which requires the computation of the residuals $\mathcal{N}_h(\mathbf{u}_h, \phi_i)$.

It should be noted that $\mathcal{N}_h(\mathbf{u}_h, \mathbf{w}), \forall \mathbf{w} \in \mathbf{S}_K^p$ should be identically null by virtue of the Galerkin orthogonality property. In practice this is not the case due to the presence of an algebraic error which is the combination of the aliasing and, for steady problems, iterative errors. Thus, in order to evaluate this contribution, we compute the quantity $\mathcal{N}_h(\mathbf{u}_h, \mathbf{w})$ by using an increased number of quadrature points compared to the ones used to compute $\mathbf{u}_h$.

4.4.6 *A novel error indicator: the small-scale lifted indicator*

Over the course of this research we have proposed a novel refinement indicator. We define the following norm of the error in the momentum density in each element as

$$e_K := \frac{1}{|K|^{\frac{1}{2}}} \left[\left\| (\rho \mathbf{v})_{h,p} - (\rho \mathbf{v})_{ex} \right\|_{L^2(K)} + h_K \sum_{i=1}^{d} \left\| \frac{\partial (\rho \mathbf{v})_{h,p}}{\partial x_i} - \frac{\partial (\rho \mathbf{v})_{ex}}{\partial x_i} \right\|_{L^2(K)} \right] \quad , \tag{81}$$

where $(\rho \mathbf{v})_{ex}$ is the exact momentum density. This norm of the error is therefore the combination of the L^2-norm of the error in the solution and the L^2-norm of the error in its gradient, equivalent to the H^1 broken Sobolev seminorm of the error, scaled by the characteristic mesh size. As the exact solution is not known, the two contributions need to be approximated.

For the first component, we employ the approach of Kuru *et al.* [113] by approximating the exact error in the solution by the error between the numerical solution and its projection on the reduced order space S_h^{p-1} as in Eq. (52).

As regards the second component, we require an approximation of the error of the gradient of the solution. For this purpose, we employ an approach inspired by the BR1 and BR2 schemes of Bassi *et al.* [12, 14] described in Sec. 3.2.2.2. This consists in approximating the exact gradient in Eq. (81) by the lifted gradient of the momentum

density $\sigma_h^{\rho\mathbf{v}}$, solution of Eqs. (42) and (43). The following approximation is therefore obtained

$$\left\| \frac{\partial(\rho\mathbf{v})_{h,p}}{\partial x_i} - \frac{\partial(\rho\mathbf{v})_{ex}}{\partial x_i} \right\|_{L^2(K)} \approx \left\| \mathbf{i} \cdot \left[\boldsymbol{\nabla}(\rho\mathbf{v})_{h,p} - \boldsymbol{\sigma}_h^{\rho\mathbf{v}} \right] \right\|_{L^2(K)} , \tag{82}$$

where $\mathbf{i}$ is the i-th unit vector defining the physical coordinate system. Employing Eq. (42) the previous equation can be rewritten as

$$\left\| \frac{\partial(\rho\mathbf{v})_{h,p}}{\partial x_i} - \frac{\partial(\rho\mathbf{v})_{ex}}{\partial x_i} \right\|_{L^2(K)} \approx \left\| \mathbf{i} \cdot \mathbf{L}_h^{\rho\mathbf{v}} \right\|_{L^2(K)} . \tag{83}$$

The following refinement indicator is thereby introduced,

$$\eta_K := \frac{1}{|K|^{\frac{1}{2}}} \left[\left\| (\rho\mathbf{v})_{h,p} - (\rho\mathbf{v})_{h,p-1} \right\|_{L^2(K)} + h_K \sum_{i=1}^{d} \left\| \mathbf{i} \cdot \mathbf{L}_h^{\rho\mathbf{v}} \right\|_{L^2(K)} \right] . \tag{84}$$

The proposed refinement indicator is therefore a combination of the SSED indicator Eq. (53) and an additional term which approximates the error in the gradient of the momentum density. This second term includes information on the jumps of the solution at internal faces and the accuracy with which boundary conditions are satisfied. The resulting refinement indicator is completely local, only requiring information from the solution within the element and the trace of the solution at the element's interfaces.

We note that the evaluation of the lifting component $\mathbf{L}_h^{\rho\mathbf{v}}$ is already required for the solution of viscous problems for the discretization of the viscous term when employing the BR1 or BR2 schemes. Additionally the projection of the solution on the reduced order space is readily available when employing hierarchical basis functions. For these reason, the evaluation of Eq. (84) only involves the computation of the integrals associated with the L^2-norms. This presents a limited computational overhead when the basis functions for both the solution and the lifting component are also orthonormal, which is the case in this work.

Note that in Eq. (84) the gradient term is scaled by the characteristic element size, which is usually defined as $h_K = |K|^{\frac{1}{d}}$. This definition might not be optimal for meshes typically employed for the simulation of flows in complex industrial applications. These are often characterized by anisotropic curvilinear meshes, which might present high aspect-ratio and distortion. In what follows, we introduce an alternative definition of η_K, better suited for general meshes,

$$\eta_K := \frac{1}{|K|^{\frac{1}{2}}} \left[\left\| (\rho\mathbf{v})_{h,p} - (\rho\mathbf{v})_{h,p-1} \right\|_{L^2(K)} + \sum_{i=1}^{d} \Delta s_i \left\| \frac{\partial \hat{\mathbf{x}}}{\partial \xi_i} \cdot \mathbf{L}_h^{\rho\mathbf{v}} \right\|_{L^2(K)} \right] , \tag{85}$$

where $\{\xi_i\}_{i=1\dots d}$ are the reference coordinates in the reference cube of unitary volume,

$$\frac{\partial \hat{\mathbf{x}}}{\partial \xi_i} := \frac{\partial \mathbf{x}}{\partial \xi_i} \left\| \frac{\partial \mathbf{x}}{\partial \xi_i} \right\|^{-1} \quad \text{and} \quad \Delta s_i := \int_{K_{ref}} \left\| \frac{\partial \mathbf{x}}{\partial \xi_i} \right\| \mathrm{d}\boldsymbol{\xi} \ .$$

This definition however requires evaluating the values of $\frac{\partial \mathbf{x}}{\partial \xi_i}$ at the quadrature points. Furthermore, numerical integration is required to compute the quantity $\left\| \frac{\partial \hat{\mathbf{x}}}{\partial \xi_i} \cdot \mathbf{L}_h^{\rho \mathbf{v}} \right\|_{L^2(K)}$, even when $\mathbf{L}_h^{\rho \mathbf{v}}$ is expressed as a linear combination of orthonormal basis functions.

Therefore, in order to avoid these issues, we define the *small-scale lifted (SSL) indicator* as

$$\eta_K^{SSL} := \frac{1}{|K|^{\frac{1}{2}}} \left[\left\| (\rho \mathbf{v})_{h,p} - (\rho \mathbf{v})_{h,p-1} \right\|_{L^2(K)} + \sum_{i=1}^{d} \left\| \mathbf{h}_{K,i} \cdot \mathbf{L}_h^{\rho \mathbf{v}} \right\|_{L^2(K)} \right] \ , \tag{86}$$

where we have introduced the characteristic length vectors of the element as

$$\mathbf{h}_{K,i} := \int_{K_{ref}} \frac{\partial \mathbf{x}}{\partial \xi_i} \mathrm{d}\boldsymbol{\xi} \ . \tag{87}$$

As an example, we represent in Fig. 4 a typical curvilinear two-dimensional element and the corresponding characteristic size h_K and characteristic length vectors $\mathbf{h}_{K,i}$. The evaluation of the SSL refinement indicator from Eq. (86) therefore presents the same computational cost of Eq. (84) but allows us to take into account the distortion and the aspect-ratio of the element. Finally, we note that in the case of a Cartesian mesh the characteristic length vectors correspond to the intuitive definitions $\mathbf{h}_{K,i} = \Delta x_i \mathbf{i}$, where Δx_i is the length of the side of the element in the $\mathbf{i}$-th direction.

The development of this refinement indicator has been guided by the experience gained through the analysis of the previously described refinement indicators presented in Chaps. 5 to 9. For this reason, results obtained using the SSL indicator are presented only in Sec. 9.5.

4.5 MARKING STRATEGIES

Marking procedures employ the distribution of the local error estimate to identify elements which require increased resolution (*refine*) and elements for which the resolution can be reduced (*coarsen*). It has therefore a strong influence on the efficiency of the adaptive algorithm.

Several marking strategies have been proposed in the literature and are here outlined

(i) The use of a *user-defined threshold* is probably the most common marking strategy [166, 185]. It consists in defining a refinement threshold η_{ref}, and refining

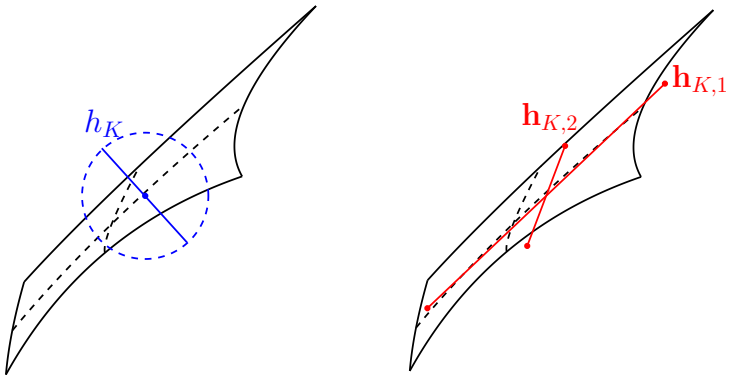

Figure 4 – Characteristic size and characteristic lengths for a curvilinear element.

elements that present a local error indicator such that $\eta_K > \eta_{ref}$. Similarly, elements are marked for coarsening if $\eta_K < \eta_{coars}$, with η_{coars} being the coarsening threshold. This strategy leads to the easiest implementation and provides the possibility for the user to ensure that at the end of the adaptive process the local value of the error indicator in each element is contained in the interval $[\eta_{coars}, \eta_{ref}]$.

The choice of suitable thresholds is however flow dependent and the efficiency of the adaptive algorithm is directly related to the experience of the user. In general, this strategy is suitable when employing DE estimators. As an example, in the case of the SSED indicator Eq. (53), the error estimator provides a measure of the average error in the momentum density within the element. A suitable error threshold can therefore be fixed as a fraction of the reference momentum density. In contrast, in the case of RE-based indicators, *e. g.* Eq. (68) or Eq. (79), no reference value is available for the evaluation *a-priori* of refinement and coarsening thresholds. These values are therefore often fixed *a-posteriori* by analysing the distribution of the relevant error indicator.

(ii) The *maximum marking strategy* [113] consists in defining the refinement threshold as a fraction of the computed error estimator, namely

$$\eta_{ref} = \theta \max_{K \in \Omega_h} \eta_K \ , \tag{88}$$

where $\theta \in [0, 1]$ is a user-defined parameter called marking fraction. This strategy does not require *a-priori* knowledge of the values of the error indicator. However, it can present a relative slow convergence in the presence of singularities, due to the very high values of the error estimate in a small number of

elements. An alternative strategy is therefore to derive a refinement threshold from the average of the domain-averaged error indicator

$$\eta_{ref} = \epsilon_{ref} \frac{\sum_{K \in \Omega_h} \eta_K}{N} \ , \tag{89}$$

with ϵ_{ref} being a user-defined parameter usually set to 1. Eq. (89) is often modified in order to avoid the inclusion of outliers, *i. e.* elements with too high or too low values of the error (see *e. g.* [8]). Similar strategies can be employed for the definition of a coarsening threshold.

(iii) The *fixed fraction strategy* [83, 84] consists in ordering elements by their estimated error and selecting for refinement/coarsening a fixed fraction of elements from the top/bottom of the list. In the case of *h*-adaptation this technique allows us to fix the relative change in the total number of dofs between two successive adaptation steps. As an example, if we only consider refinement, after one refinement step the updated total number of dofs is

$$\#\text{dofs}_{new} = \#\text{dofs}_{old}(1 + f_{ref}(n_{child} - 1)) \ ,$$

where f_{ref} is the refinement fraction and n_{child} is the number of elements in which each marked element is split.

This is not the case for *p*-adaptation as when an element is marked for refinement the relative increase in the associated number of dofs depends on the local polynomial degree. An alternative approach could be to select the smallest set of elements which presents the highest local error estimate and when refined would lead to the target number of dofs. This would require therefore an iterative procedure.

(iv) The *Dörfler marking strategy*, also called variable fraction or bulk chasing strategy [141], is based on the observation that often a small percentage of the elements contribute the most to the total error. The Dörfler marking strategy thus consists in ordering the elements based on the local error and subsequently marking for refinement the elements starting from the top until the cumulated error reaches a fixed fraction of the total error. Mathematically, this corresponds to finding the minimal subset $\Omega_h^{ref} \subseteq \Omega_h$ such that

$$\sum_{K \in \Omega_h^{ref}} \eta_K^2 \geq \gamma^2 \sum_{K \in \Omega_h} \eta_K^2 \ , \tag{90}$$

where $\gamma \in [0, 1]$ is a user-defined parameter.

It has been demonstrated that for second-order elliptic boundary value problems, if η_K is a residual-based indicator, this marking strategy leads to a fixed reduction of the error between two successive adaptation steps [36, 141]. This

condition does not necessarily hold for the NS equations. Additionally, the Dörfler marking strategy requires the use of error estimators that are cumulative, that is the global error is obtained by summing local error estimates. As an example, this is the case for the residual-based and the residuum-NCF estimators, as well as the SSED indicator in the form of Eq. (52). In contrast, the strategy would need to be modified for the variant of the SSED indicator defined in Eq. (53), the spectral decay, the NCF and the SSL indicators.

The marking strategies just outlined represent an overview of various techniques employed in the literature. It is not uncommon, however, to employ marking strategies which are modified to take into account outliers [8] or to obtain a finer control of the computational cost of simulations throughout the adaptive algorithm, *e. g.* limiting or fixing the total number of dofs.

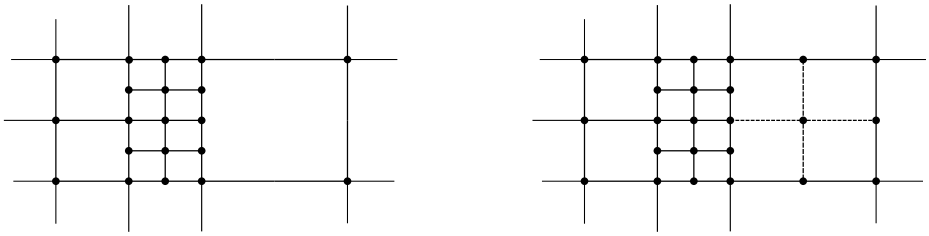

(a) unacceptable refinement (b) updated refinement

Figure 5 – Example of computational grid with invalid distribution of refinement level and updated resolution after enforcing the 2: 1 ratio.

Once the marking algorithm has been applied, additional constraints might be imposed. In the case of *h*-adaptation, for example, the jump in refinement levels between neighbouring elements is usually limited to one (see Fig. 5). This is often referred to as a resolution ratio of 2 : 1 and is enforced to avoid large variations of the mesh size.

Similarly, in the case of *p*-adaptation we have decided to limit the jump of the local polynomial degree between two neighbouring elements to be at most equal to one. Due to this constraint, additional elements might be marked for refinement to enforce this condition (see Fig. 6). Finally, we limit the local polynomial degree to be contained in an interval $[p_{min}, p_{max}]$. The maximum local polynomial degree is limited to avoid excessive memory requirements and time step restrictions.

4.6 ADAPTATION FOR UNSTEADY FLOWS

In the framework of unsteady flow simulations, two different adaptive strategies can be identified: *dynamic* and *static* adaptation.

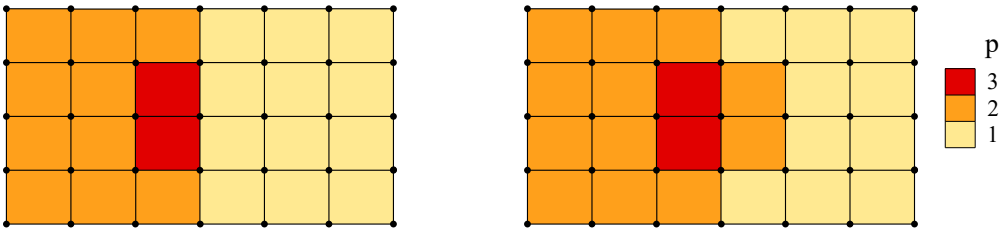

(a) unacceptable refinement (b) updated refinement

Figure 6 – Example of computational grid with invalid distribution of local polynomial degree and updated distribution after limiting the maximum jump in the local polynomial degree to one.

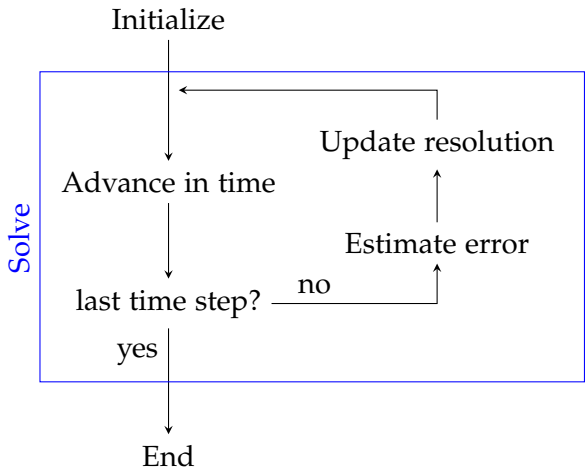

Figure 7 – Dynamic adaptation algorithm.

Dynamic adaptation consists in dynamically adapting the spatial discretization to the instantaneous resolution requirements over the course of the simulation. The adaptive algorithm takes the form illustrated in Fig. 7. Compared to the algorithm for steady flows shown in Fig. 3, the error estimation and the resolution update are part of the solution phase. The dynamically adaptive simulation can therefore be described as follows. The simulation is initialized with the prescribed initial condition on a user-defined discretization and the solution is advanced for a time interval $\Delta t_{adapt} \geq \Delta t$. At the end of this interval, the error estimator is computed from the instantaneous solution, the spatial resolution is adapted and the solution is projected on the new discretization. The simulation is then advanced in time for a new interval Δt_{adapt} and the cycle continues until the final time is reached. The time interval Δt_{adapt} is therefore the period between two successive adaptation steps.

Dynamic adaptation algorithms can therefore provide large reductions of the computational cost of simulations for unsteady problems, however they often present complex implementation. Indeed, as the adaptation algorithm is applied several times over the course of the simulation, the computational overhead produced by this algorithm becomes relevant and can reduce or even offset the computational gain provided by the local adaptation of the spatial resolution. For this reason, each phase of the adaptive algorithm must be as efficient as possible. Additionally, the efficient implementation of dynamic adaptation requires dynamic load balancing which allows the equidistribution of the computational load over the course of the simulation. In order to take full advantage of dynamic adaptation and load balancing, complex data-structures and, in general, important modifications to the solver at hand might be required.

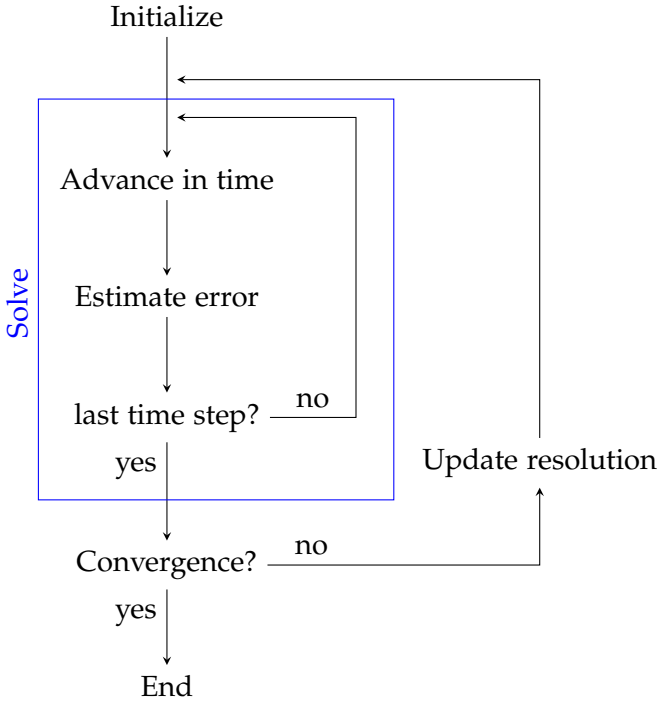

Figure 8 – Static adaptation algorithm.

By static adaptation we refer to an adaptive algorithm which has the objective of identifying the optimal fixed, *i. e.* time-independent, spatial resolution for the simulation of an unsteady flow. Two types of applications can be studied by means of static adaptation. The first type consists in the simulation of a transient flow over the time interval $[0, T]$. In this case the adaptive algorithm is conceptually identical to the adaptive algorithm for steady flows described in Sec. 4.3. Therefore at each iteration of the adaptive process, the full time interval is simulated before updating the spatial

discretization and restarting the simulation at time $t = 0$. We remark however that, differently from the algorithm in Sec. 4.3 and as further discussed in Chap. 9, depending on the error estimation strategy adopted, it might be required to compute and update the refinement indicator throughout the simulation. This algorithm is illustrated by Fig. 8. The second type of application that we might consider is the simulation of statistically steady flows. In this case, the solution is continuously advanced in time but the spatial resolution is adapted with a frequency much lower than the characteristic frequency of the flow. This is the type of application that we consider throughout this work. In this case the adaptive algorithm presents a structure in between that described by Figs. 7 and 8.

Therefore for both types of problems the objective of the statically adaptive algorithm is to optimize a fixed-in-time spatial discretization which provides the lowest error for the full simulation of the flow. This is in contrast with the dynamically adaptive algorithm, which has the objective to provide a time-dependent spatial discretization adapted to the instantaneous resolution requirements.

For static adaptation, the update of the spatial discretization, the load balancing and the projection of the solution on the updated discretization are usually performed off-line, as post-processing operations, and do not need to be evaluated at run-time. Moreover, the computational overhead of the resolution update phase is often negligible as compared to the total computational cost. A complex data-structure and optimal efficiency of the resolution adaptation technique might therefore not be necessary, leading to a relatively simple implementation. However, as the error estimator is updated at run-time, the associated computational overhead is still a critical parameter.

An important drawback of the static adaptation algorithm compared to the dynamic adaptation strategy, is that at least one preliminary simulation is required in order to evaluate the error estimator distribution and obtain the correspondingly adapted spatial resolution. In the case of scale-resolving simulations of statistically steady flows, however, long integration times are in general required in order to obtain an accurate evaluation of the statistics of the flow. Nonetheless, reasonably good estimates of the local error distribution can be obtained from a preliminary simulation with a relatively short simulation time, as demonstrated in Chap. 9. The result of a short precursor simulation can thus be employed to adapt the resolution before starting the expensive evaluation of time-averaged quantities. For this reason, static adaptation can still provide large reductions of the computational cost for this type of problems.

This property, combined with the relative ease of implementation of static adaptation, justify the interest in analysing both static and dynamic adaptation strategies despite the potential larger computational gain provided by the latter. Dynamic and static adaptation strategies are thus presented in Chaps. 8 and 9 along with further discussion on important parameters and specific issues.

4.7 ADAPTATION FOR LES

The development of resolution adaptation strategies for LES presents some specific difficulties that are not encountered in the framework of laminar and RANS simulations. One of the most controversial points of discussion is the assessment of the quality of an LES and the definition of the objective of the adaptive algorithm.

In order to illustrate this topic, we follow the analysis of Pope [154] which distinguishes between two main approaches to LES: *physical LES* and *numerical LES*.

Physical LES consists in the classical approach which identifies LES as a physical model for the solution of the filtered NS equations. In particular, we define as *pure* physical LES a framework in which the LES equations and the corresponding filter are fixed *a-priori* and are independent of the numerical discretization or the employed grid resolution. Pure physical LES approaches have been proposed by Piomelli et al. [152] and Geurts et al. [78] by defining the LES filter length Δ as a function of the flow, independent of the mesh spacing. A grid-independent LES solution is in this case well defined and can be achieved as the computational grid is progressively refined. In this context, the objective of the adaptive algorithm would therefore be to obtain the optimal resolution to minimize the error in the solution of the specified LES equations. It has been shown however by several authors [135, 193] that, for a fixed computational cost/mesh spacing, the minimum value of the error between numerical and DNS solutions is obtained for values of the ratio Δ/h with non-negligible numerical error in the solution of the continuous LES equations. Pure physical LES with negligible errors therefore does not appear to be the optimal approach.

The diametrically opposite strategy is numerical LES. It consists in analysing LES as a numerical approach to improve the prediction of the resolved scales on a given computational discretization. Examples of numerical LES are MILES [25], LES by projection onto local basis functions [153], and residual-based VMS [18].

In both numerical LES and physical LES with fixed ratio Δ/h the concept of grid-independent LES solution is debatable and often considered meaningless. In this case LES progressively converges to the DNS as the spatial resolution is refined and the smallest turbulent scales are resolved. It follows that the adaptation algorithm should not have as objective the grid-independent solution or it would lead to DNS-like resolution [140].

It can be argued, however, that the objective of LES is to resolve accurately the largest energy-containing turbulent scales that control relevant quantities of interest. In this framework, several techniques have been proposed to assess the quality of an LES which do not take into account the numerical errors. Examples of such approaches include the subgrid activity parameter of Geurts and Fröhlich [77] and the LES index of quality of Celik *et al.* [38]. Both approaches are based on the assumption that a certain fraction of the turbulent dissipation or turbulent kinetic energy should

be resolved. In particular the LES index of quality based on the kinetic energy is defined as

$$\text{LES\_IQ}_k = \frac{k_{res}}{k_{tot}} := \frac{k_{res}}{k_{res} + k_{sgs}} \ , \tag{91}$$

where k_{res} and k_{sgs} are, respectively, the resolved and unresolved turbulent kinetic energy, and k_{sgs} is estimated either from Richardson extrapolation or directly from the SGS model following the approach of Lilly [122]. The same approach is advocated by Pope [154] who suggested that at least 80% of the turbulent kinetic energy should be resolved for an LES. This estimate can be justified by the observation that for homogeneous isotropic turbulence at high Reynolds number the integral length scale is resolved if the 80% rule is satisfied [38]. In the most general case however the optimal value of LES_IQ_k might be flow dependent.

A similar strategy has already been employed in the context of DG-LES by Tugnoli *et al.* [185] who employed the spectral decay indicator Eq. (55) as an approximation of the LES index of quality. We remark however that one of the difficulties, seldom described in the application of this technique, is the separation of the turbulent kinetic energy from the total kinetic energy, especially in the presence of unsteady base flows, such as the vortex shedding past a cylinder.

An additional strategy which might be employed is to verify that the employed resolution satisfies the hypotheses employed by the LES model, *e. g.* isotropy of subgrid scales. The structure function indicator proposed by Tugnoli *et al.* [185] follows this approach and is based on the assumption that higher resolution is required in regions of poorly correlated anisotropic flow.

One of the common drawbacks of the error estimators just described is that they are specifically suited for turbulent flows and do not provide a measure of the quality of the solution in laminar regions. This represents an important limitation in their application to the simulation of transitional flows and ad-hoc corrections might be required.

An alternative approach can be derived by defining the target LES solution as the one which minimizes the error with respect to the DNS (under a suitable norm) at a fixed computational cost. This type of strategy corresponds more closely to the practical approach to LES. Error estimation strategies employed in this context can be interpreted as techniques to identify the optimal distribution of the LES filter length and are mainly based on estimates of the error between the LES and DNS solution. It is fundamental in this case that the refinement indicator employed measures the discretization error with respect to the DNS rather than the numerical error in the solution of the LES equations. As an example, Bose [28] has proposed to employ the unresolved kinetic energy extrapolated from the resolved scales as a refinement indicator. Similarly, Antepara *et al.* [8] and Toosi and Larsson [183] have proposed to estimate the error by comparing the numerical solution with the corresponding

low-pass filtered field similarly to the SSED indicator Eq. (53). An analogous concept is also applied in the context of Stochastic Coherent Adaptive LES where coherent vortices are resolved and separated from the less energetic higher frequency scales by means of a wavelet transform, see *e. g.* [172] and cited works. In this type of approaches the selection of an appropriate convergence criterion for the adaptive approach avoids achieving the DNS-like solution. This can be expressed as suitable user-defined refinement threshold or a maximum allowed resolution.

CHAPTER 5

ANALYSIS OF ERROR ESTIMATION STRATEGIES FOR *P*-ADAPTIVE SIMULATIONS

RÉSUMÉ DU CHAPITRE EN FRANÇAIS

L'objectif de ce chapitre est de fournir une comparaison approfondie des différentes stratégies d'estimation d'erreur afin d'identifier leurs avantages et leurs points faibles pour le développement des simulations *p*-adaptatives.

Nous examinons cinq indicateurs mesurant l'erreur de discrétisation et l'erreur résiduelle: l'indicateur SSED, l'indicateur spectral-decay, l'indicateur NCF, l'indicateur residual-based et l'indicateur residuum-NCF décrits dans la Sec. 4.4. La méthodologie utilisée pour comparer les performances des différents indicateurs est décrite dans la Sec. 5.2. En particulier, nous analysons la convergence des processus adaptatifs des simulations en utilisant des quantités d'intérêt (grandeurs physiques caractéristiques), la distribution du degré polynomial local à la fin du processus adaptatif, les coûts de calcul et les éventuels problèmes de mise en œuvre.

Quatre configurations sont étudiées. Dans un premier temps, dans la Sec. 5.3, nous considérons l'écoulement de fluide parfait pour un écoulement dans un canal comportant une bosse avec profil gaussien à M = 0.5. Cette analyse révèle que, bien qu'ils soient des estimateurs de l'erreur de discrétisation, les indicateurs SSED, spectral-decay et NCF sont capables d'identifier les régions où des erreurs sont produites, ce que nous souhaitons, plutôt que les régions dans lesquelles les erreurs sont transportées. Deux configurations laminaires stationnaires sont ensuite analysées: l'écoulement autour du profil d'aile de Joukowsky à Re = 1000, M = 0.5 et pour un angle d'attaque $\alpha = 0°$ dans la Sec. 5.4, et l'écoulement autour d'un cylindre à Re = 40 et M = 0.1 dans la Sec. 5.5. Il est observé que, malgré les formulations très différentes des estimateurs d'erreur utilisées, tous les indicateurs de raffinement permettent d'atteindre le niveau de précision prescrit avec une réduction du nombre de degrés de liberté requis respectivement de 50% et de 75% pour les deux configurations analysées. On a également obtenu un taux de convergence et des régions de raffinement similaires pour différents indicateurs. Cependant, on observe que l'indicateur residual-based présente une plus grande sensibilité à la qualité et aux variations de taille des éléments du maillage. De plus, l'indicateur NCF génère une distribution

spatiale irrégulière du degré polynomial après adaptation. Ceci est dû à la plus forte sensitivité à la qualité de la solution dans les éléments voisins. L'applicabilité des résultats obtenus aux écoulements instationnaires est ensuite confirmée en effectuant des simulations statiquement p-adaptatives de l'écoulement autour d'un cylindre à Re = 100 et M = 0.1 dans la Sec. 5.6.

Enfin, les coûts de calcul de différents indicateurs et les difficultés potentielles de mise en œuvre sont analysés dans la Sec. 5.7. Il est démontré que l'indicateur SSED présente le coût de calcul le plus faible dans le cas des méthodes DG basées sur des bases orthonormales hiérarchiques et peut être facilement mis en œuvre comme un module embarqué d'analyse de solution. Ces raisons, combinées à la bonne performance démontrée, font de l'indicateur SSED un candidat idéal pour les simulations d'écoulements turbulents utilisant une approche LES. Il est donc largement utilisé dans le travail présenté ici.

5.1 INTRODUCTION AND OUTLINE OF THE CHAPTER

The selection of the most appropriate refinement indicator for an adaptive algorithm is the result of a compromise between several factors. These are the computational overhead due to the evaluation of the error estimator, the desired level of accuracy of the adapted solution and the reliability of the refinement indicator in identifying regions that require increased resolution (robustness). This is of particular interest for the development of adaptive algorithms for scale resolving simulations because of the high computational cost required for this type of applications. However, a fair analysis of different refinement indicators is an arduous task. This is the consequence of the lack of a systematic comparison using the same configuration and numerical scheme, as well as the fact that a given refinement indicator can be open to multiple interpretations.

The objective of this chapter is thus to provide such an analysis identifying advantages and drawbacks of various discretization error (DE) and residual error (RE) estimators for p-adaptive simulations of steady and unsteady flows. For this purpose, we consider five of the refinement indicators presented in Sec. 4.4: the SSED, the spectral decay, the NCF, the residual-based and the residuum-NCF indicators. Both the normalized variant and the original formulation of the residual-based indicators, presented in Sec. 4.4.4, are employed. For each error estimator, we study the convergence history of the adaptive procedure, the computational gain provided and the spatial regions selected for refinement. We do not compare the efficiency of different refinement indicators on estimating the error of the numerical solution as different indicators measure different errors or employ different norms.

This chapter is organized as follows. First, the methodology employed to compare the performance of different refinement indicators is outlined in Sec. 5.2. The described methodology is first applied, in Secs. 5.3 to 5.5, to three steady inviscid and

viscous flow configurations: the inviscid flow over a Gaussian bump at $M = 0.5$, the laminar flow past a Joukowski airfoil at $Re = 1000$, $M = 0.5$ and $\alpha = 0°$, and the laminar flow past a cylinder at $Re = 40$ and $M = 0.1$. The applicability of the obtained results for the simulation of unsteady flows is then verified in Sec. 5.6 by considering static p-adaptive simulations of the periodic flow past a cylinder at $Re = 100$ and $M = 0.1$. A comparison of the different refinement indicators in terms of computational cost and potential implementation issues is then reported in Sec. 5.7. Finally, the main conclusions of this analysis are presented in Sec. 5.8.

5.2 METHODOLOGY FOR THE COMPARISON OF THE PERFORMANCE

In order to compare the different refinement indicators considered, we proceed in the following way. The p-adaptive algorithm, following the approach presented in Sec. 4.3, is applied starting from the solution corresponding to a uniform polynomial degree $p = p_{\min}$ and limiting the maximum polynomial degree to a user-defined value $p_{\max}$. At each iteration of the algorithm, the maximum marking strategy, described in Sec. 4.5, is employed to select elements for refinement based on the local error estimate. Coarsening is not performed in this study.

Different approaches can be considered to determine whether the p-adaptive algorithm is converged. One approach consists in the definition of a global error indicator, η_{glob}, which can be derived from the element-wise error estimates η_K as seen in Sec. 4.4. However, this choice would lead to different measures of accuracy and convergence criteria for the different refinement indicators analysed. In order to obtain a fair comparison, the accuracy of the adaptive solution and the convergence of the adaptive algorithm are measured by evaluating the error in the computation of prescribed target quantities. As the maximum polynomial degree is limited, the maximum local spatial resolution is also bounded and the highest possible accuracy produced by the adaptive algorithm is the same as that corresponding to uniform polynomial degree $p = p_{\max}$, albeit with a reduced number of dofs. The p-adaptive algorithm is therefore considered converged when, for all quantities of interest, the same accuracy as that of the simulation with uniform polynomial degree $p = p_{\max}$ is achieved. The reduction in computational cost provided by adaptive refinement is then measured by comparing the results from the p-adaptive simulations with those obtained from uniform p-refinement.

In order to identify possible advantages and drawbacks of the different refinement indicators, we also analyse the maps of polynomial degree obtained at a similar number of dofs. This allows us to identify the different regions selected by the adaptive algorithm and provides useful information on the sensitivity of some indicators to mesh quality, the marking algorithm or specific features of the flow. Repeating this analysis for different test cases allows us to corroborate our observations and therefore to draw general conclusions from our study.

	Physical model	$p_{\min}$	$p_{\max}$	θ	Target quantity
Case 1	Euler steady	2	4	0.5	entropy error
Case 2	NS steady	2	5	0.1	C_D, $\|(\rho\mathbf{v}) - (\rho\mathbf{v})_{\text{ref}}\|_{L^2(\Omega)}$
Case 3	NS steady	2	6	0.5	C_D, $\|(\rho\mathbf{v}) - (\rho\mathbf{v})_{\text{ref}}\|_{L^2(\Omega)}$
Case 4	NS unsteady	2	6	0.1	$\overline{C_D}$, C_L', St

Table 1 – Numerical parameters for the p-adaptive algorithm.

Table 1 compiles the main parameters that have been employed in the adaptive algorithm for the considered test cases. We further note that all simulations have been performed by employing $q = p + 5$ quadrature points in each spatial direction. For each simulation we have verified that further increasing this value has a negligible effect on the results.

5.3 STEADY INVISCID FLOW OVER A GAUSSIAN BUMP

The first test case considered is the inviscid flow over a Gaussian bump at $M = 0.5$, widely studied at the series of International Workshops on High-Order CFD methods (HiOCFD) [196]. The configuration is 2D and consists of a subsonic inlet and an outlet with a prescribed static pressure. Slip boundary conditions are imposed at the upper and bottom walls. The mesh employed in the simulations presented here is a 4^{th}-order mesh, available on the HiOCFD workshop website [1]. This mesh has been generated based on the analytical expression of the bump corresponding to a Gaussian profile.

The accuracy of the performed simulations is measured by the entropy error on the full domain, namely:

$$\|e\|^2_{L^2(\Omega)} = \int_\Omega \left(\frac{p}{p_\infty} \left(\frac{\rho_\infty}{\rho} \right)^\gamma - 1 \right)^2 \mathrm{d}\Omega \tag{92}$$

where p_∞ and ρ_∞ are the static pressure and density corresponding to the prescribed inlet conditions. For inviscid subsonic flows with uniform inlet conditions no entropy variations are expected in the domain. The quantity $\|e\|_{L^2}$ therefore represents an exact measure of the discretization error.

Figure 9 shows the variation of this error measure versus the number of dofs when uniform p-refinement is performed (solid black line with circles) as well as for the locally p-adapted simulations (coloured curves with dots). For the latter, in this case we do not consider the normalized variant of the residual-based indicator Eq. (68). Indeed, due to the very limited variation of the characteristic element size of the mesh employed, the residual-based indicator and its normalized variant provide almost identical results. For reference, we also report the results obtained by using the local

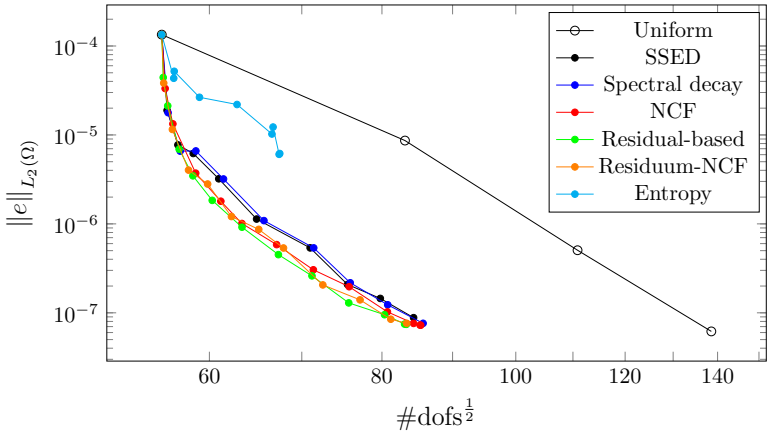

Figure 9 – Inviscid flow over a Gaussian bump at M = 0.5: Evolution of global entropy error Eq. (92) under uniform and adaptive refinement.

entropy error as refinement indicator (light blue dots in Fig. 9). Figure 10 shows the maps of local polynomial degree at the last iteration of the refinement procedure for the six indicators considered.

As seen from Figs. 9 and 10a, the results obtained for the local entropy error indicator illustrate one of the possible drawbacks of DE-based refinement indicators, as mentioned in Sec. 4.4. In fact, for this configuration it is expected that a higher spatial resolution is required in the proximity of the bump. In underresolved simulations an error in the entropy is produced in this region and is convected downstream. For this reason, as can be seen in Fig. 10a, this refinement indicator effectively selects for further refinement the region downstream of the bump. This is the cause of the suboptimal performance exhibited by this estimator, as seen in Fig. 9.

In spite of their very different formulation, implementation and computational cost, the other refinement indicators show very similar behaviour. The residual-based, residuum-NCF and NCF refinement indicators show slightly better performance after the initial refinement step. The residual-based indicator leads to a reduction in the number of dofs necessary to achieve the same convergence level as the uniform $p = 4$ simulation of approximatively 63%. In the case of the SSED and spectral decay indicators the savings in terms of dofs are of about 58%. It is also interesting to note that, despite being DE estimators, the SSED, spectral decay and NCF indicators do not share the deficiencies exhibited by the local entropy error indicator. A possible explanation for this is that the production of errors is concentrated in the high-frequency content of the solution. By definition, the above mentioned indicators identify regions where the largest amount of energy is contained in the highest order modes thus selecting for refinement regions where errors are being generated rather than those where they have been convected.

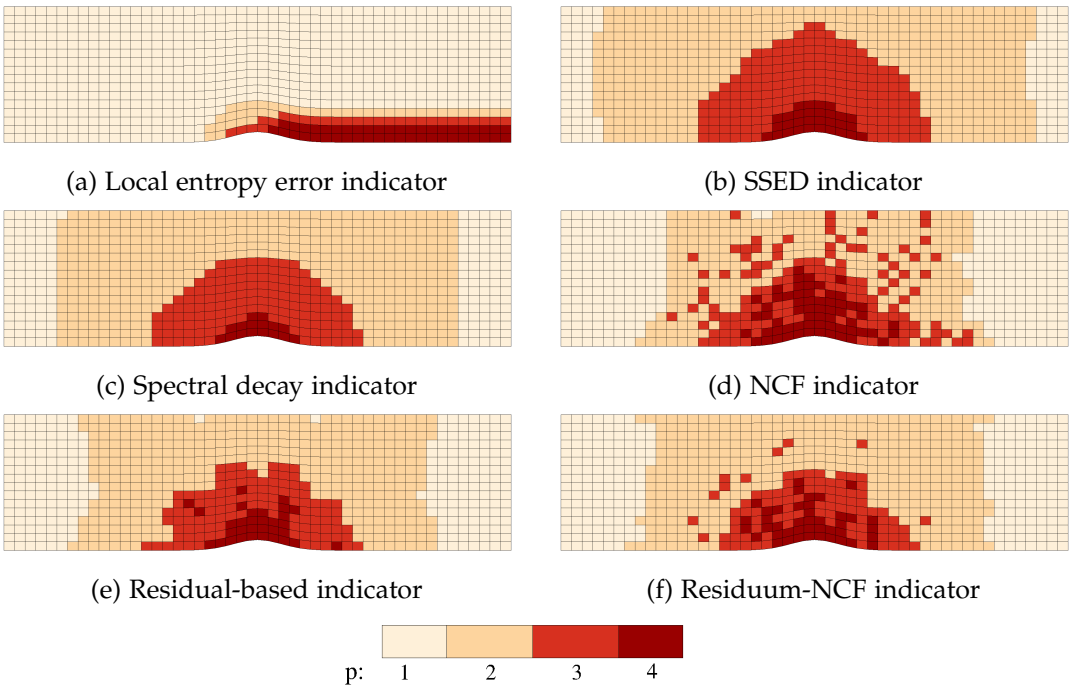

Figure 10 – Inviscid flow over a Gaussian bump at M = 0.5: Map of local polynomial degrees obtained based on different refinement indicators.

Coming back to Fig. 10, we observe that the SSED and spectral decay indicators produce almost identical maps of local polynomial degree. The residual-based, residuum-NCF and NCF indicators also provide refinement patterns which are very similar to each other. By comparing these to the pattern shown by the SSED indicator, we can observe that they present a smaller refinement region while the number of elements with higher polynomial degree is increased. As expected, the residuum-NCF indicator generates a polynomial degree map which is in between the ones produced by the residual-based and the NCF estimators. Finally, it is worth noting the checkerboard-like pattern generated by the NCF indicator and to some extent the residuum-NCF indicator. This is despite the initial smooth distribution of the refinement indicator at the beginning of the adaptive procedure. Through numerical experiments, we have observed that this pattern appears to be strongly influenced by the refinement history. Indeed modifying the marking algorithm or its parameters actually leads to the generation of a different checkerboard-like pattern. A much weaker influence has been observed for the refinement levels generated by the other refinement indicators. This specific issue is analysed in further details in the next section.

5.4 STEADY LAMINAR FLOW PAST A JOUKOWSKI AIRFOIL

The first laminar test case considered is the flow past a symmetric Joukowski airfoil at zero incidence ($\alpha = 0°$), $M = 0.5$ and $\mathrm{Re} = 1000$ based on the chord length. This configuration has been proposed as a test case of the 4^{th} and 5^{th} HiOCFD workshops [1, 2]. The flow field is two-dimensional laminar and symmetric. The solution is free of shocks or recirculation bubbles but the cusped trailing edge introduces a geometric singularity which could negatively impact the convergence rate of the p-refinement algorithm. It is therefore interesting to investigate how the different refinement indicators deal with this singularity.

Computational details

The simulations presented here are performed by considering a computational domain defined by a semicircular region of radius $R = 100$ chords centered at the leading edge, followed by a rectangular region extending up to 100 chords from the trailing edge. The dynamic viscosity coefficient is taken constant. Adiabatic wall boundary conditions are imposed on the airfoil and non-reflecting conditions are imposed at the external boundaries. From numerical experiments, we know that this extent of the computational domain is not sufficient to obtain a solution completely independent of the imposed far-field boundary conditions. However, in our numerical tests the artificial boundary does not appear to have a negative effect on the numerical solution.

All computations are performed using one of the meshes provided by the 4^{th} HiOCFD workshop. It corresponds to the first refinement level of the mesh composed of 4^{th}-order quads that can be found on [1]. We note that this mesh is characterized by a strong refinement localized in the vicinity of the trailing edge. This limits the harmful effect of the geometrical singularity on the convergence rate of the simulation.

In order to compare the accuracy of the adapted solutions obtained based on the different indicators, we consider the convergence history of both the error in the drag coefficient and in the L^2-norm of the momentum density. These error quantities are computed by considering as reference the numerical solution obtained using uniform polynomial degree $p = 7$. It has been verified that the drag coefficient computed from this reference solution ($C_D = 0.1219$) is in agreement with the results reported in the literature [1, 2].

The main results obtained from the p-adaptive simulations are now presented.

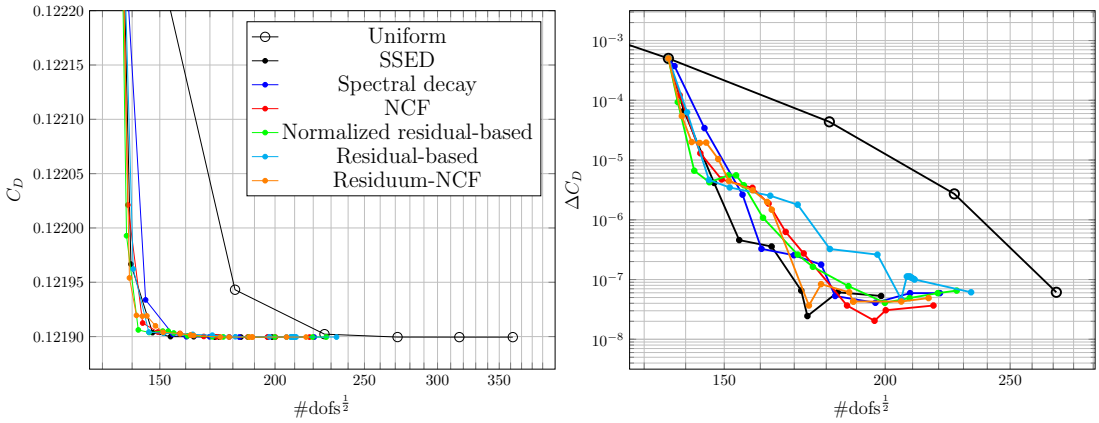

Figure 11 – Laminar flow past a Joukowski airfoil at Re = 1000, $M = 0.5$, and $\alpha = 0°$: Convergence history of the drag coefficient under uniform and adaptive p-refinement.

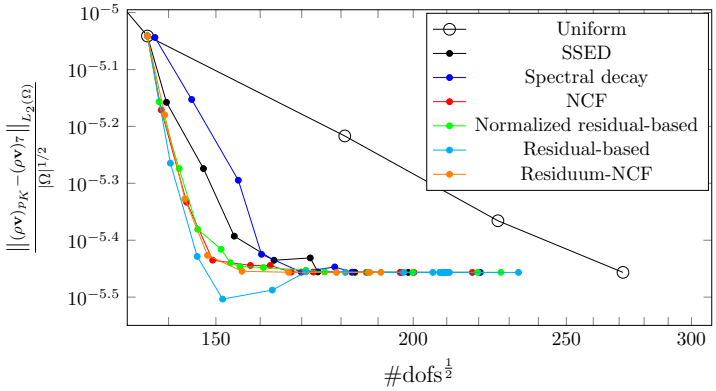

Figure 12 – Laminar flow past a Joukowski airfoil at Re = 1000, $M = 0.5$, and $\alpha = 0°$: L^2-norm of the error in momentum density under uniform and adaptive p-refinement.

Analysis of the p-adaptive results

Figures 11 and 12 show the convergence history of the drag coefficient (Fig. 11a) and its corresponding error (Fig. 11b) as well as the L^2-norm of the error in momentum density (Fig. 12) under uniform and adaptive p-refinement. From these images, we can observe that for a target value of the error in the drag coefficient, $\Delta C_D = 10^{-7}$, most refinement indicators achieve a reduction in the number of dofs with respect to the uniform refinement of approximately 53%. Only the residual-based indicator leads to a smaller reduction of about 30%.

These results show that, among the considered error estimators, the SSED indicator produces the fastest reduction of the error in the drag coefficient, followed by the spectral decay, the NCF, the residuum-NCF and the normalized residual-based

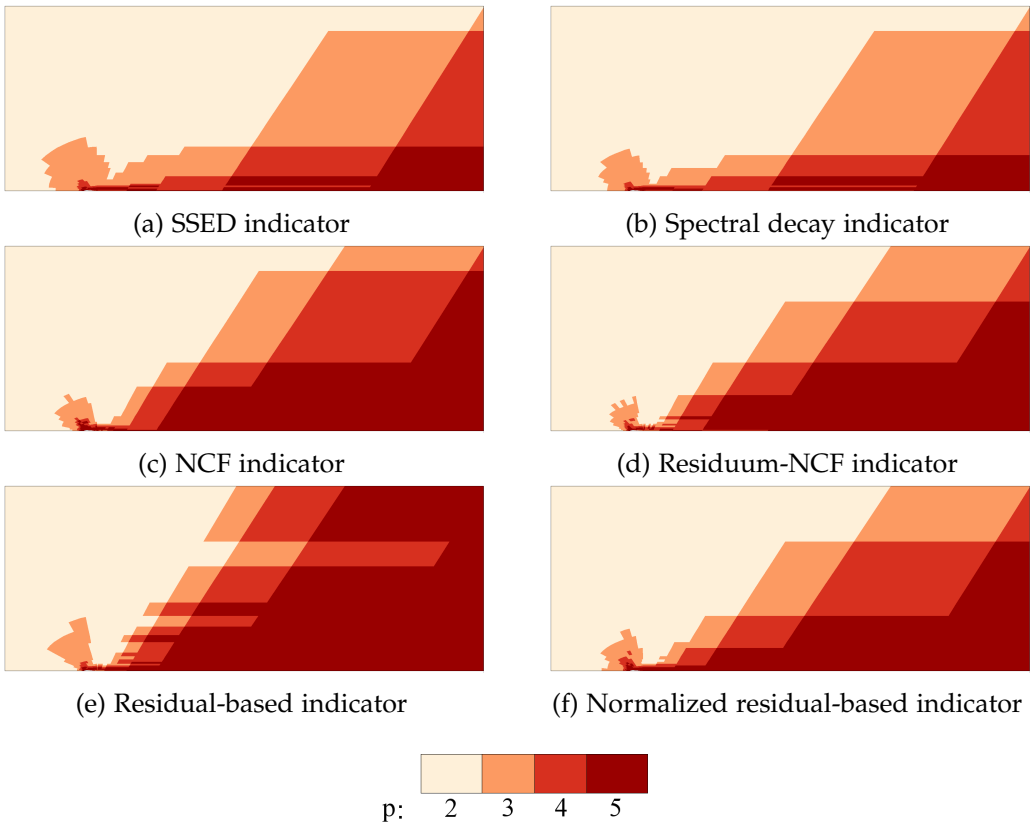

Figure 13 – Laminar flow past a Joukowski airfoil at Re = 1000, $M = 0.5$, and $\alpha = 0°$: Local polynomial degree distribution obtained for different refinement indicators.

indicator. By analysing the L^2-norm of the error in the momentum density we can observe however that the standard residual-based indicator exhibits the best performance, with the SSED and spectral decay indicators providing the slowest convergence. Nonetheless, in terms of number of dofs required to achieve the target error level, very small differences are found between the different error indicators.

These results clearly illustrate that in order to draw meaningful conclusions from the comparison of different refinement techniques it is necessary to consider more than one error measure. Moreover, it is essential to look at the full convergence history, as considering only isolated values of the error measure can lead to misleading results.

The different performance observed between the different indicators can be better analysed by studying the maps of polynomial degree obtained at a similar number of dofs (for this particular example $\#\text{dofs}^{\frac{1}{2}} \approx 180$). These are reported in Figs. 13 and 14, showing a close up in the region around the airfoil. As seen from Fig. 11, at this refinement level the p-adaptive algorithm has achieved the target level of accuracy for

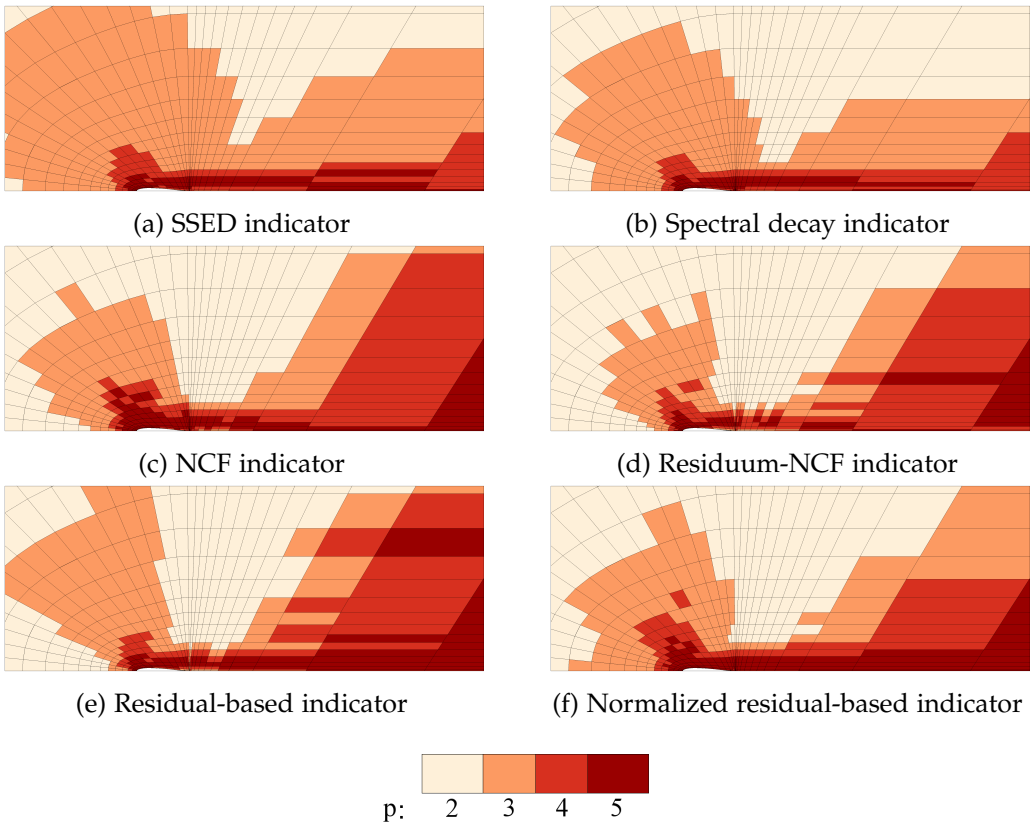

(a) SSED indicator (b) Spectral decay indicator

(c) NCF indicator (d) Residuum-NCF indicator

(e) Residual-based indicator (f) Normalized residual-based indicator

Figure 14 – Laminar flow past a Joukowski airfoil at Re = 1000, $M = 0.5$, and $\alpha = 0°$: Close up view of local polynomial degree distribution obtained for different refinement indicators.

all refinement indicators, with the exception of the standard residual-based indicator. In Figs. 13 and 14 we observe that the maps of the distribution of polynomial degrees corresponding to the SSED and spectral decay indicators are almost identical. This was also the case for the Euler configuration considered in Sec. 5.3. For the present configuration however, the spectral decay indicator presents higher refinement levels, compared to the SSED indicator, in the vicinity of the trailing edge. This behaviour suggests a strong sensitivity of this indicator to the presence of singularities in the solution. The normalized residual-based indicator also appears to be sensitive to the presence of the singularity, while all other refinement indicators select for refinement this region only after several refinement steps. Further testing would be required in order to assess the generality of these results.

Moreover, we can observe from Fig. 13 that, compared to other indicators, the SSED and spectral decay indicators generate a larger refinement region upstream of the airfoil and lower refinement levels in the far-wake region. This behaviour can explain the results shown in Figs. 11 and 12. As seen in these images, the SSED and

spectral decay indicators produce a faster reduction of the error in the drag coefficient by increasing, in the initial refinement steps, the spatial resolution in the upstream region and in the region around the airfoil (see Figs. 13a and 13b). In contrast, all the other considered indicators introduce stronger refinement in the far-wake region (Figs. 13c-f) which is characterized by large and rapid variation of element size and high aspect ratio. This poor mesh quality is possibly the source of high values of the error in the momentum density in the far-wake region. Thus increasing the spatial resolution in this region can reduce this error measure even if it has a minor effect on the error in the drag coefficient. The higher sensitivity of the residuum-NCF, residual-based and normalized residual-based indicators to the mesh quality can be explained by the fact that the employed discretization is included in their formulation. Moreover the direct dependency of the residual-based indicator on the characteristic element size in Eq. (66) is possibly the cause of its stronger sensitivity to variations in mesh size.

Similar conclusions can be drawn by analysing the maps of error distribution. As an example, we report in Fig. 15 the distribution of the considered refinement indicators evaluated for the solution obtained using a uniform polynomial degree $p = 2$. For completeness, the element-wise L^2-norm of the error in momentum density is also presented (Fig. 15g).

Finally, we note that the checkerboard-like pattern displayed by the NCF and residuum-NCF indicators in the Euler test case can also be observed in Figs. 13 and 14 as well as at intermediate steps of the p-adaptive algorithm. The generation of this pattern by the NCF indicator can be explained by its strong dependence on the resolution in neighbouring elements. Indeed, as this indicator measures the maximum jump in the solution at the element boundaries, relatively high values can still be obtained in an element where the solution is well resolved if it has neighbouring elements that require increased resolution.

In order to illustrate this behaviour, we present in Fig. 16 the NCF indicator and the corresponding polynomial degree distribution for three intermediate steps of the refinement procedure (steps 3 to 5). As can be observed in Fig. 16a a relatively smooth distribution of the NCF indicator is obtained for the solution corresponding to step 3 of the refinement process. The element marked as 1 in the picture presents a value of the NCF indicator that is above the marking threshold and is marked for refinement. The neighbouring element (marked as 2) also presents a relatively high value of the NCF indicator but is not marked for refinement. At the next refinement step element 2 still requires increased resolution leading to the appearance of a jump in the solution at the interface with element 1 (Fig. 16b). This leads to a high identical value of the refinement indicator in elements 1 and 2 and causes once more the selection of element 1 for refinement and the generation of the irregular pattern observed in Fig. 16f. The dependency of the NCF indicator on the neighbouring element with 'worst' resolution causes therefore the generation of an irregular pattern

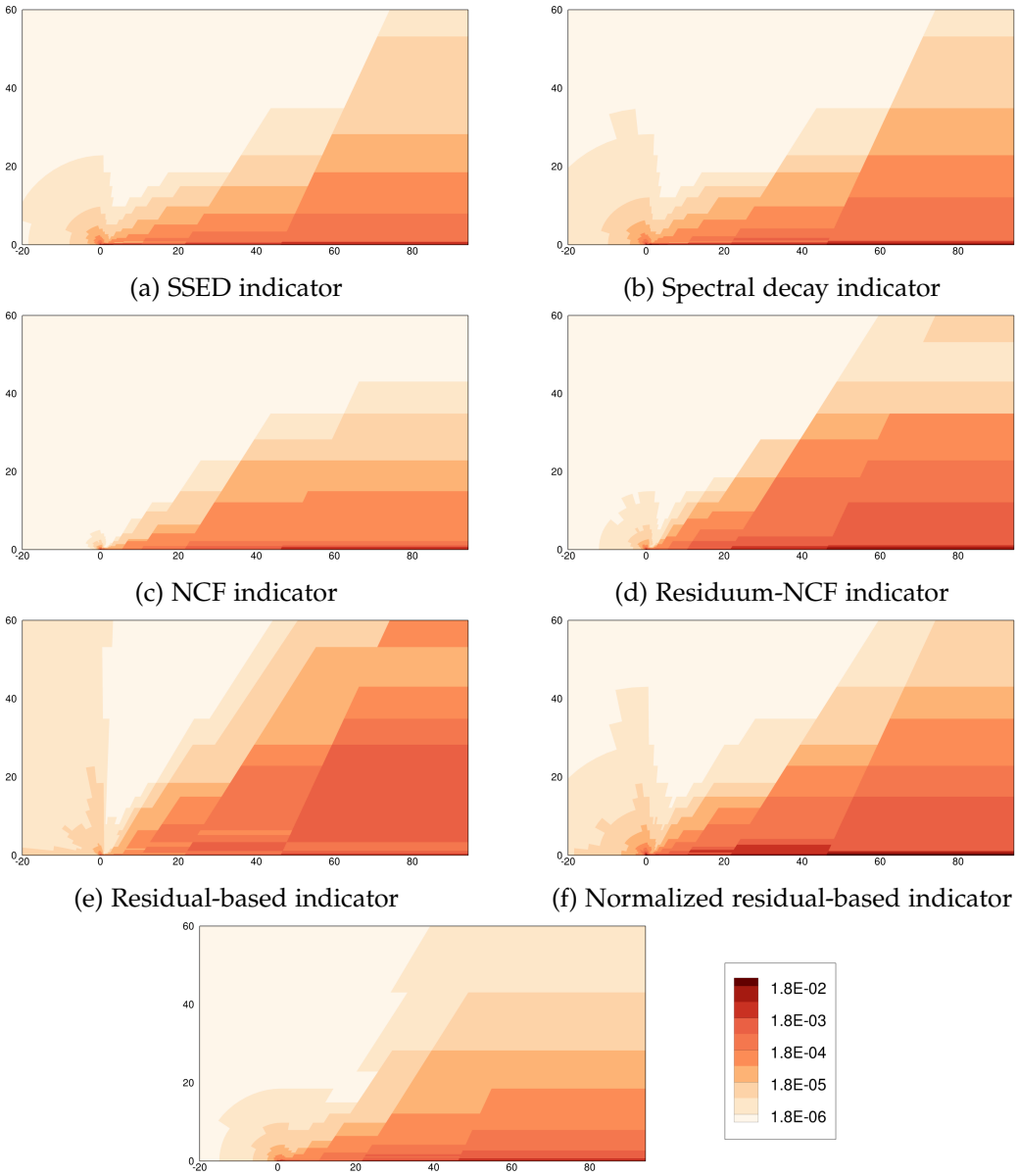

(a) SSED indicator

(b) Spectral decay indicator

(c) NCF indicator

(d) Residuum-NCF indicator

(e) Residual-based indicator

(f) Normalized residual-based indicator

(g) Exact elementwise error

Figure 15 – Laminar flow past a Joukowski airfoil at Re = 1000, $M = 0.5$, and $\alpha = 0°$: Refinement indicators (a) to (f) and error (g) for uniform polynomial degree $p = 2$.

in correspondence of boundaries between regions of different refinement levels. This also explains the observed influence of the marking strategy on the generated pattern, as the location of this boundary is controlled by the selected threshold and in general by the marking procedure.

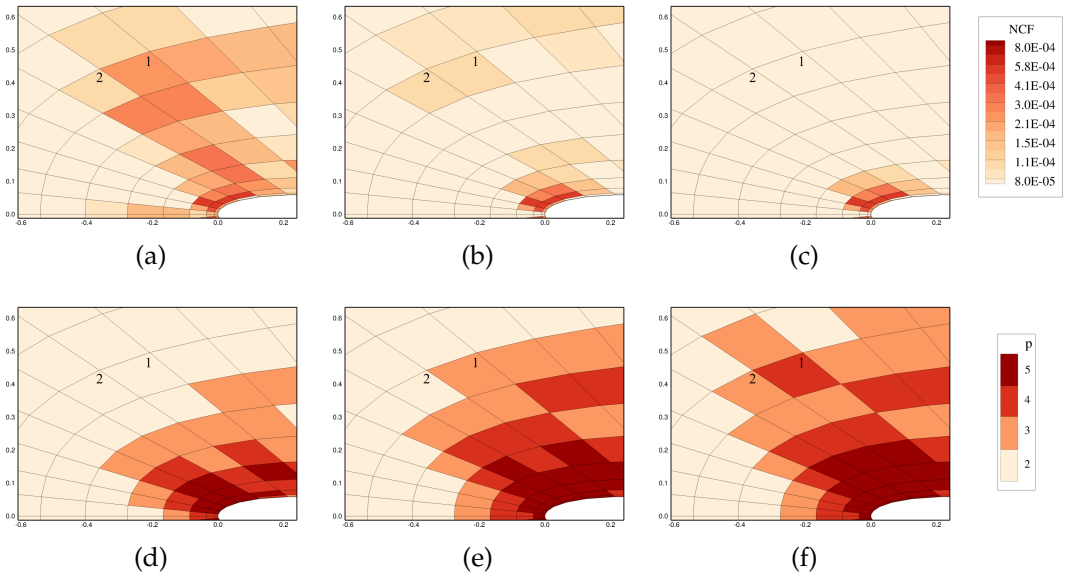

Figure 16 – Laminar flow past a Joukowski airfoil at Re = 1000, $M = 0.5$, and $\alpha = 0°$: Steps 3 to 5 of the refinement process using the NCF refinement indicator, NCF error distribution (top) and polynomial degree distribution (bottom).

A similar reasoning can be applied to the residual-based and residuum-NCF indicators due to the direct dependency of these estimators on the resolution of neighbouring elements through the surface contribution in Eq. (68) and Eq. (79). However, the dependency on all neighbouring elements, as opposed to only the 'worst' resolved one, as well as the presence of a volume term in the definition of the residual-based and residuum-NCF indicators mitigates this behaviour and reduces the generation of the checkerboard-like pattern observed for the NCF indicator.

5.5 STEADY LAMINAR FLOW PAST A CYLINDER AT RE = 40

The second viscous flow configuration considered is the laminar flow past a circular cylinder at Re = 40 and M = 0.1. For the considered Reynolds number the flow field is two-dimensional, symmetric and steady. The flow (presented in Fig. 17) separates leading to the formation of two recirculation bubbles in the near wake that need to be correctly resolved in order to compute the drag coefficient accurately. This configuration therefore constitutes an interesting test case for the validation of CFD solvers.

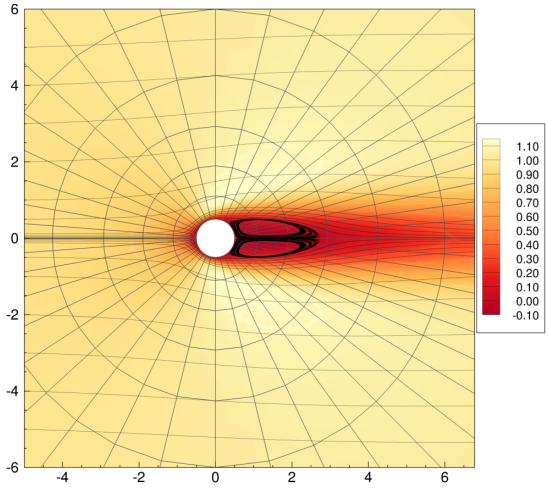

Figure 17 – Laminar flow past a cylinder at Re = 40 and M = 0.1: Streamlines and contour plot of the streamwise velocity.

Computational details

Two-dimensional simulations are thus performed by imposing no-slip boundary conditions at the wall and non-reflecting boundary conditions on the external boundary.

Extensive research has been dedicated in the literature to the analysis of the effect of the size of the computational domain on the solution of this unbounded flow. It has been shown that the presence of the artificial boundary is responsible for blockage effects and can distort phenomena generated in the internal domain and convected through the artificial boundary [75, 155]. In this research, a computational domain of radius $R = 2000D$ is therefore employed. For this extension of the computational domain, it has been verified that the effect of the external boundary on the drag coefficient is of the order of $\mathcal{O}(10^{-5})$.

The mesh employed for the following simulations is an O-type 4^{th}-order mesh with 18 and 28 elements in the radial and azimuthal directions, respectively. In the radial direction the element size changes following a geometric progression of ratio 1.25 up to $r = 6D$ and 1.65 up to the external boundary $r = R$.

Given the slow convergence in the drag coefficient observed for the standard residual-based indicator in the previous configuration, only its normalized version is considered for this test case.

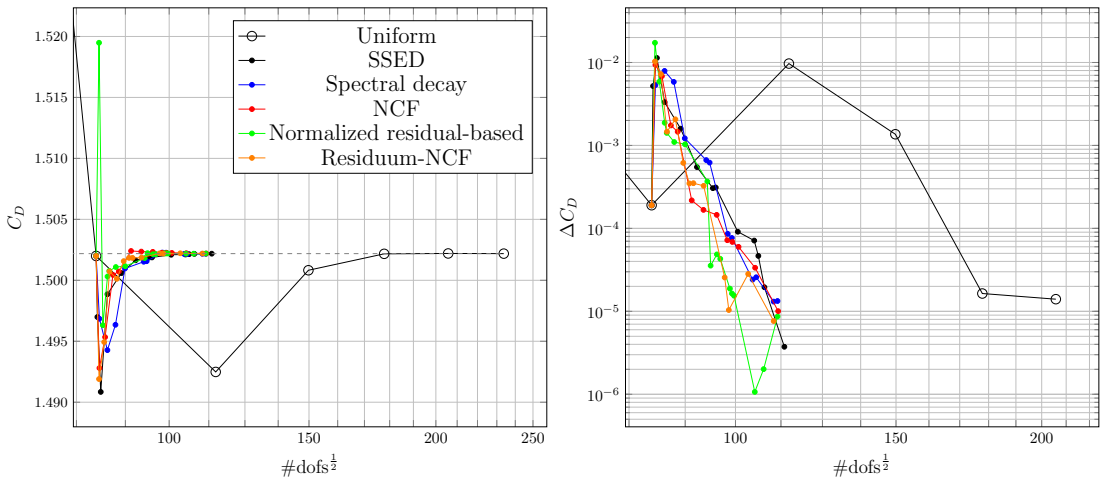

Figure 18 – Laminar flow past a cylinder at Re = 40 and $M = 0.1$: Evolution of the drag coefficient and corresponding error under uniform and adaptive p-refinement.

Analysis of the p-adaptive results

Figures 18 and 19 show the evolution of the error in the drag coefficient and in the L^2-norm of the momentum density using uniform and adaptive p-refinement with respect to a reference solution obtained using uniform $p = 7$ for which $C_D = 1.5022$.

As can be seen from these plots, all refinement indicators are able to reduce by about 75% the number of dofs necessary to achieve the same accuracy as that provided by a uniform polynomial degree $p = 6$. These results fall in line with those obtained in the previous test case, with all refinement indicators leading to a comparable computational gain in terms of number of dofs. If we consider the error in the drag coefficient shown in Fig. 18b, we can observe that the normalized residual-based and the residuum-NCF refinement indicators show slightly better performance than the other indicators considered. On the other hand, for the previous configuration the fastest convergence of the drag coefficient has been obtained using the SSED and spectral decay indicator (Fig. 11). Nonetheless, for this test case only minor differences can be observed and do not indicate a clear advantage in the use of one particular refinement indicators. As regards the discretization error plotted in Fig. 19, the residuum-NCF refinement indicator and the SSED estimator appear to provide the fastest convergence, with the residuum-NCF indicator performing best.

It is also interesting to inspect the maps of the distribution of local polynomial degree corresponding to the last iteration of the adaptive refinement procedure for the different estimators. For this last iteration, the number of dofs is approximatively 12 000 (#dofs$^{\frac{1}{2}} \approx 110$). These are shown in Figs. 20 and 21. While some differences can be observed between the different maps, the distributions of local polynomial degree are overall fairly similar for all the considered indicators. As an example,

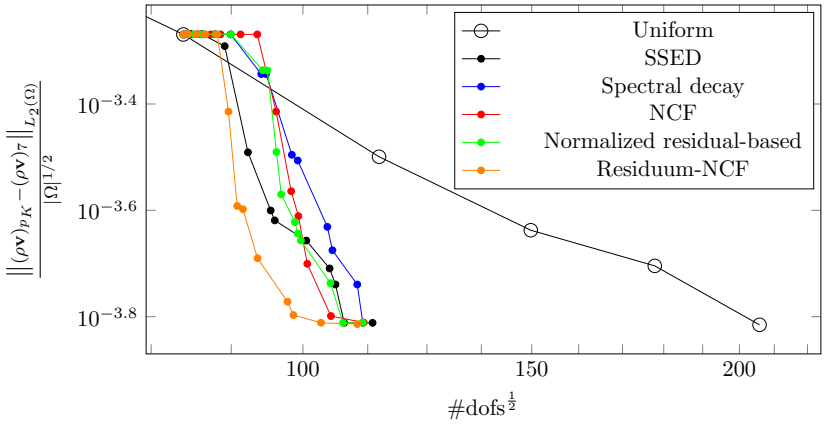

Figure 19 – Laminar flow past a cylinder at Re = 40 and $M = 0.1$: L^2-norm of the error in the momentum density under uniform and adaptive p-refinement.

all the indicators appear to select for refinement an approximately circular region around the cylinder as well as the shear region extending downstream to the outer boundary. Moreover, they all select for further refinement the regions right upstream of the cylinder and those located at an angle of 90°, before the separation of the flow which is located at 125°[75].

One of the main differences that can be observed is the disparity in the refinement levels obtained in the recirculation region and in the vicinity of the cylinder base. Among all refinement indicators, the SSED and spectral decay indicators lead respectively to the lowest and highest refinement levels in this region. This different behaviour between the SSED and spectral decay indicators, already observed in the previous configuration, is somewhat expected. Indeed the spectral decay indicator is based on a normalized estimate of DE by using the total 'energy' of the flow and therefore tends to select for further refinement regions that are characterized simultaneously by lower values of the error and of the 'energy' (e. g. recirculation regions or stagnation points). This difference could be the cause of the slower convergence rate demonstrated by the spectral decay indicator in terms of the L^2-norm of the error in the momentum density.

As already mentioned above, all refinement indicators select for refinement the far-wake region extending to the outer boundary. This is certainly due to the large size of the elements in this region requiring an increase in polynomial degree in order to correctly represent the flow. We can see from Fig. 19 that this increase in refinement level leads to a reduction of the L^2-norm of the error in the momentum density even though the effect on the convergence of the drag coefficient is rather limited as can be seen in Fig. 18. This behaviour can be compared with the one observed in the previous test case in Fig. 15. Indeed for the adaptive simulation of the laminar flow past a Joukowski airfoil, different refinement levels have been obtained

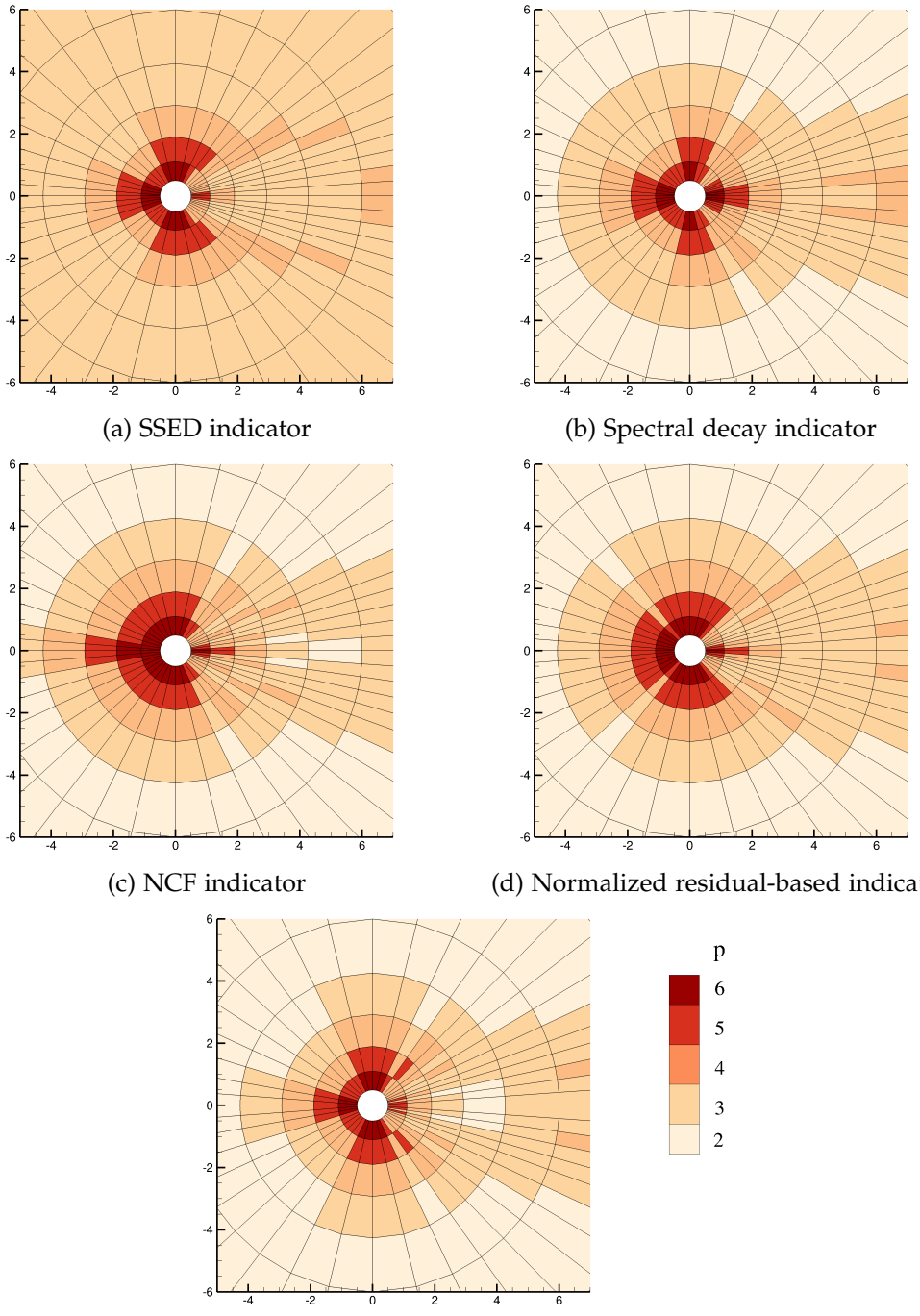

(a) SSED indicator

(b) Spectral decay indicator

(c) NCF indicator

(d) Normalized residual-based indicator

(e) Residuum-NCF indicator

Figure 20 – Laminar flow past a cylinder at Re = 40 and $M = 0.1$: Local polynomial degree distribution obtained for different refinement indicators in the near-wake region.

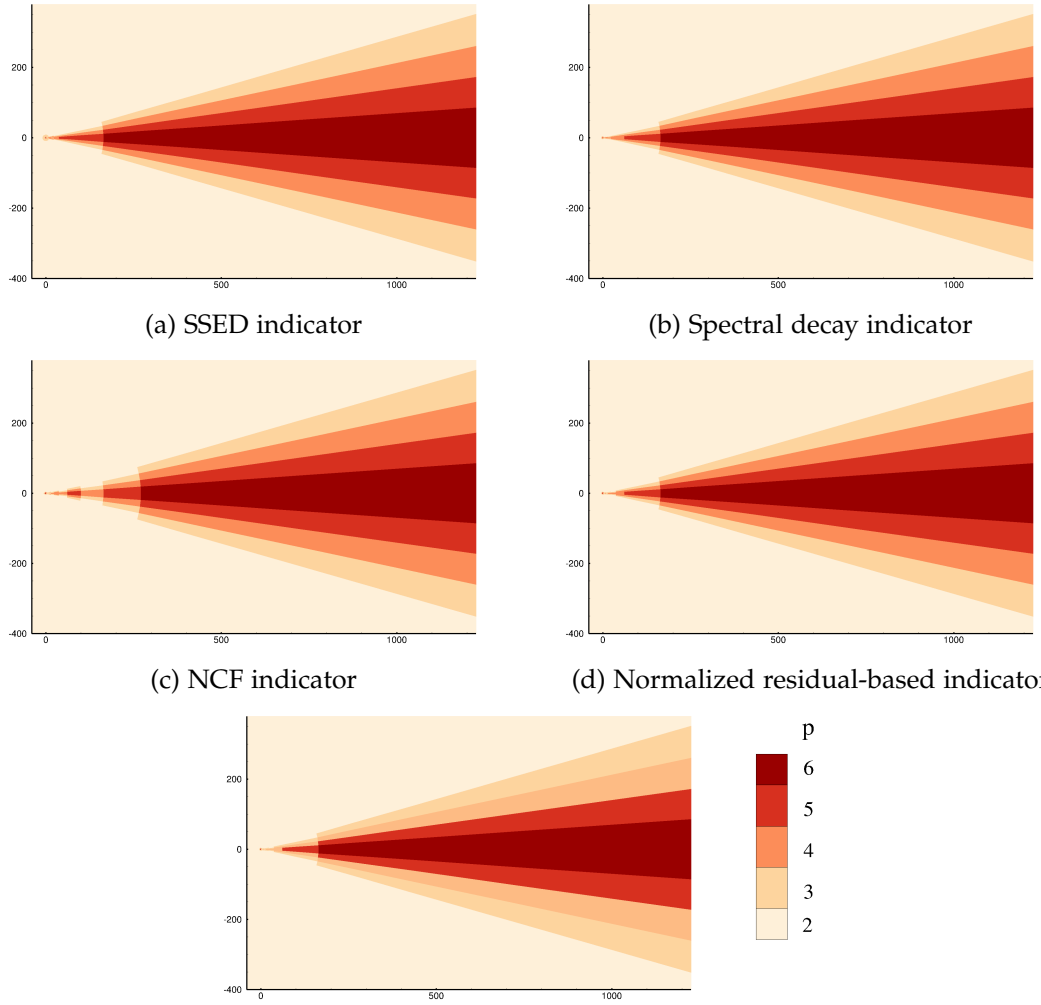

(a) SSED indicator

(b) Spectral decay indicator

(c) NCF indicator

(d) Normalized residual-based indicator

(e) Residuum-NCF indicator

Figure 21 – Laminar flow past a cylinder at Re = 40 and M = 0.1: Local polynomial degree distribution obtained for different refinement indicators in the far-wake region.

in the far-wake region depending on the refinement indicator employed, while the same refinement levels have been obtained for this configuration. This difference can be explained by a stronger sensitivity of the NCF, residuum-NCF and normalized residual-based indicators to rapid variations of the mesh size or aspect ratio rather than directly on mesh size. In fact, even though the mesh used in this test case is also characterized by large variations in element size, a more gradual variation is present here and lower values of the aspect ratio are obtained.

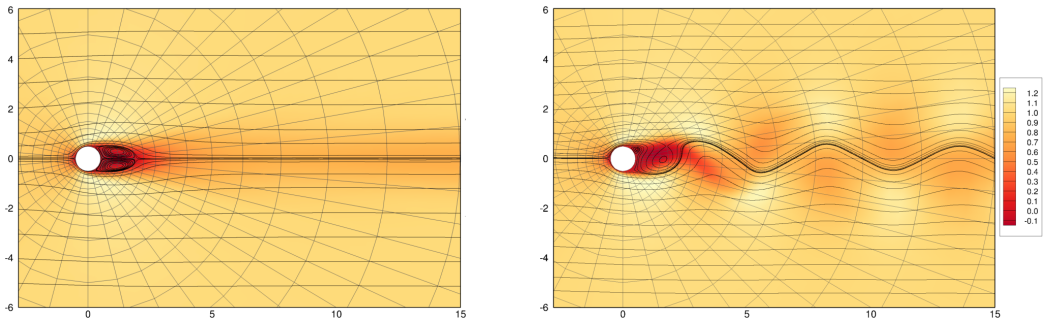

Figure 22 – Laminar flow past a cylinder at Re = 100 and M = 0.1: Streamlines and contour plots of the streamwise velocity of the average flow field (left) and one realization of the instantaneous flow field (right).

Finally, we would like to note that the checkerboard-like pattern pointed out in the previous configurations for the NCF-indicator, has also been observed for this test case over the course of the refinement process. This is however not visible in Fig. 20.

5.6 PERIODIC LAMINAR FLOW PAST A CYLINDER AT RE = 100

Finally, we investigate the applicability of the analysed refinement indicators to the simulation of unsteady flows. The considered test case is the periodic flow past a cylinder at Re $= 100$ and $M = 0.1$. The flow is two-dimensional, laminar, subsonic and unsteady periodic, characterized by the well known vortex shedding phenomenon.

The choice of a periodic flow allows for the comparison of different refinement indicators for the adaptive solution of an unsteady flow employing static p-refinement. The use of static p-refinement in place of a dynamic algorithm greatly simplifies the comparison. Indeed, as will be shown in Chap. 8, for a dynamic p-refinement algorithm the choice of the marking strategy and the frequency of adaptation have a strong influence on the accuracy of the adaptive solution. In addition, a dynamic algorithm requires the use of a coarsening criterion which makes the comparison more complex.

Computational details

The simulations are performed using a circular computational domain of radius $R = 200D$. The viscosity is assumed to be constant and adiabatic no-slip wall boundary conditions are applied on the cylinder wall. Far-field non-reflecting boundary conditions are applied at the outer boundary. An O-type 4^{th}-order mesh is employed with 28 and 42 elements in the radial and azimuthal directions respectively. In the

radial direction the element size varies following a geometric progression with ratio 1.2 up to $r = 4D$ and 1.24 up to the outer boundary.

The time discretization considered is the second-order Heun scheme with a constant time step $\Delta t = 5 \cdot 10^{-3}$ normalised by the cylinder diameter and the reference velocity. We have verified that the temporal discretization errors are negligible.

A first simulation using a uniform polynomial degree $p = 2$ is performed until the flow is fully developed and a periodic state has been reached. For each successive uniform or adaptive refinement level, the simulations are performed by restarting from the previous solution. All simulations are let to evolve for at least 40 shedding cycles before extracting the quantities of interest. The refinement indicators are then computed and the p-adaptive algorithm is applied. The periodic state is considered to be reached when the variations in the Strouhal number and the average drag coefficient measured between two shedding cycles are respectively $\Delta \mathrm{St} < 10^{-8}$ and $\Delta \overline{C_D} < 10^{-7}$.

The solution obtained from a simulation using a uniform polynomial degree $p = 7$ is used as a reference. The time-averaged flow field and one realization of the instantaneous flow field are presented in Fig. 22. The corresponding time-averaged drag coefficient $\overline{C_D}$, the Strouhal number St and the root mean square of the lift coefficient C_L' are reported in Table 2 and compared to the numerical and experimental results available in the literature.

In order to evaluate the time-independent refinement indicators used in the static p-refinement algorithm, five additional shedding cycles are simulated and the error estimators are computed at each time step once the periodic state is achieved. For each refinement indicator the element-wise maximum value in time is then used to define the time-independent error field. Further discussion on this approach, as well as a comparison with other possible strategies, can be found in Chap. 9.

For this test case, we consider the SSED, the spectral decay, the NCF and the normalized residual-based indicators. The residuum-NCF indicator is not included in this study. We have seen from the previous sections that this indicator provides a level of accuracy which is comparable to that provided by other estimators. However, as reported in Sec. 5.7 it requires a much higher computational cost for the current implementation of the solver employed.

Analysis of the p-adaptive results

We start our comparison of the different refinement indicators by analysing the convergence history of the global quantities $\overline{C_D}$, St and C_L' and their corresponding errors. These results are reported in Fig. 23. In this figure, we observe that all the refinement indicators are able to achieve the desired level of accuracy while reducing the number of dofs by about 62% compared to uniform refinement.

	$\overline{C_D}$	C_L'	St	M	domain size
Rajani et al. [157]	1.3353	0.1792	1.569	0	$R = 20D$
Ferrero et al. [65]	1.36	-	1.63	0.2	$R = 100D$
Posdziech et al. [155]	1.320	0.318	1.638	0	$h/2 = 200D$
Qu et al. [156]	1.319	0.225	1.648	0	$h/2 = 60D$
Tritton (exp) [184]	1.24 - 1.26	-	1.57 - 1.64		
Norberg (exp) [146]	-	0.227	1.64		
Wieselberg (exp) [198]	1.33	-	-		
Williamson (exp) [199]	1.33	-	1.60 - 1.64		
current	1.326	0.2266	1.638	0.1	$R = 200D$

Table 2 – Integral flow quantities obtained through numerical simulations and experiments in the literature and for the present reference simulation for the flow past a cylinder at Re = 100.

It is interesting to note that, among the considered error estimation strategies, only the normalized residual-based indicator includes in its formulation a term related to the temporal evolution of the solution (see Eqs. (61) and (68)). For this reason, we would expect this refinement indicator to exhibit the best performance. However, this does not appear to be the case and similar, if not superior, results are produced by the other three refinement indicators. These results are in agreement with the conclusions drawn from the two NS test cases previously considered.

The performance of the normalized residual-based indicator in comparison with the SSED estimator in resolving the near-wake region has also been assessed. To this end, the convergence history of the momentum density is analysed for these two estimators at two probes located respectively at $(x = 3D, y = 0D)$ on the symmetry plane and at $(x = 3D, y = 1D)$. The root mean square of the momentum density components at the first probe and the average momentum density components at the second are reported in Fig. 24. The two indicators actually lead to similar efficiency and a rapid convergence to the solution of the simulation performed using a uniform polynomial degree corresponding to the maximum value allowed for the refinement algorithm, *i.e.* $p_{\max} = 6$, as expected.

Following the same methodology employed for the previous test cases, we report in Figs. 25 and 26 the p-refinement level maps corresponding to $\#\text{dofs}^{\frac{1}{2}} \approx 145$. These results are in agreement with those obtained in the previously analysed configurations. The SSED and spectral decay indicators select the same refinement regions with higher refinement required by the latter in the low energy region at the base of the cylinder. The normalized residual-based indicator presents a smaller refinement region in the vicinity of the cylinder. Moreover, we have observed that this indicator introduces higher levels of refinement in the near and far-wake region in the initial

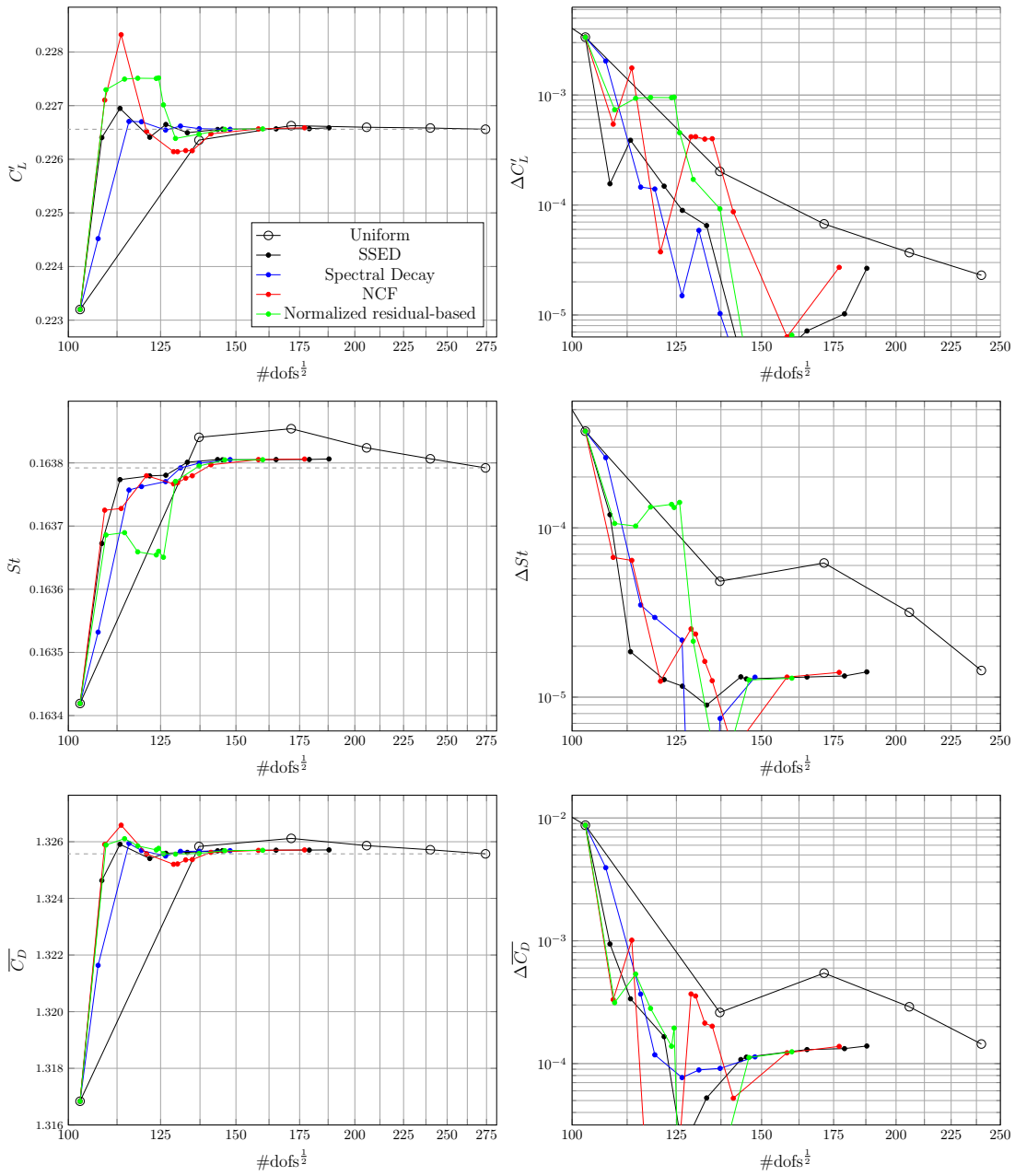

Figure 23 – Laminar flow past a cylinder at Re = 100 and $M = 0.1$: Convergence history of the time-averaged drag coefficient, the Strouhal number and the root mean square of the lift coefficient.

refinement steps. The NCF indicator shows a similar behaviour to the normalized residual-based indicator. The generation of the already described checkerboard-like pattern is also visible from the plots shown in Figs. 25c and 25d.

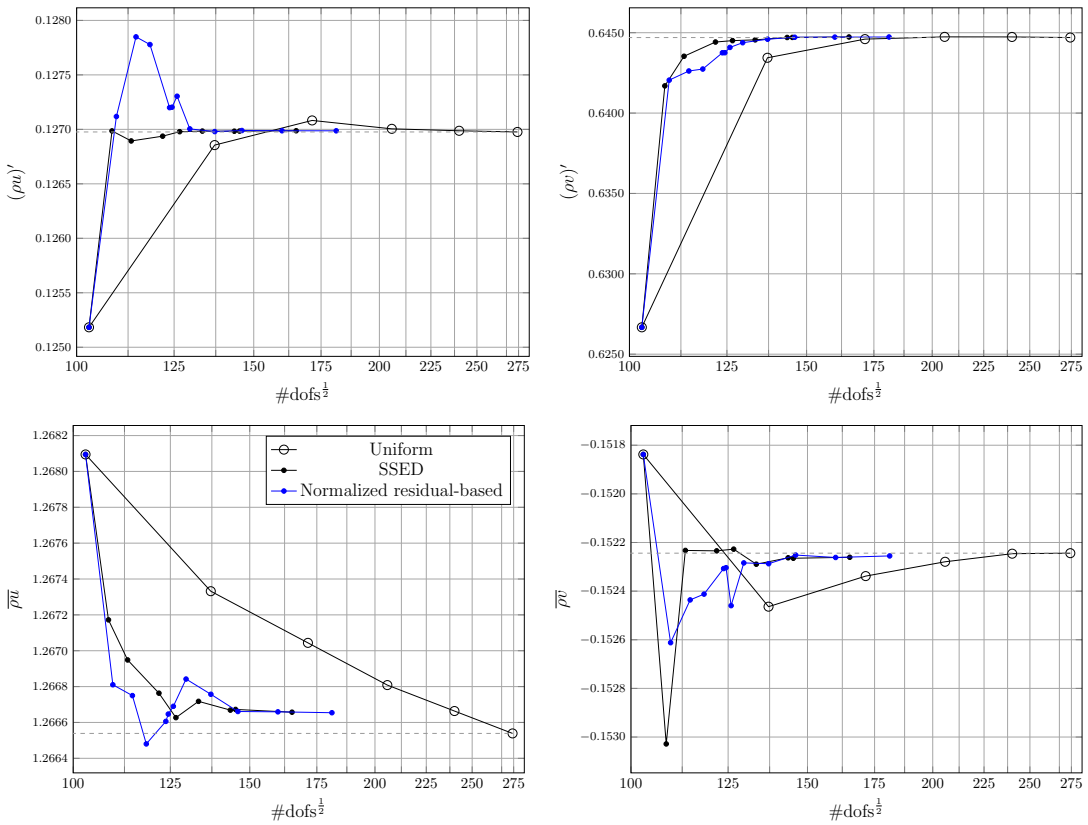

Figure 24 – Laminar flow past a cylinder at Re = 100 and M = 0.1: Convergence history of root mean square of the momentum density components at location $[3D, 0D]$ (top) and time-averaged momentum density components at location $[3D, 1D]$ (bottom).

The results obtained for this configuration thus corroborate the conclusions drawn from the steady laminar test cases. These indicate that very similar performance can be obtained for the p-adaptive simulation of unsteady flows by employing the SSED and spectral decay indicators compared to the more complex and computationally expensive residual-based indicator.

5.7 COMPUTATIONAL COST AND IMPLEMENTATION ISSUES

In the previous sections, the performance of the different refinement indicators has been analysed in terms of the reduction in the number of dofs provided by each estimator. Nonetheless, as computational time is in practice a more relevant parameter, it could be argued that more meaningful information might be obtained by comparing the performance of various refinement indicators in terms of the total computational time to achieve a prescribed level of accuracy. However, a comparison

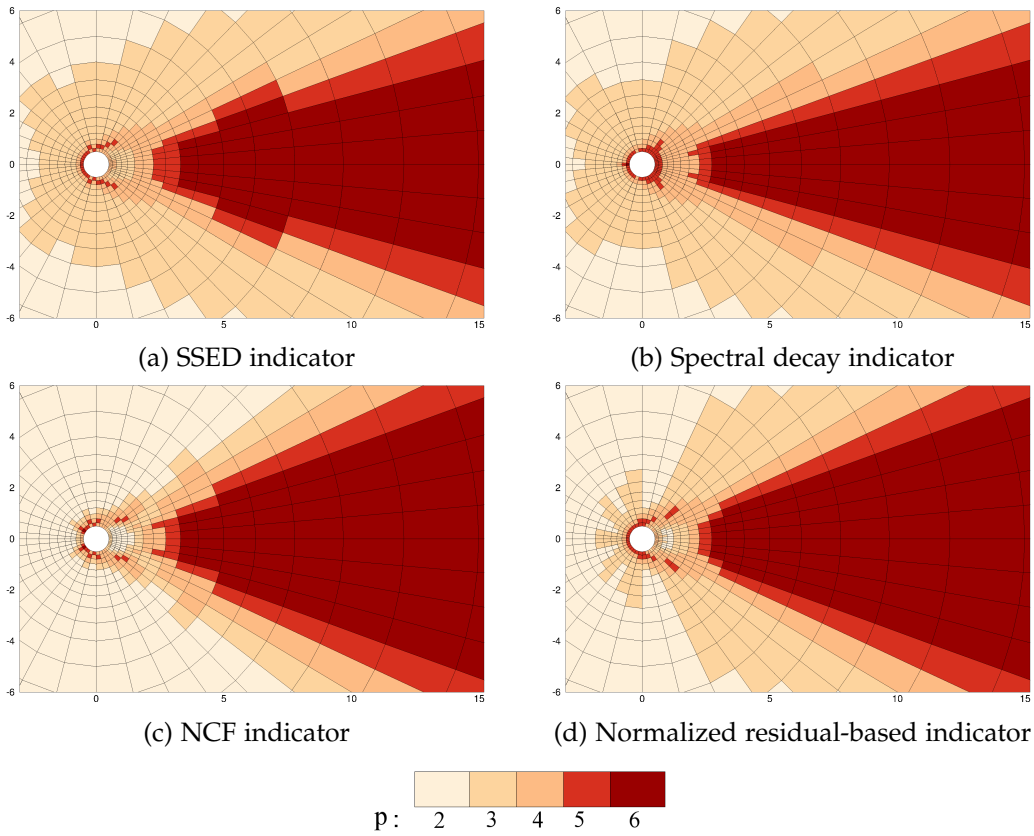

(a) SSED indicator

(b) Spectral decay indicator

(c) NCF indicator

(d) Normalized residual-based indicator

Figure 25 – Laminar flow past a cylinder at Re = 100 and M = 0.1: Local polynomial degree distribution obtained for different refinement indicators. Near-wake region.

in terms of total computational time would be extremely complex and might actually lead to wrong conclusions. This is caused by the presence of several parameters that strongly impact the total computational time. As an example, the computational cost of the refinement indicators depends on the implementation details of the DG solver (e.g. modal versus nodal approach). Additionally, even when comparing different refinement indicators using a given DG solver, the required computational time is also strongly influenced by the employed marking strategy and the rate of convergence to the steady state (for stationary problems). The latter in turn also depends on the configuration, initial solution and employed discretization.

To demonstrate the difficulties in carrying out such an analysis, we report in Fig. 27 the convergence history of the global entropy error for the inviscid flow over a Gaussian bump presented in Sec. 5.3. The convergence history obtained using uniform p-refinement is compared to the results of adaptive p-refinement based on the SSED and residual-based indicators for two values of the marking fraction parameter: $\theta = 0.5$ and $\theta = 0.1$.

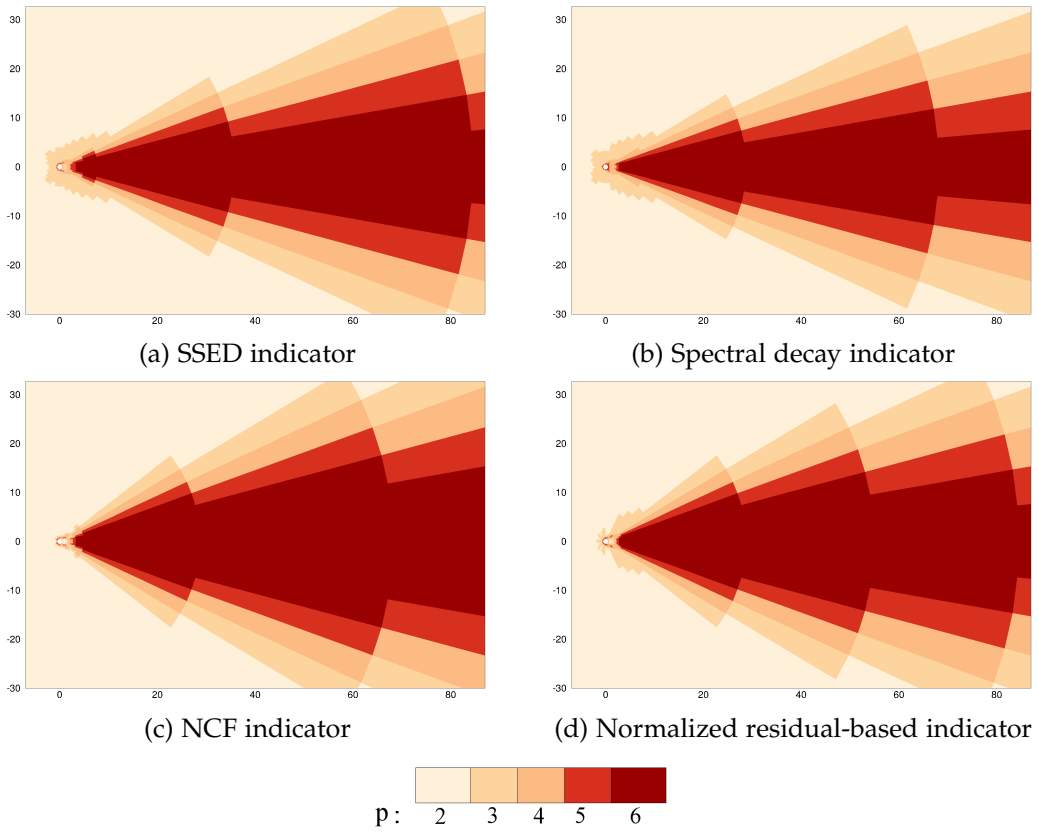

(a) SSED indicator

(b) Spectral decay indicator

(c) NCF indicator

(d) Normalized residual-based indicator

Figure 26 – Laminar flow past a cylinder at Re = 100 and $M = 0.1$: Local polynomial degree distribution obtained for different refinement indicators. Far-wake region.

The left panel of Fig. 27 plots the error versus the computational cost in terms of CPU time. Each simulation is restarted from the solution obtained at the previous refinement level and is performed on one single processor. As can be seen in this graph, the number of refinement steps and therefore the total computational time is sensitive to the marking strategy as well as to the refinement indicator. In particular, a higher value of the marking fraction θ leads to a lower number of elements being selected for refinement at each step of the adaptive algorithm. Therefore this would require a larger number of refinement steps in order to achieve the same resolution. This leads to strong variations of the CPU time and renders a fair comparison between indicators in terms of CPU time impractical as it would require the identification of the best marking strategy for each indicator.

This result can be contrasted to the right panel of Fig. 27 in which the comparison is made in terms of the number of dofs. It is interesting to see that only minor differences can be identified between the results obtained using the same indicator and the two different values of θ considered in this example. This clearly illustrates

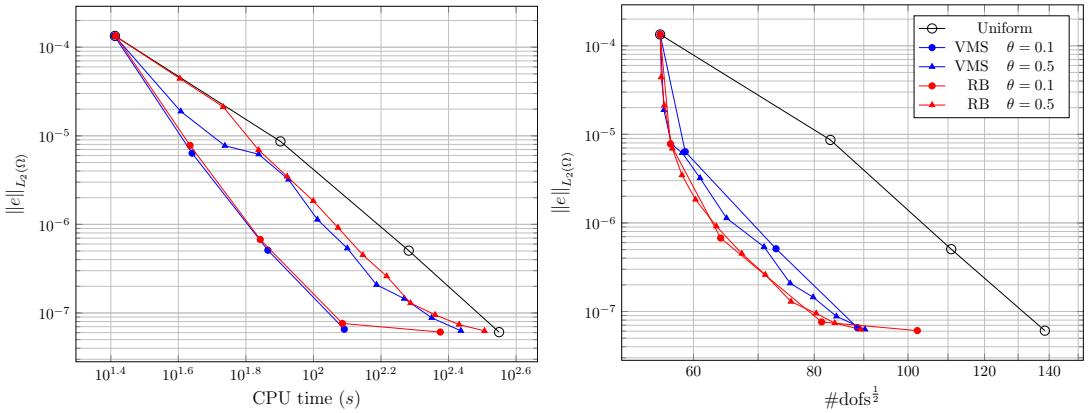

Figure 27 – Inviscid flow over a Gaussian bump at $M = 0.5$: Global entropy error vs number of dofs and CPU time under uniform and adaptive refinement.

that comparisons in terms of number of dofs are influenced to a much lower extent by the specific marking procedure employed.

These results therefore indicate that comparisons in terms of CPU time would lead to conclusions that are specific to the CFD code, the numerical implementation, the marking strategy and the test case considered. In contrast, comparing results in terms of total number of dofs and refinement levels can provide more general conclusions.

In what follows, we make some general observations that might be useful even when considering a different implementation from the one employed in our work. In particular, we consider the locality properties of the refinement indicators and their possible effect on parallel efficiency, the number of operations required by each indicator and the ease of implementation in an existing CFD code.

LOCALITY As regards locality, we can see from the definition of the different refinement indicators provided in Sec. 4.4 that the only two indicators which are fully local are the SSED and the spectral decay indicators as their computation only requires the knowledge of the solution inside the element (see Eqs. (53) and (55)). On the other hand, the computation of the NCF indicator (given in Eq. (57)) requires knowledge of the projection at the interface of the solution from the direct neighbours, while the residual-based and the residuum-NCF indicators will require additional information to be exchanged for the computation of the numerical fluxes. In the framework of distributed memory computations this lack of locality will involve blocking message passing operations which may lead to a reduced parallel efficiency.

OPERATION COUNT Considering now the number of operations involved in the computation of each indicator, we observe that the SSED and spectral decay indicators require the projection of the solution on the reduced-order space S_h^{p-1} and the

computation of the integrals required to evaluate the L^2-norm in Eq. (53) and (55). In the case of a modal DG approach based on hierarchical basis functions, the scale separation is readily available and the required integrals can be efficiently computed by employing information contained in the mass matrix (see App. B). On the other hand, if a non-hierarchical basis is employed (*e. g.* nodal approach), the additional projection operation and the integration by quadrature necessary to compute the L^2-norm will lead to higher computational cost. In this particular case, the NCF indicator would be more computationally efficient as it only requires the interpolation of the solution at the Gauss points on each interface. As regards the residual-based and residuum-NCF indicators, their computation is more expensive as compared to the other indicators in either the nodal or the modal approach. Indeed, the evaluation of the former requires the computation and integration over the elements and faces of the element residuals, numerical fluxes and the convective and diffusive fluxes obtained from the internal reconstruction $\mathcal{F}(\mathbf{u}_h^+, \nabla\mathbf{u}_h^+)$. Finally, we expect the residuum-NCF to be the most expensive among the considered indicators, regardless of the particular CFD solver considered. This is because, the contribution of the non-conformity error is more expensive to compute than the NCF indicator alone as it requires the integration of the jump terms that appear in the expression of the NCF indicator. The evaluation of the residuum-error contribution, on the other hand, requires the computation of the discrete residuals $\mathcal{N}_h(\mathbf{u}_h, \phi_i)$ with ϕ_i being the basis functions corresponding to the space S_h^{p+1}. To this we have to add the cost of the Lagrange multiplier method involved in the computation of this indicator which requires the solution of a linear system of size $(p_K + 2)^d$ for each element.

EASE OF IMPLEMENTATION Finally, with regard to the ease of implementation, it is interesting to note that the complexity of computing the residuals corresponding to the refined polynomial space S_h^{p+1}, involved in the evaluation of the residuum-NCF indicator, strongly depends on the numerical implementation of the CFD method. In the case of a CFD code based on orthonormal basis functions built in the physical space, like the one employed in this work, this requires the computation and storage of the basis functions for S_h^{p+1} as well as their derivatives at the corresponding set of quadrature points. In general, important modifications of the employed CFD solver might be required to achieve a computationally efficient implementation of the residuum-NCF indicator. Similar considerations can be drawn for the residual-based indicator for which the different terms involved in its definition (Eqs. (61) to (63)) depend directly on the set of equations being solved and the discretization employed. This is not the case for the SSED, spectral decay and NCF indicators which can be easily implemented even as external post-processing tools independently of the employed solver.

5.8 CONCLUSION

In this chapter we have compared the performance of various refinement indicators for the p-adaptive simulation of steady and unsteady flows using DG methods. Five refinement indicators based on discretization-error and residual-error estimates have been considered.

The computational gain provided by a p-adaptive procedure based on any of the employed indicators has been clearly demonstrated. For all the configurations considered we have obtained a reduction in the number of degrees of freedom necessary to achieve the prescribed level of accuracy between 50% and 75% as compared to uniform p-refinement.

Overall, very similar results have been observed for all refinement indicators both in terms of convergence history and of the spatial regions selected for refinement. This is of interest because the SSED, spectral decay and NCF indicators require a very limited computational overhead and can be easily implemented as a post-processing operation. Moreover, they do not depend on the physical model considered or the employed discretization. In contrast, the computation of the residual-based and residuum-NCF indicators might require a considerable effort in order to obtain an efficient implementation well-adapted for the solver at hand.

With regard to the SSED and spectral decay indicators, the former demonstrated similar, if not superior, performance as compared to the latter for all cases considered. The SSED indicator has also the advantage of presenting a lower computational cost regardless of the employed implementation, as the evaluation of the L^2-norm used to normalize the spectral decay indicator does not need to be computed (see Sec. 5.7).

As regards the analysis of the distribution of polynomial degree yielded by the different refinement indicators, it has revealed that the NCF, the residual-based and the residuum-NCF indicators present a stronger sensitivity to the mesh quality compared to the other indicators. Furthermore, the NCF indicator generates a checkerboard-like pattern which appears to be related to the refinement history and therefore the employed marking strategy. This pattern could potentially damage the convergence of the refinement algorithm and the accuracy of the solution as it introduces an irregularity in the spatial discretization. However, it is not excluded that this indicator could be used efficiently in conjunction with another refinement indicator, following for example an approach similar to the residuum-NCF indicator.

With all these considerations in mind, it can be argued that the SSED or spectral decay indicators constitute a good choice for p-adaptive simulations of unsteady flows, as they combine accuracy, computational efficiency and ease of implementation. For this reason, the SSED indicator is employed as refinement indicator for the p-adaptive simulations in most of the remainder of this work.

CHAPTER 6

ANALYSIS OF ERROR ESTIMATION STRATEGIES FOR *H*-ADAPTIVE SIMULATIONS

RÉSUMÉ DU CHAPITRE EN FRANÇAIS

Dans ce chapitre, nous présentons une comparaison de différents indicateurs de raffinement pour le développement des stratégies d'adaptation-*h*.

Nous considérons une approche d'adaptation-*h* basée sur la division d'éléments hexaédriques d'ordre élevé. L'algorithme employé est brièvement décrit dans la Sec. 6.2. Il consiste à diviser chaque élément marqué en 2^d éléments, d étant le nombre de dimensions spatiales. Cette opération est effectuée dans l'espace de référence de telle sorte que les éléments générés sont une tessellation de l'élément initial.

Cinq indicateurs de raffinement sont dans un premier temps comparés dans la Sec. 6.3 en effectuant des simulations *h*-adaptatives de l'écoulement non visqueux dans un canal comportant une bosse avec profil gaussien à M = 0.5. Ce sont les indicateurs SSED, spectral-decay, NCF, residual-based normalisé et l'erreur d'entropie locale. Il est montré que la plupart des conclusions obtenues pour l'adaptation-*p* dans le Chap. 5 peuvent être appliquées aux simulations *h*-adaptatives. En particulier, les indicateurs SSED, spectral-decay et residual-based normalisé conduisent à des résultats similaires avec une réduction de 60% du nombre de degrés de liberté requis pour atteindre la même précision que le raffinement-*h* uniforme. De plus, l'indicateur NCF conduit à une distribution irrégulière des niveaux de raffinement-*h*.

Deux configurations d'écoulement laminaire sont ensuite analysées dans la Sec. 6.4: l'écoulement autour du profil Joukowski à Re = 1000, M = 0.5, et $\alpha = 0°$, et l'écoulement autour d'un cylindre à Re = 40 et M = 0.1. Seuls l'indicateur SSED et l'indicateur residual-based normalisé sont considérés. Il est démontré que l'indicateur SSED fournit des performances similaires à l'indicateur residual-based normalisé pour la première configuration et des résultats améliorés pour la seconde. De plus, l'indicateur residual-based normalisé semble être plus sensible aux variations de la taille des éléments dans le domaine, comme déjà observé dans le Chap. 5. C'est pour cette raison qu'il introduit un raffinement élevé dans la région de sillage.

Les résultats obtenus démontrent donc que l'indicateur SSED peut être utilisé efficacement dans le cadre de simulations h-adaptatives.

6.1 INTRODUCTION AND OUTLINE OF THE CHAPTER

In the previous chapters we have focused on the development of p-adaptation strategies. Indeed, p-adaptation presents several interesting properties such as ease of implementation, exponential convergence rate for smooth problems and a faster reduction of dissipation and dispersion errors as compared to h-refinement.

Nonetheless, it presents some important limitations, some of which have already been outlined in Sec. 4.2. In particular, the maximum value of the polynomial degree, and therefore the maximum level of p-refinement, is limited in practical applications. This is due to the rising importance of aliasing errors and the rapid increase of the computational cost for high polynomial degree representations. Additionally, p-adaptation presents a lower flexibility compared to h-adaptation. Indeed, the locality of p-adaptation is limited by the underlying computational grid whereas h-adaptation allows for a more efficient refinement of the resolution near isolated features, including physical and geometrical singularities. This property, combined with the reduced convergence rate of the DG method and the appearance of the Gibbs phenomenon for the aforementioned physical problems, motivates the research interest in h- and hp-adaptation techniques.

Similarly to the study carried out in Chap. 5, we are here interested in the analysis of different error estimation strategies in the framework of h-adaptive simulations. The objective of the present chapter is thus to provide such an analysis and to assess the applicability of the conclusions obtained in Chap. 5 to h-adaptive simulations for the smooth configurations considered here.

The remainder of this chapter is organized as follows. In Sec. 6.2 we present the h-refinement strategy used in the present work. Following the outline presented in Chap. 5, it is then combined with various error estimation strategies. The h-refinement algorithm is firstly studied by simulating the inviscid flow over a Gaussian bump at $M = 0.5$ in Sec. 6.3. Numerical results for laminar flows are then presented in Sec. 6.4 for two configurations: the flow past a Joukowski airfoil at Re = 1000, M = 0.5 and $\alpha = 0°$ and the flow past a cylinder at Re = 40 and M = 0.1.

The study presented in this chapter is the fruit of a collaboration with A. Matas Salva, carried out in the framework of his internship from April to September 2018. Other details can be found in his Master's thesis [171].

6.2 H-REFINEMENT BY ELEMENT SPLITTING

The h-refinement algorithm considered in this work has originally been developed by Kuru et al. [113] and is designed for the generation of locally

refined non-conforming curvilinear hexahedral (and quad) meshes. Using this approach, isotropic *h*-refinement is performed by splitting elements marked for refinement into 2^d child elements, where d is the number of space dimensions.

In order to illustrate this process, let us denote by $R : \{K\} \rightarrow \{K_1, \ldots, K_{2^d}\}$ the operator that applied to an element returns the coordinates of its child elements in physical space. The operator R is then defined for each element as

$$R := \Psi_K \hat{R} \Psi_K^{-1} \ , \tag{93}$$

where $\hat{R} : \{K_{ref}\} \rightarrow \{\hat{K}_1, \ldots, \hat{K}_{2^d}\}$ is the operator which splits the reference element into 2^d identical children, and Ψ_K denotes the mapping function from the reference to the physical element. A schematic representation of this process is presented in Fig. 28 for $d = 2$.

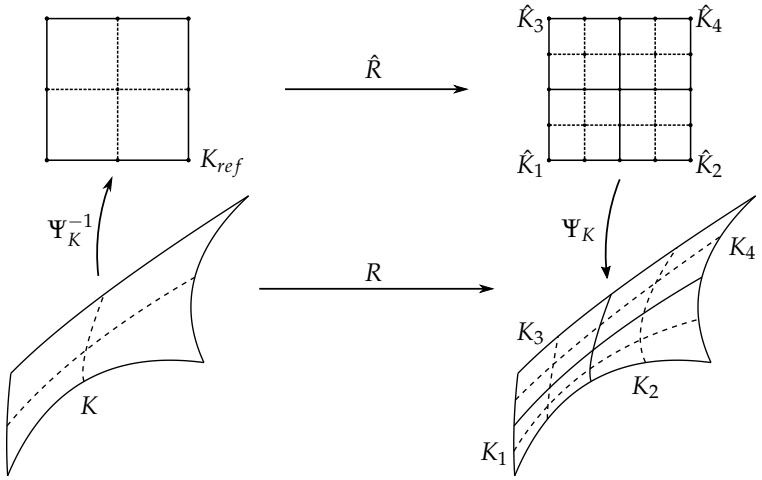

Figure 28 – Schematic representation of *h*-refinement of a two-dimensional curvilinear element.

As the refinement process is performed in the reference space, the generated child elements represent a tessellation of the physical domain associated with the parent element and the quality of the initial mesh is preserved. It should also be noted that, the geometrical representation of physical boundaries is not modified. For this reason, the initial mesh must represent sufficiently well the geometry of curved boundaries, as is also the case for the *p*-adaptive simulations presented in this work.

In order to avoid excessive variations in element size, a 2 : 1 ratio constraint is imposed to the *h*-adaptive algorithm by limiting to one the variation in refinement level between two neighbouring elements. This constraint is further described in Sec. 4.5.

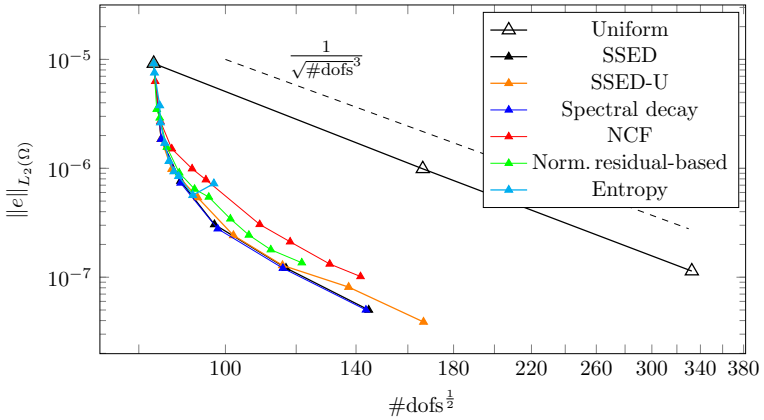

Figure 29 – Inviscid flow over a Gaussian bump at M = 0.5: Convergence history of the global entropy error under uniform and adaptive h-refinement.

6.3 INVISCID FLOW OVER A GAUSSIAN BUMP

The h-refinement technique is first applied to the adaptive simulation of the inviscid flow over a Gaussian bump. This configuration has already been presented in Sec. 5.3. The same initial computational grid and numerical discretization employed in that study are used here. The adaptive algorithm proceeds in the way described in Chap. 5. In this case, however, the polynomial degree is considered uniform and equal to $p = 2$ and marked elements are refined by element splitting, as just described.

Five refinement indicators are considered in this section: the SSED indicator, its non-normalized variant Eq. (52), the NCF indicator, the normalized residual-based indicator and the local entropy error. In order to simplify the notation, we refer to the non-normalized variant of the SSED indicator as the SSED-U indicator. Note that this corresponds to the original formulation of the refinement indicator as proposed by Mavriplis et al. [130] and Kuru et al. [113].

The performance of the h-refinement algorithm is measured by comparing the convergence history of the global entropy error provided by the h-adaptive and uniform h-refinement simulations. We remark that the maximum local refinement level is not limited in this study. For this reason the h-refinement approach can achieve higher accuracy than the uniformly refined simulations. This was not the case for the p-adaptive simulations presented in Chap. 5, as the maximum local polynomial degree was limited.

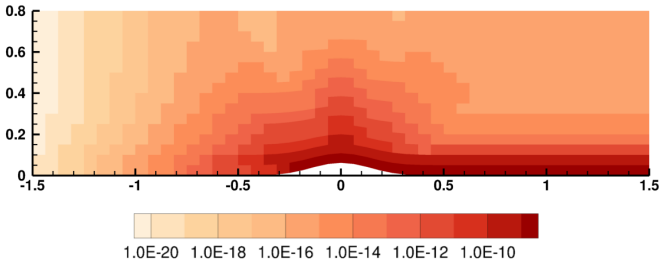

Figure 30 – Inviscid flow over a Gaussian bump at M = 0.5: Distribution of the local entropy error on the initial mesh.

Analysis of the results

We report in Fig. 29 the convergence history of the global entropy error under uniform and adaptive h-refinement. All refinement indicators, with the exception of the local entropy error, lead to a large reduction of the necessary number of dofs to achieve a prescribed level of accuracy.

The best performance is obtained for the SSED and the spectral decay indicators which achieve the same accuracy as the finest uniformly refined simulation with a reduction of approximately 60% in the number of dofs. Slightly lower performance is provided by the residual-based and NCF indicators, the latter allowing for a reduction in the number of dofs of about 49%.

We remark that, when guided by the local entropy error, the h-adaptive algorithm yields in the initial refinement steps similar results to those obtained for the other refinement indicators. However, the performance drastically deteriorates at later stages of the adaptive process. This behaviour is possibly related to the specific marking strategy employed. To illustrate this aspect, we report in Fig. 30 the distribution of the local entropy error on the initial mesh. Higher values of the local entropy error are obtained near the Gaussian bump, where the error is produced, and in the downstream region, where the error is convected. However, the h-refinement strategy relying on this quantity as refinement indicator only refines a small number of elements near the bump. This is caused by the relatively high value of the refinement threshold obtained with the maximum marking strategy here employed. The use of a lower marking fraction θ would lead to a lower refinement threshold, and thereby additional refinement in the downstream region. As a consequence, the measured efficiency in terms of number of dofs of the h-adaptive algorithm would be lower and in better agreement with that of the p-adaptive algorithm based on the same indicator and reported in Fig. 10.

In Fig. 31 we report the distribution of the local entropy error obtained by the adaptive simulations for $\#\text{dofs}^{\frac{1}{2}} \approx 120$ (100 for the entropy-based indicator). The same quantity is presented in Fig. 32 superimposed on the obtained adapted meshes.

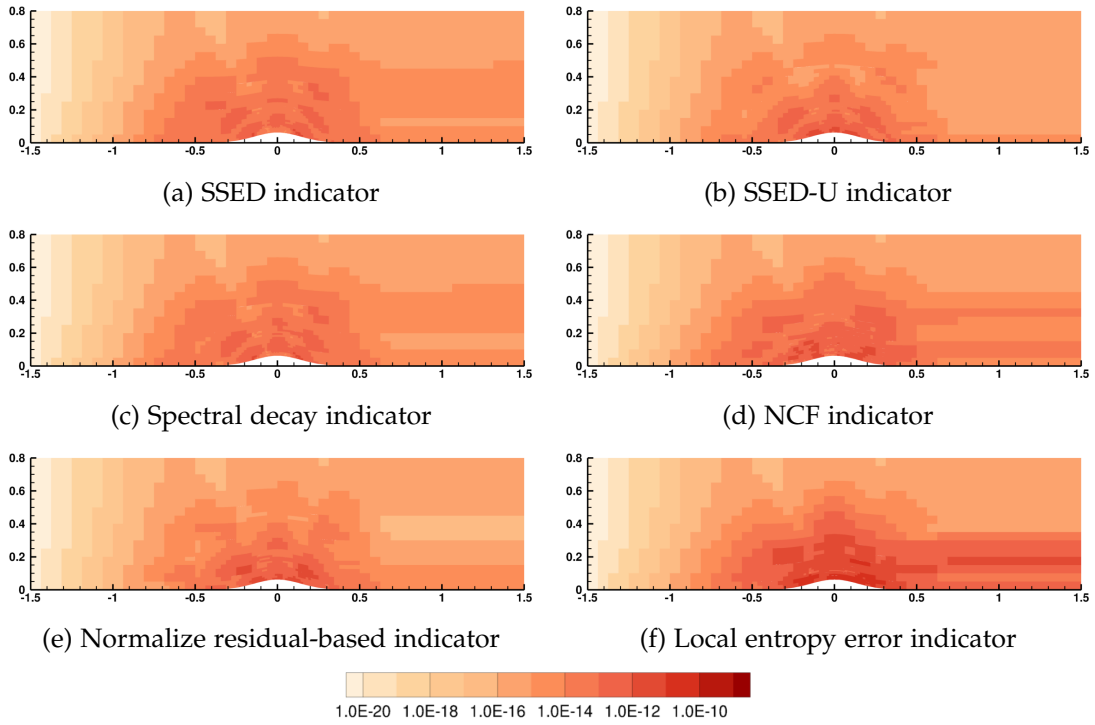

Figure 31 – Inviscid flow over a Gaussian bump at M = 0.5: Distribution of the local entropy error on the meshes obtained by adaptive h-refinement. The number of dofs is equal to $\sim 120^2$ for all refinement indicators with the exception of the local entropy error indicator, for which #dofs $\approx 100^2$.

A close-up view is provided in Fig. 33. We observe that, with the exception of the local entropy error indicator, all refinement indicators lead to a reduction of the local entropy error both near the bump and in the downstream region where no refinement is introduced.

Analysing Figs. 32 and 33, we observe that the obtained patterns of h-refinement levels are very similar to the distribution of the local polynomial degree obtained for this problem using the p-refinement algorithm in Fig. 10. As already observed in Chap. 5, the SSED and spectral decay indicators lead to almost identical refinement levels. Conversely, the SSED-U indicator yields a larger refined region and a lower level of refinement in the vicinity of the bump. This behaviour can be explained by the fact that the SSED and SSED-U indicators provide respectively an estimate of the average error and of the L^2-norm of the error in the momentum density. When an element is refined, both the average error and the element size are reduced. This leads to a faster reduction of the value of the SSED-U indicator as compared to the SSED indicator. This behaviour can induce the generation of smaller refined regions with relatively higher refinement levels for the latter. Similar results are obtained for the spectral decay indicator as the relative error presents the same distribution as the

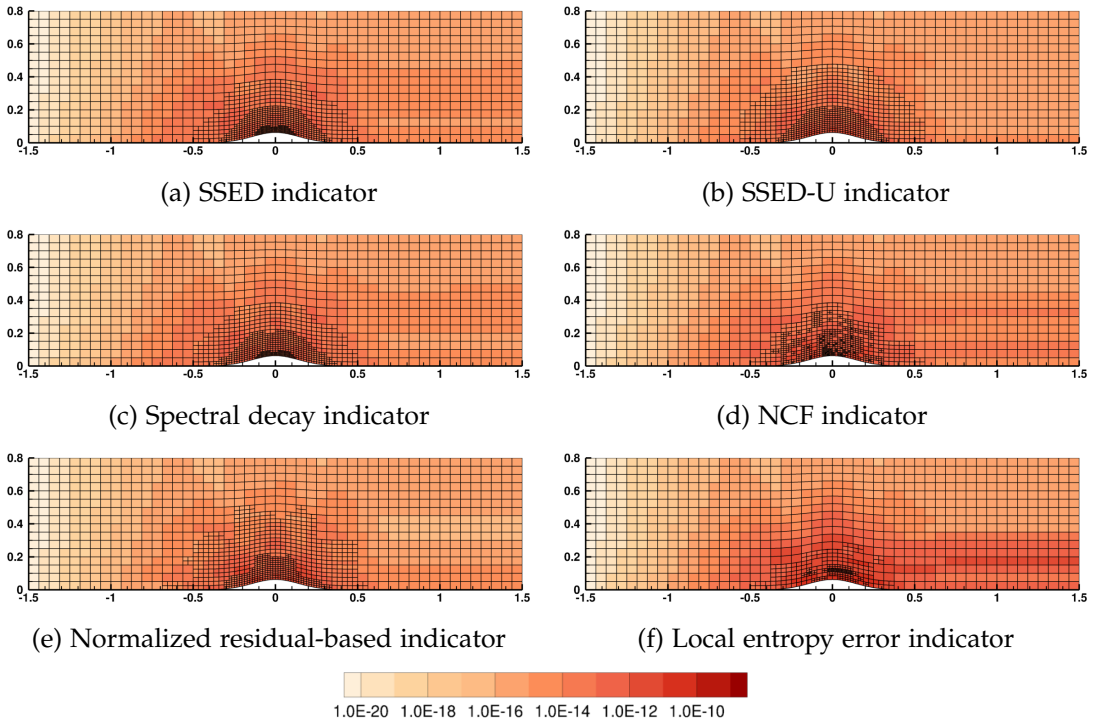

(a) SSED indicator

(b) SSED-U indicator

(c) Spectral decay indicator

(d) NCF indicator

(e) Normalized residual-based indicator

(f) Local entropy error indicator

Figure 32 – Inviscid flow over a Gaussian bump at M = 0.5: Adapted meshes and distribution of the local entropy error obtained by adaptive *h*-refinement. The number of dofs is equal to $\sim 120^2$ for all refinement indicators with the exception of the local entropy error indicator, for which #dofs $\approx 100^2$.

average error in absence of large variations of the momentum density in the domain, which is the case in this configuration.

Considering now the results obtained with the NCF indicator, in Figs. 32d and 33d we observe the same checkerboard-like pattern already observed for the *p*-adaptive simulations. Indeed, the same argument provided in Sec. 5.4 can be used here to explain the generation of this pattern in the context of *h*-adaptation.

This behaviour is not observed for the normalized residual-based indicator (see Figs. 32e and 33e) in contrast to the results obtained in Chap. 5. This suggests a higher sensitivity of the NCF indicator to jumps of the resolution quality between neighbouring elements.

Finally, the local entropy error indicator leads to a highly irregular refinement pattern with more intense refinement being applied to elements away from the solid boundary. This is a further indication that the local entropy error does not effectively identify regions where the error is produced.

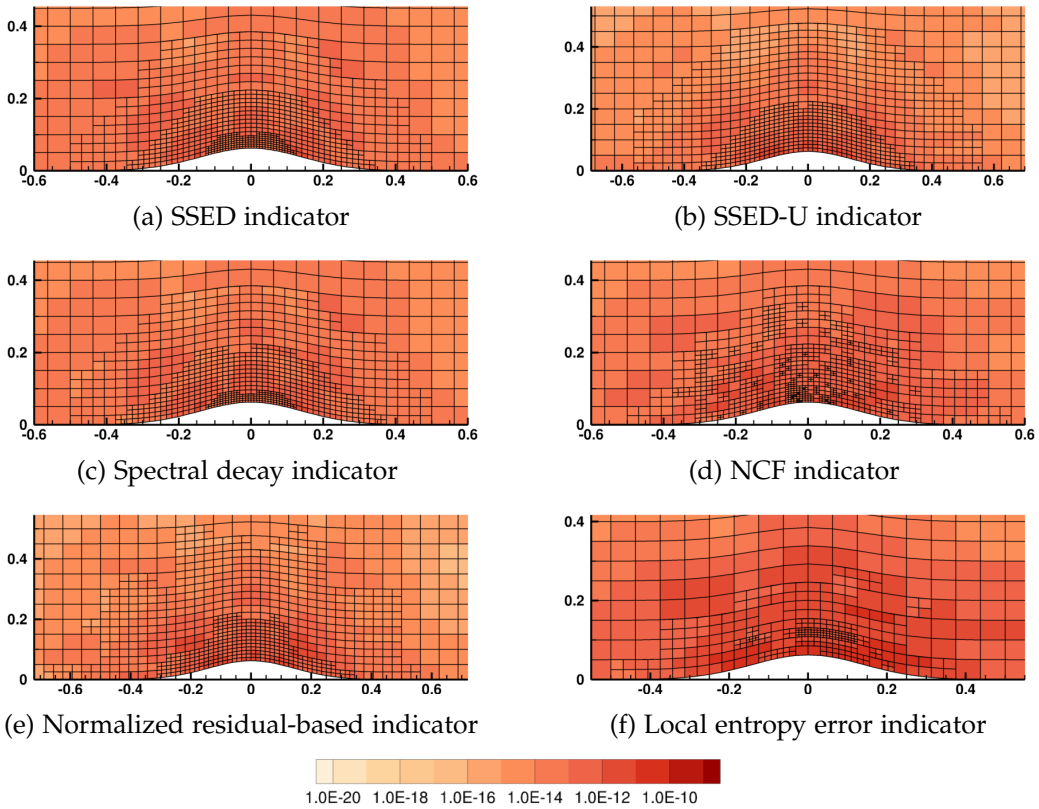

(a) SSED indicator (b) SSED-U indicator

(c) Spectral decay indicator (d) NCF indicator

(e) Normalized residual-based indicator (f) Local entropy error indicator

Figure 33 – Inviscid flow over a Gaussian bump at M = 0.5: Adapted meshes and distribution of the local entropy error obtained by adaptive h-refinement, close-up view. The number of dofs is equal to $\sim 120^2$ for all refinement indicators with the exception of the local entropy error indicator, for which #dofs $\approx 100^2$.

6.4 LAMINAR FLOW CONFIGURATIONS

We now consider two laminar flow configurations: the flow past a Joukowski airfoil at Re = 1000, M = 0.5 and $\alpha = 0°$, and the flow past a cylinder at Re = 40 and M = 0.1. These two configurations have already been described in Sec. 5.4 and 5.5 and are here analysed jointly as they provide similar conclusions. The same computational grid, numerical discretization and adaptive algorithm considered in Chap. 5 are employed here. All simulations are carried out using a uniform polynomial degree $p = 2$.

Most of the conclusions drawn for p-adaptation in Chap. 5 have been shown in the previous section to be applicable to h-adaptation. For this reason, we only consider in this section the SSED indicator and the normalized residual-based indicator. For both refinement indicators we perform a limited number of steps of the adaptive refinement algorithm and the corresponding results are compared to those based on uniform h-refinement. For the evaluation of the error, we employ as reference

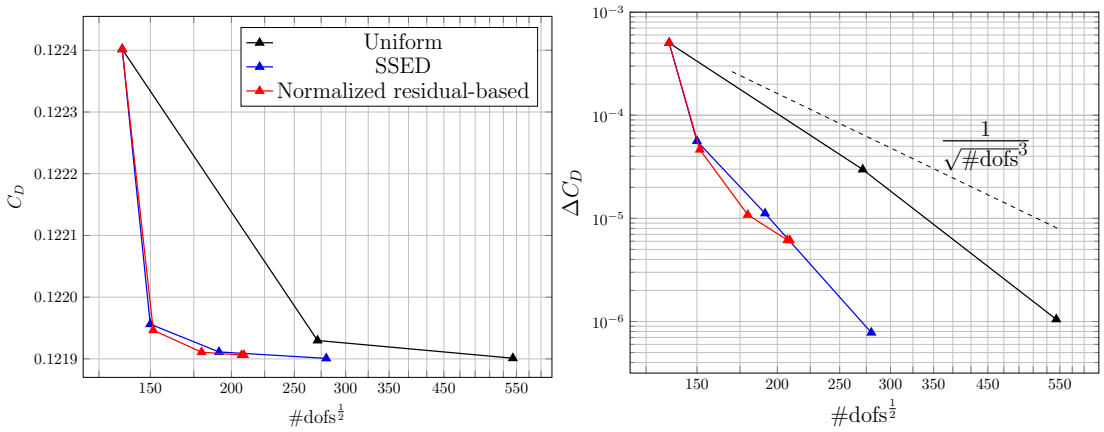

Figure 34 – Laminar flow past a Joukowski airfoil at Re = 1000, M = 0.5 and $\alpha = 0°$: Convergence history of the drag coefficient under uniform and adaptive h-refinement.

solutions the finest uniform polynomial degree simulations presented in Sec. 5.4 and 5.5, corresponding to the starting grid and $p = 7$ for both configurations.

Analysis of the results

The convergence history of the drag coefficient and the corresponding error under uniform and adaptive h-refinement is presented in Fig. 34 for the flow past a Joukowski airfoil. As we can see from this graph, for a given level of accuracy, the adaptive algorithm leads to a large reduction of the number of dofs as compared to uniform refinement. In particular, the SSED indicator leads to the same error level as the finest uniformly refined simulation, with a reduction of the total number of dofs of approximately 73%. The normalized residual-based indicator presents a very similar convergence history, however, it requires a larger number of refinement steps to reach the same accuracy. This behaviour has also been observed in Chap. 5. Nonetheless, after two refinement steps the adaptive algorithm based on this indicator leads to higher accuracy than the first uniformly refined simulation, with a reduction of the total number of dofs of about 56%.

More marked differences between the two refinement indicators can be identified from the analysis of Fig. 35. It presents the convergence history of the drag coefficient for the flow past a cylinder at Re = 40. Indeed, after four refinement steps the SSED indicator leads to a better accuracy than uniform refinement with a reduction of approximately 86% in the number of dofs. As for the Joukowsky configuration, the normalized residual-based indicator requires here a larger number of refinement iterations to reach a given level of accuracy and presents a slower convergence rate than the SSED indicator.

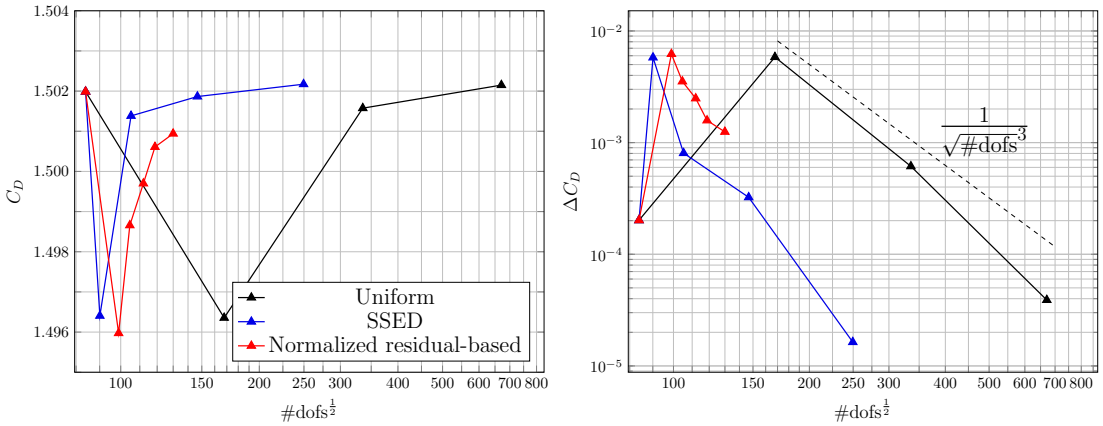

Figure 35 – Laminar flow past a cylinderat Re = 40 and M = 0.1: Convergence history of the drag coefficient under uniform and adaptive h-refinement.

These results are better analysed by comparing the refined meshes obtained at the last iteration of the adaptive algorithm. For the flow past a Joukowski airfoil these are presented in Fig. 36 and correspond to $\sim 280^2$ and $\sim 210^2$ dofs for the SSED and the normalized residual-based indicator, respectively. Similarly in Fig. 37 we report the adapted meshes for the simulation of the flow past a cylinder. These correspond to $\sim 250^2$ and $\sim 130^2$ dofs for each of the aforementioned indicators.

Despite the fact that they have different number of dofs, meaningful conclusions can be obtained by comparing the meshes provided by the two refinement indicators. In particular, we observe from Figs. 36 and 37 that similar refinement regions are selected by the two refinement indicators in the vicinity of the solid body. However, compared to the SSED indicator, the normalized residual-based indicator leads to a considerably higher refinement in the far-wake region. This is despite the overall lower number of dofs. Additionally, we observe in Figs. 36b and 37b that remarkably high refinement is introduced by the normalized residual-based indicator at the outflow boundary. This result indicates a stronger dependency of the normalized residual-based indicator on the element size. In contrast, the SSED indicator only selects for refinement a reduced number of elements near the symmetry plane.

We remark that the refinement region, especially in the far-wake, is much smaller than that obtained for p-refinement in Figs. 13a and 21a. For what regards the Joukowski airfoil configuration, this is explained by the lower accuracy requirement imposed for h-adaptation, *i. e.* the higher value of the error at the end of the adaptive process as compared to the results of the p-adaptive simulations. As for the cylinder configuration, the larger refinement region obtained for p-adaptation is linked to the propagation of p-refinement due to the constraint imposed on the jump of the polynomial degree across element interfaces. Indeed, the h-refinement algorithm successively splits only those child elements encompassed by the local feature requiring

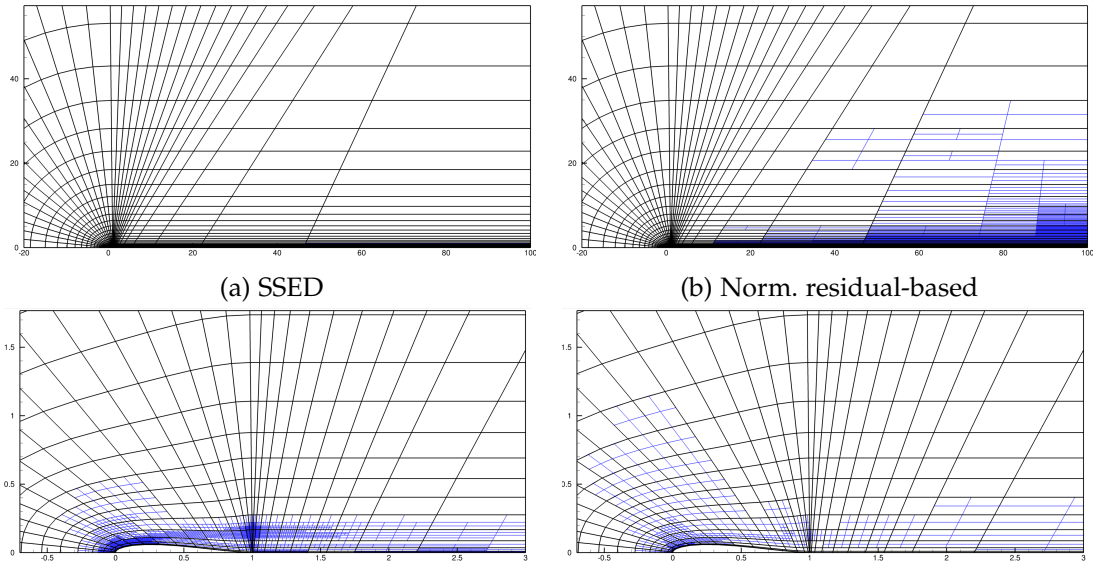

(a) SSED (b) Norm. residual-based

(c) SSED, close-up view (d) Norm. residual-based, close-up view

Figure 36 – Laminar flow past a Joukowski airfoil at Re = 1000, M = 0.5 and $\alpha = 0°$: Adapted meshes at the last iteration of adaptive *h*-refinement. Number of dofs are equal to $\sim 280^2$ and $\sim 210^2$ for the SSED and normalized residual-based indicator, respectively. Black lines: initial mesh. Blue lines: adapted mesh.

local refinement (see Fig. 37e). In contrast, *p*-adaptation can only apply uniform refinement of the elements of the initial mesh, which are not modified. This makes adaptation algorithms based on *p*-refinement less flexible.

Finally, we present in Fig. 38 a close-up view of the adapted meshes for the flow past a Joukowski airfoil. We recall that the adapted mesh for the normalized residual-based indicator corresponds to a lower number of dofs. Yet, similar regions are refined by the two indicators in the region near the leading edge of the airfoil.

More marked differences are observed in Figs. 38c and 38d, where the initial mesh is characterized by local refinement near the geometrical singularity at the trailing edge. As can be seen from Fig. 38c, the SSED indicator leads to a higher level of refinement in this region as compared to the normalized residual-based indicator. At first, one could think that the numerical oscillations induced by the geometrical singularity have an influence on the value of the SSED indicator in these elements. However, this does not appear to be the case, since higher refinement is introduced away from the singularity at $y \approx 0.15$. The most likely explanation is therefore that numerical oscillations are introduced by the sudden variation in mesh size. The SSED indicator thus marks for refinement elements in this region at each adaptation step. In contrast, the normalized residual-based indicator introduces a lower level of refinement in this region due to the fact that its formulation includes a dependency on the local mesh size, which takes very small values in this area.

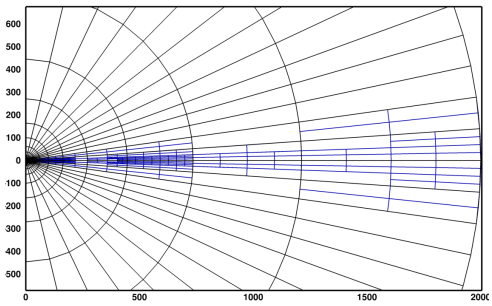

(a) SSED, far-wake region

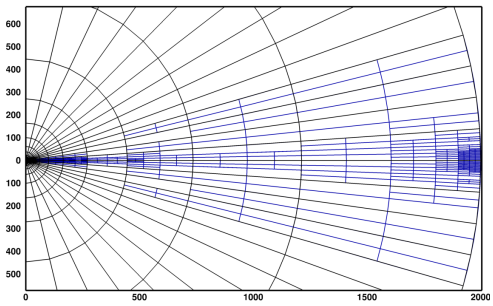

(b) Norm. residual-based, far-wake region

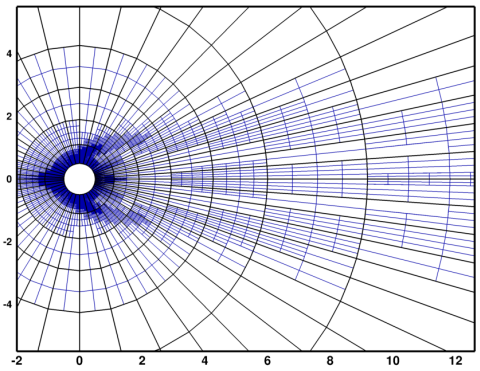

(c) SSED, near-wake region

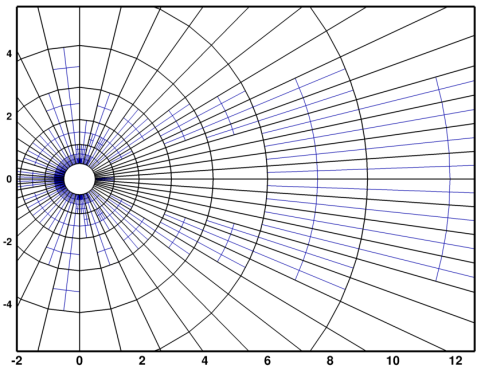

(d) Norm. residual-based, near-wake region

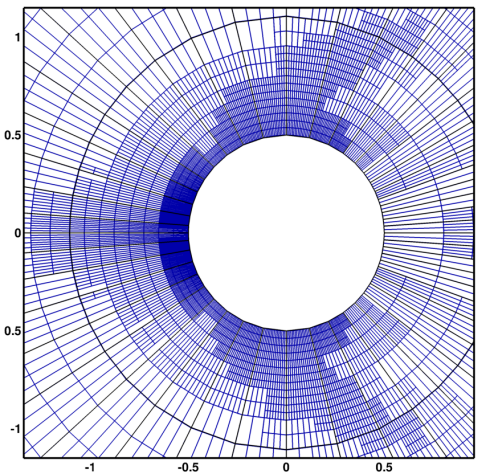

(e) SSED indicator, near-cylinder region

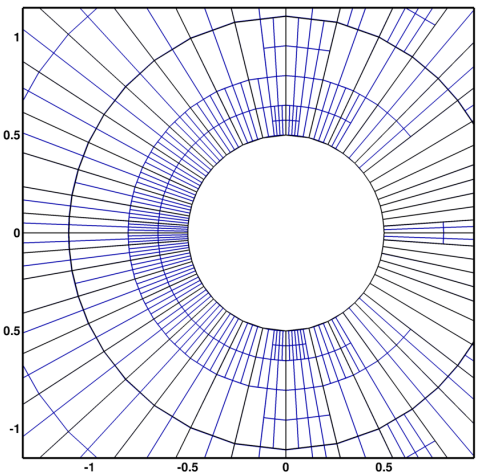

(f) Norm. residual-based, near-cylinder region

Figure 37 – Laminar flow past a cylinderat Re = 40 and M = 0.1: Adapted meshes at the last iteration of adaptive h-refinement. Number of dofs are equal to $\sim 250^2$ and $\sim 130^2$ for the SSED and normalized residual-based indicator, respectively. Black lines: initial mesh. Blue lines: adapted mesh.

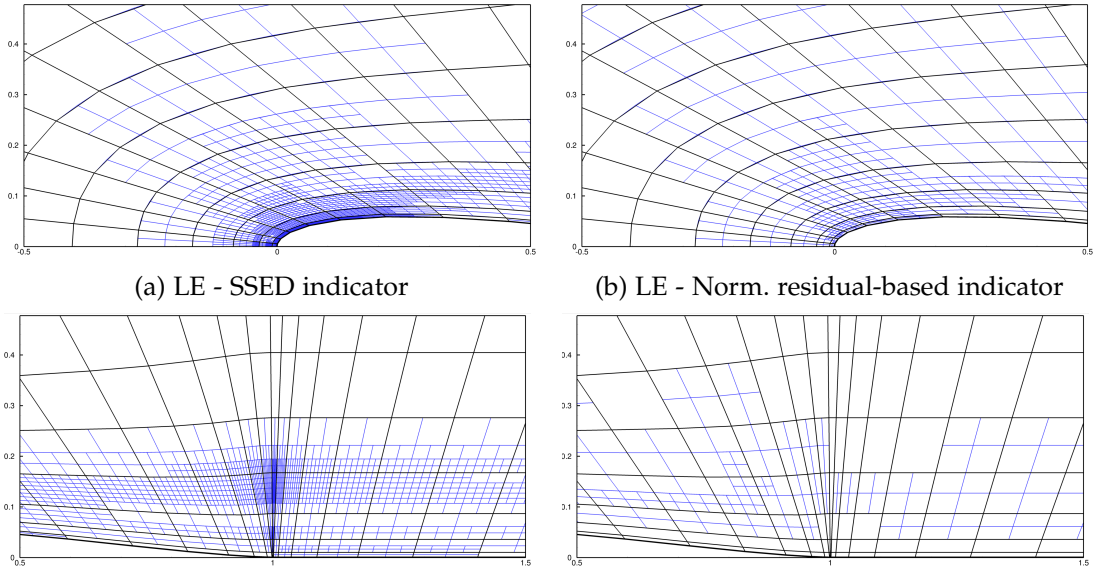

(a) LE - SSED indicator

(b) LE - Norm. residual-based indicator

(c) TE - SSED indicator

(d) TE - Norm. residual-based indicator

Figure 38 – Laminar flow past a Joukowski airfoil at Re = 1000, M = 0.5 and $\alpha = 0°$: Close-up view of adapted meshes near the leading edge (LE) and the trailing edge (TE) at the last iteration of adaptive h-refinement. Number of dofs are equal to $\sim 280^2$ and $\sim 210^2$ for the SSED and normalized residual-based indicator, respectively. Black lines: initial mesh. Blue lines: adapted mesh.

CHAPTER 7

LOAD BALANCING FOR *HP*-ADAPTIVE SIMULATIONS

RÉSUMÉ DU CHAPITRE EN FRANÇAIS

La simulation numérique des écoulements turbulents par des approches DNS ou LES présente des coûts de calcul très élevés. Afin d'obtenir des résultats dans des temps de réalisation raisonnables, il est nécessaire de tirer pleinement parti des architectures HPC modernes en utilisant des approches de mémoire distribuée ou de type thread-based. Pour ce faire, on divise le domaine de calcul en un ensemble de sous-domaines dont chacun est attribué à l'un des processeurs disponibles. Cette opération est appelée partitionnement des graphes.

L'algorithme de partitionnement des graphes doit générer un partitionnement du domaine de calcul minimisant la quantité d'informations communiquées entre les différents processus et répartissant uniformément la charge de calcul totale (load balancing). La génération d'une partition avec un équilibre de charge acceptable n'est pas triviale dans le cadre de méthodes adaptatives h et p en raison de la distribution hétérogène de la charge de calcul entre les différents éléments de l'espace discrétisé.

Pour illustrer cette difficulté, le problème du partitionnement des graphes est brièvement décrit dans la Sec. 7.2. Il est démontré qu'il est impératif d'obtenir une estimation précise de la charge de calcul pour chaque élément. Deux approches peuvent être utilisées à cette fin: l'approximation de la charge de calcul comme le nombre d'opérations nécessaires par élément ou la mesure directe du temps de calcul requis par le solveur utilisé pour différentes discritisations.

La première approche est employée dans la Sec. 7.3. Il est cependant montré que, dans le cadre des simulations adaptatives-*hp*, il ne fournit pas de méthodologie pratique pour spécifier l'estimation des coûts de calcul pour le problème du partitionnement de graphe. Les résultats obtenus sont toutefois utilisés dans la Sec. 7.4 pour guider l'estimation de la charge de calcul à partir des mesures directes des temps de calcul.

La qualité du partitionnement des graphes obtenu à l'aide de la stratégie présentée est démontrée dans la Sec. 7.5. Des tests numériques montrent que cette méthodologie réduit considérablement le déséquilibre de charge, $< 6\%$, par rapport à des approches moins élaborées basées sur le nombre de degrés de liberté ou le comporte-

ment asymptotique du nombre d'opérations, qui présentait des valeurs du déséquilibre de charge pouvant atteindre $40 - 50\%$.

7.1 INTRODUCTION AND OUTLINE OF THE CHAPTER

The numerical simulation of flows, in particular in the case of LES and DNS, can present an extremely high computational cost. It is therefore of paramount importance to use thread-based and/or distributed memory techniques to obtain results in a reasonable time frame and take full advantage of modern HPC architectures. This is achieved by dividing the computational domain into a set of subdomains, each of which is assigned to one of the available processes. This operation is commonly referred to as mesh or graph partitioning.

As numerical simulations consist in a series of computations and synchronizations, the mesh partitioning needs to generate partitions of the original computational domain that minimize the amount of data being exchanged between different processes while evenly distributing the computational load (*load balancing*). If this is not obtained, all processes need to wait at each synchronization stage for the slowest process to reach the same point of the computation. Thus, the computational time is determined by the slowest process and load imbalances lead to wasted computational resources and an overall lower efficiency, *i. e.* higher computational time.

The generation of a mesh partitioning with acceptable load balance is, however, not trivial in the case of *hp*-adaptive simulations, due to the uneven distribution of the computational load across mesh elements. In order to illustrate the encountered issues, we briefly describe in Sec. 7.2 the graph partitioning problem. It is shown that to achieve a well-balanced graph partitioning we require the accurate evaluation of the computational load associated with each element. A possible approach consists in estimating the total operation count as a surrogate of the total computational cost to advance the solution in time for each element. Alternatively, the computational cost can be obtained through direct measurements of computational times, as will be further described in this chapter.

The first approach is employed in Sec. 7.3. It is shown, however, that in the framework of *hp*-adaptive simulations it does not provide a methodology to reliably specify the computational cost estimate for the graph partitioning algorithm. Nonetheless, the presented analysis allows us to identify its dependence on the local polynomial degree, quadrature formula and number of faces of each element. The obtained results are thus exploited to guide the estimation of the computational load from direct measurements of CPU times in Sec. 7.4. Finally in Sec. 7.5 we demonstrate the efficiency of the developed procedure to obtain well-balanced partitionings and improved computational efficiency with respect to more naive approaches.

The presented analysis is carried out in the context of DG simulations with explicit time-integration schemes. Indeed, explicit time-integration methods are employed

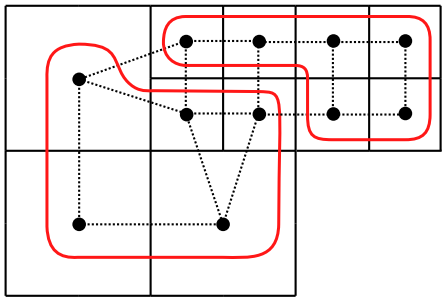

Figure 39 – Example of computational grid (continuous black), equivalent graph (nodes and dashed lines) and a possible 2-way partitioning.

for the LES presented in Chap. 9 which is the main application considered in this work. The conclusions obtained can partially be applied to implicit time-integration strategies, however, additional complications appear for these problems which are related to the use of specific preconditioners (see *e. g.* [40] pages 109-119).

The study presented in this chapter has been carried out in the framework of the development of the mesh partitioning tool *GoSplit* [124].

7.2 GRAPH PARTITIONING

The computational domain for a simulation is represented as an irregular graph where each element K is a vertex and each interior face $e \in \mathcal{E}_i$ is an edge of the graph (see Fig. 39). This is in general a *weighted graph* such that a weight is assigned to each vertex and edge, here indicated as ω_K and ω_e respectively.

The graph partitioning problem is the computation of a k-way partitioning such that the sum of the weights of the edges that connect different partitions is minimized. This objective is commonly referred to as *edge-cut* and represents an approximation of the total communication cost resulting from the partitioning [88]. Indeed the total communication cost is composed of two contributions: time required to prepare the message (latency) and necessary time to transfer the information, which is approximately proportional to the amount of data that needs to be transferred. The edge-cut represents the total communication volume and is therefore proportional to the second contribution.

This minimization problem is solved under the constraint that the computational load is equally distributed among the partitions. This corresponds to obtaining partitions with approximately the same value of the sum of the vertex weights. In the simple case where each element presents the same computational cost this is equivalent to obtaining partitions with the same number of elements.

In order to formalize this constraint, let us indicate as $P[K]$ the index of the partition to which element/vertex K belongs. Then, the load imbalance l, for a partitioning into k subdomains, is defined as

$$l = \frac{k \max\limits_{1 \le j \le k} \sum\limits_{\forall K : P[K]=j} \omega_K}{\sum\limits_{\forall K} \omega_K} \ . \tag{94}$$

A load imbalance of $l = 1 + \lambda$ indicates that the simulation of total computational cost W performed on k processes takes $(1 + \lambda)W/k$ time rather than W/k time assuming zero communication overhead. In this case we indicate that the computation is unbalanced by λ%.

The graph partitioning problem can therefore be defined as an optimization problem with the objective of minimizing the edge-cut under the constraint

$$l \le \omega_{imb} \ , \tag{95}$$

where $\omega_{imb} \ge 1$ is the user-defined maximum allowed load imbalance, with typical values between 1.01 and 1.10. In this work the graph partitioning problem is solved using the multilevel k-way partitioning algorithm implemented in the *Metis* library [102] with $\omega_{imb} = 1.03$.

The quality of the obtained partitioning is thus controlled by the appropriate definition of the vertex and edge weights. In the framework of *hp*-adaptive computations this needs to be obtained by the careful analysis of the solver employed.

As regards the definition of the edge weights, we observe that the communication volume associated with each edge is not constant for p-adaptive simulations. Thanks to the compact nature of the DG method, only the information at the quadrature points of each edge belonging to the common matching interface between two partitions is communicated.

The communication volume is therefore proportional to the total number of quadrature points on each edge and we define

$$\omega_e = q_e^{d-1} \ , \tag{96}$$

where q_e is the number of quadrature points per space direction on the face $e \in \mathcal{E}_i$.

The definition of the vertex weights requires a more detailed discussion and is therefore the subject of the following sections.

7.3 ESTIMATION OF THE COMPUTATIONAL LOAD FROM OPERATION COUNTS

As mentioned above, a possible approach to derive an appropriate definition of the vertex weights is to evaluate an estimate of the number of operations required to advance the solution in time. At each pseudo-time step the largest contribution to the computational cost is due to the evaluation of the right hand side of Eq. (48).

Two blocks of operations can therefore be identified:

- for each element K we evaluate the volume integral contribution;
- for each edge e we evaluate the surface integral contribution.

The computational cost as considered in Eq. (94), however, is simply the sum of the vertex weights. Thus, it is implicitly assumed that the edges of the graph do not contribute to the computational cost but only to the communication cost. The total computational cost per element must include both contributions and is therefore expressed as

$$C_K = C_v + \sum_{e \in \mathcal{E} \cap \partial K} C_{e,K} \ , \tag{97}$$

where C_v and $C_{e,K}$ are the volume and surface integral terms, respectively. The operation count associated with both volume and surface integrals is therefore now separately analysed. Note that the actual number of operations depends on the specific problem and implementation. For this reason, the unknown proportionality coefficients are indicated as α and β.

Volume integral contribution

The evaluation of volume integrals for each element can be described as a sequence of three steps:

*a*1) evaluation of the solution and its gradients at quadrature points,

*a*2) evaluation of the fluxes at the quadrature points,

*a*3) evaluation of volume integrals from values known at quadrature points.

Operation *a*1 consists in the product of a matrix of size $N_{eq} \times (p_K + 1)^d$, with N_{eq} number of equations, and a matrix of size $(p_K + 1)^d \times (d + 1) q_K^d$ (basis functions and their gradients at each quadrature point). Operation *a*2 for each equation only involves the manipulation of values at each quadrature point and therefore requires a number of operations proportional to $N_{eq}\, q_K^d$. Finally, operation *a*3 requires the product between matrices of size $N_{eq} \times d q_K^d$ and $d q_K^d \times (p_K + 1)^d$.

The total operation count can accordingly be expressed as

$$C_v = \underbrace{\alpha_1' N_{eq} (d+1)(p_K+1)^d q_K^d}_{a1} + \underbrace{\alpha_2' N_{eq}\, q_K^d}_{a2} + \underbrace{\alpha_3' N_{eq} d (p_K+1)^d q_K^d}_{a3} \ . \tag{98}$$

As N_{eq} and d are fixed for a given problem, we can simply write

$$C_v(p_K, q_K) = \alpha_1 (p_K + 1)^d q_K^d + \alpha_2 q_K^d \ , \tag{99}$$

i. e. C_v is composed of two terms: a first contribution proportional to the product of the number of degrees of freedom and the number of quadrature points and a second contribution proportional only to the number of quadrature points.

Surface integral contribution

The evaluation of the surface integrals on each internal face $e = \partial K^+ \cap \partial K^-$ can be described as a series of 5 operations:

*b*1) evaluation of the trace of the solution in K^+ at the quadrature points of e;

*b*2) evaluation of the trace of the solution in K^- at the quadrature points of e;

*b*3) evaluation of the numerical fluxes at the quadrature points;

*b*4) evaluation of the residual contribution for the degrees of freedom in K^+;

*b*5) evaluation of the residual contribution for the degrees of freedom in K^-;

Following the same procedure outlined above, we obtain that the operation count for each edge can be expressed as

$$C_s = \underbrace{\beta_1 (p_{K^+} + 1)^d q_e^{d-1}}_{b1+b4} + \underbrace{2\beta_2 q_e^{d-1}}_{b3} + \underbrace{\beta_1 (p_{K^-} + 1)^d q_e^{d-1}}_{b2+b5} \tag{100}$$

This quantity is split into two contributions which can be assigned to K^+ and K^-, respectively, namely

$$C_s(p_{K^+}, p_{K^-}, q_e) = C_{e,K^+} + C_{e,K^-} \ , \tag{101}$$

where

$$C_{e,K} = \beta_1 (p_K + 1)^d q_e^{d-1} + \beta_2 q_e^{d-1} \ . \tag{102}$$

In order to estimate the total operation count, the same analysis should be repeated for boundary faces. We make here the assumption that this contribution takes the same expression as Eq. (102), derived for internal edges. This approximation does not modify the conclusions drawn from this study and circumvents the problem of taking into account the details of the specific boundary conditions imposed.

Injecting Eqs. (99) and (102) in Eq. (97), the total number of operations per element can thus be expressed as

$$C_K = \alpha_1 (p_K + 1)^d q_K^d + \alpha_2 q_K^d + \sum_{e \in \mathcal{E} \cap \partial K} \left[\beta_1 (p_K + 1)^d q_e^{d-1} + \beta_2 q_e^{d-1} \right] \ . \tag{103}$$

Given that $q_K \geq p_K + 1$, for large values of p_K the first term in Eq. (103) is dominant. The total number of operations could therefore be assumed to be asymptotically proportional to $(p_K + 1)^d q_K^d$. For typical values of p_K and q_K, however, all contributions in Eq. (103) are of similar order of magnitude, as shown later in this chapter. As a consequence, the total computational cost is not simply proportional to a single term defined by the product of powers of $p_K + 1$ and q_K. The definition of the vertex

weights from the operation count would therefore require knowledge of each of the coefficients α_1, α_2, β_1, and β_2. These coefficients depend on the problem being solved, the choice of numerical fluxes and the implementation details. As a result, obtaining a closed expression for the vertex weights from the operation count does not represent a practicable approach.

Additionally, this strategy relies on the often employed premise that the total computational cost is proportional to the number of operations. This assumption is however almost never valid on modern HPC architectures.

As an example consider the product of an $L \times M$ matrix by an $M \times N$ matrix, similar to operation $a1$. The evaluation of this product requires $2LMN$ operations. Nonetheless, for relatively small values ($L, M, N \lesssim 100$) the actual computational cost is influenced by cache misses and data alignment (see *e. g.* [110] page 16). The computational cost is thus proportional to the operation count, or equivalently to LMN, only for very large matrices.

In practice, each contribution to the total computational cost and its relative importance depends on several parameters including hardware, implementation details, compiler optimization, and the optimization of mathematical libraries (BLAS, LAPACK). For this reason, directly employing the operation count would provide at best suboptimal results.

7.4 ESTIMATION OF THE COMPUTATIONAL LOAD BY MEASURING PERFORMANCE

The natural conclusion drawn from the previous discussion is that the appropriate evaluation of the computational load associated with each element can only be obtained by measuring the performance in the actual simulation conditions. Following the analysis used to derive Eq. (103), in the graph partitioning problem we assign to each vertex of the graph a weight ω_K which takes the form

$$\omega_K = \omega_v(p_K, q_K) + \sum_{e \in \mathcal{E} \cap \partial K} \omega_s(p_K, q_e) \ , \tag{104}$$

where ω_v and ω_s are the volume and surface contributions to the element weight.

The values of ω_v and ω_s are then estimated by performing a series of computations on the selected hardware using the same executable employed for the target simulation. This procedure, takes into account the characteristics of the hardware as well as the specific implementation details and compiler optimization. These simulations are performed on a simplified configuration employing the same spatial discretization and physical model (Euler, RANS, LES or DNS) as the target simulation. A computation is then performed, for each couple of values p and q considered, while separately measuring the total computational time required for the evaluation of volume terms $c_v(p, q)$ and of surface terms on internal faces $c_s(p, q)$ for a number of

pseudo-time steps N_t. The number of pseudo-time steps should be sufficiently high to obtain a representative average of the CPU time costs required by these operations. The weight contributions are then computed as

$$\omega_v(p,q) = \frac{c_v(p,q)}{N_t \#\text{elements}} \quad \text{and} \quad \omega_s(p,q) = \frac{c_s(p,q)}{N_t 2\#\text{int. faces}} \ . \tag{105}$$

The value of ω_s is evaluated only for the internal faces and is used to estimate the contribution of boundary faces to Eq. (104).

We report in Fig. 40 the volume and surface weights as calibrated for the simulation of an inviscid flow using the LLF flux on an Intel Xeon Broadwell E5-2680v4. The values of c_v and c_s are obtained by performing simulations with $d = 3$ on a regular Cartesian mesh composed of $50 \times 50 \times 1$ elements, thus presenting a total of 2500 elements and 4900 internal faces. As we are only interested in the evaluation of the performance, each simulation is initialized with a uniform flow and non-reflecting boundary conditions at each physical boundary. The solution is advanced in time for 1000 pseudo time-steps using $\Delta t = 10^{-12}$.

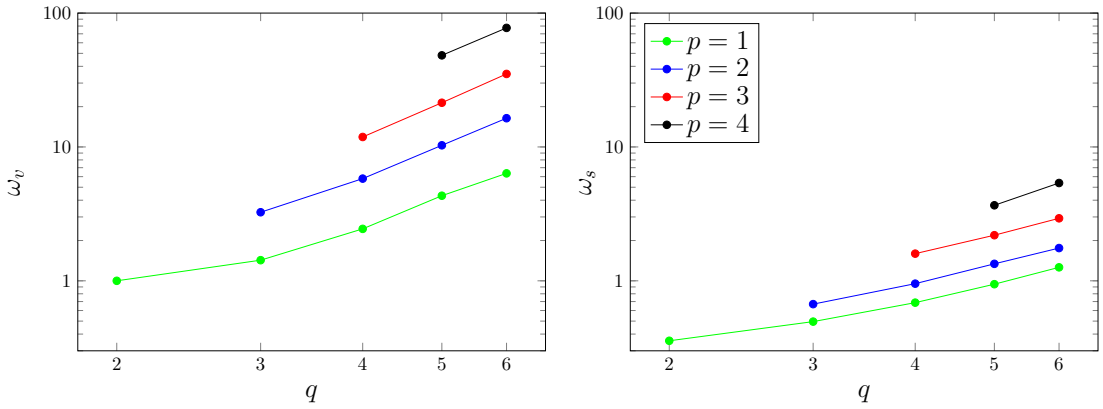

Figure 40 – Example of the evaluation of the volume and surface contributions to the vertex weights for an inviscid computation with the LLF flux on Intel Xeon Broadwell E5-2680v4 cores. Values are normalized by $\omega_v(1,2)$.

We can observe in Fig. 40 that, as expected, neither the volume nor the surface contribution can be approximated by a simple power law. Additionally the surface terms are as important as the volume terms. As an example $\omega_s(4,5)$, corresponding to the contribution of the surface integral on a single face with $p_K = 4$ and $q_K = p_K + 1$, is higher than both $\omega_v(1,2)$ and $\omega_v(2,3)$. Thus neglecting the surface contributions could lead to important load imbalance.

This is further illustrated in Fig. 41, reporting the vertex weight, the volume contribution and the total surface contribution (second term in Eq. (104)) that would be obtained with $q = p + 1$ on a conforming hexahedral mesh. In this case $\omega_K = \omega_v(p, p+1) + 6\omega_s(p, p+1)$.

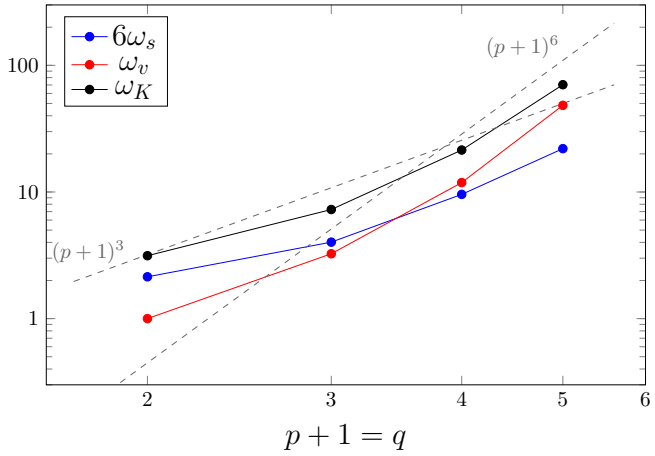

Figure 41 – Example of the evaluation of the vertex weights, volume and total surface contribution for $q = p+1$ and an inviscid computation based on the LLF flux on Intel Xeon Broadwell E5-2680v4 cores. Values are normalized by $\omega_v(1,2)$.

We observe that the total surface integral contribution is higher than the volume contribution for $p < 3$. As the polynomial degree increases the volume contribution becomes dominant and the total computational cost starts scaling as $(p+1)^6$. However, this is not the case for the relatively low values of p employed in practice. Therefore neither $(p+1)^3 = \#\text{dofs}$ nor $(p+1)^3 q^3 = (p+1)^6$ can approximate the effective dependency of the computational cost on the local polynomial degree.

For comparison, we report in Fig. 42 the same quantities as measured for the LES of a turbulent flow using the Roe flux, the BR2 scheme and employing the Vreman SGS model on an Intel Xeon Broadwell E5-2690v4. As observed in the previous figure, the volume and total surface contributions are of similar order of magnitude. However, in this case the surface contribution is dominant for $p \leq 5$. These examples therefore emphasize the necessity of evaluating the vertex weights from direct measurements and the fact that a general law cannot be derived.

Additional remarks on the calibration of weights

As described in this section, the values of ω_v and ω_s must be computed by performing preliminary simulations for each value of p and q, using the same discretization, and the same executable as for the target simulation, and on the same hardware. This can appear as a daunting task. Nonetheless, we point out that this procedure does not need to be repeated for each target simulation. Once the calibration has been carried out for a given combination of discretization, physical model, and hardware, these values can be reused for each new simulation sharing the same parameters. Additionally, the recalibration of the weights might not be necessary

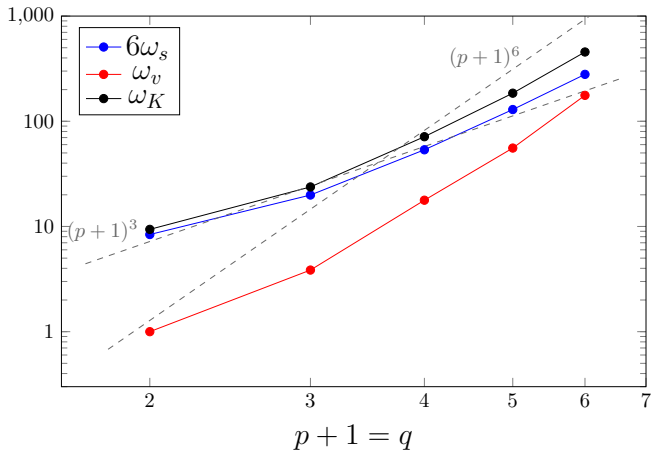

Figure 42 – Example evaluation of the vertex weights, volume and total surface contribution for $q = p + 1$ and an LES using the Roe flux, BR2 scheme and Vreman model on Intel Xeon Broadwell E5-2690v4 cores. Values are normalized by $\omega_v(1, 2)$.

for small changes of these conditions *e. g.* when considering a different RANS or LES model or when employing the Roe flux in place of the LLF flux.

Special care is however required while performing the calibration. In practical parallel simulations on modern HPC architectures it is common practice to use all the processes available on a given computational node of the employed cluster. As a result, in general the processes need to share resources, *i. e.* a single process does not have the full cache available.

This condition needs to be reproduced during the precursory computations. For this purpose, several copies of each precursory simulation are performed at the same time, each assigned to a different core of a single node. The measured computational costs are then averaged thus reducing the influence of random events on the calibration of the weights.

7.5 ANALYSIS OF THE GRAPH PARTITIONING ALGORITHM

We evaluate the ability of the partitioning algorithm based on the described calibration to generate well-balanced k-way partitions when considering variable polynomial degree. For this purpose, we perform five tests differing in the distribution of the local polynomial degree, number of quadrature points and number of partitions required.

For each configuration we consider four graph partitioning approaches. The first approach consists in a crude partitioning without taking into account the uneven distribution of the local polynomial degree. The second and third approaches consist in defining the vertex weights respectively as the number of degrees of freedom

$(p+1)^3$ = #dof and its product with the number of quadrature points $(p+1)^3 q^3$. Finally, the last approach is based on the vertex weights defined by Eq. (104), where the volume and surface contributions are obtained by measuring the performance of the solver as described in the previous section. With the exception of the first approach, we always define the edge weights as in Eq. (96).

The quality of the produced partitioning is assessed by performing the simulations and evaluating the load imbalance by means of *MPI Performance Snapshot* [126]. *MPI Performance Snapshot* provides a measure of the MPI imbalance defined as the mean unproductive wait time per process. We remark that this quantity, albeit similar in concept, is different from the load imbalance defined in Eq. (94). Therefore, even if the load estimate employed for the graph partitioning algorithm were perfect, we should not expect the MPI imbalance to be equal to the load imbalance measured by *Metis* at the end of the partitioning algorithm.

The five configurations considered are reported in Fig. 43. Tests 1 and 2 employ the configuration presented in Fig. 43a corresponding to a grid composed of a block of $40 \times 40 \times 1$ elements with $p_K = 4$ and a block of $100 \times 40 \times 1$ elements with $p_K = 2$. For test 1 the computational grid is decomposed into two domains, whereas 7 partitions are generated for test 2.

The configuration employed for tests 3 and 4 is presented in Fig. 43b. It is composed of $252 \times 100 \times 1$ elements with p_K varying from 2 to 4. The two tests differ in that for test 3 (as for tests 1, 2 and 5) the number of quadrature points per direction is set equal to $q = p+1$, whereas for test 4 one additional quadrature point per space direction is considered for those elements with $p_K = 4$, *i.e.* $q = p+2$. For both tests the computational grid is decomposed into 7 domains.

Finally, test 5 employs the computational grid reported in Fig. 43c. It is composed of $100 \times 50 \times 20$ elements and is decomposed into 28 domains.

For all configurations, inviscid flow simulations are performed on an Intel Xeon Broadwell E5-2680v4. The LLF flux is used for the discretization of the convective flux and the SSP Runge-Kutta scheme is employed to advance the solution in time for 1000 time steps. These conditions correspond to those described in the previous section to obtain the calibration of the vertex weight contributions illustrated in Fig. 40. Each test is repeated 5 times and the obtained values of the MPI imbalance are averaged.

The measured MPI imbalance is reported in Fig. 44. For all the considered configurations, partitioning without taking into account the dependency of the computational cost on the local polynomial degree leads to high levels of imbalance, up to 64%. A reduction of the MPI imbalance is obtained by defining the vertex weights as either the number of degrees of freedom or its product with the number of quadrature points. However the results do not appear consistent and in general still relatively high values of MPI imbalance are obtained, between 15% and 50% as seen in Fig. 44. Additionally, the two latter approaches perform similarly and depending on the test one approach might perform better than the other.

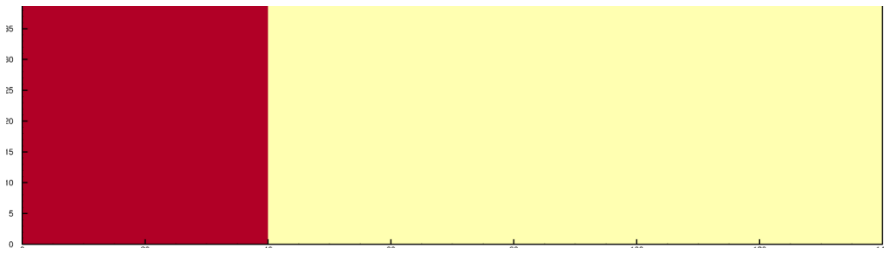

(a) test 1 and 2

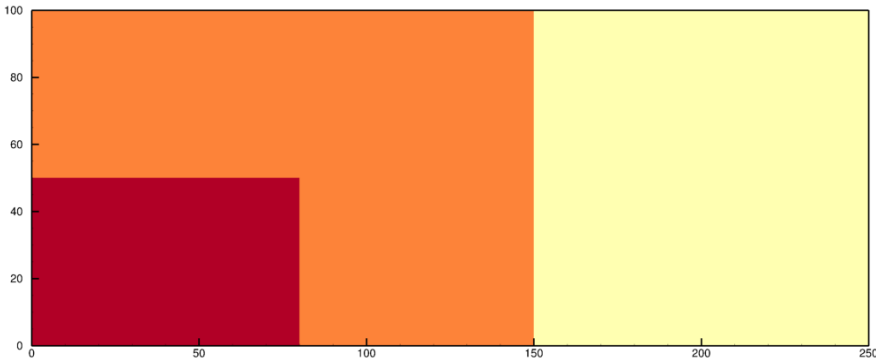

(b) test 3 and 4

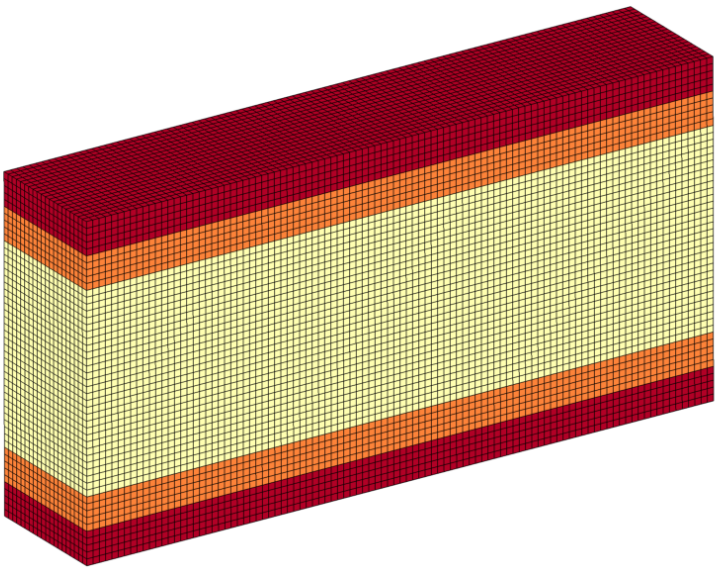

(c) test 5

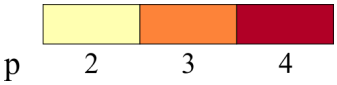

Figure 43 – Test configurations employed to analyse the graph partitioning algorithm.

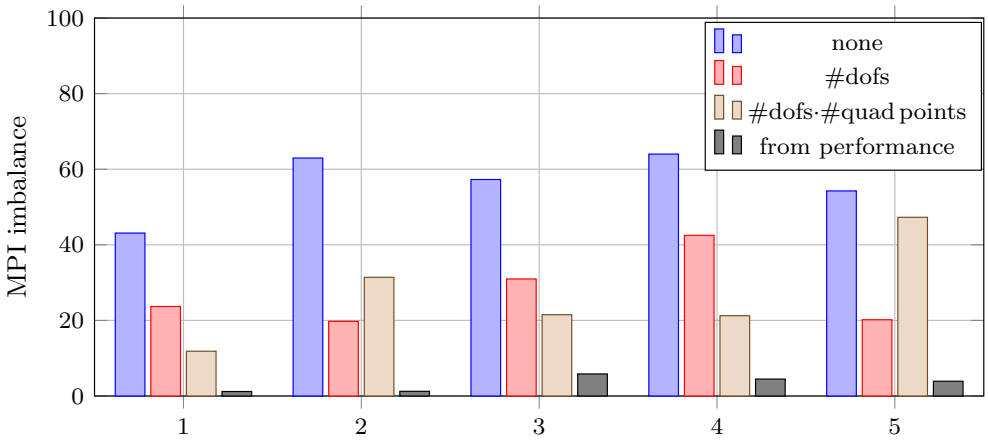

Figure 44 – Measured MPI imbalance for parallel computations for different definitions of the vertex weights in the graph partitioning algorithm.

The best results for all test cases are those provided by the proposed methodology of measuring the performance of the solver to derive the various contributions to the computational load and defining the vertex weights by Eq. (104). The remaining non-negligible MPI imbalance is partially a consequence of some of the considered simplifications. As an example, we assume that the contribution of the physical boundary faces to the total computational cost is equivalent to that of an internal face. Additionally, in the actual simulation, some operations are duplicated at the faces connecting two partitions (*e. g.* operation $b3$ described in Sec. 7.3). This leads to discrepancies between the predicted and effective computational load. Finally, as discussed by Hendrickson [88], one of the shortcomings of the employed graph partitioning algorithm is that it does not distribute evenly the communication cost among partitions. Possible communication imbalances can therefore further influence the MPI imbalance.

Nonetheless, for all the considered configurations the proposed approach leads to an MPI imbalance lower than 6%, which leads to a large reduction of the total computational cost as compared to the other strategies employed. This methodology is thus used throughout this work to generate mesh partitionings for parallel h- and p-adaptive simulations.

CHAPTER 8

DYNAMIC P-ADAPTIVE SIMULATION OF UNSTEADY FLOWS

RÉSUMÉ DU CHAPITRE EN FRANÇAIS

L'objectif principal de ce chapitre concerne l'analyse et le développement d'un algorithme dynamique p-adaptatif.

Sur la base des résultats du Chap. 5, l'indicateur SSED est utilisé dans la Sec. 8.2 pour développer un algorithme permettant d'adapter dynamiquement la valeur locale du degré polynomial en fonction de l'évolution des besoins de résolution des écoulements instationnaires.

L'algorithme dynamique p-adaptatif est appliqué dans la Sec. 8.3 à la simulation du transport d'un tourbillon par un écoulement uniforme de fluide parfait. Il est mis en évidence que l'algorithme adaptatif permet de réduire le temps de calcul total de 42% par rapport à une simulation uniforme au cinquième ordre pour atteindre la même précision. Il est également caractérisé que, pour un temps de calcul donné, une réduction des erreurs sur les champs de vitesse et de pression de plus d'un ordre de grandeur peut être obtenue par rapport aux simulations avec degré polynomial uniforme. Nous étudions ensuite l'influence sur les simulations adaptatives des seuils de raffinement et de déraffinement ainsi que la fréquence de l'adaptation. Enfin, il est observé que les coûts de calcul introduits par l'étape d'estimation d'erreur et l'étape de mise à jour de la solution et des bases fonctionnelles sont négligeables. Ceux-ci correspondent respectivement à moins de 1% et 5% du coût total de calcul pour tous les paramètres considérés.

L'algorithme adaptatif est ensuite appliqué à la résolution des équations de Navier-Stokes dans la Sec. 8.4 à la simulation de la collision d'un dipôle impactant une paroi. Il est mis en évidence que le coût de calcul de la simulation peut être réduit d'un facteur allant jusqu'à 75% du coût d'une simulation utilisant un degré polynomial uniforme. Il est également montré que le coût de calcul de l'algorithme adaptatif est inférieur à 2% du coût total de calcul. Ces résultats mettent en évidence l'efficacité de l'algorithme développé.

Enfin, des simulations adaptatives du vortex de Taylor-Green sont présentées dans la Sec. 8.5. L'algorithme d'adaptation dynamique permet une réduction de 33% du

temps de calcul total requis pour la simulation numérique directe de cet écoulement transitionnel.

8.1 INTRODUCTION AND OUTLINE OF THE CHAPTER

The analysis carried out Chap. 5 has allowed us to identify the SSED indicator as a suitable error estimator for statically adaptive simulation strategies. Starting from these results, we now shift our attention to the development and analysis of algorithms for the dynamically adaptive simulation of unsteady flows.

As discussed in Sec. 4.6, dynamic adaptation strategies can improve the accuracy and provide a large reduction of the computational cost for unsteady flow simulations. This is notably the case for transient flows, for which the instantaneous resolution requirements significantly change over time. Nonetheless, in order to achieve this, special care is required in the implementation of the error estimation and the resolution update algorithms. As both algorithms are applied multiple times over the course of the simulation, the associated overhead must be minimized to take full advantage of the computational gain provided by the dynamic adaptation. Additionally, the particular choice of the parameters involved in the dynamic adaptation process can considerably influence its efficiency and accuracy. These include the marking strategy employed, the associated thresholds, and the frequency of adaptation.

The objective of the present chapter is to propose and analyse a dynamically p-adaptive algorithm based on the SSED indicator. The developed strategy is presented in Sec. 8.2. The performance of the adaptive algorithm and the influence of the aforementioned parameters are then analysed on three configurations: the transport of a vortex by a uniform inviscid flow in Sec. 8.3, the collision of a dipole with a no-slip boundary in Sec. 8.4, and the DNS of the Taylor-Green Vortex at $\mathrm{Re} = 500$ in Sec. 8.5.

8.2 THE DYNAMICALLY p-ADAPTIVE ALGORITHM

The dynamically p-adaptive simulation of an unsteady flow is initialized by defining a discretization of the computational domain Ω_h, which is kept fixed over the course of the simulation, and an initial distribution of the local polynomial degree.

For transient problems, the initial resolution must be sufficient to correctly represent the prescribed initial condition. In the simulations presented in this chapter, we consider an initially uniform polynomial degree indicated as p_0. An alternative approach would consist in adapting the initial polynomial degree distribution to the prescribed initial condition $\mathbf{u}_0$. For this purpose, the static p-adaptive algorithm, described in Sec. 4.3, can be employed to adapt the initial resolution using the local L^2-projection error $\|\mathbf{u}_{h,0} - \mathbf{u}_0\|_{L^2(K)}$ as a refinement indicator. As the initial condition

is known, this quantity is an exact discretization error measure and does not require any approximation. The aforementioned procedure ensures therefore the accurate representation of the initial condition up to a user-prescribed error.

Once the initial resolution is fixed and the initial condition has been projected onto the discretization space, the solution is advanced in time for a user-defined interval Δt_{adapt}.

The SSED indicator is then computed from the instantaneous solution and the marking procedure is applied to identify elements to be refined/coarsened. In this chapter, we employ the marking strategy based on the user-defined refinement/coarsening thresholds, as described in Sec. 4.5. Additionally, we constrain the updated polynomial degree to the range $[p_{min}, p_{max}]$ and the maximum jump in p between neighbouring elements to be at most equal to one.

The spatial discretization in marked elements is thus modified by reallocating and updating all variables that directly depend on the local polynomial degree. This includes in particular the evaluation of the polynomial basis for the updated local polynomial degree and quadrature formula.

The numerical solution is thereafter evaluated on the updated discretization space by L^2-projection. As the employed basis is hierarchical, this operation is trivial and requires little computational time. In elements marked for refinement the first N_p dofs are kept the same and the added $N_{p+1} - N_p$ dofs are initialized to zero. Conversely, in elements selected for coarsening the $N_p - N_{p-1}$ dofs corresponding to the highest order modes are discarded. We point out that, if a different expansion basis was selected, *e. g.* the nodal basis, the L^2-projection step could represent a significant contribution to the total computational cost of the adaptive algorithm.

Once the solution has been projected on the updated discretization space, the simulation is advanced in time for a time interval Δt_{adapt} and the cycle is repeated until the end of the simulation.

Implementation details for the update of the polynomial basis

As in this work we employ a set of hierarchical orthonormal basis functions, the evaluation of the expansion basis on the updated set of quadrature points provides the highest contribution to the computational overhead of the dynamic p-adaptation algorithm. This is due to the significant computational cost of the MGS algorithm, described in Sec. 3.5, used for the generation of this basis. In order to minimize this computational cost, the local coefficients r_{ij}^K for $i, j \leq N_{p_{max}}$, required for the MGS algorithm for the generation of the local basis of maximum partial polynomial degree p_{max}, are computed only once at the beginning of the simulation. These are then stored in memory together with the values of the expansion basis at the integration points for the currently employed local polynomial degree and quadrature formula.

This allows for a large reduction of the computational cost of the dynamic algorithm for a limited increase of the memory storage.

We remark that the coefficients r_{ij}^K are computed using the highest-order quadrature formula which might be employed throughout the simulation. In the case of curvilinear meshes this can lead to an expansion basis which is not orthonormal with respect to the currently employed quadrature formula. However, this choice leads to the lowest error and fixes the corresponding analytical expression of the expansion basis throughout the simulation.

Effect of adaptation frequency

In the described strategy, the time interval Δt_{adapt} constitutes an important parameter controlling the efficiency and accuracy of the adaptive algorithm. Indeed, we remark that the spatial discretization employed in the time interval $[n\Delta t_{adapt}, (n+1)\Delta t_{adapt}]$ is derived from the resolution requirements estimated at the beginning of the interval, at $t = n\Delta t_{adapt}$. The adaptation algorithm is therefore effectively shadowing the actual evolution in time of the spatial resolution requirements. Accordingly, Δt_{adapt} must be small enough to avoid the divergence of the used and required resolution and the excessive growth of the error. However, a small value of Δt_{adapt} corresponds to a higher number of adaptation steps and therefore, in theory, to a higher computational overhead of the adaptive algorithm. In practice, the optimal value of Δt_{adapt} can be estimated by identifying a physical time-scale associated with variations of the spatial resolution, such as the convective time-scale.

An alternative approach is employed by Belme *et al.* [21] and Alauzet *et al.* [6] among others. In this case, the solution is at first advanced in time from $n\Delta t_{adapt}$ to $(n+1)\Delta t_{adapt}$. The refinement indicator is then computed to estimate the resolution requirements for the simulated time interval. The simulation over the same interval $[n\Delta t_{adapt}, (n+1)\Delta t_{adapt}]$ is thereafter repeated on the updated discretization before further advancing in time. As there is no delay in the adapted spatial resolution, this procedure presents increased accuracy. Nonetheless, it comes at the additional cost of having to repeatedly solve the evolution of the flow, thus considerably increasing the simulation time. Consequently, this option does not appear suitable for scale-resolving simulations.

For this reason, only the first strategy introduced in this section is employed. In the next sections, the effect of the parameter Δt_{adapt} on the efficiency and accuracy of adaptive simulations is analysed on three different unsteady flow configurations.

8.3 TRANSPORT OF A VORTEX BY A UNIFORM FLOW

The dynamically p-adaptive algorithm presented in the previous section is now analysed by performing simulations of a vortex transported by a uniform inviscid flow.

This problem, in the formulation proposed by Yee *et al.* [200], is often considered as a useful test case to demonstrate the capability of numerical methods to preserve vorticity in an unsteady inviscid flow. The transport of vortices is in fact of fundamental interest for LES and detached-eddy simulations, which require the accurate simulation of the smallest resolved turbulent scales over long integration periods. This is therefore a relatively simple and interesting configuration to measure the dissipation and dispersion properties of numerical methods and, in this work, the performance of our dynamically p-adaptive algorithm. For this reason it has been selected as a benchmark problem in several research projects focused on the assessment of the performance of high-order methods [33, 196].

Description of the problem

The domain is the unit square $\Omega := [0,1]^2$ with periodic boundary conditions. The initial condition is obtained by the superposition of a uniform flow, at pressure p_∞, temperature T_∞ and Mach number M_∞, and an isentropic vortex of characteristic radius R and strength β centered at $(x_c, y_c) = (0.5, 0.5)$.

Taking U_∞, ρ_∞ and T_∞ as the reference quantities, the normalized initial condition takes the form:

$$u(\mathbf{x},0) = 1 - \beta\frac{y-y_c}{R}\exp\left(-\frac{r^2}{2R^2}\right) \tag{106}$$

$$v(\mathbf{x},0) = \beta\frac{x-x_c}{R}\exp\left(-\frac{r^2}{2R^2}\right) \tag{107}$$

$$T(\mathbf{x},0) = 1 - \frac{\gamma-1}{2}M_\infty^2\beta^2\exp\left(-\frac{r^2}{2R^2}\right) \tag{108}$$

$$\rho(\mathbf{x},0) = (T(\mathbf{x},0))^{\frac{1}{\gamma-1}} \tag{109}$$

where $r^2 = (x-x_c)^2 + (y-y_c)^2$ is the distance from the vortex center.

The exact solution is the pure convection of the vortex at constant velocity and is periodic on the considered domain with period $t_c = 1$. The exact solution is therefore known at all times and can be employed to assess the accuracy of the numerical unsteady solution.

In the present work, we consider the testing conditions corresponding to the *Fast vortex* configuration of the HiOCFD workshop [196]: $M_\infty = 0.5$, $\beta = 0.2$ and $R = 0.05$. The accuracy and computational cost of the simulations are evaluated by simulating the flow for a time interval $10t_c$.

Computational details

In order to assess the performance of the dynamically p-adaptive algorithm, both adaptive and uniform polynomial degree simulations are carried out.

All computations are performed on a uniform Cartesian grid composed of 32^2 elements, corresponding to the coarsest mesh employed in the HiOCFD workshop. Uniform polynomial degree simulations are carried out for $p = 1, 2, 3$ and 4. The dynamically adaptive algorithm is employed with $p_{min} = 1$ and $p_{max} = 4$ and initialized using a uniform polynomial degree $p_0 = 4$. The number of quadrature points per space direction is $q_K = p_K + 1$.

The LLF flux is employed for the discretization of the convective term with the upwind contribution scaled by a parameter $k = 0.1$. As regards the temporal discretization scheme, the third-order four-stage SSP Runge-Kutta scheme is employed and the time step is set to $\Delta t = 5 \cdot 10^{-4}$ for all computations.

We analyse in particular the effect of the parameters Δt_{adapt}, η_{ref} and η_{coars} on the accuracy and computational cost of the dynamic p-adaptation algorithm. To this end, simulations are carried out for three values of $\Delta t_{adapt} = \Delta t$, $10\Delta t$ and $100\Delta t$, and five values of η_{ref} uniformly distributed in a logarithmic scale from 10^{-2} to 10^{-6}. For each value of η_{ref} we consider two values of the coarsening threshold, namely, $\eta_{coars} = 10^{-2}\eta_{ref}$ and $10^{-3}\eta_{ref}$.

The accuracy of each simulation is measured in terms of the L^2-norm of the error in the streamwise velocity component and in the pressure with respect to the exact solution. All simulations are performed on a single core. The computational cost is presented normalized following the guidelines provided in the HiOCFD workshop [196]. The computer performance is thus measured by means of the TauBench code [63]. The TauBench code mimics the run-time performance of the Tau code, a solver for the RANS equations on hybrid grids developed by the German aerospace research DLR. The CPU time required by TauBench for ten time steps considering 250 000 dofs is employed as a reference to express the runtime cost in terms of nondimensional work units.

Analysis of results

Figure 45 shows the convergence history of the L^2-norm of the error in the streamwise velocity component and in the pressure, under uniform p-refinement and for the dynamically p-adaptive simulations for various values of η_{ref} and η_{coars}. The adaptation time interval is taken here $\Delta t_{adapt} = 10\Delta t$. Each symbol of this figure corresponds to a single uniform or dynamically adaptive simulation. These results clearly demonstrate that, compared to uniform polynomial degree simulations, the dynamically p-adaptive algorithm can provide a large reduction of the computational cost to achieve a prescribed level of accuracy. In particular, the dynamically

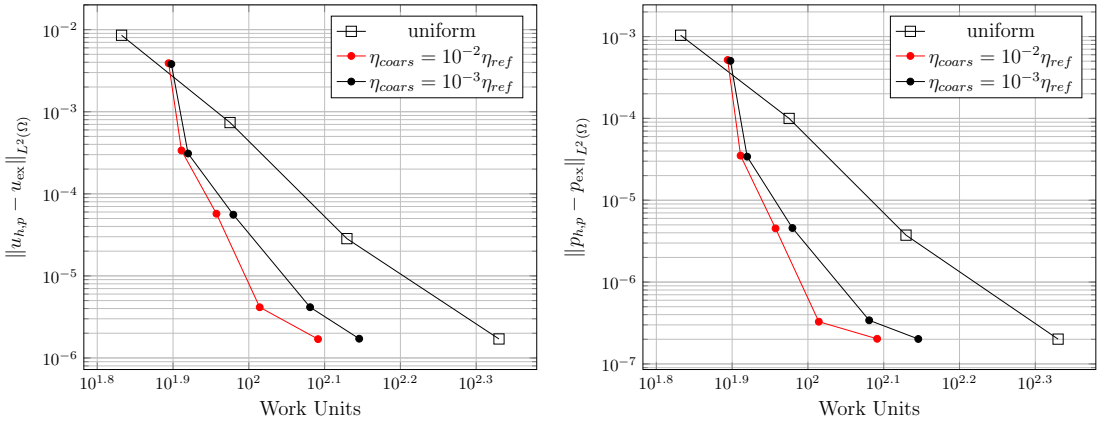

Figure 45 – Transport of a vortex by a uniform flow: Convergence history of the L^2-norm of the error in the streamwise velocity component u (left) and in the pressure (right) for uniform polynomial degree simulations and for dynamically p-adaptive simulations using various values of η_{ref} and η_{coars}. In these tests, $\Delta t_{adapt} = 10\Delta t$.

p-adaptive simulation with $\Delta t_{adapt} = 10\Delta t$, $\eta_{ref} = 10^{-6}$ and $\eta_{coars} = 10^{-8}$, achieves the same accuracy as the computation using a uniform polynomial degree $p = 4$ with a 42% reduction of the computational cost. The dynamic algorithm can also reduce the error by more than one order of magnitude as compared to the uniform $p = 2$ and $p = 3$ simulations at a lower computational cost, as seen in Fig. 45.

For each of the curves represented in Fig. 45, we observe that reducing the value of η_{ref} by one order of magnitude leads to a corresponding reduction of the global error. This is valid until the same accuracy as that of the computation using a uniform $p = p_{max}$ is achieved. Further reducing η_{ref} leads to a negligible increase of the accuracy and a rise in of the computational cost.

Conversely, reducing the value of η_{coars} from $10^{-2}\eta_{ref}$ to $10^{-3}\eta_{ref}$ only leads to a negligible reduction of the error and, for the lowest values of η_{ref}, to a large increase of the computational cost. This is due to the fact that those elements that are characterized by relatively higher values of the error indicator are the major contributors to the total error production. Nonetheless, the coarsening threshold must be sufficiently lower than the refinement threshold. If this is not the case a flickering effect might be observed where elements marked for coarsening are immediately selected for refinement at the next adaptive iteration. This leads to a significant increase of the computational overhead of the adaptive algorithm and can reduce the overall accuracy of the simulation.

In Fig. 46 we report the distribution of the adapted polynomial degree and of the SSED indicator at the end of the adaptive simulation for $\Delta t = 10\Delta t$ and three pairs of values η_{ref} and η_{coars}. For all three cases, the highest resolution patches are located at the vortex core and its neighbouring area, partially extending upstream of the

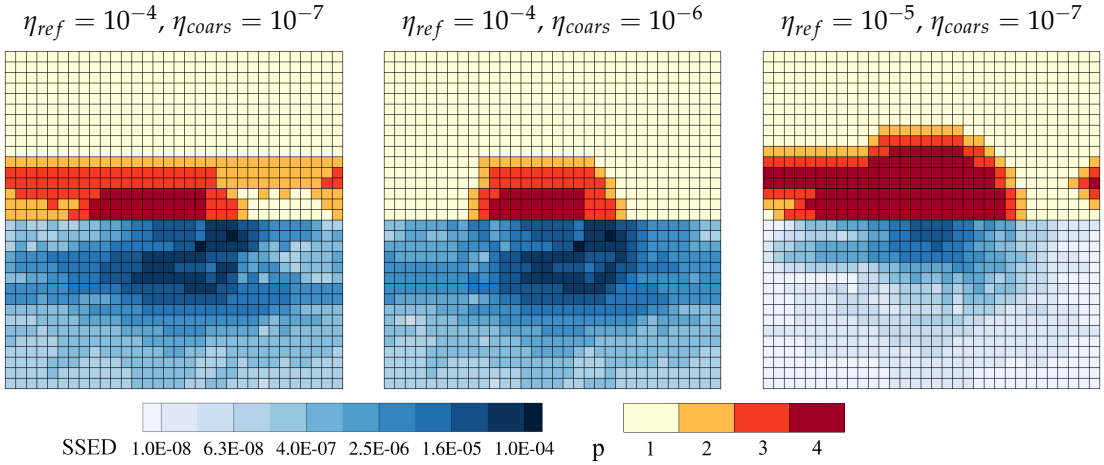

Figure 46 – Transport of a vortex by a uniform flow: Distribution of the local polynomial degree (top half) and of the SSED indicator (bottom half) using the adaptive simulations for different values of η_{ref} and η_{coars} at $t = 10t_c$. In these tests, $\Delta t_{adapt} = 10\Delta t$.

vortex region. Additionally, for $\eta_{ref} = 10^{-4}$ (left and center panel of Fig. 46) the highest values of the SSED indicator (bottom half maps) are located ahead of the adapted region, corresponding to elements which would be selected for refinement at the next adaptation step. This is caused by the time shift between the flow and the adaptation process.

Conversely, for $\eta_{ref} = 10^{-5}$ (on the right panel of Fig. 46), the highest value of the error is located at the core of the vortex. Indeed, in these elements the adaptive algorithm is not able satisfy the refinement criterion. This is due to the constraint imposed on the maximum local polynomial degree, $p_{max} = 4$, which appears insufficient to achieve the level of accuracy imposed by this value of the refinement threshold.

Finally, we observe on the left and right panels of Fig. 46 that, when the refinement and coarsening thresholds are sufficiently low, additional refinement is present upstream of the vortex. The resolution in this region is actually adapted due to the presence of high-order oscillations caused by the dispersion error of the method.

The influence of the parameter Δt_{adapt} on the performance of the dynamic algorithm is investigated in Fig. 47. Considering the curves for $\Delta t_{adapt} = \Delta t$ and $10\Delta t$, we observe that the lower value of Δt_{adapt} leads to a negligible increase of the overall accuracy and, for most simulations, an increase of the computational cost. This is mainly related to the increase of the computational overhead of the dynamic algorithm. Nonetheless, as already pointed out by Gassner *et al.* [73], when Δt_{adapt} is excessively small, one can observe a flickering phenomenon by which an element marked for refinement is immediately marked for coarsening. This might be

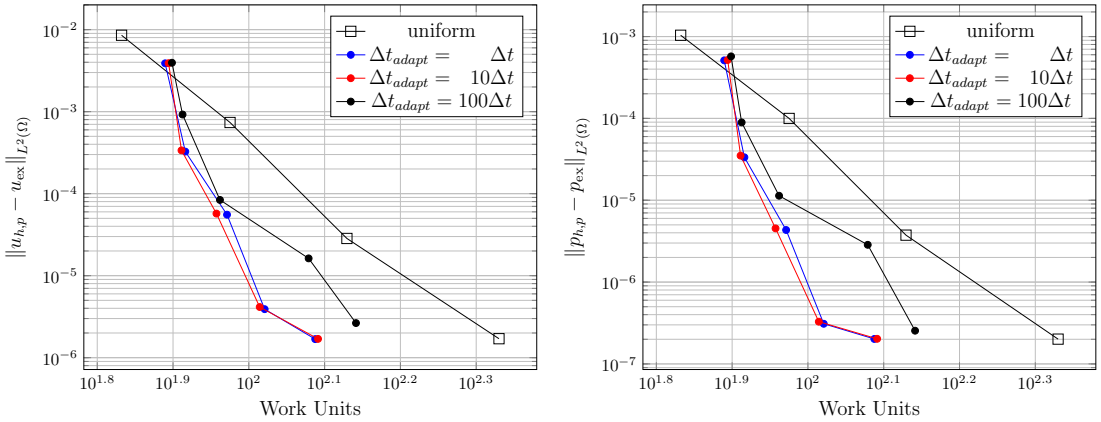

Figure 47 – Transport of a vortex by a uniform flow: Convergence history of the L^2-norm of the error in the streamwise velocity component (left) and in the pressure (right) for uniform polynomial degree simulations and for dynamically p-adaptive simulations using various values of η_{ref} and Δt_{adapt}. The coarsening threshold is set here to $\eta_{coars} = 10^{-2}\eta_{ref}$.

caused by the higher-order modes of the solution not being yet populated at the next adaptation iteration. Gassner *et al.* [73] and Kubatko *et al.* [112] have thus suggested to modify the marking procedure by preventing coarsening in elements that have been recently marked for refinement.

The plots in Fig. 47, also show that for high values of Δt_{adapt} a large increase in the error of the adaptive simulations and, in some cases, an increase in the computational cost takes place. The reduction of the accuracy is due to the time shift between the flow and the adapted resolution, which does not react sufficiently rapidly to the evolving resolution requirements. As the adapted region lags behind the real resolution requirements, a larger amount of error is then produced, as compared to simulations with lower Δt_{adapt}, and is transported in the domain. This eventually leads to a larger number of elements being selected for refinement and thus to a higher computational cost.

In Fig. 48 we report for each simulation the percentage of the total computational time spent in performing the error estimation step (left panel) and in updating the spatial resolution (right panel). Considering the left panel of Fig. 48, we observe that a very limited time is spent to compute the SSED refinement indicator. The computational overhead introduced by this procedure presents a limited variation with respect to the threshold values η_{ref} and η_{coars} and is mostly controlled by Δt_{adapt}, *i. e.* the frequency with which the refinement indicator is computed. Nonetheless, even for the lowest value $\Delta t_{adapt} = \Delta t$, the total CPU time required by the error estimation step is lower than 0.6% of the total computational time. This demonstrates the efficiency of the considered error estimation strategy.

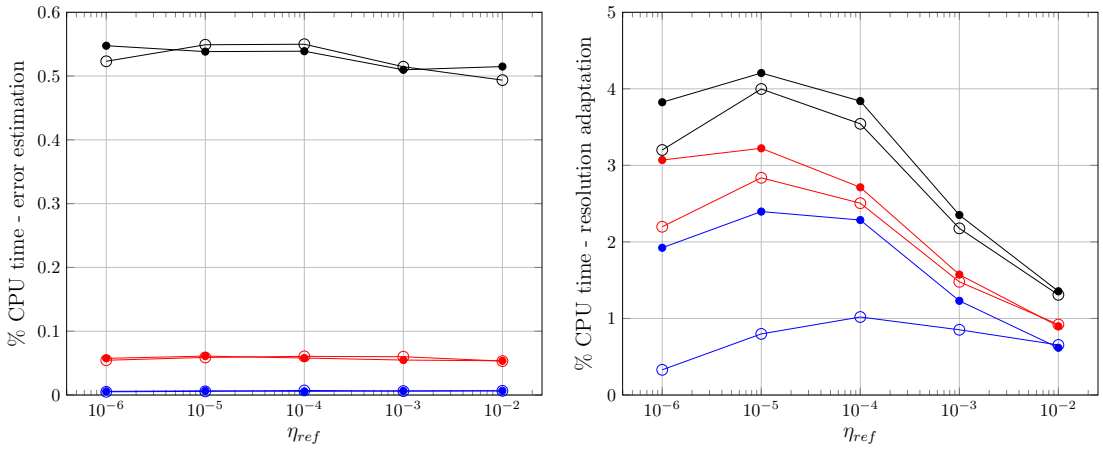

Figure 48 – Transport of a vortex by a uniform flow: percentage of the total computational time of the simulation required by the error estimation procedure (left) and the resolution update step (right) as a function of η_{ref} for two values of $\eta_{coars} = 10^{-2}\eta_{ref}$ (filled circles) and $10^{-3}\eta_{ref}$ (empty circles), and three values of Δt_{adapt}: Δt (black), $10\Delta t$ (red) and $100\Delta t$ (blue).

Considering now the right panel of Fig. 48, we observe that the update of the spatial resolution represents the costliest step of the adaptation process. This is the computational time required for the application of the marking procedure, reallocation of variables depending on p_K, update of the local expansion set and projection of the solution. As already mentioned, for the employed discretization, the reallocation and basis functions update operations are responsible for most of the computational overhead.

We point out that, for the considered problem, the transient phenomenon implies a continuous variation of the spatial resolution requirements over a large portion of the domain. This leads to a relatively high number of elements being adapted at each step of the algorithm and, consequently, a high computational overhead is introduced by the dynamic adaptation procedure. Nonetheless, for all the presented simulations, the computational time required by the resolution update is lower than 5% of the total computational cost, demonstrating the efficiency of the developed algorithm.

As seen in the right panel of Fig. 48, overall, the computational overhead of the resolution update presents a lower dependency on Δt_{adapt} as compared to the error estimation. This is due to the fact that the update of the spatial resolution is applied only to elements that have been marked for coarsening or refinement, thus it is more influenced by the effective variation of resolution requirements rather than the frequency of adaptation.

Finally, a lower value of η_{coars} leads to a lower percentage of CPU time required by the resolution update process. This is explained by the relatively higher cost of

the simulation and the lower number of elements selected for coarsening at each adaptation step.

8.4 COLLISION OF A DIPOLE WITH A NO-SLIP BOUNDARY

The developed dynamically adaptive algorithm is now applied to the simulation of the collision of a dipole with a no-slip boundary. Despite the simplicity of the configuration, it has been shown that the accurate simulation of this flow requires high resolution [45] and is challenging even for Fourier or Chebyshev methods achieving spectral accuracy.

The dipole-wall interaction is responsible for the formation and detachment of thin boundary layers, involving the generation of vorticity and small-scale structures. Small errors in the evaluation of these high-vorticity regions can lead to important discrepancies in the prediction of the evolution of the flow over long integration times. It represents therefore a challenging benchmark for CFD methods aiming at the accurate and efficient simulation of wall-bounded flows or flows around solid obstacles [51, 104, 107, 114, 149, 150].

In order to provide accurate results, the dynamically adaptive algorithm must be able to automatically resolve the travelling dipole and identify error production during the collision and dipole-wall interaction phases. For these reasons, it also represents an interesting benchmark for adaptive algorithms.

Description of the problem

The configuration considered in this section is the one analysed by Keetels et al.[104]. The physical domain is a square $\Omega := [-1,1]^2$ with no-slip adiabatic wall boundary conditions at the two boundaries located at $x = \pm 1$ and periodic conditions at $y = \pm 1$. The problem is symmetric with respect to $y = 0$ and the initial condition consists in the superposition of two counter rotating vortices.

The vorticity distribution of the isolated vortex is

$$\omega_0 = \omega_e(1 - (r/r_0)^2)\exp\left[-(r/r_0)^2\right] \ , \tag{110}$$

where ω_e is the vorticity at the core of the vortex, r_0 is the vortex radius and r is the distance from the vortex core. The two counter rotating vortices are located at $(0, \pm r_0)$, r_0 is set equal to 0.1 and the value of ω_e is set such that at $t = 0$ the total kinetic energy, defined as

$$\mathcal{K}(t) = \int_\Omega \frac{\rho \mathbf{v}\cdot\mathbf{v}}{2} \mathrm{d}\mathbf{x} \ , \tag{111}$$

is normalized to $\mathcal{K}(0) = 2$, which leads to $\omega_e = 299.528385375226$. Using this value, the vorticity at all boundaries is virtually zero and the boundary conditions are satisfied up to machine accuracy.

The normalized initial condition expressed in terms of the primitive variables takes the form

$$\rho(\mathbf{x},0) = 1 \ , \tag{112}$$

$$u(\mathbf{x},0) = -\frac{1}{2}|\omega_e|(y-r_0)\exp\left[-(r_1/r_0)^2\right] + \frac{1}{2}|\omega_e|(y+r_0)\exp\left[-(r_2/r_0)^2\right] , \tag{113}$$

$$v(\mathbf{x},0) = -\frac{1}{2}|\omega_e|x\exp\left[-(r_1/r_0)^2\right] + \frac{1}{2}|\omega_e|x\exp\left[-(r_2/r_0)^2\right] , \tag{114}$$

$$p(\mathbf{x},0) = \frac{1}{\gamma M^2} - \left(\frac{\omega_e r_0}{4}\right)^2 \left(\exp\left[-2(r_1/r_0)^2\right] + \exp\left[-2(r_2/r_0)^2\right]\right) , \tag{115}$$

where r_i is the distance from the i-th vortex core. Over the course of the simulation, we monitor the evolution of the total enstrophy defined by

$$\zeta = \int_\Omega \frac{\rho\boldsymbol{\omega}\cdot\boldsymbol{\omega}}{2} \mathrm{d}\mathbf{x} \ , \tag{116}$$

with $\boldsymbol{\omega} = \nabla \wedge \mathbf{u}$. From Eqs. (112)-(114), we obtain that $\zeta(0) \approx 800$.

The Reynolds number based on the reference velocity $U = \sqrt{\mathcal{K}_0/2}$ and the domain half width is set to Re = 1000. The value of the Mach number is set equal to 0.01, allowing to simulate nearly incompressible conditions.

Evolution of the flow

Due to the initial velocity distribution, the vortex dipole starts moving in the direction of the solid wall located at $x = 1$. A secondary, less energetic, vortex structure is generated at the same time and starts travelling at lower speed in the opposite direction.

As the primary vortices approach the solid wall at $t \approx 0.3$, two thin boundary layers with vorticity of opposite sign to that of the primary vortices are formed near the wall. At $t \approx 0.35$ the primary vortices impinge on the wall generating a large amount of vorticity. This drives the formation of new high-vorticity structures that are stripped from the boundary layer. After the primary impact, the vortices present a curved trajectory which leads to a second collision at $t \approx 0.6$. After $t \approx 0.8$ no further production of vorticity is observed and the present vortices progressively dissipate. At $t \gtrsim 0.9$ the secondary vortex structure interacts with the wall at $x = -1$ with a similar evolution, albeit with lower energy dissipation and enstrophy production.

Clercx and Bruneau [45] have shown that an extremely fine resolution is required to correctly capture the enstrophy production caused by the vortex-wall interaction. Indeed, if the resolution is not sufficient, the intensity of the second collision can be significantly underpredicted.

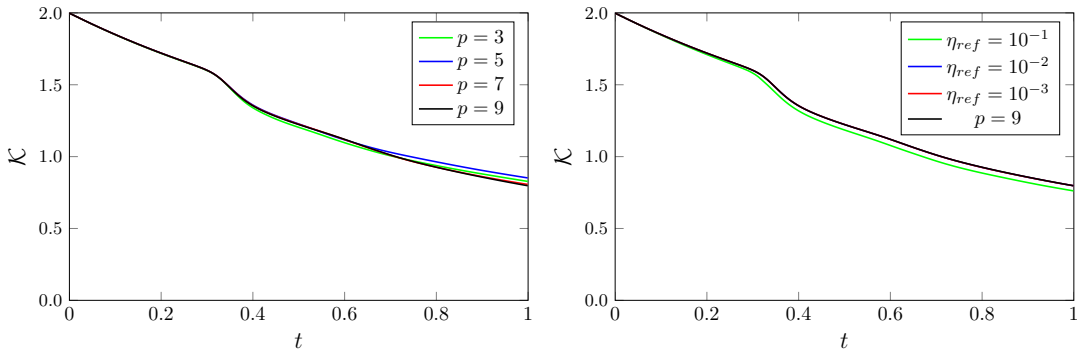

Figure 49 – Dipole-wall collision at Re = 1000: Evolution of the total kinetic energy for uniform polynomial degree simulations (left) and dynamically p-adaptive simulations (right).

Computational detalis

Uniform polynomial degree and dynamically p-adaptive simulations of this configuration are carried out. As for the previous test case, the computational domain is discretized by means of a uniform Cartesian grid composed of 32^2 elements. The uniform polynomial degree simulations are carried out using a polynomial degree varying from 1 to 9. The local polynomial degree for the adaptive simulations is initialized to the uniform value $p_0 = 4$ and constrained to the interval $[1, 8]$. Numerical integration is performed using quadrature formulae accurate for polynomials of degree $3p_K$.

The Roe flux and the BR2 scheme with $\eta_{br2} = 1$ are used for the discretization of the convective and viscous fluxes respectively. Time integration is performed by means of the third-order four-stage SSP Runge-Kutta scheme using a constant time step $\Delta t = 10^{-5}$.

As in Sec. 8.3, several dynamically p-adaptive simulations are performed for different values of η_{ref}. For all simulations $\Delta t_{adapt} = 5\Delta t$ and $\eta_{coars} = 10^{-2}\eta_{ref}$.

The accuracy of the computations is measured by evaluating the error in the evolution of the total kinetic energy and the total enstrophy in the nondimensionalized time interval $T = [0, 1]$. For this purpose, the solution obtained using a uniform polynomial degree $p = 9$ is used as reference. Computational times are measured by performing each simulation on a single core.

Analysis of results

In Figs. 49 and 50 we report the evolution of the total kinetic energy and the total enstrophy obtained by the uniform polynomial degree and the dynamically p-adaptive simulations.

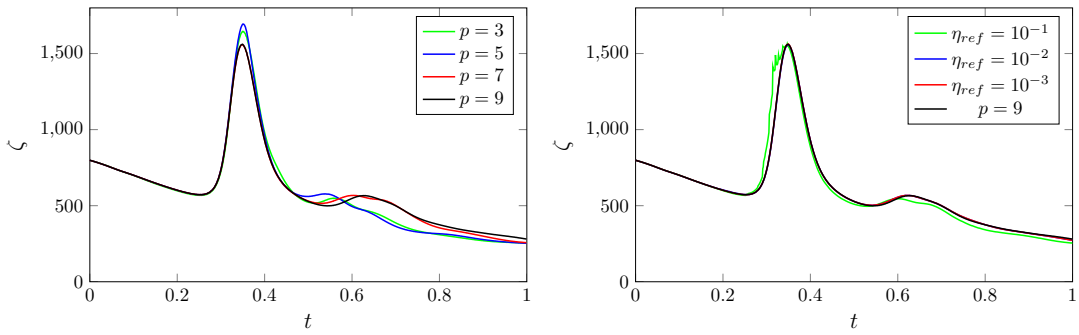

Figure 50 – Dipole-wall collision at Re = 1000: Evolution of the total enstrophy for uniform polynomial degree simulations (left) and dynamically p-adaptive simulations (right).

Analysing the left panels of Figs. 49 and 50, we observe that the uniform polynomial degree simulations using $p < 7$ overestimate the amount of vorticity produced over the course of the primary impact of the dipole with the wall. This leads to an early prediction of the second impact and to important differences in the evolution of the total kinetic energy and enstrophy with respect to the reference solution. Even for $p = 7$, the uniform polynomial degree simulation underpredicts the time of the second impact and the total enstrophy for $t \gtrsim 0.6$.

As regards the p-adaptive simulations, we observe that the threshold value $\eta_{ref} = 10^{-1}$ is excessively high. The simulation with $\eta_{ref} = 10^{-1}$ leads to high values and an unphysical evolution of the total enstrophy during the first impact, between $t \approx 0.3$ and $t \approx 0.35$. The total kinetic energy and the total enstrophy are also underpredicted for $t \gtrsim 0.2$ and $t \gtrsim 0.6$ respectively. This indicates that for $\eta_{ref} = 10^{-1}$ the adaptive algorithm increases the resolution near the wall only when a significant error has already been produced. Surprisingly, however, a good qualitative agreement is obtained at $t \gtrsim 0.35$ and the adaptive simulation predicts the correct time of the second impact.

For lower values of $\eta_{ref} \leq 10^{-2}$ the quality of the adaptive simulations is greatly improved. In this case the evolution of the total kinetic energy is indistinguishable from the reference computation and the evolution of the total enstrophy almost overlaps the reference simulation and coincides with the solution corresponding to uniform polynomial degree $p = p_{max} = 8$ (not shown here).

More quantitative results are presented in Fig. 51. Here we report the error in the evolution of the total kinetic energy and total enstrophy as a function of the computational cost expressed in terms of work units. The dynamically p-adaptive algorithm with $\eta_{ref} = 10^{-2}$ leads to a reduction of both error measures by more than one order of magnitude with respect to the uniform $p = 5$ simulation with a approximately 15% lower computational cost. We also observe that this simulation presents the same accuracy as the uniform polynomial degree simulation for $p =$

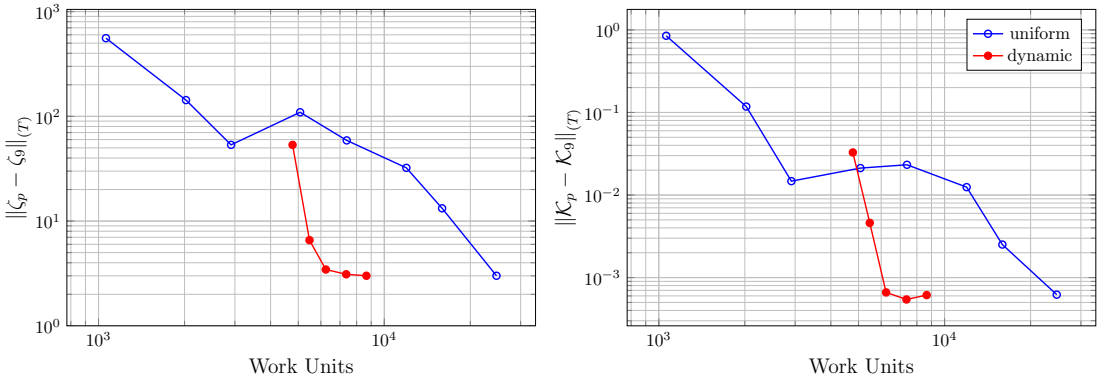

Figure 51 – Dipole-wall collision at Re = 1000: Error in the evolution of the total enstrophy (left) and total kinetic energy (right) as a function of the computational cost for uniform polynomial degree and dynamic p-adaptive simulations.

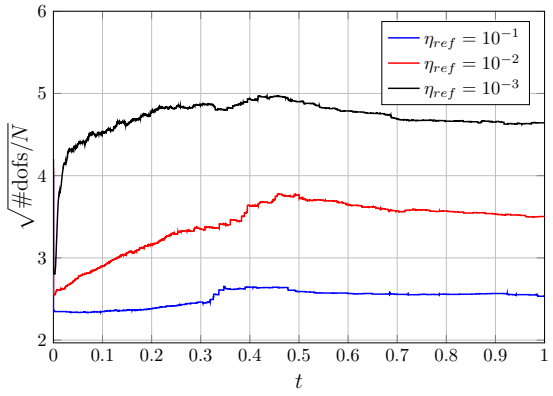

Figure 52 – Dipole-wall collision at Re = 1000: Evolution of the total number of dofs divided by the total number of elements N for the dynamic p-adaptive simulations for different values of the refinement threshold η_{ref}.

$p_{max} = 8$ with a reduction of the total computational cost of about 75%. Further reducing the value of η_{ref} leads to a negligible reduction of the error and an increase of the computational cost, as observed in Fig. 45.

In Fig. 52 we report the evolution of the total number of dofs over the course of the simulations. It illustrates that for $\eta_{ref} = 10^{-1}$ the number of dofs remains almost constant until the dipole impinges on the wall and the resolution is increased only after $t \gtrsim 0.3$. This is in agreement with the conclusions drawn from Figs. 49 and 50.

In contrast, for $\eta_{ref} = 10^{-2}$ the total number of dofs progressively increases as the dipole approaches the wall and continues to increase until $t \approx 0.5$ as the dynamic algorithm refines a larger region following the curvilinear trajectory of the vortices. After $t \approx 0.5$ the resolution is progressively decreased following the second collision and the dissipation of the vortex structures. A similar evolution is obtained for

$\eta_{ref} = 10^{-3}$, albeit with a smaller variation over time and an overall larger number of dofs.

The contours of the enstrophy (top half plots in the panels), as well as the distribution of the local polynomial degree (bottom half plots in the panels), at various times for the adaptive simulation with $\eta_{ref} = 10^{-2}$ are shown in Fig. 53. The regions characterized by higher resolution are those coinciding with the position of the primary and secondary vortices and follow their evolution during the initial phase of the simulation. For $t \gtrsim 0.2$ higher values of the polynomial degree are present near the wall as the resolution requirements increase due to the formation of a thin boundary layer. From $t \approx 0.3$ to $t \approx 0.7$ the local polynomial degree distribution follows the curvilinear trajectory of the primary vortex and the new vortices generated by the vortex-wall interaction. At later times, for $t \gtrsim 0.8$, the distribution of local polynomial degree remains almost unvaried while the resolution is slowly reduced as the vortex structures dissipate. During this phase, the values of p_K increase only near the wall at $x = -1$ as the secondary weaker dipole starts interacting with it.

We can conclude, therefore, that the adaptive algorithm correctly identifies the regions requiring increased resolution and responds accordingly. Nonetheless, we notice that, in some regions, relatively high values of p_K persist for some time after the transient phenomenon has passed. This suggests that the choice of a higher, *i. e.* less stringent, coarsening threshold might lead to a further reduction of the computational cost for this test case.

Finally, in Fig. 54 we report for this configuration the percentage of the total computational time required for the error estimation and resolution adaptation procedures. We observe that, for all values of the refinement threshold, the computational time required for the evaluation of the SSED indicator is less than 0.02% of the total computational time. These values are considerably smaller than those obtained for the previous configuration (see Fig. 48). Indeed, we recall that the SSED indicator formulation is independent of the equations being solved. Thus, the increase of the computational cost required to advance the solution in time for this viscous problem is the reason for the lower overhead of the error estimation strategy relative to the total cost.

Additionally, the computational cost required to update the spatial resolution corresponds, for all values of η_{ref}, to less than 2% of the total run-time. In particular, as observed for the previous configuration, as η_{ref} is reduced below 10^{-2} the relative computational cost of the adaptive algorithm decreases. This is due to the increased cost to advance the simulation and the lower variation over time of the distribution of local polynomial degree as observed in Fig. 52.

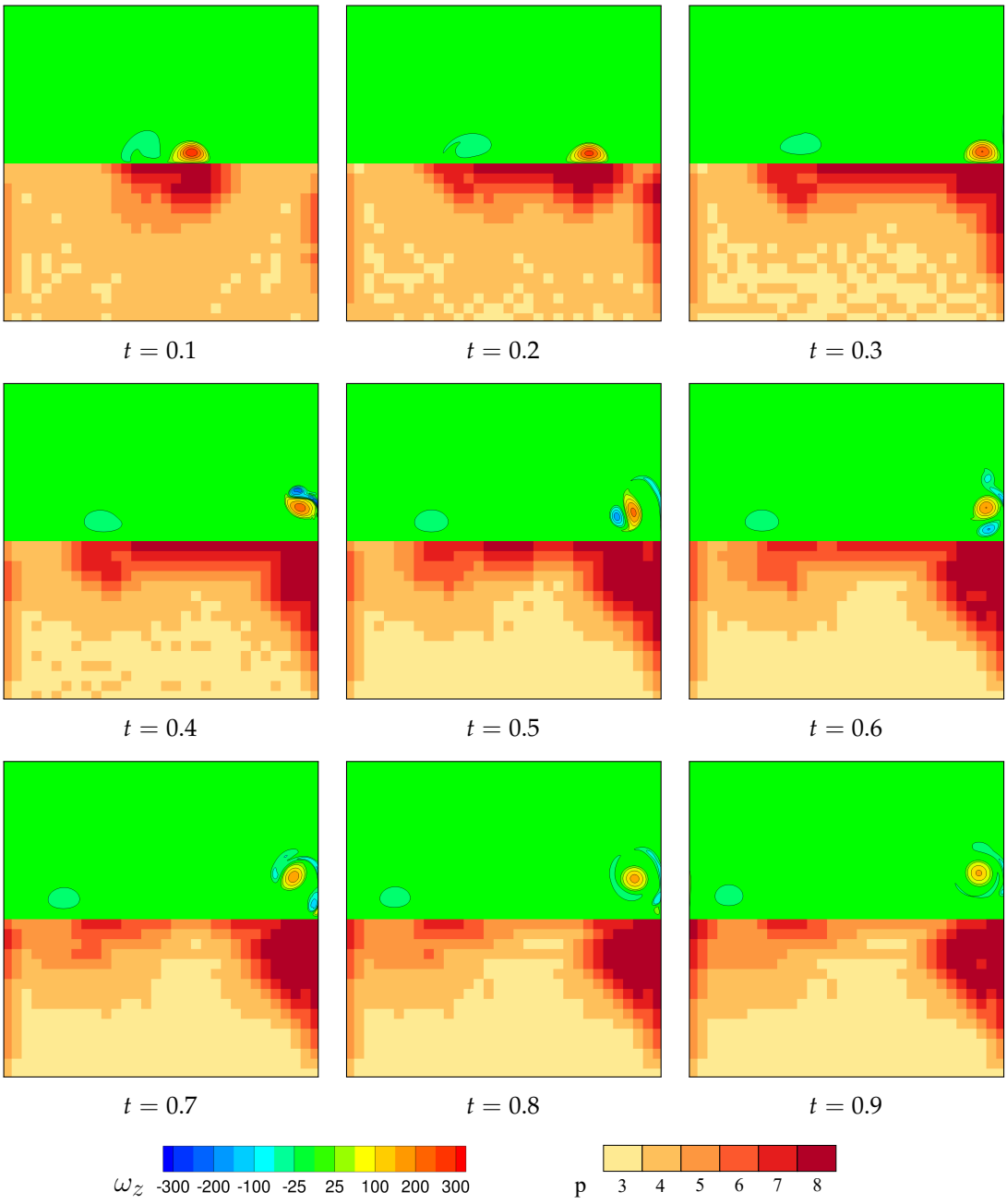

Figure 53 – Dipole-wall collision at Re = 1000: Contour plots of the vorticity field (top half) and distribution of the local polynomial degree (bottom half) at various instants of the dynamically p-adaptive simulation using $\eta_{ref} = 10^{-2}$.

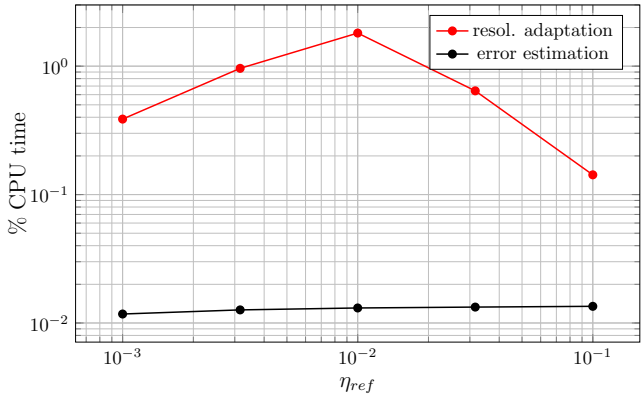

Figure 54 – Dipole-wall collision at Re = 1000: Percentage of the total computational time required for the error estimation and the update of the spatial resolution.

8.5 THE TAYLOR-GREEN VORTEX

The last configuration analysed is the Taylor-Green Vortex (TGV). It is a model problem in which the initial large-scale vortex, specified as an initial condition, evolves leading to laminar-to-turbulence transition, followed by freely decaying homogeneous turbulence.

This configuration was originally introduced by Taylor and Green [180] and later analysed by Brechet *et al.* [30, 31] by means of DNS simulations. The simple geometry, combined with the complex physical behaviour, make it an ideal test case for the validation and comparison of CFD tools aimed at the simulation of vortex dynamics and turbulent flows.

Description of the problem

The computational domain is a triperiodic box $\Omega := [-\pi L, \pi L]^3$. The reference quantities are the initial uniform density ρ_0, the length L, the velocity V_0 and the reference temperature T_0. The initial condition expressed in terms of the primitive variables takes the form

$$\rho(\mathbf{x}, 0) = 1 \tag{117}$$
$$u(\mathbf{x}, 0) = \sin(x)\cos(y)\cos(z) \ , \tag{118}$$
$$v(\mathbf{x}, 0) = -\cos(x)\sin(y)\cos(z) \ , \tag{119}$$
$$w(\mathbf{x}, 0) = 0 \ , \tag{120}$$
$$p(\mathbf{x}, 0) = \frac{1}{\gamma M^2} + \frac{1}{16}\left(\cos(2x) + \cos(2y)\right)\left(\cos(2z) + 2\right) \ . \tag{121}$$

As for the previous configuration, the evolution of the flow is analysed by monitoring the total kinetic energy Eq. (111) and total enstrophy Eq. (116).

In this section we consider the TGV at Re = 500 and near incompressible conditions corresponding to $M_0 = 0.1$. Under these conditions, the initial vortex structures are stretched over the course of the first part of the simulation until $t \lesssim 3$. Small vortex structures appear between these larger vortices and become progressively unstable eventually leading to transition and a rapid enstrophy production. A single peak of the enstrophy is observed at $t \approx 9$. At later times, the flow becomes fully turbulent, isotropic, and homogeneous and the kinetic energy decays under the action of molecular viscosity.

Computational details

The computational domain is discretized by a uniform Cartesian grid composed of 16^3 elements. Uniform polynomial degree simulations are carried out for $p = 3$, 5 and 7. The dynamically p-adaptive simulations are initialized using uniform $p_0 = 7$ and performed with $p_K \in [2, 7]$. As for the dipole configuration, quadrature formulae accurate for polynomials of degree $3p_K$ are used for the numerical integration.

The LLF flux and the BR2 scheme with $\eta_{BR2} = 4$ are used for the discretization of the convective and diffusive terms. Time integration is performed using the third-order four-step SSP Runge-Kutta scheme with time step $\Delta t = 10^{-3}$.

Two dynamically p-adaptive simulations are performed using $\eta_{ref} = 10^{-2}$ and 10^{-3} and $\eta_{coars} = 10^{-2}$. For both simulations, the SSED refinement indicator is estimated and the resolution is adapted with a frequency $\Delta t_{adapt} = 5 \cdot 10^{-3} = 5\Delta t$.

In contrast to the previous 2D test cases, all TGV simulations are performed in parallel using 128 cores. As dynamic load balancing is not available in the current implementation, high levels of load imbalance can be obtained over the course of the simulation thus increasing the overall computational time. For this reason, the relative contribution of the error estimation and resolution update to the total computational time is not analysed in detail for this configuration. Indeed, measured values would be strongly influenced by the obtained load imbalance. It is expected, however, that the same conclusions drawn from the previous test cases apply for other configurations.

Analysis of results

The evolution of the total kinetic energy and the total enstrophy for the uniform polynomial degree and the p-adaptive simulations are reported in Figs. 55 and 56. Regarding the former, it is well captured by all simulations with the exception of that using a uniform polynomial degree $p = 3$. For this simulation, large discrepancies also appear in the evolution of the total enstrophy starting from $t \approx 4$, during the

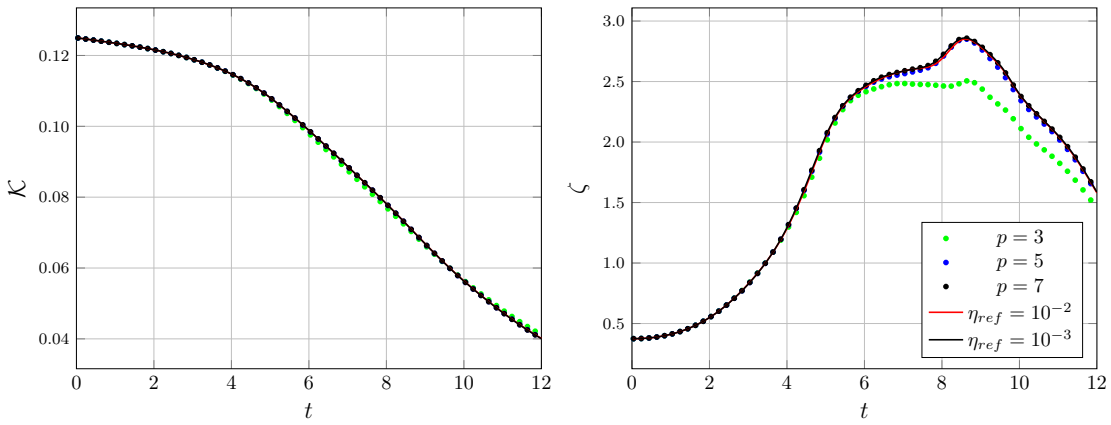

Figure 55 – TGV at Re = 500: Evolution of the total kinetic energy (left) and of the total enstrophy (right) for the uniform polynomial degree and the adaptive simulations.

laminar-to-turbulent transition. Conversely, the uniform polynomial degree simulation with $p = 5$ is almost identical to the best resolved simulation at $p = 7$ until $t \approx 6$, while slightly lower values of the total enstrophy are obtained at later times. This indicates that for $p = 3$ the resolution is not sufficient to capture the transition mechanism. This is not the case for $p = 5$ for which the discrepancies observed in the total enstrophy can be related to an insufficient resolution at the fine-scale level.

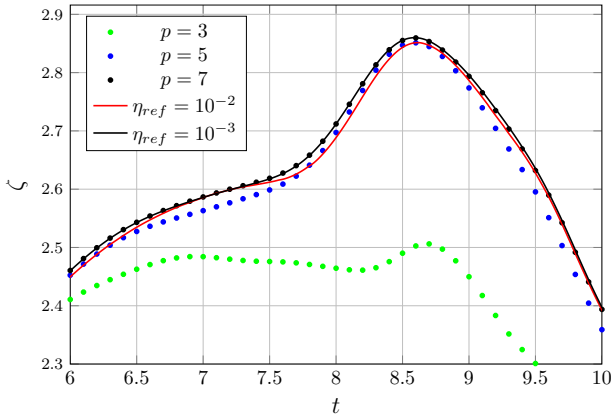

Figure 56 – TGV at Re = 500: Close up view of the evolution of the total enstrophy.

We observe from Figs. 55 and 56 that both dynamically p-adaptive simulations present a remarkable agreement with the reference simulation. The computational cost of these simulations is reported in Table 3 alongside the computational cost of the uniform polynomial degree simulations. We conclude that the dynamically p-adaptive simulation with $\eta_{ref} = 10^{-2}$ improves the accuracy of the results with

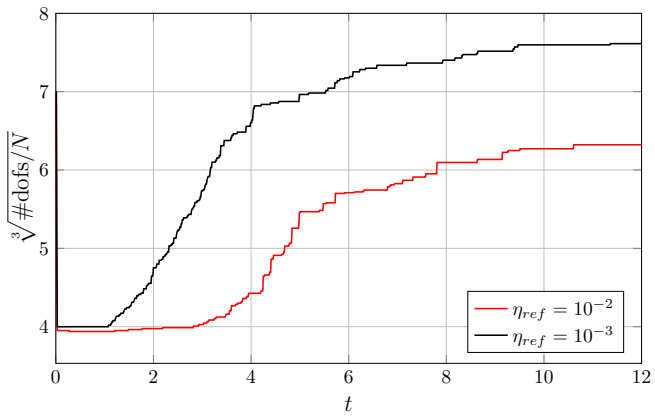

Figure 57 – TGV at Re = 500: Evolution of the total number of dofs for the dynamically p-adaptive simulations for two values of the refinement threshold.

respect to the uniform $p = 5$ simulation, with an increase of the computational cost of approximately 13%. Similarly, the adaptive simulation with $\eta_{ref} = 10^{-3}$ perfectly matches the reference computation at $p = 7$ while providing a reduction of the computational cost of about 33%. These results confirm that the proposed algorithm efficiently responds to the varying resolution requirements.

p	Work Units	η_{ref}	Work Units
3	143	10^{-2}	1343
5	1239	10^{-3}	3168
7	4758		

Table 3 – TGV at Re = 500: Computational cost of uniform polynomial degree and dynamically p-adaptive simulations.

This is further illustrated by Fig. 57 which reports the evolution of the total number of dofs for the dynamically p-adaptive simulations for the two different values of the refinement threshold. Indeed, the adaptive algorithm rapidly increases the spatial resolution during the transition phases leading to a rise in the total number of dofs as the flow becomes isotropic and a larger number of elements are refined.

Two snapshots of the distribution of the local polynomial degree are illustrated in Fig. 58 for the dynamically p-adaptive simulation with $\eta_{ref} = 10^{-3}$, corresponding to $t = 7$ and 12. We also show the vortex structures identified by the isosurfaces of the Q-criterion by Hunt et al [96], with $Q = \frac{1}{2}[\|\boldsymbol{\Omega}\|^2 - \|\boldsymbol{S}\|^2]$ and $\boldsymbol{\Omega} = \frac{1}{2}[\boldsymbol{\nabla}\mathbf{u} - (\boldsymbol{\nabla}\mathbf{u})^T]$. This figure highlights that, as expected, the adaptive algorithm provides the highest resolution in the regions where the vortex breakdown takes place. At $t = 7$, the maximum allowed polynomial degree has already been attained in these regions and

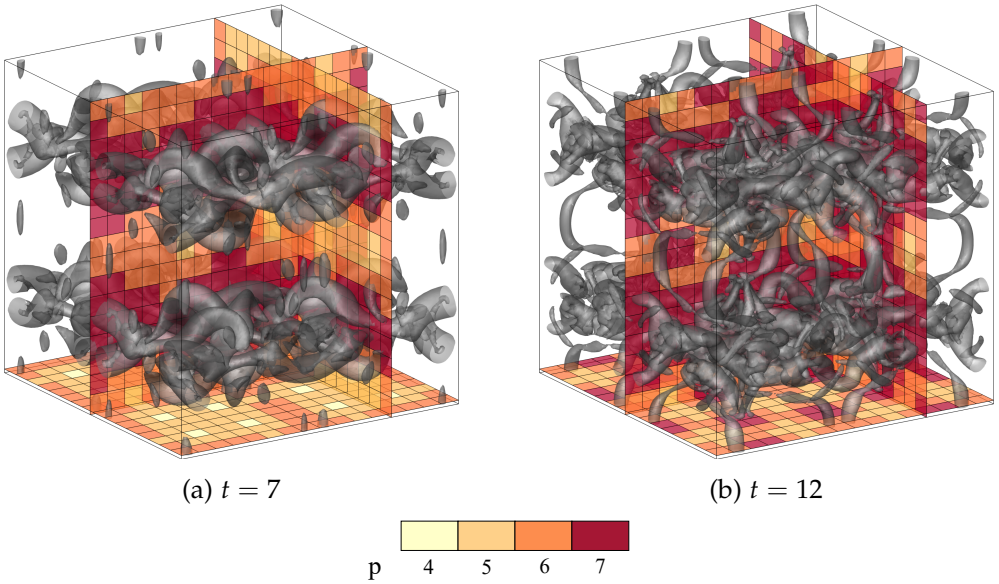

(a) $t = 7$ (b) $t = 12$

Figure 58 – TGV at Re = 500: Isosurfaces of the Q-criterion ($Q = 0.5$) and slices of the local polynomial degree distribution for the dynamically p-adaptive simulation with $\eta_{ref} = 10^{-3}$ at times $t = 7$ and 12.

the local p values vary from $p = p_{max} = 7$ to $p = 4$ away from them. As time advances, the flow becomes more homogeneous and a larger number of elements are refined.

The local polynomial degree distribution is therefore inhomogeneous over the course of most of the simulation. This leads to a significant load imbalance for the current computations. Consequently, if we take into account that dynamic load balancing is not employed, the performance of the dynamic algorithm measured for this configuration (see Table 3) represents a particularly promising result. A considerable further reduction of the computational could therefore be obtained by using an appropriate load balancing technique. This is further supported by the significant reduction of the required number of dofs shown in Fig. 57.

CHAPTER 9

STATIC P-ADAPTIVE SIMULATION OF UNSTEADY FLOWS

RÉSUMÉ DU CHAPITRE EN FRANÇAIS

L'objectif de ce chapitre est de présenter et d'analyser un algorithme statique p-adaptatif. L'adaptation statique peut fournir une réduction significative du coût de calcul des simulations pour des écoulements statistiquement stationnaires.

Afin de développer l'algorithme d'adaptation statique, il faut définir un estimateur d'erreur approprié qui fournit une estimation de la qualité nécessaire de résolution locale indépendante du temps. Dans cette perspective, nous présentons dans la Sec. 9.2 trois stratégies différentes pour étendre l'indicateur SSED à l'adaptation statique des problèmes instationnaires. La première approche consiste à appliquer l'indicateur SSED à la solution moyenne dans le temps (indicateur SSED-A). Les deuxième et troisième approches consistent en l'évaluation des normes temporelles L^2 et L^∞ de l'indicateur SSED calculé à partir de la solution instantanée, appelés indicateurs L^2-SSED et L^∞-SSED.

Ces stratégies sont comparées dans la Sec. 9.3 en effectuant des simulations statiquement p-adaptatives de l'écoulement périodique autour d'un cylindre à Re = 100. Il est montré que l'utilisation des indicateurs L^2-SSED et L^∞-SSED donne des résultats très similaires et une convergence plus rapide que l'indicateur SSED-A. Ils permettent de réduire de 60% le nombre de degrés de liberté requis pour atteindre la précision requise, par rapport aux simulations utilisant un degré polynomial uniforme.

Des simulations statiquement p-adaptatives de l'écoulement turbulent pour le cas classique du canal périodique avec bosse à Re = 2800 sont ensuite effectuées dans la Sec. 9.4. Les résultats obtenus indiquent que de longs temps d'intégration sont nécessaires pour obtenir la valeur convergée de l'indicateur SSED-A. Si des temps d'intégration courts sont considérés, l'indicateur SSED-A est influencé par les oscillations spatiales de la solution moyenne dues à un moyennage insuffisant des fluctuations turbulentes. Il est démontré que la meilleure performance est obtenue pour l'indicateur L^∞-SSED. Il identifie les régions de sous-résolution près de la paroi et dans le sillage turbulent.

Ensuite, l'algorithme statique d'adaptation-p est appliqué aux simulations LES de l'écoulement transitionnel autour d'une aile NACA0012 à Re = 50 000 et $\alpha = 5°$ dans

la Sec. 9.5. Pour cette configuration, deux stratégies d'estimation des erreurs sont utilisées: l'indicateur L^∞-SSED et la norme L^∞ de l'indicateur Small Scale Lifted (SSL) développé dans ce travail. Il est démontré que l'algorithme statiquement p-adaptatif développé peut être utilisé pour améliorer efficacement la précision des simulations LES des écoulements turbulents et transitionnels. De plus, le nouvel indicateur SSL proposé a donné de meilleurs résultats que l'indicateur SSED.

Enfin, malgré l'amélioration de la précision, des différences importantes avec les données DNS de référence sont toujours présentes et sont du même ordre de grandeur que l'influence du modèle LES sur la solution. Il est clair que la précision du modèle LES représente toujours un paramètre important pour les simulations LES adaptatif.

9.1 INTRODUCTION AND OUTLINE OF THE CHAPTER

As described in Sec. 4.6, static adaptation strategies can be employed for the simulation of unsteady problems. Compared to dynamic adaptation, in a static adaptation strategy the spatial resolution does not evolve dynamically and can be updated as an off-line phase. It presents therefore a simpler implementation and the computational overhead introduced by the adaptive process is often negligible. Additionally, as the resolution is fixed over the course of the simulation, complex dynamic load balancing techniques are not required.

The application of a static adaptation approach would provide only a limited computational gain for the simulation of transient flows, or for simulations with large variations of the resolution requirements over time. However, in many applications of practical interest we are only concerned with the analysis of statistical properties of flow configurations with limited variations of the spatial resolution requirements throughout the simulated time. Static adaptation strategies can therefore provide a large reduction of the computational cost for the simulation of statistically steady turbulent flows.

In this chapter, we present a static p-adaptive algorithm for the simulation of statistically steady turbulent flows. The first step in the development of this algorithm is the identification of a suitable refinement indicator. In Sec. 9.2 we therefore present three different approaches for extending the SSED indicator to static p-adaptive simulations of unsteady flows. The proposed strategies are at first assessed in Sec. 9.3 by performing adaptive simulations of the laminar periodic flow past a cylinder. The results obtained are then validated and extended by performing adaptive simulations of the turbulent flow over periodic hills in Sec. 9.4. Finally, in Sec. 9.5 the optimal strategy identified based on the previous analysis is applied to the LES of the transitional flow past a NACA0012 airfoil.

9.2 REFINEMENT INDICATORS FOR STATIC ADAPTATION OF UNSTEADY FLOWS

In the framework of static adaptation of unsteady flows, the refinement indicator must be able to identify in an optimal way the regions where the spatial resolution should be increased/reduced to improve the quality and efficiency of the simulation over the full integration time. This requires the definition of a time-independent refinement indicator from the time-dependent solution.

Additionally, for scale-resolving simulations the refinement indicator needs to present two fundamental properties: its evaluation should introduce a limited computational overhead and it should be computable at runtime, if it requires information from the instantaneous solution. This second requisite is due to the very high memory requirements of LES and DNS simulations and the high computational overhead introduced by frequent I/O operations.

Suitable refinement indicators can be derived by extending the error estimation strategies described in Sec. 4.4, as already shown in Sec. 5.6.

One possible approach consists in applying an error estimation strategy directly to the time-averaged solution [22]. This approach is motivated by the observation that in many engineering problems only the average solution or the statistical properties of the flow are of interest. Additionally, this strategy introduces an extremely limited overhead as the error estimator is computed only at the end of the simulation. However, by only analysing the average solution, no information is obtained regarding the evolution of the resolution requirements over time. Furthermore, a large contribution to the generation of the error in turbulent flow simulations is due to the potential inaccuracy of the LES model and the under-resolution of the fluctuating scales. Information regarding the resolution of the smallest turbulent scales is however lost when analysing the usually considerably smoother averaged quantities.

A second type of approach consists in deriving a refinement indicator from the error estimator evaluated from the instantaneous solution. This can be obtained as the average (L^1-norm) [185], the L^2-norm [183] or the L^∞-norm over time of the instantaneous error estimator. The evaluation of such refinement indicator can introduce an important computational overhead as the error estimate is updated over the course of the simulation. Nonetheless, this procedure allows us to take into account the variation over time of the resolution requirements. As an example, the L^1- and the L^2-norms of the error estimator identify regions where high values of the error are present/produced for most of the simulated time. The L^∞-norm can, on the other hand, identify regions where large errors are produced over short time intervals. Additionally, the use of the L^∞-norm of the error can be interpreted as identifying all the elements that would satisfy the refinement criterion applied to the instantaneous error measure at any moment of the simulation.

Due to the complexity and computational cost of LES and DNS simulations, only few works have been dedicated to the investigation and comparison of error estima-

tion strategies in this context, see *e. g.* [183, 185]. In the next sections we therefore analyse possible strategies for the application of the SSED indicator to the static p-adaptation of unsteady flows. As concluded in Chap. 5 and shown in Chap. 8, this error estimator is robust and has demonstrated accurate results whilst presenting an extremely limited computational overhead. Additionally, as discussed in Sec. 4.7, similar refinement indicators have already been successfully applied to h- and p-adaptation of turbulent flows, see *e. g.* [8, 183].

In this work, we consider the following three strategies:

- the SSED indicator is evaluated from the time-averaged solution $\langle \mathbf{u} \rangle$, indicated as η_A,
- the L^2-norm over time of the SSED indicator evaluated from the instantaneous solution, indicated as η_2,
- the L^∞-norm over time of the SSED indicator evaluated from the instantaneous solution, indicated as η_∞.

For clarity, we provide below the mathematical definition of these refinement indicators

$$\eta_A := \left(\frac{\left\| \langle \rho \mathbf{v} \rangle_{h,p} - \langle \rho \mathbf{v} \rangle_{h,p-1} \right\|^2_{L^2(K)}}{|K|} \right)^{\frac{1}{2}}, \tag{122}$$

$$\eta_2 := \left(\frac{\int_0^T \left\| \rho \mathbf{v}(t)_{h,p} - \rho \mathbf{v}(t)_{h,p-1} \right\|^2_{L^2(K)} \mathrm{d}t}{T|K|} \right)^{\frac{1}{2}}$$

$$= \left(\frac{\left\| \rho \mathbf{v}_{h,p} - \rho \mathbf{v}_{h,p-1} \right\|^2_{L^2(K,[0,T])}}{T|K|} \right)^{\frac{1}{2}}, \tag{123}$$

$$\eta_\infty := \max_{t \in [0,T]} \left(\frac{\left\| \rho \mathbf{v}_{h,p} - \rho \mathbf{v}_{h,p-1} \right\|^2_{L^2(K)}}{|K|} \right)^{\frac{1}{2}}, \tag{124}$$

where $[0, T]$ is the time interval over which the indicators are computed. To simplify the notation, these are referred to as the SSED-A, L^2-SSED and L^∞-SSED indicators in the following text.

9.3 PERIODIC FLOW PAST A CYLINDER AT RE = 100

The three refinement indicators Eqs. (122) to (124) described in the previous section are now compared by performing p-adaptive simulations of the periodic laminar flow past a cylinder at Re = 100 and M = 0.1. This configuration has already been

described in Sec. 5.6. The same mesh and numerical discretization are employed for the simulations presented in this section.

The employed adaptive algorithm is similar to that described in Sec. 5.6. A first simulation using a uniform polynomial degree $p = 2$ is carried out until the periodic state is achieved. The simulation is then continued for at least 10 shedding cycles in order to evaluate the time-averaged drag coefficient $\overline{C_d}$, the Strouhal number St and the root mean square of the lift coefficient C_l'. Over the course of this phase, the solution is averaged in time in each element. Additionally, the SSED indicator is evaluated from the instantaneous solution with a period equal to $10\Delta t$ and is used to update the value of η_2 and η_∞ in each element. The value of η_A is evaluated from the time-averaged solution at the end of the simulation, *i. e.* after the tenth cycle has been completed.

Once the error estimation step has been completed, the adaptive algorithm marks an element for refinement if the local value of the considered refinement indicator η_K is above the threshold η_{ref} defined as the volume weighted average of η_K, that is

$$\eta_{ref} = \frac{\sum_{K \in \Omega_h} \eta_K |K|}{\sum_{K \in \Omega_h} |K|} \quad . \tag{125}$$

and the local polynomial degree is increased by one in marked elements. The solution is then projected on the updated discretization space and advanced in time for at least 40 additional shedding cycles until the periodic state is achieved again. The process is then repeated for a total of five adaptation steps.

In the simulations performed in this section, the maximum polynomial degree is set to $p_{max} = 6$. In practice, the definition of the refinement threshold is also modified so that the volume weighted average is computed only considering elements with $p_K \leq 5$, *i. e.* only those elements which can be further refined.

Analysis of the results

In Fig. 59 we report the convergence history of the time-averaged drag coefficient, the Strouhal number and the root mean square of the lift coefficient for the p-adaptive and the uniformly p-refined simulations. As seen from these plots, all the adaptive simulations lead to a significant reduction of the number of dofs required to achieve the same accuracy as the uniform polynomial degree simulation using $p = 6$. In particular, the L^2-SSED and L^∞-SSED indicators lead to a reduction of about 60% of the total number of dofs. The differences in the convergence history obtained for these two refinement indicators are negligible. More marked differences can be identified when comparing to the results obtained using the SSED-A indicator. In this case the adaptive algorithm requires one additional refinement step to achieve the same accuracy as for the two other indicators. This leads to a reduction of

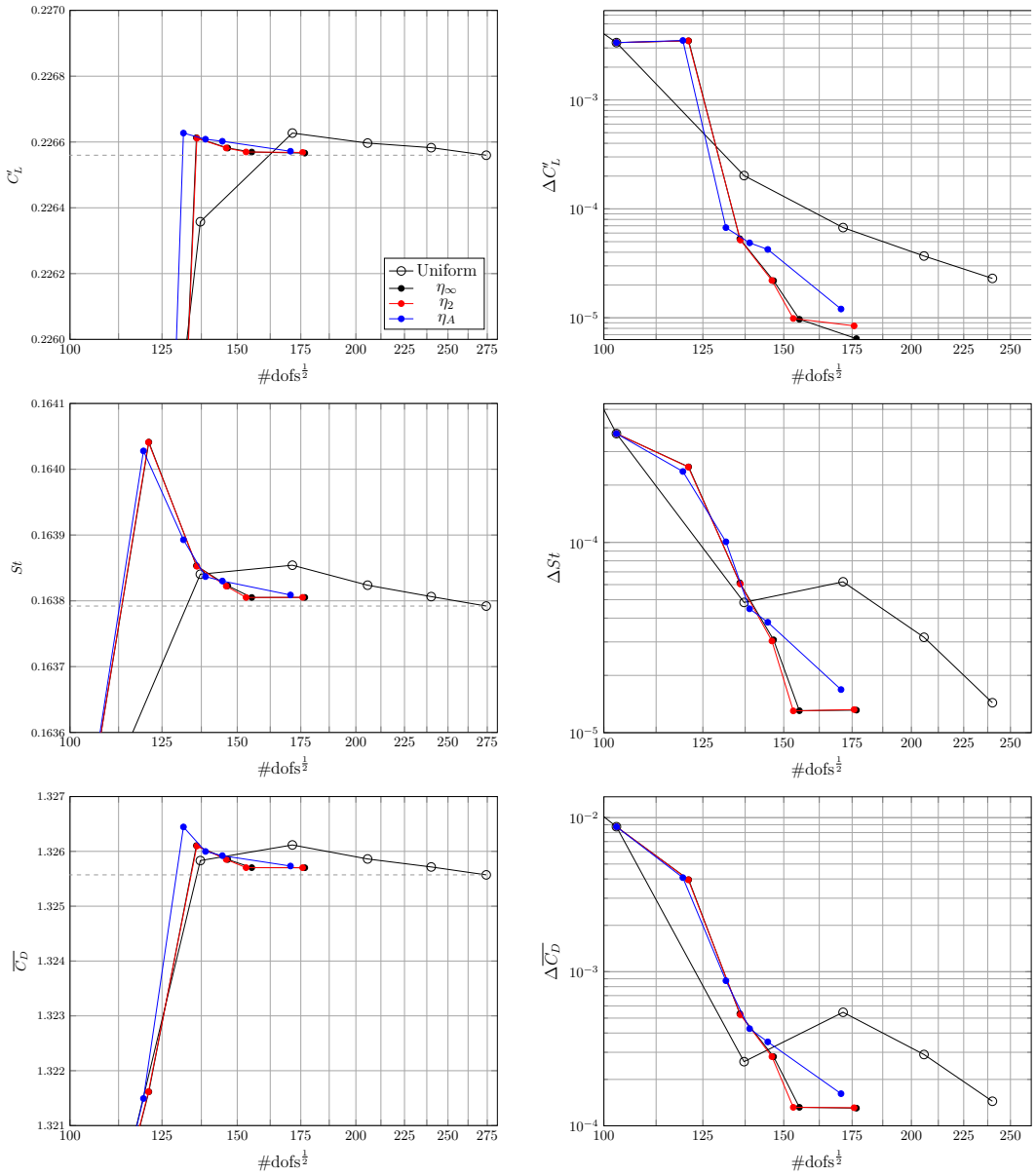

Figure 59 – Laminar flow past a cylinder at Re = 100 and M = 0.1: Convergence history of the time-averaged drag coefficient, the Strouhal number and the root mean square of lift coefficient for the p-adaptive and uniformly p-refined simulations.

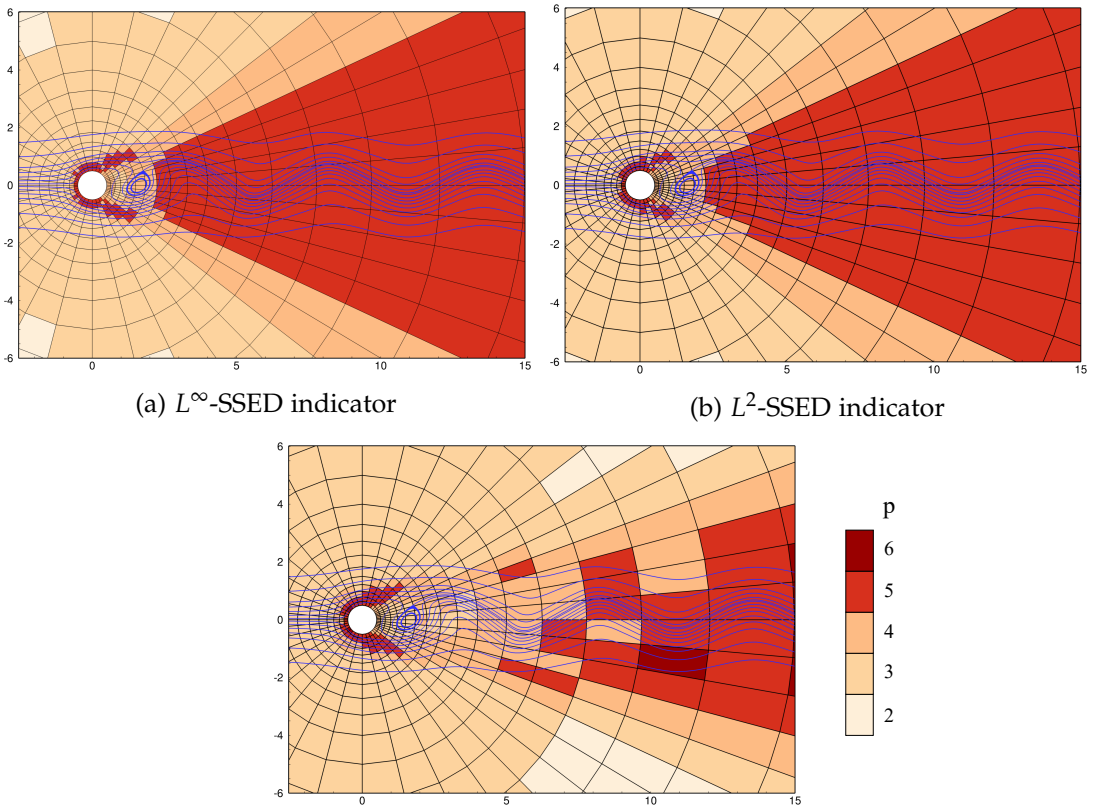

(a) L^∞-SSED indicator

(b) L^2-SSED indicator

(c) SSED-A indicator

Figure 60 – Laminar flow past a cylinder at Re = 100 and M = 0.1: Distribution of local polynomial degree obtained based on different refinement indicators, close-up view and streamlines.

approximately 50% of the number of dofs with respect to the reference simulation at uniform $p = 6$.

In Figs. 60 and 61 we report the distribution of the local polynomial degree obtained from the adaptive algorithm based on the three different strategies for a number of dofs $\approx 143^2$. These correspond to the third step of the adaptive algorithm employing L^∞-SSED and L^2-SSED indicators, and the fourth step employing the SSED-A indicator. In Fig. 60 we also represent the streamlines computed from a snapshot of the solution.

Analysing Figs. 60a and 60b and Figs. 61a and 61b, we observe that almost identical distributions of the local polynomial degree are produced by the L^∞-SSED and L^2-SSED indicators. Both refinement indicators identify for refinement a circular region around the cylinder, with the highest values of the polynomial degree being located near the cylinder, from the stagnation point up to the region where flow

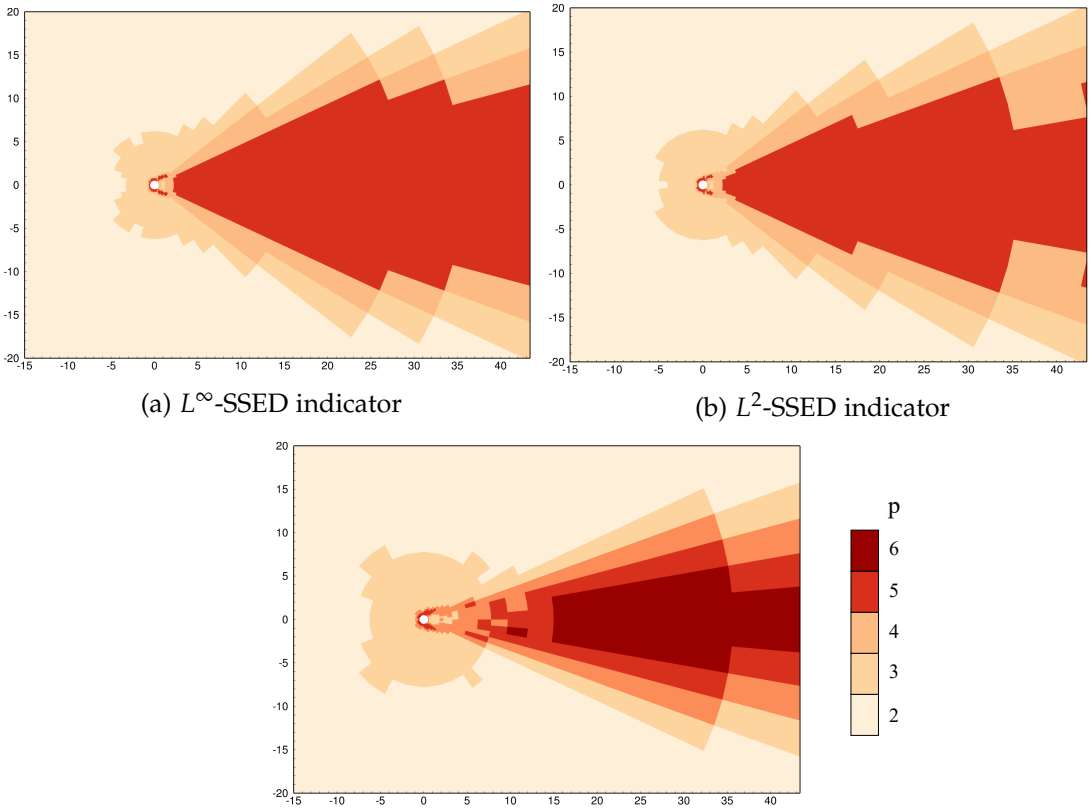

(a) L^∞-SSED indicator

(b) L^2-SSED indicator

(c) SSED-A indicator

Figure 61 – Laminar flow past a cylinder at Re = 100 and M = 0.1: Distribution of local polynomial degree obtained based on different refinement indicators.

separation takes place. Additionally, high refinement is introduced in the near wake starting from $x \approx 2D$ due to the increase of the local mesh size.

The results obtained using the SSED-A indicator present more marked differences. First, we observe that, in contrast to the results obtained for the two other indicators, the distribution of local polynomial degree is not symmetric. This is due to asymmetries in the average solution caused by the insufficiently long integration time employed. This is an undesirable effect as it engenders the loss of the symmetry of the original configuration.

Comparing Figs. 61a and 61b with Fig. 61c, we notice that a similar distribution of local polynomial degree is obtained in the region upstream of the cylinder. This is somewhat expected as the flow is essentially steady in this region.

Conversely, a markedly different distribution is obtained in the downstream region. When employing the SSED-A indicator the local polynomial degree takes values $p_K \geq 5$ only after $x \approx 7D$ in the wake region. Indeed, the resolution in the region close to the cylinder base appears sufficient to capture the average flow in this area.

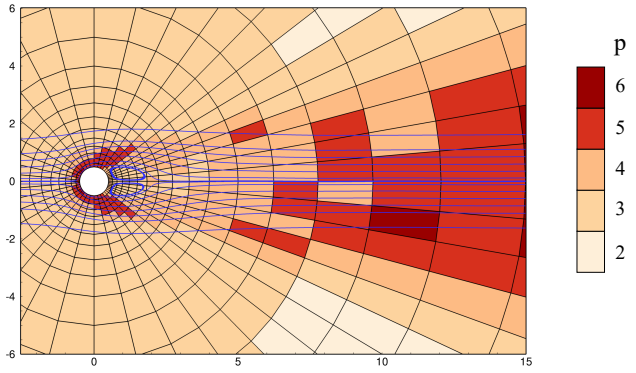

Figure 62 – Laminar flow past a cylinder at Re = 100 and M = 0.1: Distribution of local polynomial degree obtained based on the SSED-A indicator. Close-up view and streamlines of the average flow.

This can also be observed from Fig. 62 where we represent the streamlines computed from the average flow superimposed on the local polynomial degree map. As a consequence, for the same number of dofs, this refinement indicator leads to higher values of the polynomial degree in the far wake rather than in the near wake, due to the relatively larger mesh size.

These results suggest that better results are provided by evaluating the refinement indicator from the instantaneous solution, *i. e.* using the L^2-SSED or the L^∞-SSED indicators, rather than from the average solution. Additionally, we recall that one of the fundamental advantages of the latter approach is the lower computational overhead as the refinement indicator is computed only at the end of the simulation. Nonetheless, we have shown in Chap. 8 that the evaluation of the SSED indicator requires an extremely limited overhead. The reduction of the total computational time is therefore negligible and not sufficient to justify the use of the SSED-A indicator.

9.4 TURBULENT FLOW OVER PERIODIC HILLS

The conclusions drawn from the previous section are now assessed by performing static p-adaptive simulations of the turbulent flow over periodic hills. This test case was initially proposed in an ERCOFTAC/IAHR workshop in 1995 [163] and was then employed in the ERCOFTAC/IAHR/COST *Workshops on Refined Turbulence Modeling*. In the present work we consider the configuration proposed by Mellen *et al.* [132].

A detailed description of the geometry and of the flow can be found on the ERCOFTAC QNET-CFD website [61]. The geometry of the domain is presented in Fig. 63 and its dimensions are as follows: the total height of the channel is $L_y = 3.035h$, the streamwise length is $L_x = 9h$ and the spanwise dimension is $L_z = 4.5$, where h is the height of the hill and is considered as the reference length.

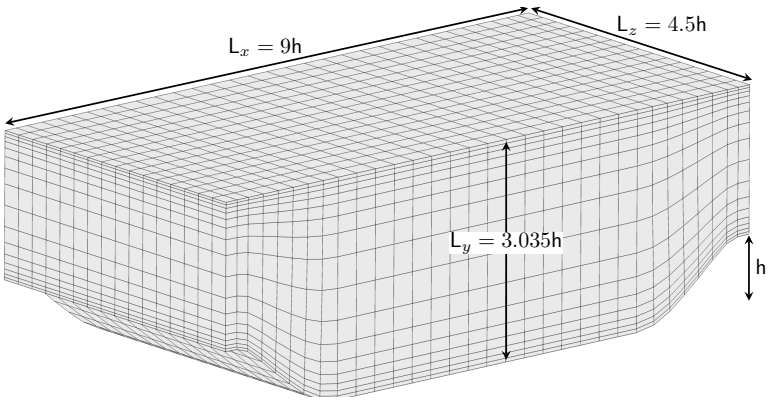

Figure 63 – DNS of the turbulent flow over periodic hills at Re = 2800: Geometrical configuration and employed mesh.

The configuration is assumed periodic in both the spanwise and streamwise directions and isothermal no-slip boundary conditions are imposed at the upper and lower walls. The choice of periodic boundary conditions in the spanwise direction reduces the computational cost as compared to configurations including the sidewalls. The periodic boundary condition in the streamwise direction removes possible issues related to the implementation of inlet and outflow conditions and the unknown level of turbulence at the inflow.

The flow is driven by a pressure gradient $\frac{\mathrm{d}p}{\mathrm{d}x}$ which is enforced by introducing a source term in both the x-momentum and energy equations. The pressure gradient is computed in order to achieve a target mass flow-rate at the crest of the hill $\dot{m}_0$. For this purpose, at each time step we evaluate

$$\left(\frac{\mathrm{d}p}{\mathrm{d}x}\right)^{n+1} = \left(\frac{\mathrm{d}p}{\mathrm{d}x}\right)^{n} - \frac{1}{L_z(L_y-1)}(\dot{m}_0 - 2\dot{m}^n + \dot{m}^{n-1}) \ . \tag{126}$$

In this work we consider the flow at $\mathrm{Re}_b = 2\,800$, where Re_b is the Reynolds number based on the bulk velocity u_b and the hill height h, namely

$$u_b = \frac{1}{L_z(L_y-1)} \int_0^{L_z} \int_h^{L_y} u(0,y,z)\mathrm{d}y\mathrm{d}z \quad , \quad \mathrm{Re}_b = \frac{u_b h}{\nu} \ . \tag{127}$$

Additionally, near-incompressible conditions are employed by imposing the Mach number based on the bulk velocity and the temperature at the wall as equal to $\mathrm{M}_b = 0.1$.

For this Reynolds number, the flow separates at the curved wall, reattaches leading to the formation of a recirculation bubble, and accelerates again before reaching the crest of the next hill (recovery region). It represents therefore a relatively challenging configuration on a simple geometry as both the turbulent shear layer and the recirculation bubble must be correctly represented. As seen in Fig. 64 representing the

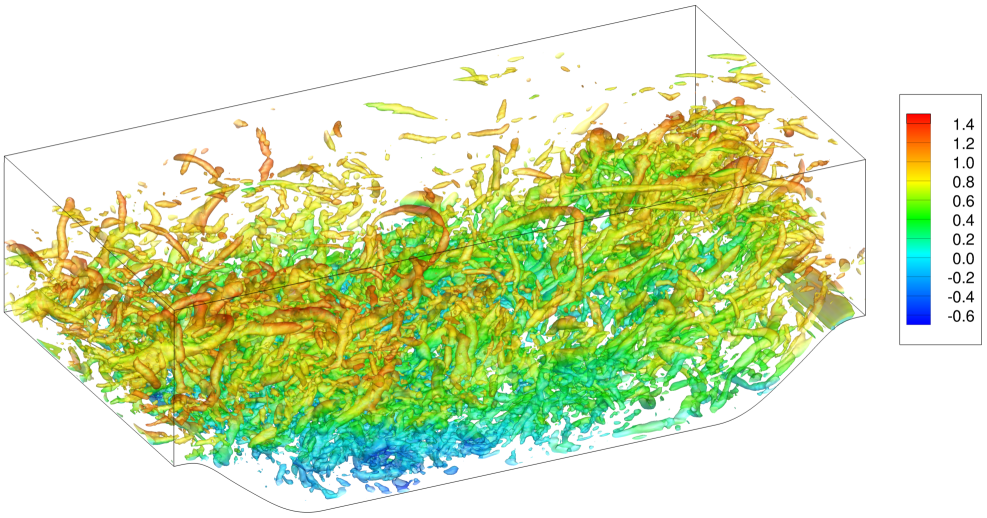

Figure 64 – DNS of the turbulent flow over periodic hills at Re = 2800: Isosurface of the Q-criterion ($Q = 5$) coloured by the streamwise velocity.

vortex structures identified by the Q-criterion, the flow is fully turbulent. However, for this low value of the Reynolds number, it presents a relatively low computational cost and it is possible to perform DNS simulations [205]. Additionally, high accuracy DNS simulations are available in the literature.

The static p-adaptive algorithm is therefore analysed by comparing the results obtained with a reference computation obtained by means of the incompressible second-order FV code LESOCC on a very fine mesh [32].

For the employed value of the Mach number, the compressibility effects can be considered negligible, thus allowing for the comparison with results from an incompressible solver. This is confirmed by the close agreement between the incompressible calculations of Breuer using the LESOCC solver [32] and the compressible simulations at $M_b = 0.2$ by Balakumar and Park [10].

Computational details

In order to assess the performance of the static p-adaptive algorithm, several p-adaptive simulations are performed and compared to a series of uniformly p-refined simulations by de la Llave *et al.* [205].

All computations are performed on a 4^{th}-order grid, generated using the high-order mesh generator *Gmsh* [79], composed of $32 \times 16 \times 16$ hexahedra corresponding to a total of 8192 elements. This grid is shown in Fig. 63.

The uniform polynomial degree simulations by de la Llave *et al.* [205] correspond to $p = 3$, 4 and 5. The adaptive simulations here performed present a variable local

polynomial degree p_K between 3 and 5. The number of quadrature points per space direction is set equal to $q = p + 2$ for $p = 3$ and 4 and equal to $q = p + 3$ for $p = 5$. These values correspond to those employed in [205]. The LLF flux and SIP scheme are employed for the discretization of the convective and viscous terms respectively.

Time integration is performed using the third-order four-stage SSP Runge-Kutta scheme. The time step is limited by the convective time scale of the acoustic waves due to the low value of the Mach number $M_b = 0.1$. The time step Δt is therefore of the order of $10^{-4} h/u_b$. Each simulation is advanced in time until a statistically steady state is reached. From this point, the flow statistics are gathered over a time $T_{avg} > 60 t_c$, where $t_c = \frac{L_x}{u_b}$ is the convective time. A smaller integration time equal to $T_{avg} = 30 t_c$ is employed for the uniform $p = 5$ simulation. The flow statistics are also averaged in the homogeneous spanwise direction to achieve more rapidly statistical convergence.

The adaptive algorithm is initialized by considering the solution corresponding to $p = 3$ as baseline and proceeds as described in Sec. 9.3. When employing the L^2-SSED and L^∞-SSED indicators, the value of η_2 and η_∞ are updated by evaluating the SSED indicator from the instantaneous solution every 100 time steps. In order to obtain more rapidly the statistically converged values of the refinement indicators, for η_∞ we consider the maximum of the refinement indicator over the elements aligned in the spanwise direction. Similarly, for η_2 the value in each element is obtained as root mean square in the spanwise direction. Finally the value of η_A is simply averaged in the spanwise direction. We note that a more consistent approach would have consisted in evaluating the SSED indicator after averaging the time-averaged solution in the spanwise direction.

By exploiting the homogeneity of the flow, the resulting refinement indicator and, as a consequence, the adapted distribution of local polynomial degree is also homogeneous in the spanwise direction.

Analysis of the results

In Fig. 65, we report the distribution of the refinement indicators computed from the baseline computation using uniform polynomial degree $p = 3$. As observed for the previous configuration, the L^2-SSED and L^∞-SSED indicators present a very similar distribution. Indeed, higher values of both error indicators are obtained near the separation point in the turbulent detached flow. Relatively high values are also obtained near the upper wall in the turbulent boundary layer region. We observe, nonetheless, that the L^∞-SSED indicator presents a more irregular distribution and relatively high values also near the wall at the top of the hill.

Conversely, the SSED-A indicator presents a markedly different distribution. Relatively high values of this indicator are obtained only near the lower wall and the separation point. In contrast with the two other indicators, negligible values are also

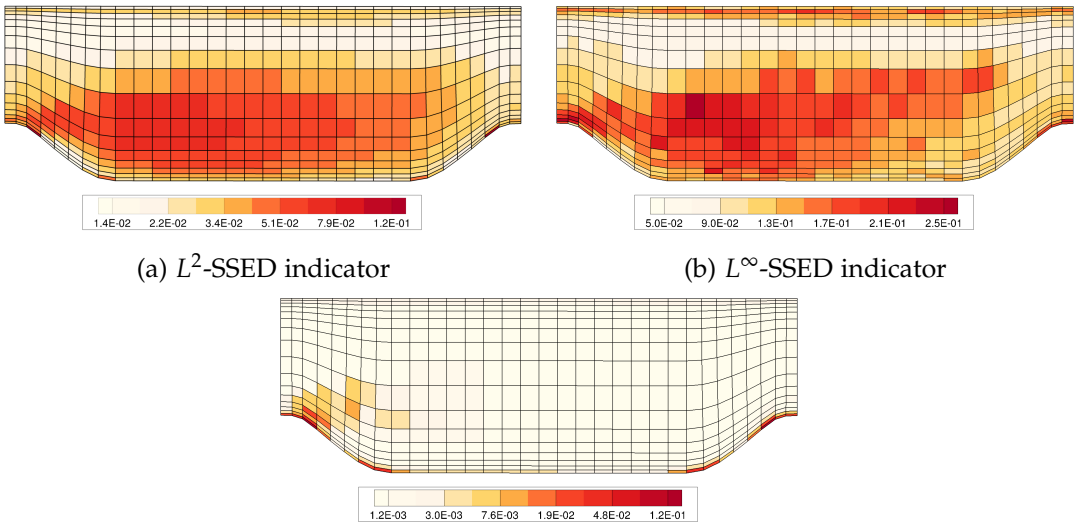

(a) L^2-SSED indicator (b) L^∞-SSED indicator

(c) SSED-A indicator

Figure 65 – DNS of the turbulent flow over periodic hills at Re = 2800: Distribution of the refinement indicators computed from the baseline simulation with uniform polynomial degree $p = 3$.

obtained in most of the turbulent region, in the middle of the domain. Therefore, as expected, this refinement indicator presents high values only in regions which are relevant to the mean flow and is unable to detect the presence of under-resolved turbulent scales.

We recall that the result presented in Fig. 65 correspond to the distribution of the refinement indicators computed over an integration time $T_{avg} = 60t_c$. This value is prohibitively high and in practical simulations an accurate value of the refinement indicator should be obtained over relatively short simulation times. We are therefore interested in analysing the influence of this parameter T_{avg} on the considered refinement indicators. For this purpose, we report in Fig. 66 the distribution of the refinement indicators obtained for three different values of the integration time $T_{avg} = 2t_c$, $10t_c$ and $18t_c$, without exploiting the homogeneity of the flow in the spanwise direction. We observe from Figs. 66a and 66b that the L^2-SSED and the L^∞-SSED indicators rapidly converge to the asymptotic value and even after a relatively short integration time the distribution of the refinement indicator does not change considerably.

Conversely, the distribution of the SSED-A indicator presents a stronger dependency on the value of T_{avg}. As observed in Fig. 66c, relatively high values of the error estimator are obtained in the middle region of the domain for $T_{avg} = 2t_c$. As the value of T_{avg} is increased, the refinement indicator progressively decreases in this region, whereas it remains almost unvaried near the wall. Indeed, for relatively low

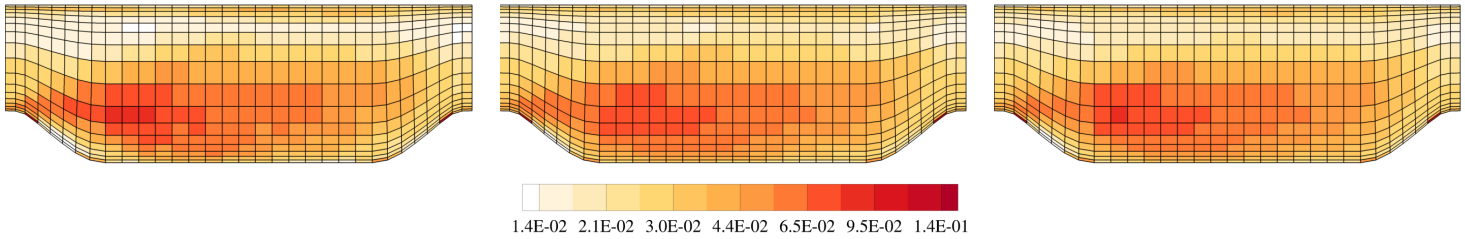

(a) L^2-SSED indicator

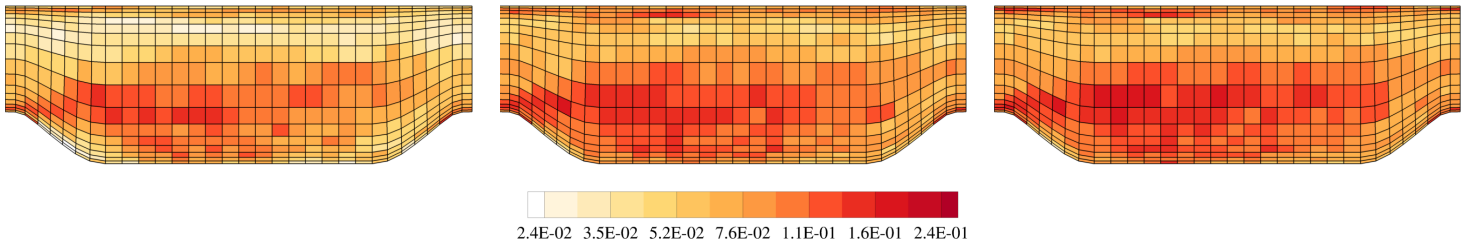

(b) L^∞-SSED indicator

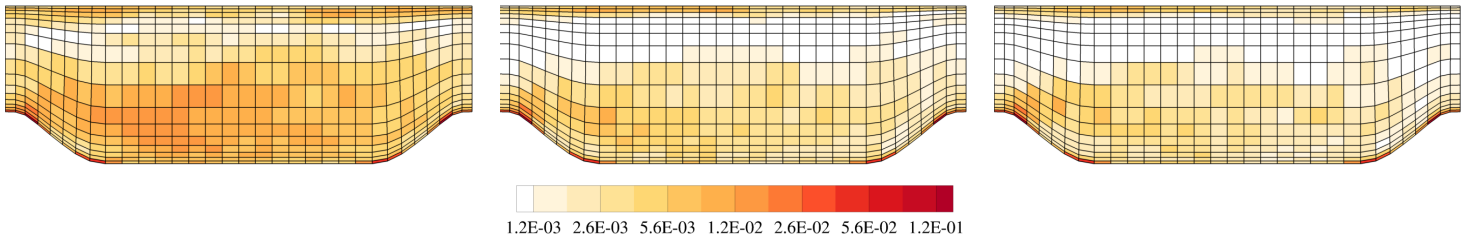

(c) SSED-A indicator

Figure 66 – DNS of the turbulent flow over periodic hills at Re = 2800: Distribution of the three considered refinement indicators for three different values of the averaging time: from left to right $T_{avg} = 2t_c$, $10t_c$ and $18t_c$.

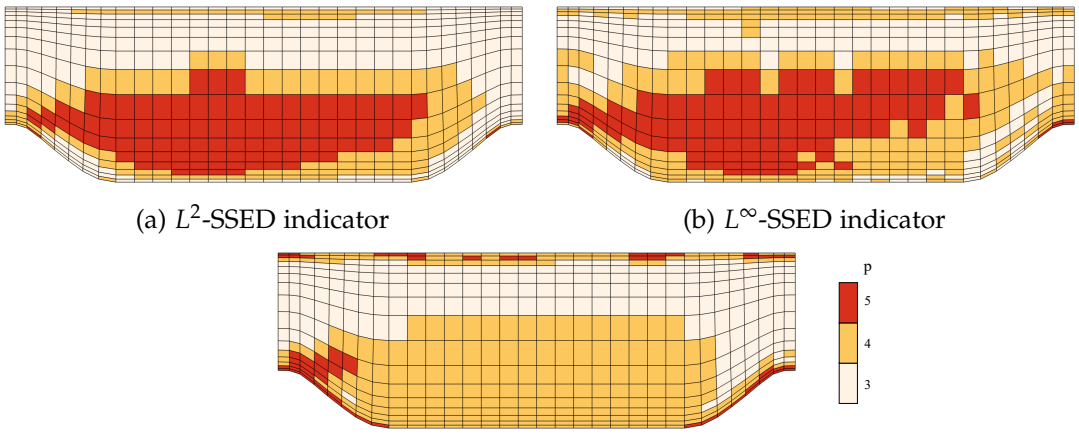

(a) L^2-SSED indicator (b) L^∞-SSED indicator

(c) SSED-A indicator

Figure 67 – DNS of the turbulent flow over periodic hills at Re = 2800: Distribution of the local polynomial degree generated by the adaptive algorithm.

values of the integration time, the computed mean flow is not converged and still presents oscillations due to the insufficient averaging of the turbulent fluctuations. As T_{avg} is increased, the intensity of these fluctuations is reduced and the computed average solution converges to the real time-averaged field. This effect is further evident by comparing these results with those shown in Fig. 65c, obtained for a much longer $T_{avg} = 60t_c$. For this reason, the SSED-A indicator identifies for refinement the under-resolved turbulent regions only if the integration time is sufficiently small. Thus, this conclusion suggests that the relative importance assigned by this indicator to under-resolution in the mean flow and in the instantaneous turbulent scales is dependent on the specific value of T_{avg}.

In practical simulations this situation is likely to be encountered as long time averages can only be computed on the final p-adapted grid at the end of the adaptive process. These conclusions are also in line with those obtained for the previous configuration from Fig. 62, for which the insufficient integration time led to asymmetries in the adapted polynomial degree.

We now report in Fig. 67 the distribution of the local polynomial degree obtained after two steps of adaptive refinement. These are very similar to the previously described distributions of the refinement indicators computed from the baseline solution and shown in Fig. 65. Indeed, in agreement with the results shown in Fig. 65, the L^2-SSED and the L^∞-SSED indicators lead to higher polynomial degree values in the under-resolved turbulent region and near the acceleration region at the top of the hill. As regards the SSED-A indicator, it selects for refinement the elements near the wall and the separation point, in accordance with the previous results. However, for this indicator, additional refinement is also introduced in the middle

	ref. DNS [32]	$p=3$	$p=4$	$p=5$	η_2	η_∞	η_A
#Mdofs	13.6	0.52	1.02	1.77	0.87	0.98	0.92
CPU time (hCPU)	-	8.07	89.2	319	90.4	108	85.5

Table 4 – DNS of the turbulent flow over periodic hills at Re = 2800: Computational cost of simulations expressed in terms of number of dofs and computational time required to simulate a time interval h/u_b measured on 280 Intel Xeon Broadwell E5-2690v4 cores. Note: the uniform polynomial degree simulation with p = 3 presents a value of Δt that is 2.5 times that of all the other simulations.

region during the second adaptation step. Nonetheless, as already discussed, the presence of high error indicator values in this region is due to oscillations in the average field caused by insufficient time-averaging of the turbulent fluctuations and only partially to under-resolution of the mean flow.

The computational cost of each of the adapted simulations is presented in Table 4 in terms of computational time and total number of dofs. These values are compared to those corresponding to the uniform polynomial degree simulations, as well as to the number of dofs of the reference DNS of Breuer *et al.* [32]. From this table we observe that, at the end of the adaptive algorithm, the resulting discretizations present a number of dofs and computational cost similar to that of the uniform polynomial degree computation using $p = 4$. Therefore, the adapted simulations must provide an increased accuracy with respect to this computation in order to consider the proposed adaptive algorithm a viable strategy for the reduction of the computational cost of turbulent flow simulations.

The quality of the adaptive simulations is assessed by analysing the statistics of the flow at several locations. For this purpose, we present in Figs. 68 to 71 the mean velocity profiles and the velocity fluctuations for the adaptive simulations and compare them with the refence DNS data. In each figure we also report the same comparison for the uniformly refined simulations by de la Llave *et al.* [205]. This facilitates the analysis of the adaptive results.

Overall, the results for all three estimators present a remarkable agreement with the reference DNS. In Fig. 68 only minor differences can be observed between the different simulations in the mean velocity $\langle u \rangle / u_b$. For the uniform polynomial degree simulations using $p = 3$ and $p = 4$, we can observe the effects of under-resolution at the location x = 0.5, corresponding to the appearance of strong numerical oscillations. These numerical oscillations disappear when employing a uniform polynomial degree p = 5 or the adaptive approach, which lead to mean streamwise velocity profiles in good agreement with the reference DNS.

Similar considerations are valid for the mean vertical velocity profile $\langle v \rangle / u_b$ shown in Fig. 69. Analogous numerical oscillations are present at x = 0.5, for the uniform polynomial degree simulations using $p = 3$ and $p = 4$. The adaptive algorithm

significantly reduces the intensity of these numerical oscillations similarly to the uniform $p = 5$ simulation. As regards the profiles at other locations, we observe that, among the considered indicators, the L^2-SSED indicator presents somewhat higher discrepancies with the reference DNS, visible in particular at $x = 2.0$.

In Figs. 70 and 71 we report the profiles of the velocity fluctuations $\langle u'u' \rangle / u_b^2$ and $\langle u'v' \rangle / u_b^2$. The under-resolution in the turbulent wake leads to the presence of spikes in these profiles, especially visible in Fig. 70 for the uniform $p = 3$ and 4 simulations. The adaptive simulations largely improve the results. In particular, the L^∞-SSED indicator provides the largest reduction of the intensity of the spikes and a slightly better agreement with the reference data, as compared to the two other indicators. A similar reduction of the intensity of the spikes is obtained using the L^2-SSED indicator. Nonetheless, this indicator presents some discrepancies with the reference DNS, especially from $x = 3$ to $x = 6$. Finally, the profiles in Fig. 70 corresponding to the use of the SSED-A indicator presents spikes which have similar intensity to those of the uniform polynomial degree simulation with $p = 4$. This is an indication of further under-resolution for this indicator.

The results presented in this section therefore demonstrate the ability of the adaptive strategy to improve the quality of under-resolved turbulent flow simulations. Indeed, for a similar computational cost, the adaptive simulations provide a better agreement with the reference DNS than the uniform polynomial degree simulation using $p = 4$. Among the considered refinement indicators, the L^∞-SSED indicator has provided the best results. The L^2-SSED indicator has shown somewhat worse results, possibly due to the lower refinement introduced near the top of the hill as compared to the two other indicators. Finally, the SSED indicator computed from the average solution has improved the quality of the simulations by refining the separation region. Nonetheless, it does not appear to detect the under-resolution present in the turbulent wake. The outcome of this study, thus suggests the L^∞-SSED indicator as the optimal refinement indicator allowing us to identify under-resolved regions both near the wall and in the fully turbulent wake.

9.5 LES OF THE TRANSITIONAL FLOW PAST A NACA0012 AIRFOIL

In this section, the developed static p-adaptive algorithm is applied to the LES of the transitional flow past a NACA0012 airfoil. The configuration considered is representative of the flow past airfoils at low-to-moderate Reynolds numbers, which is of great interest for many unmanned and microaerial vehicles. At relatively low angles of attack the flow is characterized by a laminar separation due to the adverse pressure gradient. A complex transition mechanism can lead to laminar-to-turbulent transition with subsequent reattachment of the flow and the formation of a recirculation bubble, also referred to as laminar separation bubble (LSB).

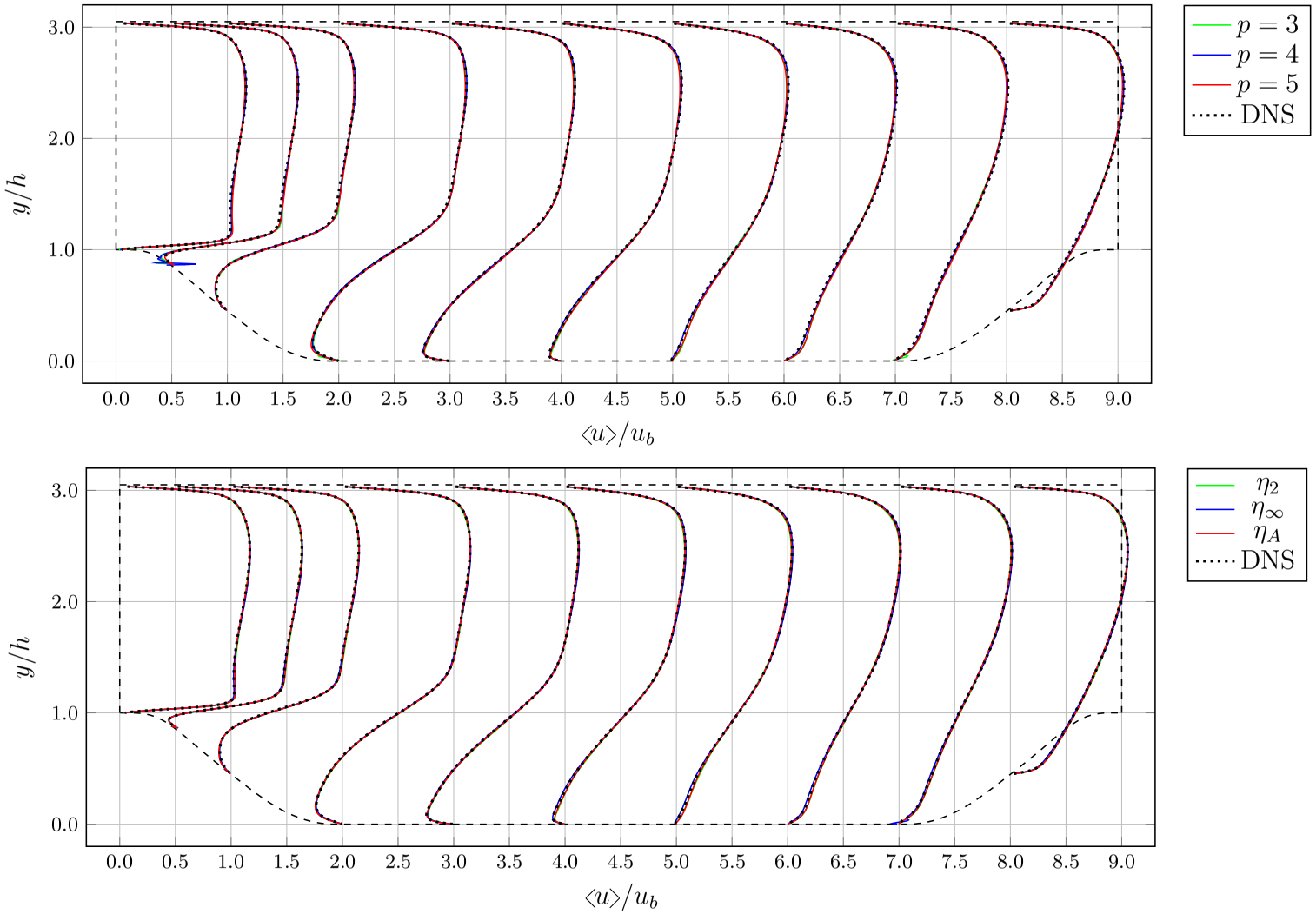

Figure 68 – DNS of the turbulent flow over periodic hills at Re = 2800: Averaged velocity $\langle u \rangle / u_b$ at various locations obtained with uniform polynomial degree and adaptive simulations compared to the reference DNS [32].

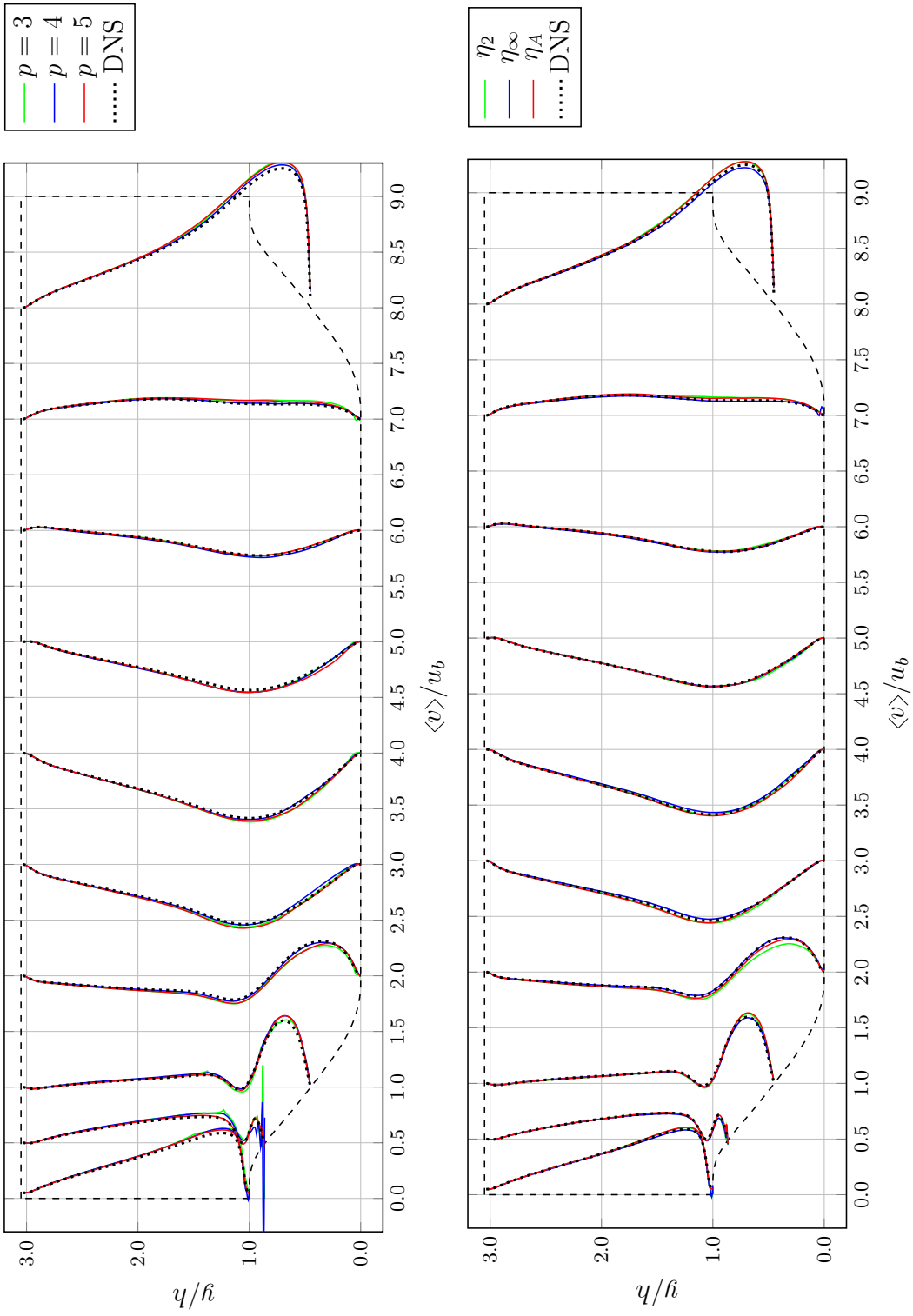

Figure 69 – DNS of the turbulent flow over periodic hills at Re = 2800: Averaged velocity $\langle v \rangle / u_b$ at various locations obtained with uniform polynomial degree and adaptive simulations compared to the reference DNS [32]. Values are shifted and scaled by a factor of 5.

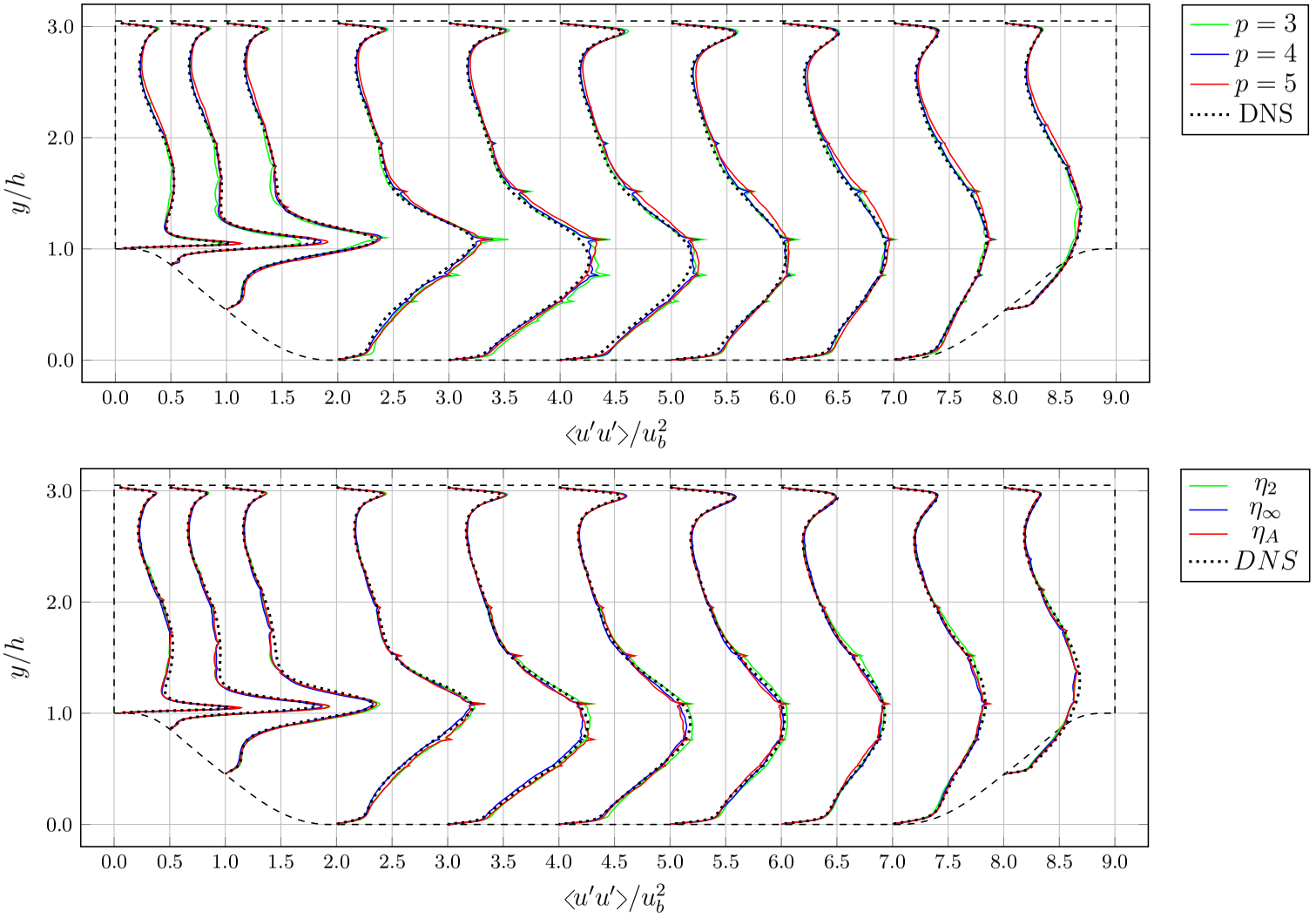

Figure 70 – DNS of the turbulent flow over periodic hills at Re = 2800: Averaged velocity fluctuations $\langle u'u' \rangle / u_b$ at various locations obtained with uniform polynomial degree and adaptive simulations compared to the reference DNS [32]. Values are shifted and scaled by a factor of 10.

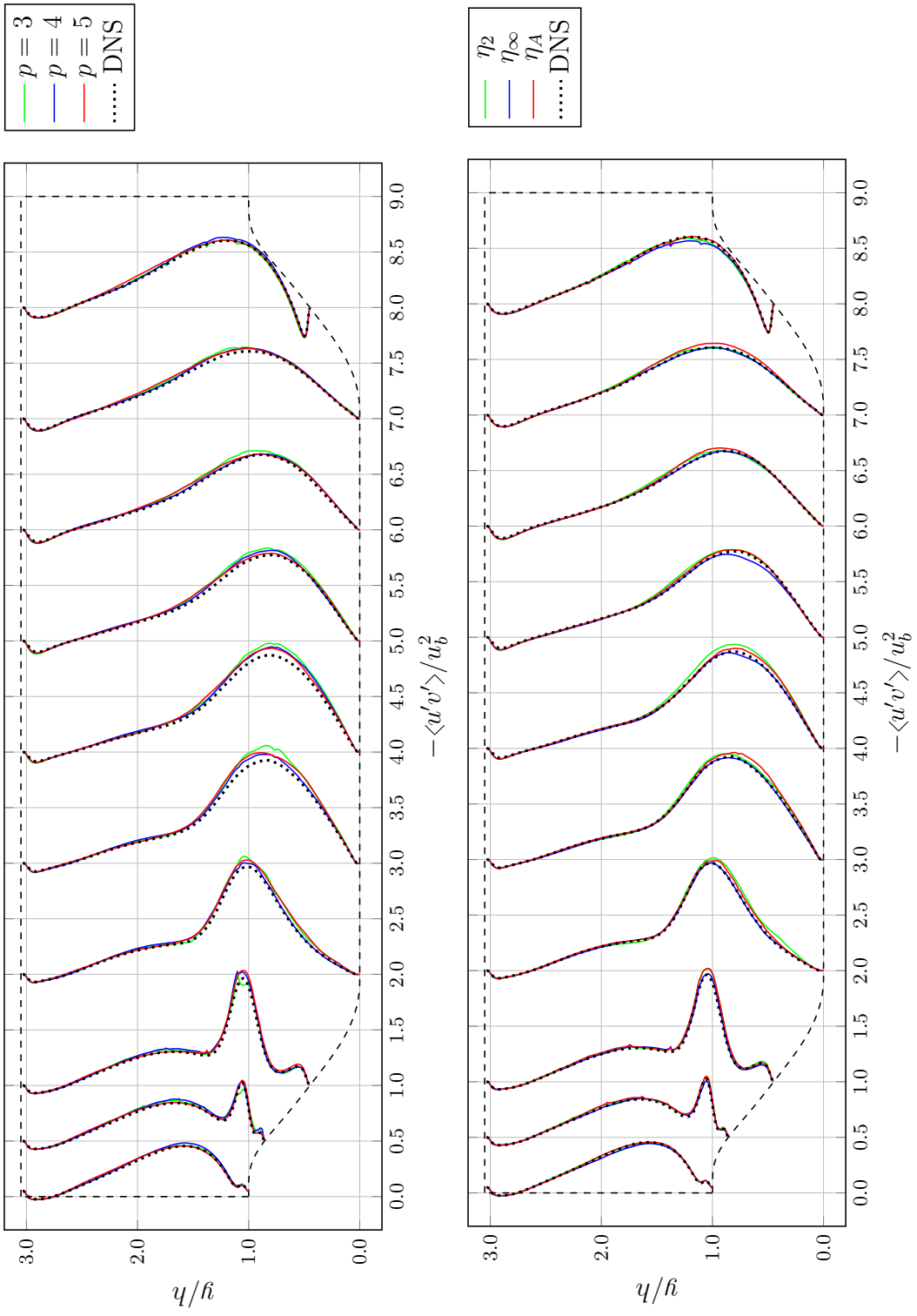

Figure 71 – DNS of the turbulent flow over periodic hills at Re = 2800: Averaged velocity fluctuations $\langle u'v' \rangle / u_b$ at various locations obtained with uniform polynomial degree and adaptive simulations compared to the reference DNS [32]. Values are shifted and scaled by a factor of 30.

The fully three-dimensional and unsteady reattachment renders the prediction of many quantities of interest, such as lift and drag, a challenging task. Several works have shown that RANS models often fail to predict the accurate behaviour of this type of flow. Additionally, results are strongly dependent on the RANS model employed if no particular treatment of the transition is used [179]. That said, relatively good results can be obtained by employing RANS models provided that the transition location is fixed *a-priori*, often requiring results from LES/DNS or experiments [37].

On the other hand, even though LES has proved accurate for the prediction of such flows, LES solutions appear to be very sensitive to mesh resolution, as shown *e. g.* in the LESFOIL project [54]. Several works, see *e. g.* [20, 71], have also demonstrated that the use of high-order methods can improve the accuracy of the LES of such configurations thanks to the low dissipation and dispersion errors of these methods.

The objective of this section is therefore to demonstrate that the proposed static p-adaptive DG method can be effectively used to improve the efficiency and accuracy of LES of practical configurations. The considered configuration thus represents an ideal test case thanks to the availability of accurate DNS simulations [119, 202]. In fact, direct comparison with DNS simplifies the analysis of the results, as compared to employing experimental data. This is because several unknown parameters, such as three-dimensional effects and turbulence intensity at the inflow, are removed.

The adaptive simulations presented in the remainder of this section have been performed by employing two different refinement indicators. At first, we employ the L^∞-SSED indicator, which has been shown in the previous section to provide the best performance. For the sake of conciseness, in the following, this is referred to as simply SSED indicator. Secondly, the novel Small-Scale Lifting (SSL) indicator, developed in Sec. 4.4.6, is also used to drive the p-adaptation process. The same strategy outlined for the SSED indicator is followed for this new indicator, *i. e.* we employ the L^∞-norm in time and in the spanwise homogeneous direction of the SSL indicator computed from the instantaneous solution.

Problem definition and computational details

The configuration considered is the transitional flow past a NACA0012 airfoil at angle of attack $\alpha = 5^\circ$, free-stream Mach number $M_\infty = 0.2$ and Reynolds number 50 000, based on the airfoil chord c and the free-stream velocity U_∞. The analytical expression of the airfoil geometry is modified by extending the upper and lower surfaces to obtain a sharp trailing edge. The use of $M_\infty = 0.2$ allow for the comparison with the reference incompressible DNS.

We consider a C-type domain of radius $R = 20c$ with the outflow boundary located at a distance $W = 40c$ and spanwise lenght $L_z = 0.2\,c$. In Table 5 we compare these parameters to those employed in the literature for DNS and LES of the same configuration.

	Re	α	M	R	W	L_z
current (LES)	$5\,10^4$	5°	0.2	$20c$	$40c$	$0.2c$
Lehmkuhl *et al.* [119] (DNS/LES)	$5\,10^4$	5°	-	$20c$	$20c$	$0.2c$
Zhang *et al.* [202] (DNS)	$5\,10^4$	5°	-	$10c$	$6c$	$0.1c$-$0.8c$
Thomareis *et al.* [181] (DNS)	$5\,10^4$	5°	-	$18c$	$20c$	$0.2c$
Jones *et al.* [99] (DNS)	$5\,10^4$	5°	0.4	$7.3c$	$5c$	$0.2c$
Shan *et al.* [173] (DNS)	10^5	4°	0.2	$4c$	$3c$	$0.1c$

Table 5 – Summary of geometrical parameters for the computational domain of selected studies of the flow past a NACA0012 airfoil at medium Reynolds numbers and low incidence.

We note that Zhang *et al.* [202] have shown that for $L_z = 0.2$ the spanwise extension of the domain influences the simulation and has an effect on the prediction of the skin friction coefficient and the turbulent statistics. Care is therefore required when comparing simulation results with experimental data. The currently employed value is however selected to limit the computational cost of the simulations and allow for the comparison with both the DNS and the LES results of Lehmkuhl *et al.* [119] and the DNS results of Zhang *et al.* [202]. The radius of the domain is chosen to be the same as that employed by Lehmkuhl *et al.* [119], whereas the outflow boundary is located further downstream to reduce the reflection of acoustic waves.

The computational domain is discretized by a quadratic mesh composed of $135 \times 28 \times 8$ hexahedral elements and is shown in Fig. 72. Non-reflecting boundary conditions are imposed at the inflow and outflow boundaries, and no-slip adiabatic conditions are imposed at the solid wall. The flow is assumed periodic in the spanwise direction.

Time integration is performed using the third-order four-stages SSP Runge-Kutta scheme with time step $\Delta t = \mathcal{O}(10^{-5})$. The discretization of the convective term is performed by employing the Roe flux with the upwind component scaled by a parameter $k = 0.1$. Finally, the BR2 scheme with $\eta_{BR2} = 4$ is used for the discretization of both the diffusive and the LES model terms.

Unless stated otherwise, the subgrid-scale stress is modelled by the Vreman model [190], described in Sec. 2.4.1.3, with model coefficient $C_V = 0.2688$. The influence of the LES model on the results of the adapted simulations is also assessed by employing the WALE model [145], described in Sec. 2.4.1.2, with $C_W = 0.3250$. For both models, the LES filter width is evaluated as $\Delta = |K|^{1/3}/(p_K + 1)$.

A first baseline simulation is performed by employing a uniform polynomial degree $p = 3$. The result of a first coarser simulation with $p = 1$ is used to accelerate the initialization of the flow. The simulation is then carried out for $40\,t_c$ to achieve a statistically steady state, with the convective time defined as $t_c = c/U_\infty$. From this

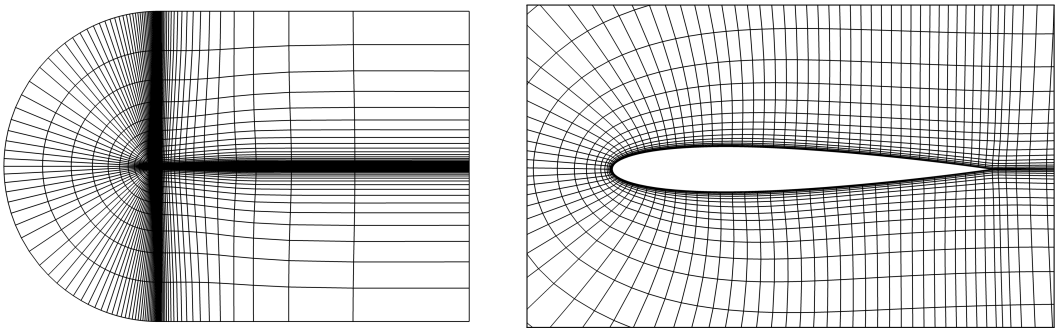

Figure 72 – Transitional flow past a NACA0012 airfoil: Computational grid.

point, the statistics of the flow are gathered over an additional time interval equal to $35\,t_c$.

Two sets of adaptive simulations are then performed using the L^∞-norm of the SSED and of the SSL indicators. The adaptive algorithm based on these indicators is described below.

Starting from the baseline computation, the refinement indicator is computed for $5\,t_c$ and updated every $100\,\Delta t$. Elements are therefore marked for refinement and coarsening by comparing the local value of the refinement indicator with the user-defined refinement and coarsening thresholds. These are here respectively fixed to $\eta_{ref} = 10^{-2}$ and $\eta_{coar} = 10^{-3}$ for the SSL indicator and $\eta_{ref} = 10^{-3}$ and $\eta_{coars} = 10^{-5}$ for the SSED indicator. The local polynomial degree is then increased or reduced in marked elements and the solution is projected onto the updated solution space.

Several adaptation steps are performed before computing the statistics of the flow. For this reason, starting from the newly updated resolution, a shorter simulation is performed over an interval equal to $10\,t_c$. The refinement indicator is then computed once more over an interval $5\,t_c$ and the resolution is adapted again. Subsequently, the process is repeated twice more, for a total of three adaptation steps, with the local polynomial degree limited in the interval $p_K \in [1,5]$. Note that the refinement threshold for the SSED indicator is lowered to $\eta_{ref} = 5 \cdot 10^{-4}$ at the last adaptation step. This is done in order to achieve a similar number of dofs as for the SSL indicator.

Once the final adapted spatial resolution has been obtained the simulation runs for $30\,t_c$ and the statistics of the flow are computed over an additional interval of $30\,t_c$.

The simulations performed on the p-adapted grids obtained based on the SSL and SSED indicators and the Vreman model are referred to as V-SSL and V-SSED respectively.

Finally, in order to assess the influence of the subgrid model on the obtained resutls, a second simulation is performed on the p-adapted discretization obtained based on the SSL indicator using the WALE model. This simulation is referred to as W-SSL.

	C_L	C_D	x_{sep}	x_{reatt}	#Mdofs	CPU time (h)	Δt ($10^{-5} t_c$)
DNS Lehmkuhl *et al.* [119]	0.569	0.0291	0.169	0.566	25.30		
LES M2 Lehmkuhl *et al.* [119]	0.565	0.0282	0.164	0.571	4.78		
LES M1 Lehmkuhl *et al.* [119]	0.582	0.0248	0.140	0.541	0.74		
DNS Zhang *et al.* [202]	0.568	0.0285	0.138	0.578	33.56		25.0
Uniform $p = 3$	0.583	0.0288	0.118	0.552	1.93	71.4	1.2
V-SSED	0.583	0.0279	0.126	0.545	2.22	104	1.2
V-SSL	0.580	0.0284	0.126	0.562	2.27	109	1.2
W-SSL	0.581	0.0272	0.129	0.547	2.27	105	0.9

Table 6 – Transitional flow past a NACA0012 airfoil: Comparison between current LES results and reference computations from the literature. From the left: Aerodynamic coefficients, separation and reattachment points, number of dofs, CPU time to advance the simulation for 10^5 time steps, and physical time step Δt. CPU time measured on 840 Intel Xeon Broadwell E5-2690v4 cores.

For each simulation, numerical integration is performed using a number of quadrature points dependent on the local polynomial degree p_K and the effective Jacobian order $\mu_{J,K}$ (see App. A). The local number of quadrature points per space direction is thus set to $q_K = p_K + 4$ for $p_K = 1$ and 2, $q_K = p_K + 5$ for $p_K = 3$ and 4, and $q_K = p_K + 6$ for $p_K = 5$. One additional quadrature point per space direction is employed if $\mu_{J,K} \geq 2$.

Analysis of the results

The total number of dofs and the computational time required for the p-adapted simulations are reported in Table 6. These values are compared to those obtained for the baseline simulation and to the total number of dofs employed in the reference simulations.

Both adapted simulations present a limited increase of the computational time and of the number of dofs with respect to the baseline computation at $p = 3$. These correspond to an increase of approximately 45% and 17%, respectively. Nonetheless, the total number of dofs is at least one order of magnitude lower than that employed in the reference DNS computations and less than half that of the fine LES by Lehmkuhl *et al.* [119].

In Fig. 73 we report the distribution of the local polynomial degree obtained for the two considered refinement indicators. We observe that both indicators behave as expected. Indeed, they increase the spatial resolution near the leading edge of the airfoil and in the fully turbulent region, downstream from the vicinity of the transition point (as will be further shown later). Additionally, both refinement

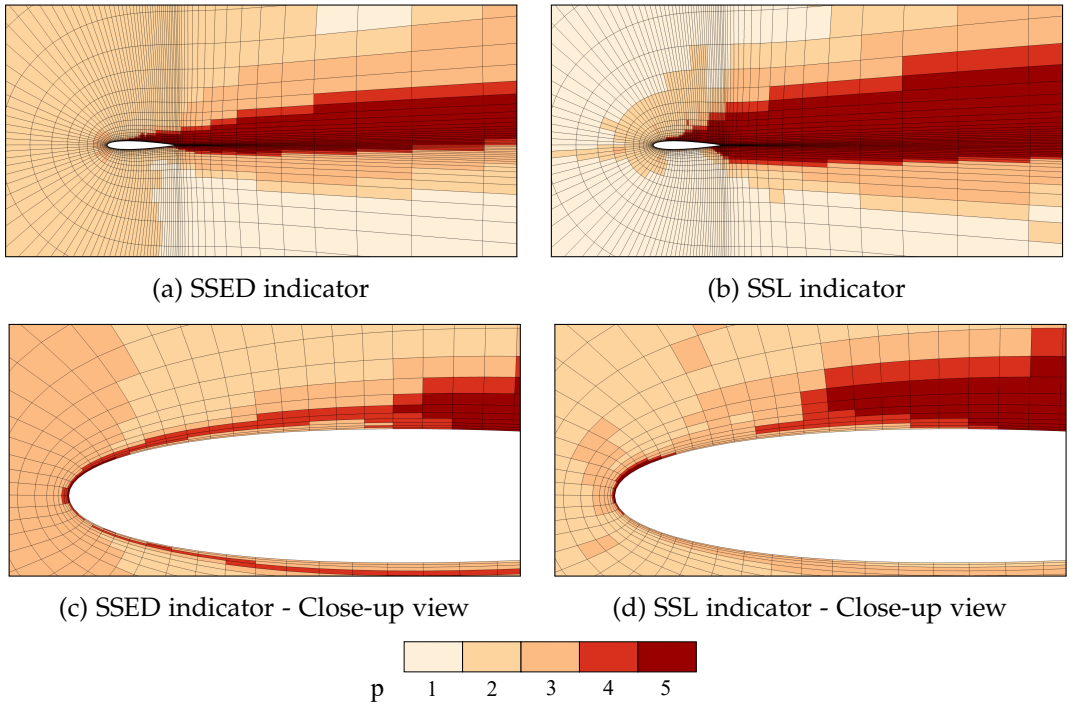

Figure 73 – Transitional flow past a NACA0012 airfoil: Distribution of the local polynomial degree generated by the adaptive algorithm.

indicators reduce the spatial resolution in the upstream region and in the downstream region away from the turbulent wake.

Some important differences can be nonetheless observed between the p-maps provided by the two indicators. In particular, for the same number of dofs, the SSED indicator leads to a higher value of the polynomial degree in the upstream region and to a smaller extent of the refined region in the turbulent wake. Furthermore, the SSED indicator increases the local polynomial degree in a thin region surrounding the recirculation bubble, while the maximum polynomial degree is selected further downstream than for to the SSL indicator. Finally, higher refinement is attained by the SSED indicator in the boundary layer on the pressure side of the airfoil.

A first assessment of the quality of the employed discretizations can be performed by analysing the grid resolution near the wall. This is usually expressed in terms of the characteristic lengths of the first element at the wal normalized by a reference viscous length-scale defined as ν/u_τ, where $u_\tau = \sqrt{\tau_w/\rho}$ is the friction velocity. In the framework of the DG method, we define the wall-normal length as $y^+ = u_\tau y/\nu(p+1)$, with y the characteristic length of the element in the wall-normal direction. A similar definition is employed for the streamwise Δx^+ and spanwise Δz^+ lengths. Several works have shown that the near-wall resolution should be sufficient to correctly resolve the turbulent kinetic energy production in the viscous sub-layer,

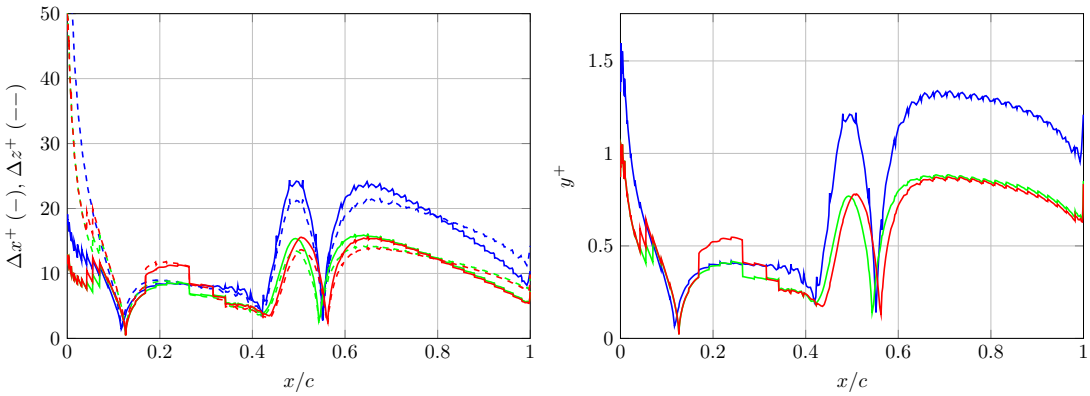

Figure 74 – Transitional flow past a NACA0012 airfoil: Mesh resolution near the wall for the uniform polynomial degree simulation with $p = 3$ (blue) and for the adaptive simulations: V-SSED (green) and V-SSL (red).

see *e. g.* [170]. Typical values of the grid spacings for wall-resolved LES are therefore $y^+ < 2$, $\Delta x^+ \approx 50 - 150$ and $\Delta z^+ \approx 15 - 40$, respectively.

The values obtained for the uniform polynomial degree and the adaptive simulations are reported in Fig. 74. As seen from these plots, for the uniform polynomial degree simulation these values are well within the suggested ranges, especially in the turbulent region $x \gtrsim 0.4$. As for the p-adaptive simulations, the resulting Δx^+ and Δz^+ have values lower than 20 and $y^+ < 1$ in the turbulent boundary layer. As in this work we are employing isotropic adaptation, it is not possible to distinguish at this stage which direction required further refinement.

An additional qualitative analysis of the simulations performed is provided in Fig. 75 which shows the isosurfaces of the Q-criterion. For all the performed simulations, we can clearly identify the presence of the recirculation bubble, the vortex shedding, and the laminar-to-turbulent transition with the formation of smaller interacting vortical structures. We further note that the adapted simulations allow us to obtain a sharper representation of the vortex shedding and of smaller scale vortical structures. Indeed, as also shown in Fig. 76, these turbulent regions are fully enveloped in the refined region for both error indicators. Additionally, the most refined region generated by the SSED indicator covers a small area immediately surrounding the turbulent region near the airfoil, whereas a wider p-refined region is obtained for the SSL indicator, as already mentioned above.

A quantitative assessment of the quality of these simulations can be obtained, from Table 6, by comparing the time-averaged drag and lift coefficients, as well as the location of the separation and reattachment points, with the corresponding values reported in the literature. We remark that the latter two quantities are particularly

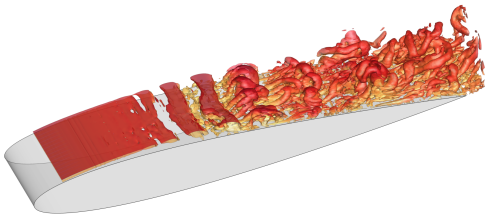

(a) Uniform $p = 3$

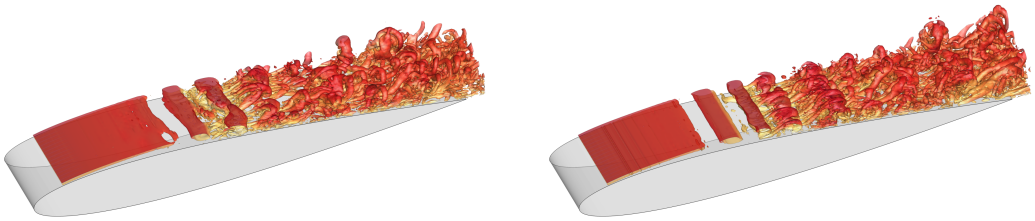

(b) V-SSED (c) V-SSL

Figure 75 – Transitional flow past a NACA0012 airfoil: Isosurfaces of the Q-criterion (Q = 50) coloured by the streamwise velocity for the adaptive and the uniform polynomial degree simulations.

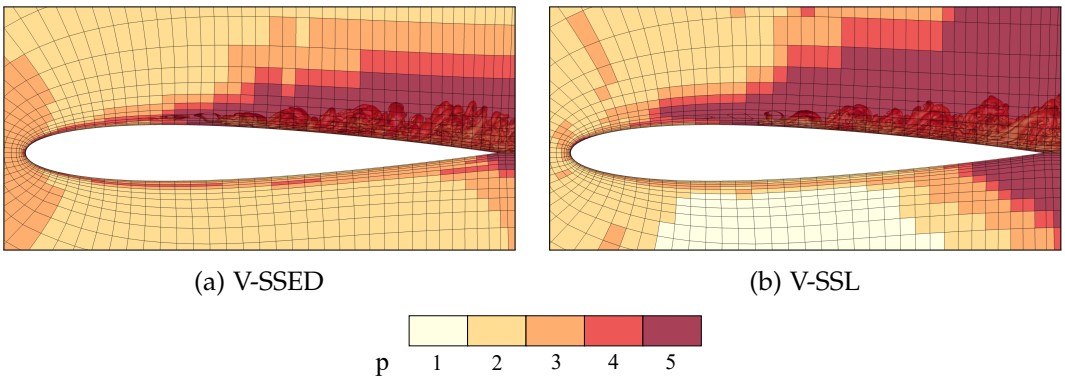

(a) V-SSED (b) V-SSL

Figure 76 – Transitional flow past a NACA0012 airfoil: Isosurfaces of the Q-criterion (Q = 50) and distribution of the local polynomial degree for the adaptive simulations.

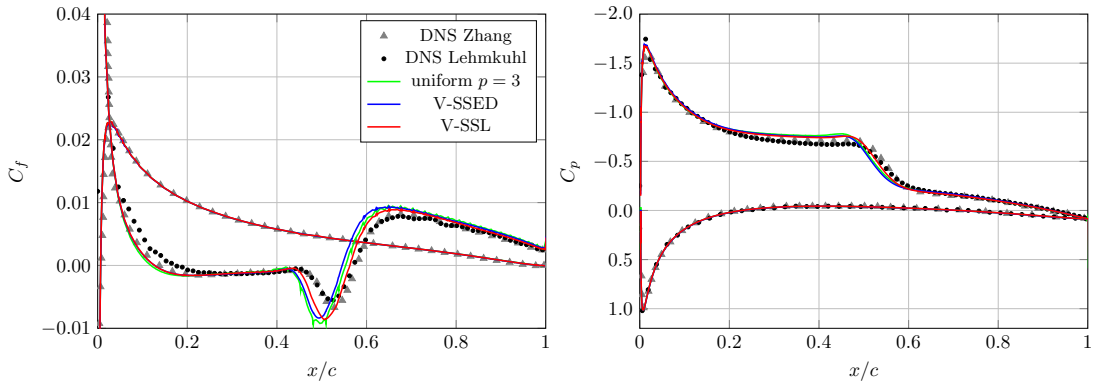

Figure 77 – Transitional flow past a NACA0012 airfoil: Skin friction coefficient (left) and pressure coefficient (right) for the uniform and and for the adaptive simulations compared to the reference DNS data from Lehmkuhl *et al.* [119] and Zhang *et al.* [202] (extracted).

sensitive to the LES resolution and to the correct prediction of the transition phenomenon.

The baseline $p = 3$ simulation appears to present an accuracy in between that of the two LES of Lehmkuhl *et al.* [119]. Indeed, the drag coefficient is in relative good agreement with the DNS data. However, the lift coefficient is over-predicted and both the separation and reattachment locations are under-predicted.

Considering now the adaptive simulations, the V-SSED simulation does not lead to a substantial improvement in the prediction of these global quantities. Indeed, the error in the drag coefficient and the reattachment point is higher than for the $p = 3$ simulation. Yet, the position of the separation point is predicted with higher accuracy. On the other hand, the V-SSL simulation considerably improves the prediction of global quantities, yielding a better agreement with the reference DNS for the lift coefficient and both the separation and the reattachment points.

A more detailed explanation of these results can be obtained inspecting the graphs of the skin friction and pressure coefficients reported in Fig. 77. Considering the former, the uniform polynomial degree simulation appears to be under-resolved near the wall from $x \gtrsim 0.4$. This is inferred from the presence of spikes in the skin-friction coefficient profile. This result is in agreement with the under-resolution measured by both refinement indicators in this region, despite the relatively good near-wall resolution observed in Fig. 74.

Both adaptive simulations largely improve the near-wall resolution and smaller intensity spikes can be observed only for $x \gtrsim 0.6$. The V-SSL simulation in particular provides the best agreement, presenting a more accurate prediction of the location of the reattachment point.

We remark that the under and over-prediction of the skin friction coefficient at different locations leads to an error cancellation when evaluating the drag coefficient. This is possibly the cause for the good prediction of this value provided by the baseline computation.

Considering now the pressure coefficient in Fig. 77, we observe that a remarkable agreement with the DNS is obtained for all DG simulations except in the separated flow region. The error in the evaluation of the location of the separation point is therefore the cause for the under-prediction of the value of the pressure plateau and over-prediction of the lift coefficient observed in Table 6. We observe that the current results, in particular for the V-SSL simulation, provide a considerably better agreement for the pressure coefficient than the fine LES of Lehmkuhl *et al.*, see Fig. 10a in [119]. Indeed the more accurate prediction of the lift coefficient provided by the authors is caused by the cancellation of over- and under-prediction errors, similar to what we just described above. The overwhelming presence of such effects is one of the principal difficulties in the analysis and comparison of LES and adaptive approaches in this framework.

In Figs. 79 and 80 we report the time-averaged velocity and velocity fluctuation profiles at different stations along the airfoil and in the near wake.

The baseline simulation predicts an average streamwise velocity which is in relatively accurate agreement with the reference DNS. More marked discrepancies are observed for the wall-normal velocity and in the velocity fluctuation profiles. Indeed, the uniform polynomial degree simulation largely over-predicts the values of both $\langle u'u' \rangle / U_\infty^2$ and $\langle u'v' \rangle / U_\infty^2$ over most of the airfoil.

As regards the V-SSED and V-SSL simulations, they largely improve the prediction of the statistics of the flow at all locations. In particular, the V-SSL simulation provides the most accurate agreement, especially in terms of the velocity fluctuation profiles $\langle u'u' \rangle / U_\infty^2$ in the top panel of Fig. 80.

The presented analysis indicates that, for the considered configuration, the novel proposed SSL refinement indicator can yield improved results with respect to the SSED indicator. Nonetheless, still important discrepancies are observed between the current LES and reference DNS results. These might be caused by both the limitation imposed on the maximum resolution as well as the influence of the LES model. Both effects are likely to be present in most practical applications due to the limitations in the available computational time.

In order to analyse the effect of the LES model on the quality of the present computations, we have performed an additional simulation using the WALE model and the adapted discretization obtained using the SSL indicator.

In Fig. 78 we compare the skin friction and the pressure coefficients obtained with the two considered turbulence models. The main factor controlling the accuracy of these results appears to be the predicted location of the reattachment point. While a more accurate agreement is provided by the Vreman model, the discrepancies

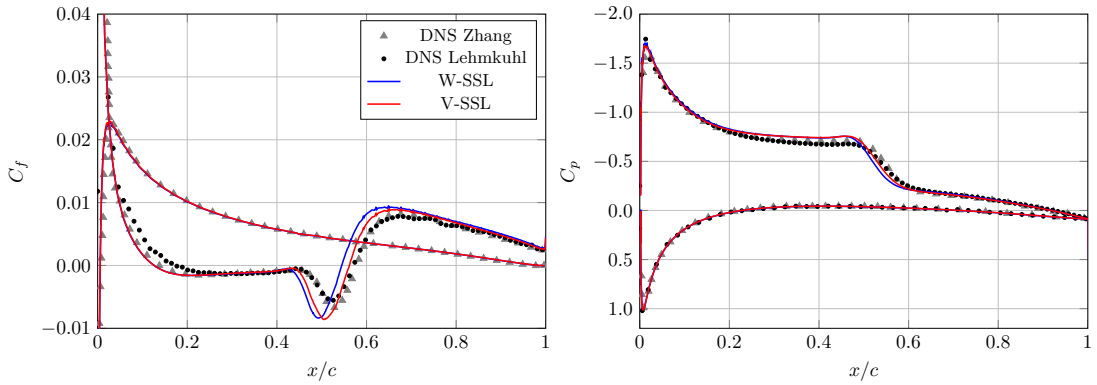

Figure 78 – Transitional flow past a NACA0012 airfoil: Pressure coefficient (left) and skin friction coefficient (right) for the adaptive simulations with the SSL indicator using the WALE and Vreman model compared to the reference DNS data from Lehmkuhl *et al.* [119] and Zhang *et al.* [202] (extracted)

between results obtained with the two turbulence models are of the same order of magnitude as those with the DNS data. This clearly indicates the role of the LES model in the accuracy of the computed results.

Finally, we report in Figs. 81 and 82 the mean velocity and velocity fluctuations profiles for the two LES models. Once again, the discrepancies between the results provided by the two LES models are of the same order of magnitude as those with respect to the reference DNS. In particular, in Fig. 81 we observe that, with the exception of the vertical velocity profiles at locations $x = 0.4$ and $x = 0.7$, the WALE model provides improved results for all the average velocity profiles. Additionally, in Fig. 82 the DNS velocity fluctuation profiles are in between those provided by the two LES models, with the results from the WALE model providing a closer agreement with the DNS. These findings indicate that, despite the improved accuracy provided by the adaptation algorithm, the adaptive simulations are still strongly influenced by the employed turbulence model.

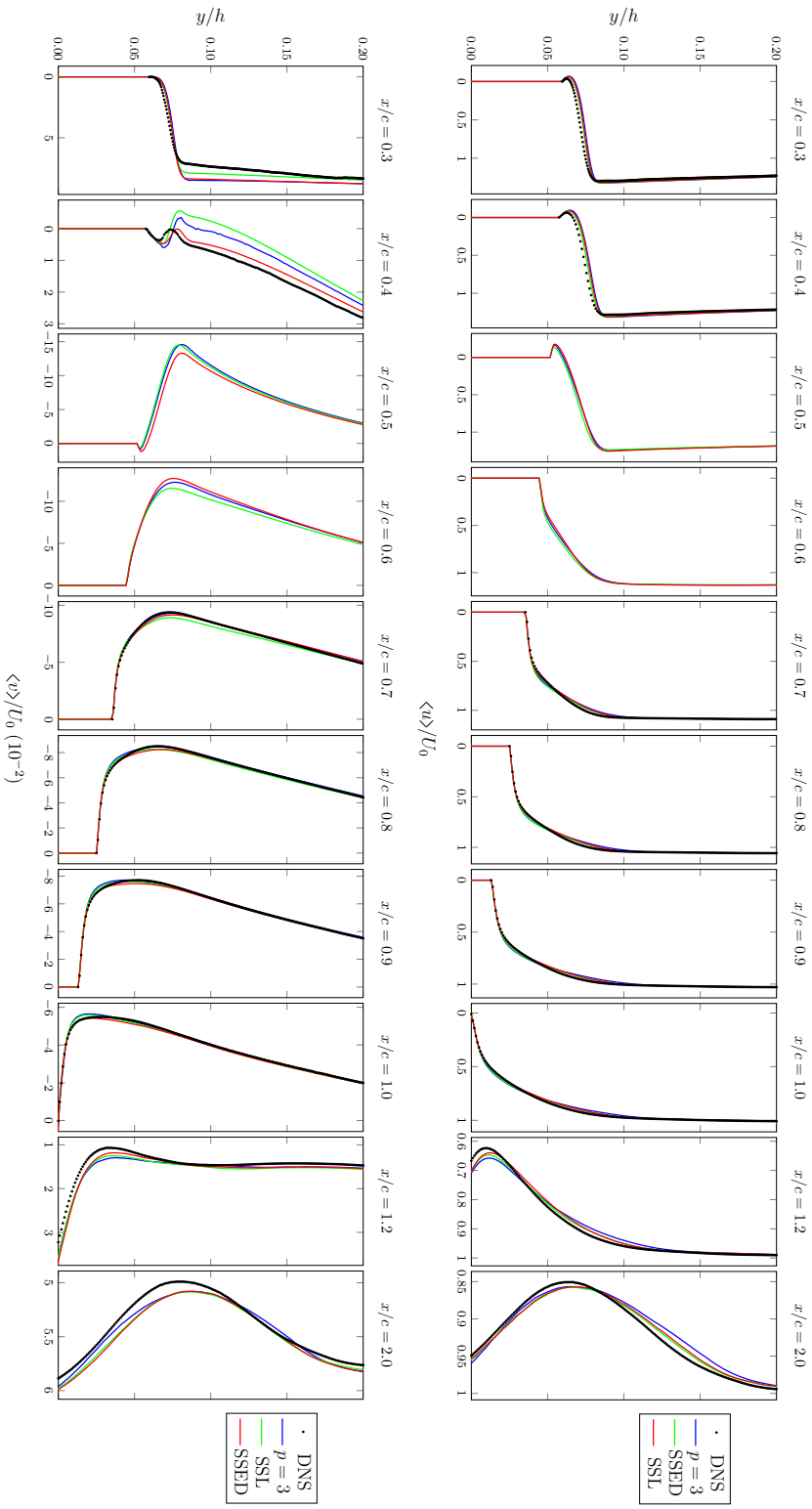

Figure 79 – Transitional flow past a NACA0012 airfoil: Averaged velocity profiles $\langle u \rangle / U_\infty$ and $\langle v \rangle / U_\infty$ at various locations obtained with uniform polynomial degree and adaptive simulations compared to the reference DNS data from Lehmkuhl *et al.* [119].

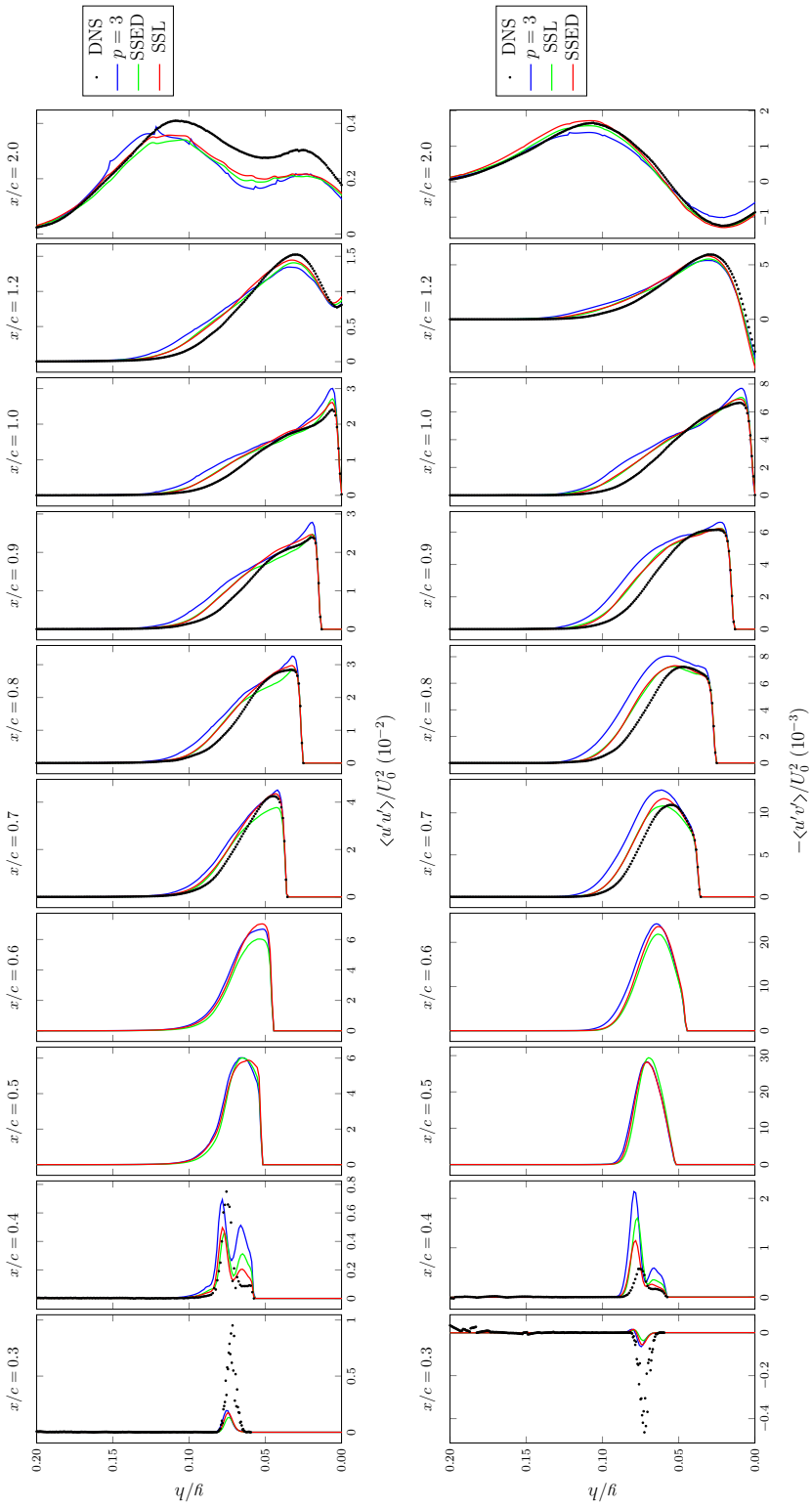

Figure 80 – Transitional flow past a NACA0012 airfoil: Averaged velocity fluctuations profiles $\langle u'u' \rangle / U_\infty^2$ and $\langle u'v' \rangle / U_\infty^2$ at various locations obtained with uniform polynomial degree and adaptive simulations compared to the reference DNS data from Lehmkuhl *et al.* [119].

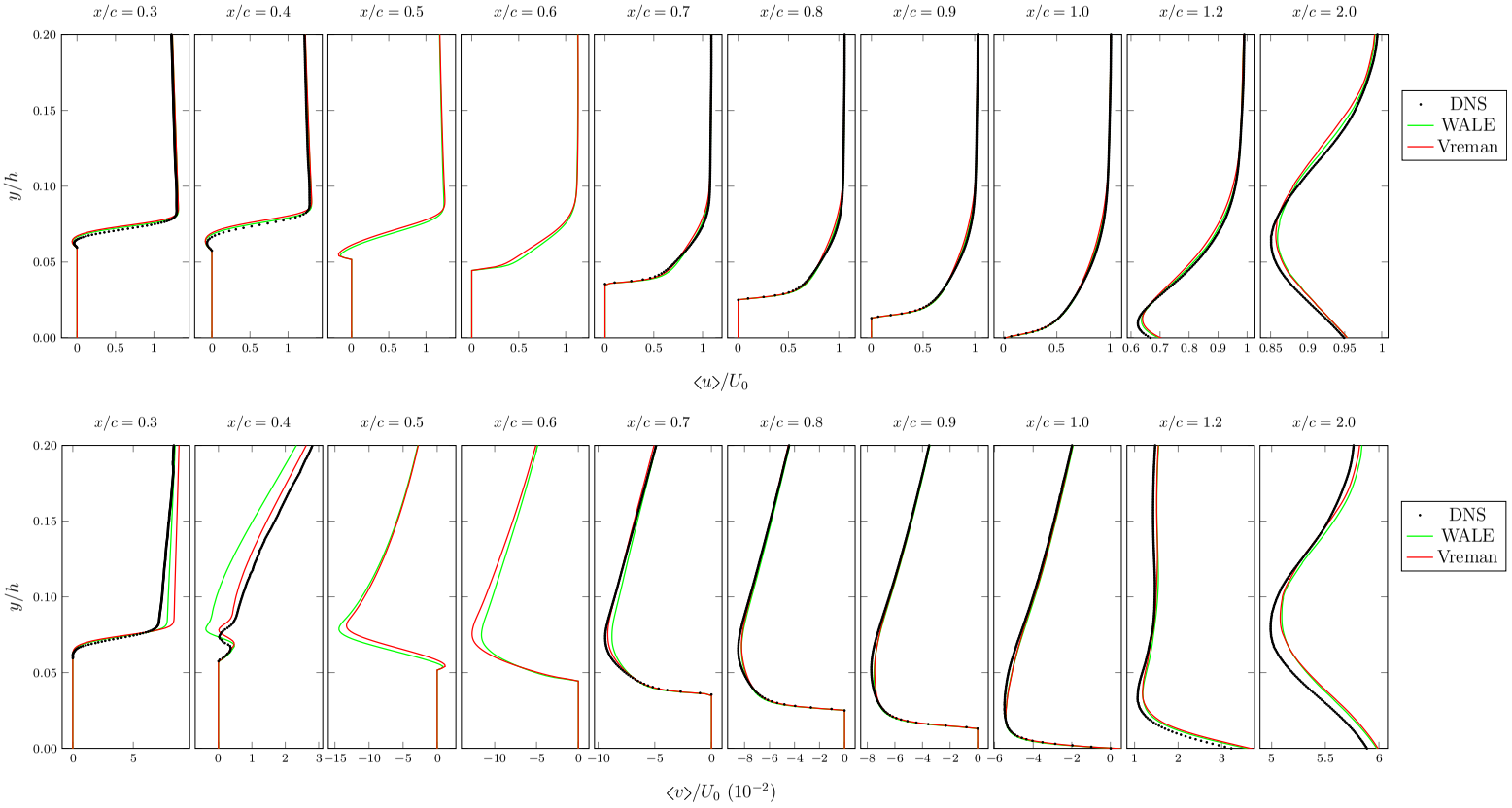

Figure 81 – Transitional flow past a NACA0012 airfoil: Averaged velocity profiles $\langle u \rangle / U_\infty$ and $\langle v \rangle / U_\infty$ at various locations obtained with the adaptive simulations using the WALE and Vreman model, compared to the reference DNS data from Lehmkuhl *et al.* [119].

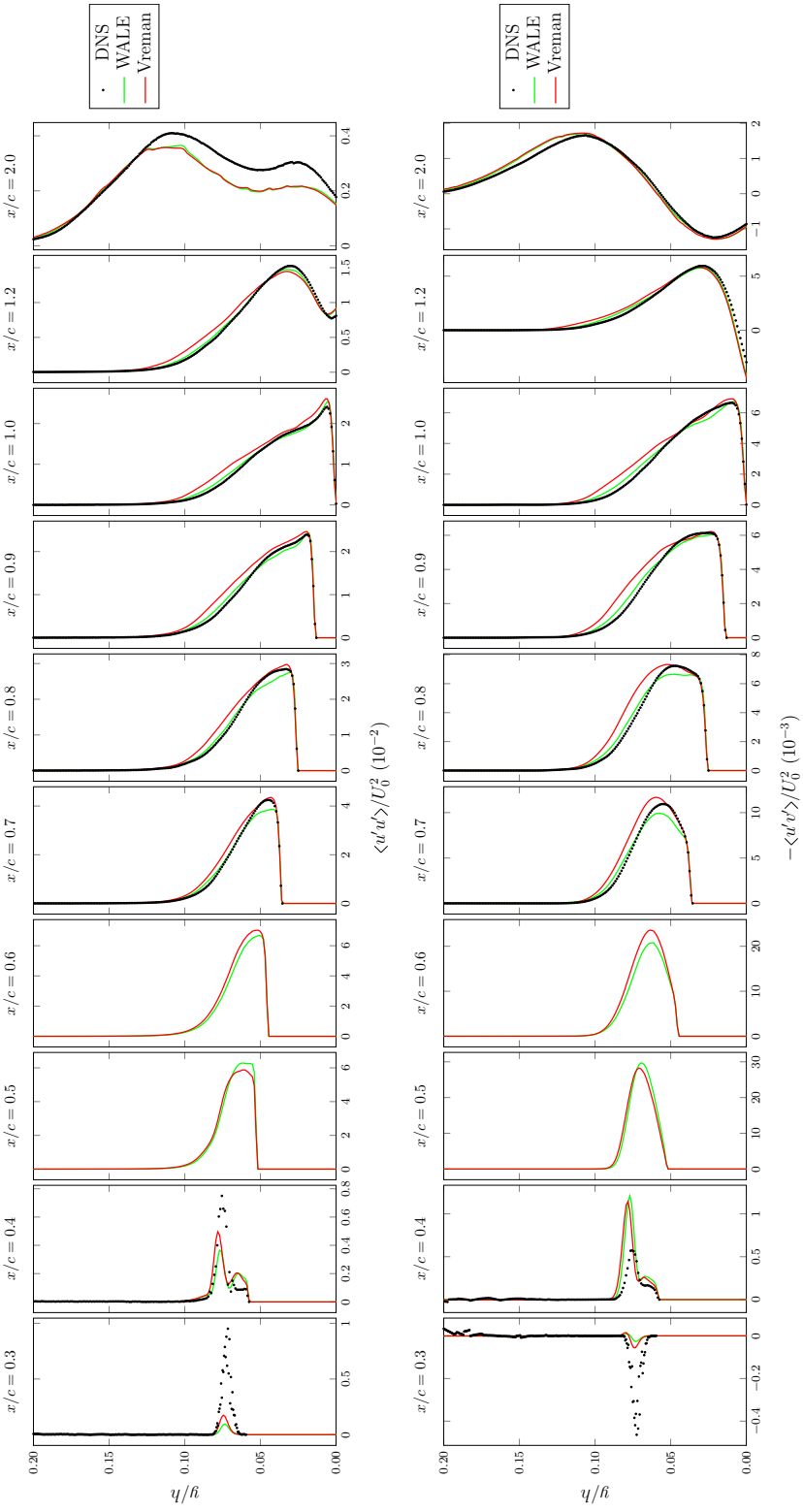

Figure 82 – Transitional flow past a NACA0012 airfoil: Averaged velocity fluctuations profiles $\langle u'u' \rangle / U_\infty^2$ and $\langle u'v' \rangle / U_\infty^2$ at various locations obtained with the adaptive simulations using the WALE and Vreman model, compared to the reference DNS data from Lehmkuhl *et al.* [119].

CHAPTER 10

A-PRIORI ANALYSIS OF DG-LES MODELS

RÉSUMÉ DU CHAPITRE EN FRANÇAIS

Dans ce chapitre, nous effectuons des analyses *a priori* de l'approche Variational Multiscale (VMS) pour la méthode DG présentée dans la Sec. 2.6. Il a été mie en évidence que ce modèle permet d'obtenir des simulations numériques précises d'écoulements turbulents. Un certain nombre de questions restent toutefois ouvertes qui entravent l'application systématique des approches DG-VMS. Un aperçu des travaux antérieurs pertinents et des thèmes de recherche ouverts est donc présenté dans la Sec. 10.2. Il est montré que ceux-ci incluent le rôle de la discrétisation DG dans la définition du filtre LES et de l'opérateur de séparation des échelles.

La définition du filtre DG et la solution DG-LES idéale sont donc examinées dans la Sec. 10.3. Celles-ci sont utilisées dans les Sec. 10.4 et 10.5 pour introduire un nouveau cadre analytique pour l'analyse *a priori* des modèles DG-LES, cohérent avec la discrétisation des simulations DG-LES. Ce cadre permet d'étudier le mécanisme idéal de transfert d'énergie entre les échelles résolues et non-résolues. Le concept de viscosité tourbillonnaire modale est également introduit. Ce concept peut être utilisé pour l'analyse *a priori* de la méthode DG-VMS ou des approches spectral-vanishing viscosity.

Le cadre élaboré est ensuite appliqué dans la Sec. 10.6 à l'analyse du mécanisme de transfert d'énergie dans les simulations DG-LES en utilisant une base de données DNS du Taylor-Green Vortex (TGV) à Re = 5 000, 20 000 et 40 000. Cette analyse identifie le transfert d'énergie spectrale et modale idéal qui devrait être fourni par un modèle DG-LES optimal pour imiter l'effet des échelles non-résolues sur celles qui sont résolues.

Des analyses *a priori* sont effectuées dans la Sec. 10.7 pour trois variantes de l'approche DG-VMS : *small-small*, *Vreman*, et *all-all*. Il est démontré que lorsque la limite de résolution du DG-LES se situe au début de la bande de dissipation, l'hypothèse de grandes échelles exemptes d'interaction avec les échelles non-résolues est valide et l'approche DG-VMS peut reproduire le spectre de dissipation SGS idéal. Pour des résolutions plus grossières, typiques des simulations LES à nombre de Reynolds élevé, l'approche DG-VMS est incapable de reproduire le mécanisme idéal

de transfert d'énergie aux grandes échelles. Il est montré, *a priori*, qu'un accord plus précis peut être obtenu en utilisant une approche mixte Smagorinsky et DG-VMS avec une valeur fixe du paramètre fraction-échelle.

10.1 INTRODUCTION AND OUTLINE OF THE CHAPTER

The work presented in this chapter is motivated by the need to develop SGS models that take into consideration the details of the numerical discretization at hand.

At the end of Chap. 9 we have seen that, despite the considerable improvement of the accuracy provided by the adaptive algorithm, the SGS model presents a strong influence on the results of the adaptive LES simulations. It is therefore of paramount importance to analyse and improve the accuracy of LES models in the context of *hp*-adaptive DG methods.

Recent works [43, 204] have shown that the VMS approach, described in Sec. 2.6, can provide accurate DG-LES predictions of turbulent flows. Indeed, the VMS approach allows for the reduction of one of the most common drawbacks of standard LES models, namely the excessive SGS dissipation applied to the largest resolved turbulent scales. There are however several open questions that still hinder the systematic and robust application of the DG-VMS approach.

One of the most important difficulties is represented by the definition *a-priori* of the scale-separation between large and small resolved scales described in Sec. 2.6. In most works found in the literature on VMS, the scale separation is defined either heuristically or, alternatively, *a-posteriori* by performing simulations of a given configuration based on different definitions of the scale separation operator. These approaches present serious limitations, especially when dealing with inhomogeneous or (statistically) unsteady turbulent simulations. Additionally, in the framework of resolution adaptive simulations, further difficulties arise due to the variable resolution and the interaction of the DG-LES model with the dispersion and dissipation properties of the method, which depend on the locally employed polynomial degree.

The main goal of this chapter is therefore to extend our understanding of the requirements of DG-LES models and of the accuracy of the DG-VMS approach in modelling the effect of the unresolved scales. To this end, in the next section we provide an overview of the research justifying the interest in the VMS model. Thereafter, we outline some of the research topics which need to be investigated in order to promote the systematic application of the DG-VMS approach. It is shown that this includes the role of the DG discretization in defining the LES filter and the scale separation operator.

These topics are studied by means of *a-priori* analyses of the DG-VMS method in the remainder of the chapter. For this purpose, in Sec. 10.3 we discuss the DG-filter and the ideal DG-LES solution. Their definition is then employed in Sec. 10.4 and 10.5 to introduce a novel framework for the *a-priori* analysis of DG-LES models. It

can be used to study the ideal and modelled energy transfer between resolved and unresolved scales, and is consistent with the discretization used for DG-LES.

The presented methodology is applied in Sec. 10.6 to a DNS database of the TGV configuration at Re = 5 000, 20 000 and 40 000. Obtained results are then compared in Sec. 10.7 to the energy transfer provided by three variants of the DG-VMS approach: the small-small [95], Vreman [189], and all-all variants [42].

10.2 PREVIOUS RESEARCH AND OPEN QUESTIONS

One of the fundamental traits of turbulence, that must be correctly reproduced by SGS models, is the physical mechanism of energy transfer between the resolved turbulent scales and the unresolved scales. This energy transfer mechanism can be studied by analysing the non-linear interaction of the full velocity field such as that obtained from DNS or by theoretical analyses by employing an analytical energy spectrum.

Early theoretical analyses of the energy transfer mechanisms in turbulent flows were performed by Heisenberg [87] and Kraichnan [106]. These studies involved the choice of an analytical energy spectrum and an arbitrary convolution filter to separate resolved and unresolved scales and evaluate the corresponding non-linear interactions and energy transfer. The energy transfer mechanism was represented by means of an additional *spectral eddy viscosity* acting on the resolved modes. Kraichnan [106] employed a sharp cut-off filter in Fourier space to separate resolved and unresolved scales in theoretical turbulence characterized by an infinite inertial range (*i. e.* assuming infinite Reynolds number). Under these conditions, Kraichnan identified the presence of a cusp in the spectral eddy viscosity, near the cut-off, and a plateau at lower wavenumbers, which is a manifestation of the significant interaction between the unresolved scales and the large resolved scales away from the cut-off.

A-priori numerical analyses were carried out by Domaradzki *et al.* [60] based on DNS of the TGV flow at Re = 3 000 by applying a sharp spectral filter to define the ideal LES solution. This work confirmed the presence of the cusp of the spectral eddy viscosity near the cut-off. However, differently from the studies of Kraichnan, a negligible energy transfer was observed at relatively low wavenumbers. A similar result was observed by McComb and Young [131] who analysed the spectral eddy viscosity for homogeneous isotropic turbulence at microscale Reynolds number $\mathrm{Re}_\lambda = 190$. In their work a plateau in the eddy viscosity was observed only for the coarsest resolution, indicating a negligible interaction between large resolved and unresolved scales. In contrast, Métais and Lesieur [134] identified a plateau in the spectral eddy viscosity evaluated from an LES of homogeneous isotropic turbulence at infinite Reynolds number.

Using *a-priori* testing, the ideal energy transfer and the effective eddy viscosity obtained by applying the LES filter to DNS data can be employed to evaluate SGS

models and aid in their improvement. As an example, the Smagorinsky model [174] presented in Sec. 2.4.1.1, still widely employed due to its simplicity and robustness, has been shown in *a-priori* analyses to be overdissipative on the large-scale structures, confirming the observations from *a-posteriori* tests [98]. Using the same approach, it has been shown that even though its dynamic variant by Germano *et al.* [76] is able to provide the correct global SGS dissipation and near-wall scaling, it fails to reproduce the ideal energy transfer spectrum (also called SGS dissipation spectrum). Indeed, it introduces an insufficient amount of dissipation at high frequencies while exhibiting an overdissipative behaviour at low frequencies as shown *e. g.* by Hughes *et al.* [94].

The VMS approach proposed by Hughes *et al.* [93], described in Sec. 2.6, has been developed with the aim of reducing these shortcomings of traditional LES techniques. As seen in Sec. 2.6, the VMS approach advocates the strict separation of the resolved velocity field into a large-scale component, containing the largest coherent structures of the flow, and a small-scale component. This separation of scales is usually performed by means of a high-pass projection filter. The model then relies on the assumption that the large resolved scales are virtually free of SGS dissipation. Thus the model (*e. g.* the Smagorinsky model or its dynamic version) only acts on the small-scale resolved component of the velocity field. This approach therefore mimics the ideal energy transfer mechanism as described by Domaradzki *et al.* [60].

The combination of the VMS approach with DG methods presents several properties which are of great interest for the improvement of the quality and efficiency of LES [49]. Indeed, the variational framework on which these methods rely allows for the local separation of scales using polynomial basis functions. In contrast to the spectral method, the DG framework allows for the efficient separation of scales even while working on completely unstructured meshes without requiring complex spatial filters. Moreover, the high-order polynomial representation of the solution allows for a higher flexibility in the decomposition into large and small scale components, as compared to FV and low order FE methods. Finally, the use of discontinuous solution spaces allows for the straightforward local adaptation of the scale-separation operator.

There are however still several open questions which require specific analysis in the context of the DG-VMS method. These are: the effect of the LES filter on the effective eddy viscosity, the effect of the scale-separation operator and the calibration of the coefficient involved in the SGS model. While these questions are still the subject of current research in the context of the DG-VMS approach, several studies have been already carried out in the context of standard LES approaches based on convolution filters. The main conclusions of these works are briefly outlined below.

THE EFFECT OF THE LES FILTER Leslie and Quarini [121] performed theoretical analyses by considering an infinite inertial range and a Gaussian filter. Their results demonstrated that, in contrast to what is obtained for a sharp spectral filter, the use of

a Gaussian filter leads to an spectral eddy viscosity characterized by a plateau from low to high wavenumbers and a sharp decay as the wavenumber approaches $1/\Delta$. Moreover, in the case of a production-type spectrum, the shape of the ideal spectral eddy viscosity strongly depends on the ratio between the LES cut-off frequency k_c and that corresponding to the energy production phenomena. Similar conclusions can be drawn from the work of Cerutti *et al.* [39] who evaluated the eddy viscosity from experimental measurements corresponding to the use of a mixed filter (spectral cut-off in one direction and top-hat filter in the other two directions). The outcome of this study led the authors to conclude that the use of a mixed viscosity-hyperviscosity model can improve the accuracy of LES simulations. More recently Lamballais *et al.* [115] have evaluated the eddy viscosity from the DNS of the TGV configuration at Re = 20 000 and observed the presence of the plateau described by Kraichnan [106] employing a spectral cut-off filter.

It appears, therefore, that the assumption of large scales free of SGS dissipation needs to be carefully analysed depending on the LES filter employed in the simulation. The extension of these analyses to the case of the DG-VMS approach presents additional complications as the DG-projection filter is not a convolution filter (as explained in Sec. 10.3). Thus this topic deserves special attention.

THE EFFECT OF THE HIGH-PASS FILTER The second open question is the effect of the high-pass filter on the quality of the VMS model. As regards the choice of the cut-off frequency $\bar{k}$ associated with the high-pass filter, in actual simulations, this parameter is often selected heuristically or by trying to match reference results. In early numerical experiments, Hughes *et al.* [93] and Hughes *et al.* [95] have used a high-pass spectral filter with $\bar{k}$ corresponding to a scale-fraction parameter $\beta = \bar{k}/k_c$ equal to 0.59 and 0.5, respectively, when employing the VMS approach with constant model coefficient. In later works Hughes *et al.* [94] employed a scale-fraction parameter $\beta = 0.5$ for the VMS approach based on the dynamic Germano procedure for the determination of the model constant. Holmen *et al.* [90] carried out a sensitivity analysis for the LES of the turbulent channel flow. The authors showed that the use of the dynamic procedure reduces the sensitivity of the VMS-LES to the scale-fraction parameter and optimal results were obtained for $\beta \approx 0.5$. In contrast, for the static variants optimal results were obtained for $\beta \approx 0.7$ and the quality of the solution quickly deteriorated for other values. Ramakrishnan and Collis [158] have shown that the optimal scale-fraction parameter might depend on the flow considered and resolution available. It was observed that the optimal high-pass filter length can be related to the characteristic length of coherent structures of the flow. However they remarked that the small-scale space should contain at least $50\% - 60\%$ of all modes to provide high quality first and second-order statistics.

The effect of the type of the high-pass filter in VMS was also analysed by Sagaut and Levasseur [169] and Meyers and Sagaut [137]. It was observed that the sharp

cut-off filter (orthogonal in Fourier space) can provide an overdissipative behaviour at high frequencies leading to a bottleneck effect and the generation of a middle-wavenumber pile-up. Moreover, a discrete jump might appear in the energy spectrum near the high-pass filter cut-off (as observed by Meyers and Sagaut [137]). The use of a non-orthogonal high-pass filter (*e. g.* Gaussian filter) led to improved results by rendering all scales sensitive to the subgrid closure. Similar results were reported by Meyers and Sagaut [137] who further noted a reduced dependency on β when employing a Gaussian filter.

CALIBRATION OF THE SGS MODEL CONSTANT As regards the value of the constant involved in the VMS model, a calibration has been derived by Hughes *et al.* [93] using the procedure due to Lilly [122]. The procedure assumes an infinite Reynolds number (infinite inertial range) and the calibration was obtained considering an isotropic sharp spectral filter for both the LES and high-pass filters. The most comprehensive work on the calibration of the model constant for the VMS approach is however the study by Meyers and Sagaut [136]. One of the most important results of this research is that the optimal model coefficient strongly depends on the choice of the LES and high-pass filters. Moreover, the authors have provided an analytical framework for the evaluation of the optimal model coefficient in the case of convolution filters. As already mentioned, the DG-projection filter is not a convolution filter and therefore special care is required to extend the conclusions of these works.

The studies cited above clearly outline that the performance of the VMS approach is strongly influenced by a number of parameters primarily associated with the LES and high-pass filters. Therefore the systematic and robust application of the DG-VMS approach can be improved by analysing these questions in the context of the DG-projection filter as both the LES filter and scale-separation operator. We analyse for this purpose the effect of the DG-LES filter on the ideal energy transfer and the validity of the assumption of absence of SGS dissipation acting on the largest resolved scales. The accuracy of the DG-VMS approach and the associated high-pass filter in replicating the ideal energy transfer will then be considered with the objective of identifying guidelines for the selection of the scale-fraction parameter.

10.3 THE IDEAL DG-LES SOLUTION

A-priori testing can provide valuable information about the accuracy of LES modeling approaches. The central question with this type of analysis is the definition of an appropriate ideal LES solution, which in the general case is not straightforward. It is, however, essential to answer this question, as the way in which this ideal solution is defined has a direct impact on the way the ideal SGS quantities are computed.

As discussed in Chap. 2 and in Sec. 4.7, two main approaches are used to derive the LES equations and to define the ideal LES solution. The classical approach, described in Sec. 2.4, consists in defining the ideal LES solution as the spatially filtered DNS solution. For this purpose convolution filters are conventionally employed such that for any function f we define the filtered function $\overline{f}(x) := \int_\Omega G(x-\xi)f(\xi)\mathrm{d}\xi$ with $G(x-\xi)$ being the filter kernel. The convolution filter can be applied to the Navier-Stokes (NS) equations such that the ideal LES solution satisfies the filtered NS equations in their strong form. One of the advantages of this approach is that the application of the convolution filter can be expressed in the Fourier space as $\hat{\overline{f}}(k) = \widehat{G}(k)\hat{f}(k)$ where $\widehat{(\cdot)}$ denotes the Fourier transform and it is easy to demonstrate that the convolution filter commutes with spatial derivatives. This approach however entirely ignores the details of the discretization employed and the fact that the LES solution so defined might not be an admissible solution of the considered discrete problem. Thus this approach presents serious limitations when extending the results of *a-priori* and theoretical analyses to FV and FE type methods.

As seen in Sec. 2.6, a second approach has been proposed by Pope [153] in which the LES solution is conceived as the projection of the DNS solution onto a set of local basis functions. It has been shown by Vreman [191] that an arbitrary orthogonal projection operator can be reformulated as a kernel filter such that for any function f we can indicate its projection as $f_h(x) := \mathbb{P}_h[f] = \int_\Omega K_p(x,\xi)f(\xi)\mathrm{d}\xi$. The use of a non uniform filter kernel $K_p(x,\xi)$ implies that in general the projection operation and differentiation do not commute. For this reason the closure problem needs to be redefined employing the semidiscrete weak form of the equations as described by Pope [153] and in the context of the VMS approach (*e. g.* in [50]).

This methodology provides a definition of the ideal resolved field which is consistent with the employed numerical discretization. Following this approach Beck *et al.* [19] have defined the ideal DG-LES solution as the L^2-projection of the DNS solution on the discretization space and identified the ideal subgrid stress to develop a Deep Neural Network turbulence model. Similarly van der Bos and Geurts [26] have defined the ideal DG-LES solution by means of a face-based projection to perform a systematic analysis of computational errors of DG-FEM for LES.

The use of a projection type filter however can introduce significant aliasing errors at wavenumbers close to the grid cut-off, producing unphysical reference data. This is a direct consequence of the approximation properties of polynomial basis functions [80].

In this work we propose to employ an alternative approach in which the ideal DG-LES solution is defined as the result of the application of two successive filtering operations. A first convolution filter is applied to the DNS data which filters out frequencies beyond the LES grid cut-off. Next, a L^2-projection of this filtered field is performed on the hp-discretization space (referred to in the following as DG-projection). This procedure reduces considerably the aliasing errors, introduced

by Pope's approach, while allowing the inclusion in the analysis of the effect of the *hp*-discretization associated with the adopted numerical method.

The following section provides a formal framework for the definition of the ideal DG-LES solution as described above and the expression of the corresponding ideal SGS energy transfer.

10.4 THE DG-LES FRAMEWORK AND THE IDEAL ENERGY TRANSFER

The *a-priori* analysis framework proposed in the present work is developed for incompressible flows. The NS equations for an incompressible flow read

$$\frac{\partial \mathbf{u}}{\partial t} + \boldsymbol{\nabla} \cdot \boldsymbol{\mathcal{F}}_c(\mathbf{u}, q) + \boldsymbol{\nabla} \cdot \boldsymbol{\mathcal{F}}_v(\mathbf{u}, \boldsymbol{\nabla}\mathbf{u}) = 0 \ , \qquad \forall \mathbf{x} \in \Omega, t \geq 0 \ , \tag{128}$$

$$\boldsymbol{\nabla} \cdot \mathbf{u} = 0 \ , \tag{129}$$

where we indicate as $\mathbf{u}$ is the velocity field, q is the pressure, and $\boldsymbol{\mathcal{F}}_c$ and $\boldsymbol{\mathcal{F}}_v$ are the convective and viscous fluxes, defined respectively as

$$\boldsymbol{\mathcal{F}}_c(\mathbf{u}, q) = \mathbf{u} \otimes \mathbf{u} + q\boldsymbol{I} \ , \tag{130}$$

$$\boldsymbol{\mathcal{F}}_v(\mathbf{u}, \boldsymbol{\nabla}\mathbf{u}) = \nu(\boldsymbol{\nabla}\mathbf{u} + (\boldsymbol{\nabla}\mathbf{u})^T) \ . \tag{131}$$

Following the DG discretization approach described in Chap. 3, we indicate as Ω_h a shape regular partition of Ω into N non-overlapping, non-empty elements of characteristic size h and as S_h^p the broken Sobolev space of piecewise polynomials of partial degree at most p. Then we indicate as $f_h := \mathbb{P}_{S_h^p}[f]$ the projection of any function f on the *hp*-discretization defined by the space S_h^p.

Following the approach described in the previous section, we define the ideal DG-LES solution as $\overline{\mathbf{u}}_h := \mathbb{P}_{S_h^p}[\overline{\mathbf{u}}]$, which is the result of the successive application to the velocity field $\mathbf{u}$ of a convolution filter and the DG-projection filter defined by the space S_h^p. The convolution filter employed in this work is a sharp spectral anisotropic filter with expression in spectral space $G(\mathbf{k}) = H(k_{\text{DG}} - \|\mathbf{k}\|_\infty)$ where $k_{\text{DG}} = \pi(p+1)/h$ and H is the Heaviside function.

Applying the convolution and DG-projection filter to Eq. (128), we derive the evolution equations for the ideal DG-LES solution

$$\begin{aligned}\frac{\partial}{\partial t}\int_{\Omega_h} \overline{\mathbf{u}}_h \phi \,\mathrm{d}\mathbf{x} + \sum_K \Bigg[\int_{\partial K} \overline{\boldsymbol{\mathcal{F}}}_c(\mathbf{u}, q) \cdot \mathbf{n}^+ \phi^+ \,\mathrm{d}\sigma - \int_K \overline{\boldsymbol{\mathcal{F}}}_c(\mathbf{u}, q) \cdot \boldsymbol{\nabla}\phi \,\mathrm{d}\mathbf{x} \\ + \int_{\partial K} \overline{\boldsymbol{\mathcal{F}}}_v(\mathbf{u}, \boldsymbol{\nabla}\mathbf{u}) \cdot \mathbf{n}^+ \phi^+ \,\mathrm{d}\sigma - \int_K \overline{\boldsymbol{\mathcal{F}}}_v(\mathbf{u}, \boldsymbol{\nabla}\mathbf{u}) \cdot \boldsymbol{\nabla}\phi \,\mathrm{d}\mathbf{x} \Bigg] = 0 \ , \quad \forall \phi \in S_h^p \ ,\end{aligned} \tag{132}$$

where we have used the commutation property of the convolution filter with spatial derivatives and the definition of the L^2-projection, which implies, $\int_{\Omega_h} (\overline{\mathbf{u}} - \overline{\mathbf{u}}_h)\phi = 0, \forall \phi \in S_h^p$.

As done in Chap. 3, the DG-LES equations can now be defined by rewriting Eq. (132) as

$$\frac{\partial}{\partial t}\int_{\Omega_h}\overline{\mathbf{u}}_h\phi\,\mathrm{d}\mathbf{x}+\overbrace{\sum_K\left[\int_{\partial K}\mathbf{h}_c(\overline{\mathbf{u}}_h^+,\overline{q}_h^+,\overline{\mathbf{u}}_h^-,\overline{q}_h^-,\mathbf{n}^+)\phi^+\,\mathrm{d}\sigma-\int_K\boldsymbol{\mathcal{F}}_c(\overline{\mathbf{u}}_h,\overline{q}_h)\cdot\boldsymbol{\nabla}\phi\,\mathrm{d}\mathbf{x}\right]}^{\mathcal{L}_c(\overline{\mathbf{u}}_h,\overline{q}_h,\phi)}+\underbrace{\sum_K\left[\int_{\partial K}\mathbf{h}_v(\overline{\mathbf{u}}_h^+,\overline{\mathbf{u}}_h^-,\mathbf{n}^+)\phi^+\,\mathrm{d}\sigma-\int_K\boldsymbol{\mathcal{F}}_v(\overline{\mathbf{u}}_h,\boldsymbol{\nabla}\overline{\mathbf{u}}_h)\cdot\boldsymbol{\nabla}\phi\,\mathrm{d}\mathbf{x}\right]}_{\nu\mathcal{L}_v(\overline{\mathbf{u}}_h,\phi)}=-\mathcal{R}(\mathbf{u},\overline{\mathbf{u}}_h,\phi)\quad,\quad\forall\phi\in S_h^p\quad. \tag{133}$$

In Eq. (133), $\mathcal{R}(\mathbf{u},\overline{\mathbf{u}}_h,\phi)$ is the subgrid-scale residual representing the effect of the unresolved scales $\mathbf{u}-\overline{\mathbf{u}}_h$ on the resolved field, which can be obtained by comparing Eq. (132) and Eq. (133). Note that, as the DG-projection filter does not commute with spatial derivation nor the convolution filter, in general both the pressure and viscous terms contribute to the subgrid-scale residual. In this work, however, we assume that the SGS term is dominated by convective effects thus the contribution of the viscous and pressure terms is neglected. This leads to the following form for the subgrid residual,

$$\begin{aligned}\mathcal{R}(\mathbf{u},\overline{\mathbf{u}}_h,\phi)\approx\sum_K\Bigg[&\int_K\left(\boldsymbol{\mathcal{F}}_c(\overline{\mathbf{u}}_h)-\overline{\boldsymbol{\mathcal{F}}}_c(\mathbf{u})\right)\cdot\boldsymbol{\nabla}\phi\,\mathrm{d}\mathbf{x}\\&-\int_{\partial K}\left(\mathbf{h}_c(\overline{\mathbf{u}}_h^+,\overline{\mathbf{u}}_h^-,\mathbf{n}^+)-\overline{\boldsymbol{\mathcal{F}}}_c(\mathbf{u})\cdot\mathbf{n}^+\right)\phi^+\,\mathrm{d}\sigma\Bigg]\quad.\end{aligned} \tag{134}$$

Indicating as $\{\psi_K^1\dots\psi_K^{N_p}\}\in\mathcal{P}^p(K)$ an orthonormal basis for $\mathcal{P}^p(K)$ with $\psi_K^i(\mathbf{x})=0$, $\forall\mathbf{x}\in K',K'\neq K$, the solution $\overline{\mathbf{u}}_h$ is expressed as a linear combination of the basis functions such that

$$\overline{\mathbf{u}}_h(\mathbf{x},t)=\sum_K\sum_{i=1}^{N_p}\widetilde{\overline{\mathbf{u}}}_h^{i,K}(t)\psi_K^i(\mathbf{x})\quad,\qquad\forall\mathbf{x}\in\Omega_h\quad, \tag{135}$$

where the modal coefficients $\widetilde{\overline{\mathbf{u}}}_h^{i,K}$ obey the following equation derived from Eq. (133)

$$\frac{\partial\widetilde{\overline{\mathbf{u}}}_h^{i,K}}{\partial t}+\mathcal{L}_c(\overline{\mathbf{u}}_h,\overline{q}_h,\psi_K^i)+\nu\mathcal{L}_v(\overline{\mathbf{u}}_h,\psi_K^i)+\mathcal{R}(\mathbf{u},\overline{\mathbf{u}}_h,\psi_K^i)=0\quad,\quad\forall K\in\Omega_h,\forall i=1\dots N_p\quad. \tag{136}$$

These equations can be combined to rewrite the semidiscrete DG-LES equations (133) as

$$\frac{\partial\overline{\mathbf{u}}_h}{\partial t}+\mathrm{L}_c(\overline{\mathbf{u}}_h,\overline{q}_h)+\nu\mathrm{L}_v(\overline{\mathbf{u}}_h)+\mathrm{R}(\mathbf{u},\overline{\mathbf{u}}_h)=0\quad, \tag{137}$$

where

$$\mathrm{L}_c := \sum_K \sum_i \mathcal{L}_c(\overline{\mathbf{u}}_h, \overline{q}_h, \psi_K^i)\psi_K^i \ , \tag{138}$$

$$\mathrm{L}_v := \sum_K \sum_i \mathcal{L}_v(\overline{\mathbf{u}}_h, \psi_K^i)\psi_K^i \ , \tag{139}$$

$$\mathrm{R} := \sum_K \sum_i \mathcal{R}(\mathbf{u}, \overline{\mathbf{u}}_h, \psi_K^i)\psi_K^i \ . \tag{140}$$

This leads to the following equation for the evolution of the energy associated to each wavenumber $\mathbf{k}$ of the resolved scales as

$$\frac{\partial E(\mathbf{k})}{\partial t} + \widehat{\overline{\mathbf{u}}_h}(\mathbf{k}) \cdot \widehat{\mathrm{L}}_c(\mathbf{k}) + \nu\widehat{\overline{\mathbf{u}}_h}(\mathbf{k}) \cdot \widehat{\mathrm{L}}_v(\mathbf{k}) + \widehat{\overline{\mathbf{u}}_h}(\mathbf{k}) \cdot \widehat{\mathrm{R}}(\mathbf{k}) = 0 \ . \tag{141}$$

The ideal energy transfer from the resolved modes of wavenumber k to all unresolved scales can therefore be obtained from the subgrid residual as

$$T_{sgs}(k) = \sum_{\|\mathbf{k}\|=k} \widehat{\overline{\mathbf{u}}_h}(\mathbf{k}) \cdot \widehat{\mathrm{R}}(\mathbf{k}) \ . \tag{142}$$

Positive values of T_{sgs} correspond to kinetic energy being transferred from resolved to unresolved scales, whereas negative values correspond to energy being transferred from unresolved to resolved scales, commonly indicated as backscatter.

Note that the use of the DG-projection filter introduces discontinuities in the filtered velocity field that need to be taken into account. It also requires the definition of the numerical flux $\mathbf{h}_c$ that appears in the surface integral in Eq. (134). The subgrid stress thus depends in general on both, the definition of the filter and the choice of this numerical flux. While this choice might appear arbitrary, it reflects the notion that the subgrid term which needs to be modelled must take into account the choice of the numerical discretization and the numerical dissipation thereby introduced.

In the *a-priori* analyses presented in the following, we are interested in investigating the ideal SGS dissipation in absence of dissipation introduced by the discretization of the convective flux. For this purpose we consider the central flux, namely

$$\mathbf{h}_c(\overline{\mathbf{u}}_h^+, \overline{\mathbf{u}}_h^-, \mathbf{n}) = \{\!\{\boldsymbol{\mathcal{F}}_c(\overline{\mathbf{u}}_h)\}\!\} \cdot \mathbf{n} \ . \tag{143}$$

10.4.1 *The modal energy transfer and eddy viscosity*

The analysis presented up to this point represents an extension of the classical energy transfer spectral/Fourier analysis. In the context of the DG method useful information can be extracted by performing this analysis in the modal/polynomial space. For this purpose, let us consider now Ω to be a cubic domain with Ω_h being a uniform Cartesian grid. We further consider a basis for S_h^p which is formed by

the tensor product of normalized Legendre polynomials of maximum degree p. We indicate as $\psi_K^{\mathbf{m}}$ the generic element of this basis such that $\mathbf{m} = (m_x, m_y, m_z)$ and

$$\psi_K^{\mathbf{m}} = l^{m_x}\left(\tfrac{x-x_{K,c}}{h/2}\right) l^{m_y}\left(\tfrac{y-y_{K,c}}{h/2}\right) l^{m_z}\left(\tfrac{z-z_{K,c}}{h/2}\right) \tag{144}$$

where $x_{K,c}$, $y_{K,c}$ and $z_{K,c}$ are the coordinates of the barycenter of K and l^i is the i-th Legendre polynomial normalized such that $\|\psi_K^{\mathbf{m}}\|_{L^2(\Omega_h)} = 1$.

We then define $W_h^m = \text{span}\left\{\psi_K^{\mathbf{m}}, \forall K \in \Omega_h, m - \frac{1}{2} < \|\mathbf{m}\| \leq m + \frac{1}{2}\right\}$, we call m the mode-number and define $\mathbb{P}_{W_h^m}[\overline{\mathbf{u}}_h]$ as the component of the DG-LES solution $\overline{\mathbf{u}}_h$ of mode-number m and the modal energy spectrum as

$$\tilde{E}(m) = \frac{1}{2}\int_{\Omega_h} \mathbb{P}_{W_h^m}[\overline{\mathbf{u}}_h] \cdot \mathbb{P}_{W_h^m}[\overline{\mathbf{u}}_h] \mathrm{d}\mathbf{x} \ . \tag{145}$$

As $\int_{\Omega_h}(\mathbb{P}_{W_h^m}[\overline{\mathbf{u}}_h] - \overline{\mathbf{u}}_h)\phi \mathrm{d}\mathbf{x} = 0$, $\forall \phi \in W_h^m$ and $W_h^m \subset S_h^p$, from Eq. (132) we can write

$$\int_{\Omega_h} \frac{\partial}{\partial t}\mathbb{P}_{W_h^m}[\overline{\mathbf{u}}_h]\phi \mathrm{d}\mathbf{x} + \mathcal{L}_c(\overline{\mathbf{u}}_h, \phi) + \nu\mathcal{L}_v(\overline{\mathbf{u}}_h, \phi) + \mathcal{R}(\mathbf{u}, \overline{\mathbf{u}}_h, \phi) = 0 \ , \qquad \forall \phi \in W_h^m \ , \tag{146}$$

and it can be immediately obtained that

$$\frac{\partial \tilde{E}(m)}{\partial t} + \mathcal{L}_c(\overline{\mathbf{u}}_h, \mathbb{P}_{W_h^m}[\overline{\mathbf{u}}_h]) + \nu\mathcal{L}_v(\overline{\mathbf{u}}_h, \mathbb{P}_{W_h^m}[\overline{\mathbf{u}}_h]) + \mathcal{R}(\mathbf{u}, \overline{\mathbf{u}}_h, \mathbb{P}_{W_h^m}[\overline{\mathbf{u}}_h]) = 0 \ . \tag{147}$$

Thus the modal energy transfer from the resolved scales of mode-number m to the unresolved scales can be evaluated as

$$\widetilde{T}_{sgs}(m) \coloneqq \mathcal{R}(\mathbf{u}, \overline{\mathbf{u}}_h, \mathbb{P}_{W_h^m}[\overline{\mathbf{u}}_h]) \ . \tag{148}$$

It is can be easily shown that Eq. (148) can be rewritten as

$$\widetilde{T}_{sgs}(m) = \sum_{K\in\Omega_h} \sum_{m-\frac{1}{2}<\|\mathbf{m}\|\leq m+\frac{1}{2}} \widetilde{\overline{\mathbf{u}}_h}^{\mathbf{m},K} \cdot \mathcal{R}(\mathbf{u}, \overline{\mathbf{u}}_h, \psi_K^{\mathbf{m}}) \ , \tag{149}$$

with $\widetilde{\overline{\mathbf{u}}_h}^{\mathbf{m},K} = \int_{\Omega_h} \overline{\mathbf{u}}_h \psi_K^{\mathbf{m}} \mathrm{d}\mathbf{x}$, which closely resembles Eq. (142) obtained in Fourier space. We thus introduce the concept of a modal eddy viscosity, defined as

$$\tilde{\nu}_e(m) \coloneqq \frac{\mathcal{R}(\mathbf{u}, \overline{\mathbf{u}}_h, \mathbb{P}_{W_h^m}[\overline{\mathbf{u}}_h])}{\mathcal{L}_v(\overline{\mathbf{u}}_h, \mathbb{P}_{W_h^m}[\overline{\mathbf{u}}_h])} \ , \tag{150}$$

which can be interpreted as an additional eddy viscosity which acts on the resolved modes similarly to the spectral eddy viscosity defined by Kraichnan [106].

We point out that neither the modal energy transfer nor the modal eddy viscosity necessarily have a physical meaning. This methodology is however useful as it can

be directly compared to the VMS approach and LES models based on a spectral vanishing viscosity such as that proposed by Karamanos and Karniadakis [100]. In the context of DG methods, these approaches are based on modifying the modal energy transfer or eddy viscosity provided by an SGS model as a function of $\mathbf{m}$. A similar energy transfer analysis has already been employed by Oberai *et al.* [147] to perform *a-priori* analyses of the VMS approach based on a FE method.

In the following, the modal eddy viscosity is presented normalized by the laminar viscosity

$$\tilde{\nu}_e^{\dagger}(m) := \frac{\tilde{\nu}_e(m)}{\nu} \ . \tag{151}$$

We point out that Eq. (150) depends on the discretization of the viscous terms. Therefore it provides the modal eddy viscosity which must be provided by the SGS model employing a chosen discretization. This approach highlights the relevance of taking into account the dissipation properties of the numerical scheme used for the discretization of the model term. In Sec. 10.6 and 10.7 results will be presented which are based on the BR1 scheme [15] and the BR2 scheme [16] described in Sec. 3.2.2.2.

10.5 THE MODELLED ENERGY TRANSFER AND THE DG-VMS APPROACH

As discussed in Sec. 2.5, the effect of the subgrid scales is approximated by a model term, here indicated as $\mathcal{L}_m(\overline{\mathbf{u}}_h, \phi)$, that depends only on the resolved field. This is usually obtained by discretizing an eddy-viscosity model like the Smagorinsky model described in Sec. 2.4.1.1.

By applying the same numerical treatment used for the viscous fluxes, the DG-LES model term can be written as,

$$\mathcal{L}_m(\overline{\mathbf{u}}_h, \phi) = \sum_K \left[\int_{\partial K} \mathbf{h}_m(\overline{\mathbf{u}}_h^+, \overline{\mathbf{u}}_h^-, \mathbf{n}^+)\phi^+ \mathrm{d}\sigma - \int_K \boldsymbol{\mathcal{F}}_m(\overline{\mathbf{u}}_h)\boldsymbol{\nabla}\phi \mathrm{d}\mathbf{x} \right] \ , \quad \forall \phi \in S_h^p \ , \tag{152}$$

where $\boldsymbol{\mathcal{F}}_m$ indicates here the model flux and $\mathbf{h}_m$ is the model numerical flux.

Following the approach presented above (see Sec. 10.4.1), the modelled spectral energy transfer can therefore be evaluated as

$$T_m(k) = \sum_{\|\mathbf{k}\|=k} \widehat{\overline{\mathbf{u}}_h}(\mathbf{k}) \cdot \widehat{\mathrm{L}_m}(\mathbf{k}) \quad \text{with} \quad \mathrm{L}_m := \sum_K \sum_{\mathbf{m}} \mathcal{L}_m(\overline{\mathbf{u}}_h, \psi_K^{\mathbf{m}})\psi_K^{\mathbf{m}} \ , \tag{153}$$

and the modelled modal energy transfer and eddy viscosity take the form

$$\widetilde{T}_m(m) := \mathcal{L}_m(\overline{\mathbf{u}}_h, \mathbb{P}_{W_h^m}[\overline{\mathbf{u}}_h]) \ , \quad \text{and} \quad \widetilde{\nu}_m^{\dagger}(m) := \frac{\mathcal{L}_m(\overline{\mathbf{u}}_h, \mathbb{P}_{W_h^m}[\overline{\mathbf{u}}_h])}{\nu \mathcal{L}_v(\overline{\mathbf{u}}_h, \mathbb{P}_{W_h^m}[\overline{\mathbf{u}}_h])} \ . \tag{154}$$

The DG-VMS approach is based on the separation of the resolved scales into large and small resolved scales by means of a projection filter. To this end, we separate

the solution space into a large-scale space $V^L := \bigcup_{m \leq p_L} W_h^m$ and a small-scale space $V^S := S_h^p \setminus V^L$, where p_L is the so-called scale-separation parameter and we indicate as $\beta = (p_L + 1)/(p + 1)$ the scale-fraction parameter. We note that other choices can be employed for the definition of the large-scale space and a further discussion on this topic is presented in App. D.

The original formulation of the VMS approach proposed by Hughes *et al.* [93] relies on two assumptions: the absence of energy transfer between the large resolved and the unresolved scales and the fact that the SGS model, here assumed to be the Smagorinsky model, should be evaluated from the small-resolved scales.

This leads to a model term which takes the form

$$\left(\boldsymbol{\nabla} \cdot \boldsymbol{\mathcal{F}}_m(\overline{\mathbf{u}}_h)\right)_{\text{s-s}} = \mathbb{P}_{V^s}\left[\boldsymbol{\nabla} \cdot \left(2\nu_{Smag}(\mathbb{P}_{V^s}[\boldsymbol{\nabla}\overline{\mathbf{u}}_h])\boldsymbol{S}(\mathbb{P}_{V^s}[\boldsymbol{\nabla}\overline{\mathbf{u}}_h])\right)\right] \quad . \tag{155}$$

This approach is commonly referred to as the *small-small* approach, as both the eddy viscosity and the strain rate tensor in the model term are computed directly from the small resolved scales. The outer filter operation restricts the action of the LES model only to the small-scale solution corresponding to mode-numbers higher than the scale-separation parameter. It corresponds therefore to the assumption $\widetilde{T}_{sgs}(m) \approx 0$ and $\widetilde{\nu}_{sgs} \approx 0$ for $m \leq p_L$.

We point out once more that the L^2-projection and differentiation do not commute, thus the order of the operations is important in the definition of the model term. In particular, we remark that while the effect of the model is applied to the small-scale solution, the model flux is computed from the filtered gradient [1] which does not correspond to the gradient of the small-scale solution. This distinction disappears in the original formulation employing a convolution filter.

Other variants of the VMS model have been proposed in the literature. They include the *large-small* [93] and the *all-small* [90] approaches which correspond to evaluating the eddy viscosity from either the low-pass filtered gradients or all the resolved scales.

Vreman [189] has proposed to discard the outer filter in Eq. (155) leading to

$$\left(\boldsymbol{\nabla} \cdot \boldsymbol{\mathcal{F}}_m(\overline{\mathbf{u}}_h)\right)_{\text{Vrem}} = \boldsymbol{\nabla} \cdot \left(2\nu_{Smag}(\mathbb{P}_{V^s}[\boldsymbol{\nabla}\overline{\mathbf{u}}_h])\boldsymbol{S}(\mathbb{P}_{V^s}[\boldsymbol{\nabla}\overline{\mathbf{u}}_h])\right) \quad . \tag{156}$$

This approach has led to qualitatively similar results to the *small-small* approach [189]. However it is not consistent with the original formulation by Hughes *et al.* [93] and is more closely related to the high-pass filtered Smagorinsky model [176]. This formulation has nonetheless the advantage of reducing the number of filtering operations required for the evaluation of the model. A large reduction of its computational cost can therefore be obtained for some formulations of the DG method (*e. g.* nodal DG).

1. When employing the BR1 and BR2 schemes this requires the use of the filtered lifted derivatives (see e.g. [68]).

Chapelier *et al.* [42] have proposed an *all-all* approach consisting in retaining only the outer filtering operation

$$(\boldsymbol{\nabla}\cdot\boldsymbol{\mathcal{F}}_m(\overline{\mathbf{u}}_h))_{\text{a-a}} = \mathbb{P}_{V^s}\left[\boldsymbol{\nabla}\cdot\left(2\nu_{Smag}(\boldsymbol{\nabla}\overline{\mathbf{u}}_h)\boldsymbol{S}(\boldsymbol{\nabla}\overline{\mathbf{u}}_h)\right)\right] \quad . \tag{157}$$

This approach is specifically tailored for the DG-modal formulation employing orthonormal hierarchical bases. In this case the outer filtering operation can be implicitly applied by removing the model term from the equation of the modal coefficients associated with the large-scale space basis functions. Thus the *all-all* approach presents the same computational cost as the standard Smagorinsky model for this class of methods.

In Sec. 10.7 the three variants of the DG-VMS approach here described are compared by analysing their accuracy in replicating the ideal energy transfer mechanism.

10.6 IDEAL ENERGY TRANSFER FROM DNS DATA

The methodology laid out in the Sec. 10.4 is applied to three DNS data sets of the TGV configuration at Re = 5 000, 20 000 and 40 000. The reference DNS have been performed using the sixth-order incompressible flow solver *Incompact3D* [115]. The considered computations have been obtained on a regular Cartesian mesh of respectively 1280^3, 3456^3 and 5400^3 nodes in a triperiodic domain of $[-\pi,\pi]^3$ using symmetries to divide by 8 the number of degrees of freedom (dofs) actually computed. A snapshot of each of these data sets at $t = 14$ (non-dimensional time units) is selected for analysis. At this time the flow is fully developed in a state close to isotropic and homogeneous conditions with values of the Reynolds number based on the Taylor microscale Re_λ = 136, 286 and 400 for Re = 5 000, 20 000 and 40 000 respectively.

In Fig. 83 we report the energy spectrum of the snapshot corresponding to Re = 5 000. On the same figure we report the energy spectra of the ideal DG-LES solution for $p = 7$ and respectively 72^3, 144^3 and 288^3 dofs, computed as described in App. C.

When analysing DG-LES simulation results it is assumed that the resolution limit is defined by the cut-off frequency $k_{\text{DG}} = \frac{\pi(p+1)}{h} = \frac{(p+1)n_{el}}{2}$ (marked by black dashed lines in Fig. 83) where n_{el} is the number of elements in one direction. By analysing Fig. 83, however, it can be observed that the DG-LES spectrum is almost undistinguishable from that corresponding to the DNS up to a frequency $\tilde{k}_{\text{DG}} = \frac{(p+1)n_{el}}{3}$ and decays rapidly for higher frequencies. Moreover, the energy spectrum is 'polluted' by the presence of discontinuities for frequencies close to k_{DG}. Additionally the discontinuities generate a tail on the energy spectrum that decays as k^{-2}. It is argued therefore that $\tilde{k}_{\text{DG}}$ is more relevant in identifying the resolving capabilities of the DG discretization. We will see in Sec. 10.6.2 that these observations are valid for other values of the polynomial degree p.

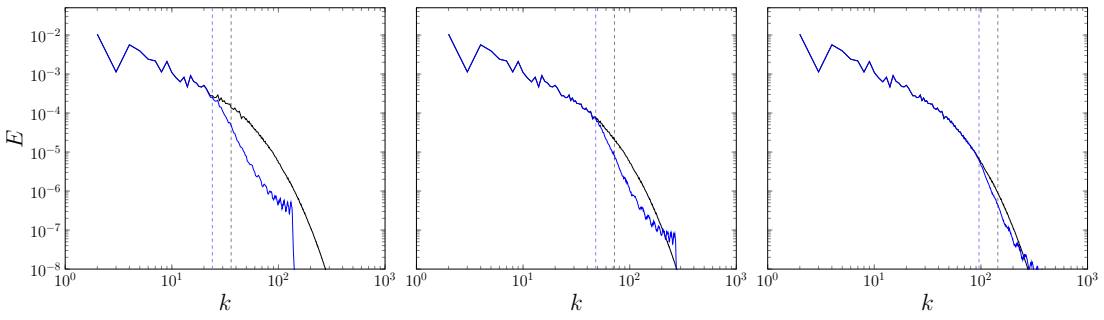

Figure 83 – TGV at Re = 5 000: Energy spectra from the DNS computation (black) and the ideal DG-LES solution (blue) for various discretizations: $p = 7$ and 72^3, 144^3 and 288^3 dofs. Dashed lines indicate the corresponding value of k_{DG} (black) and $\tilde{k}_{\mathrm{DG}}$ (blue).

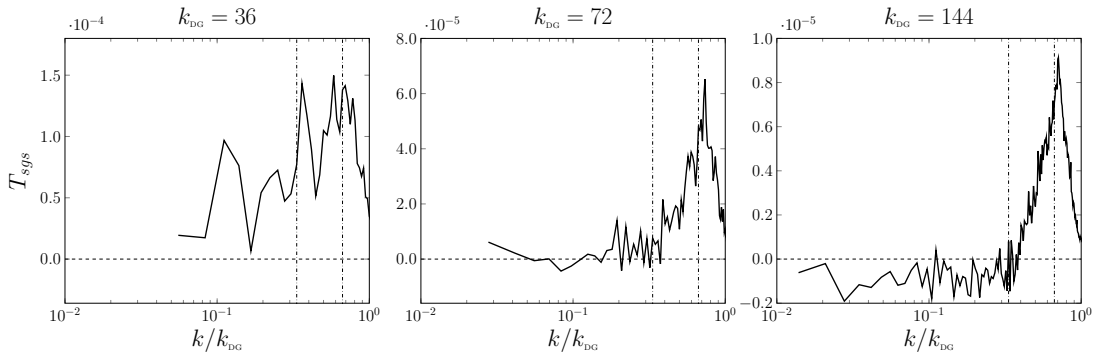

Figure 84 – TGV at Re = 5 000: Ideal SGS dissipation spectrum for three discretizations with $p = 7$. The values $\tilde{k}_{\mathrm{DG}}$ and $\tilde{k}_{\mathrm{DG}}/2$ are marked by dash-dotted lines.

The values of $\tilde{k}_{\mathrm{DG}}$ for the three discretizations considered are therefore also reported in Fig. 83. These frequencies fall respectively within the inertial range ($E \propto k^{-5/3}$), at the end of the inertial range and in the dissipation range.

In Fig. 84 we report the ideal SGS dissipation spectra, as defined in Eq. (142), computed for the three considered resolutions. In each plot, we observe that the dissipation spectrum presents a peak at $\tilde{k}_{\mathrm{DG}}$ and rapidly decays for higher frequencies. This behaviour is remarkably different as compared to the case of sharp spectral filters for which a cusp appears at the cut-off frequency. This observation further confirms the relevance of $\tilde{k}_{\mathrm{DG}}$ in identifying the resolving capabilities of the employed discretization.

As regards the lower frequencies, we observe that for the coarsest employed discretization the interaction between the largest-resolved scales and the unresolved scales is non-negligible. As the value of $\tilde{k}_{\mathrm{DG}}$ is moved toward the dissipation range, we observe from the middle and right panel of Fig. 84 a clearly different behaviour. In this case the ideal energy transfer is negligible up to a frequency corresponding

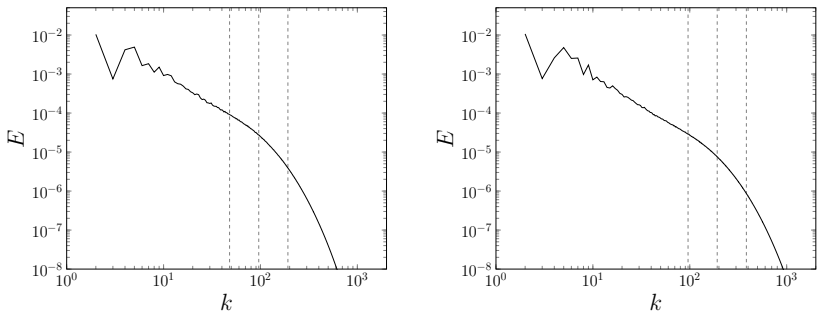

Figure 85 – Energy spectra and relevant values of $\tilde{k}_{DG}$ for the TGV at Re = 20 000 (left), 40 000 (right).

to $\tilde{k}_{DG}/2 = k_{DG}/3$ and the dissipation spectrum rapidly increases up to $\tilde{k}_{DG}$ corresponding to a hyperviscous-type behaviour. A sharper peak of the SGS dissipation spectrum is observed as the resolution is increased. Additionally for the finest resolution considered $k_{DG} = 144$ the ideal energy transfer is negative for frequencies below $k_{DG}/3$ corresponding to backscatter. While similar results are seldom presented in the literature, we mention that both Domaradzki [60] and Métais and Lesieur [134] reported negative values of the eddy viscosity in the smallest wavenumber range employing an isotropic sharp spectral filter with cut-off frequency in the dissipation range. Moreover Métais and Lesieur [134] have shown that with this type of LES filter a negative value of the plateau of the eddy viscosity is obtained assuming an energy spectrum $E(k) \propto k^{-m}$ with $m \geq 5$.

In order to analyse the generality of these observations we consider now the TGV configuration at higher Reynolds numbers, namely Re = 20 000 and 40 000. The corresponding energy spectra are reported in Fig. 85 as well as the values of $\tilde{k}_{DG}$ corresponding to three discretizations considered. These discretizations correspond to $p = 7$ and a number of dofs equal to 144^3, 288^3 and 576^3 for the lower Reynolds number and 288^3, 576^3 and 1152^3 for the higher Reynolds number configuration. For both configurations the coarsest discretizations correspond to $\tilde{k}_{DG}$ in the inertial range, whereas the finer discretizations correspond respectively to $\tilde{k}_{DG}$ at the end of the inertial range and $\tilde{k}_{DG}$ in the dissipation range.

For both configurations and all resolutions considered we observe in Figs. 86 and 87 again a peak of the dissipation spectrum at $\tilde{k}_{DG}$ and a rapid decay towards k_{DG}, confirming the results obtained for the configuration at Re = 5 000. In this case, however, for the two lower resolutions, with $\tilde{k}_{DG}$ located in the inertial range, we observe a mixed viscous-hyperviscous behaviour. The viscous type behaviour, corresponding to an ideal SGS dissipation spectrum which scales as $k^{\frac{1}{3}}$, is dominant for the low and intermediate wavenumbers up to approximately $k_{DG}/3$ whereas the hyperviscous behaviour is dominant for higher frequencies up to $\tilde{k}_{DG}$.

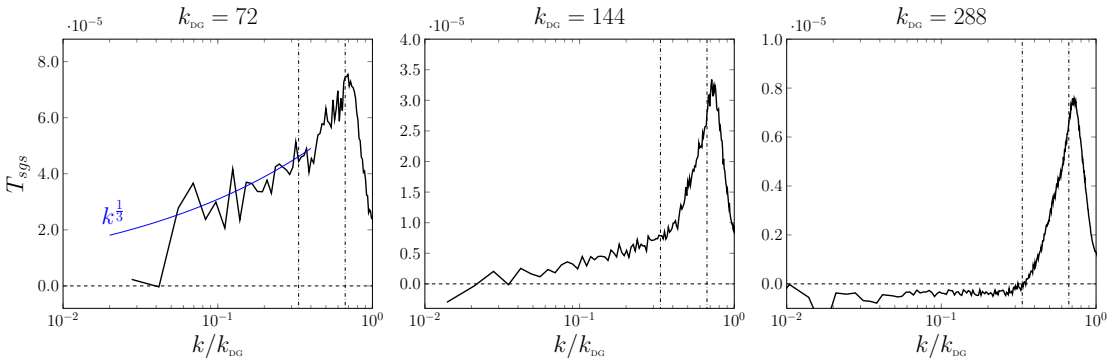

Figure 86 – TGV at Re = 20 000: Ideal SGS dissipation spectrum for three discretizations with $p = 7$. The values $\tilde{k}_{DG}$ and $\tilde{k}_{DG}/2$ are marked by dash-dotted lines.

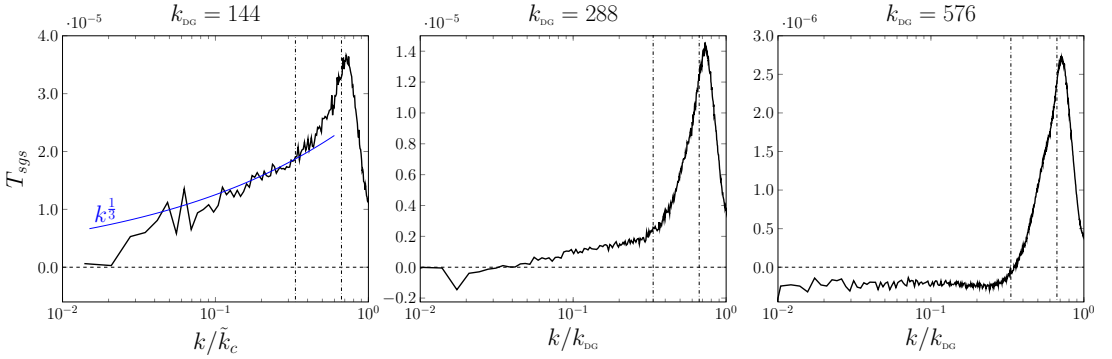

Figure 87 – TGV at Re = 40 000: Ideal SGS dissipation spectrum for three discretizations with $p = 7$. The values $\tilde{k}_{DG}$ and $\tilde{k}_{DG}/2$ are marked by dash-dotted lines.

However, as resolution is increased, the contribution of wavenumbers below $k_{DG}/3$ to the total SGS dissipation is progressively reduced and most of the SGS dissipation acts on the frequencies $[k_{DG}/3, k_{DG}]$. Eventually, as the resolution is further increased and $\tilde{k}_{DG}$ moves into the dissipation range, the interaction between the large-resolved scales and unresolved scales becomes negligible. This can be observed in the right panels of Figs. 86 and 87. In this case, the energy transfer is dominated by the SGS dissipation acting on frequencies $[k_{DG}/3, k_{DG}]$. For frequencies below $k_{DG}/3$ the energy transfer is predominantly negative corresponding to backscatter.

The results obtained therefore indicate that the large-resolved scales are free of interaction with the unresolved ones only when the DG-LES limit of resolution falls at the end of the inertial range and within the dissipation range. When a coarser resolution is employed, a mixed viscous-hyperviscous type behaviour can be observed and the SGS dissipation acting on the large-resolved scales is not negligible.

The mixed type behaviour is not observed in Fig. 84 as the TGV at Re = 5 000 presents a very short inertial range.

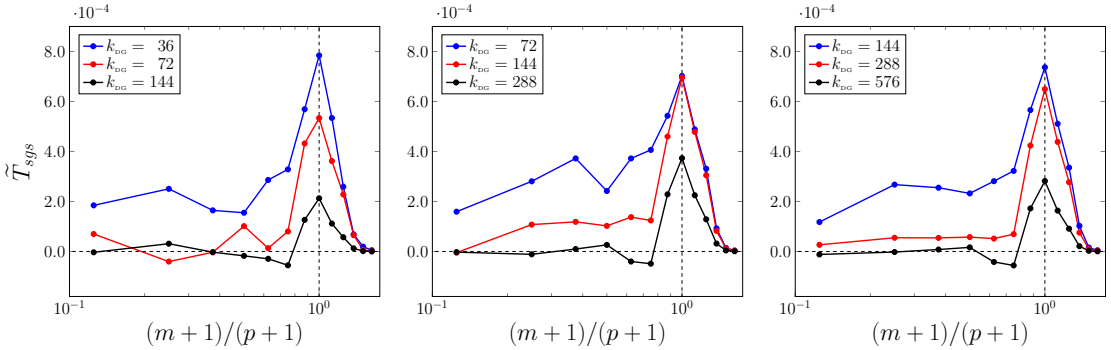

Figure 88 – Modal energy transfer for the ideal SGS stress for the TGV at Re = 5 000 (left), 20 000 (center), and 40 000 (right) for various discretizations with $p = 7$.

10.6.1 *Ideal modal energy transfer and eddy viscosity*

We now analyse the modal energy transfer as defined by Eq. (148) for the same configurations described in the previous section. Obtained results are reported in Fig. 88. We observe a remarkably consistent behaviour across all resolutions and Reynolds numbers considered. A first region can be identified which is characterized by a nearly constant modal energy transfer for mode-numbers m from 0 to 5. The modal energy transfer then increases rapidly presenting a peak at $m = p$ and then decreases smoothly for higher mode-numbers. We remark that these two different behaviours are separated by the same mode-number corresponding to $(m+1)/(p+1) = 0.75$ for all the discretizations and Reynolds numbers considered.

As we would expect from the previous analysis in Fourier space, the energy transferred to modes corresponding to low mode-numbers is not in general negligible. As the discretization is refined this value progressively decreases and the energy transfer mechanism is dominated by the SGS dissipation acting on modes $(m+1)/(p+1) > 0.75$.

To further verify that this result is not specific to the chosen resolutions, we report in Fig. 89 the modal energy transfer obtained at Re = 20 000 for 9 discretizations with $p = 7$ and a number of dofs between 144^3 and 576^3. This figure clearly illustrates the consistency of the described behaviour. We further observe that for relatively coarse discretizations as the resolution is increased, the main effect is to reduce the modal energy transfer at low mode-numbers. Only when the resolution limit is in the dissipation range ($k_{DG} > 168$) we observe a significant reduction of the peak value as the discretization is further refined.

The ideal modal eddy viscosity, as defined in Eq. (150) using the BR1 scheme for the viscous discretization, is reported in Fig. 90 for the three Reynolds numbers and discretizations.

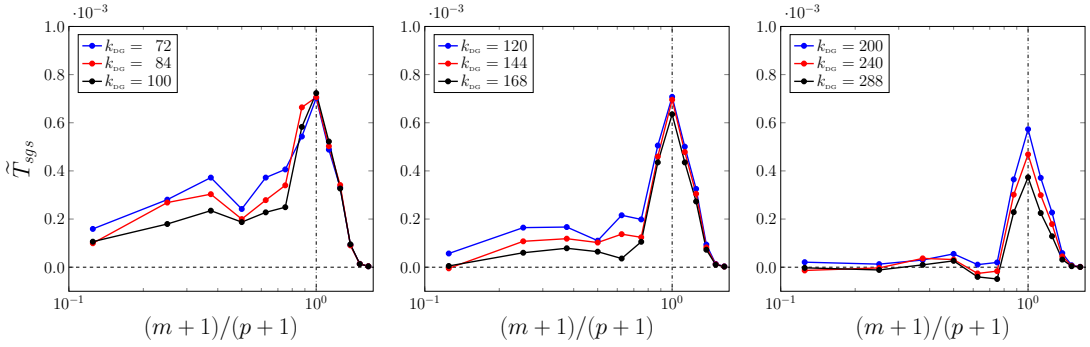

Figure 89 – TGV at Re = 20 000: Modal energy transfer for the ideal SGS stress for several discretizations with $p = 7$.

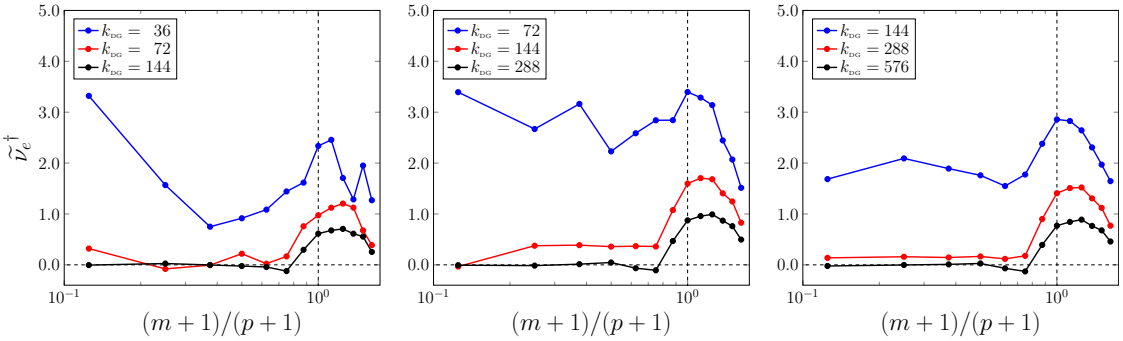

Figure 90 – Ideal modal eddy viscosity for the ideal subgrid stress for the TGV at Re = 5 000 (left), 20 000 (center), 40 000 (right) for various discretizations with $p = 7$.

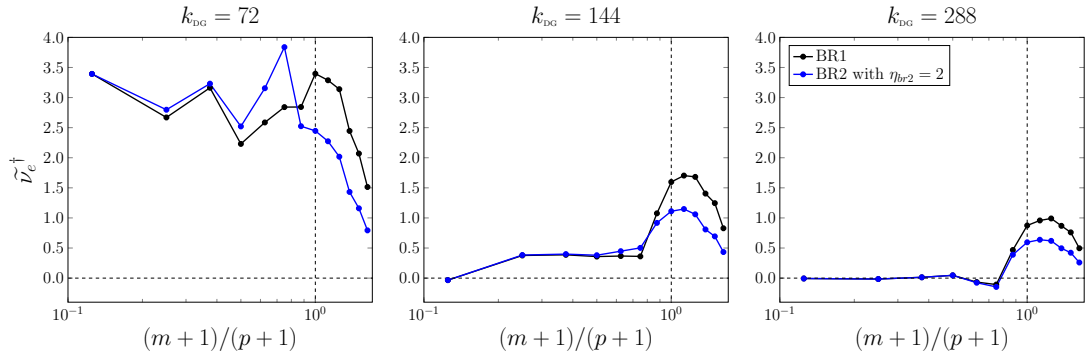

Figure 91 – TGV at Re = 20 000: Ideal modal eddy viscosity for the ideal SGS stress using the BR1 and BR2 schemes.

Similarly to what has been observed for the modal energy transfer, the modal eddy viscosity presents a plateau at mode-numbers $m \leq 5$ and increases for higher mode-numbers. In contrast to the modal dissipation spectrum, however, the modal eddy viscosity presents in general a 'parabolic' shape (in place of a spike) with a smoother increase and decay for relatively high mode-numbers.

We remark that the values reported in Fig. 90 correspond to the ideal modal eddy viscosity that should be provided by the SGS model employing the BR1 discretization. In Fig. 91 we compare this value with the modal eddy viscosity corresponding to the BR2 scheme with $\eta_{br2} = 2$.

As expected the additional dissipation provided by the BR2 scheme leads to a reduction of the modal eddy viscosity required at the higher mode-numbers. This result agrees with the observation that the optimal LES model must be aware of the discretization employed due to their interaction in actual simulations.

To conclude this analysis we observe that all the obtained results indicate that the interaction between large-resolved scales and unresolved ones, when employing the DG-LES filter, is negligible only for finite Reynolds numbers when the turbulent scales are resolved up to the end of the inertial range. Based on these findings, it could be argued that models based on this assumption present a limited applicability as they would rely on high resolution being available and thus provide a limited computational gain as compared to (underresolved) DNS. We want to remark however that the resolution requirements in an actual simulation vary in space and time and thus this assumption might be locally valid. This is the case for transitional or spatially inhomogeneous flows.

As an example, we illustrate in Fig. 92 the modal energy transfer for the TGV at Re = 20 000 at various times for a discretization corresponding the intermediate resolution considered ($p = 7$, $n_{el} = 36$ and 288^3 dofs). It can be observed that the SGS dissipation rapidly increases during the transition phase (left panel of Fig. 92) and

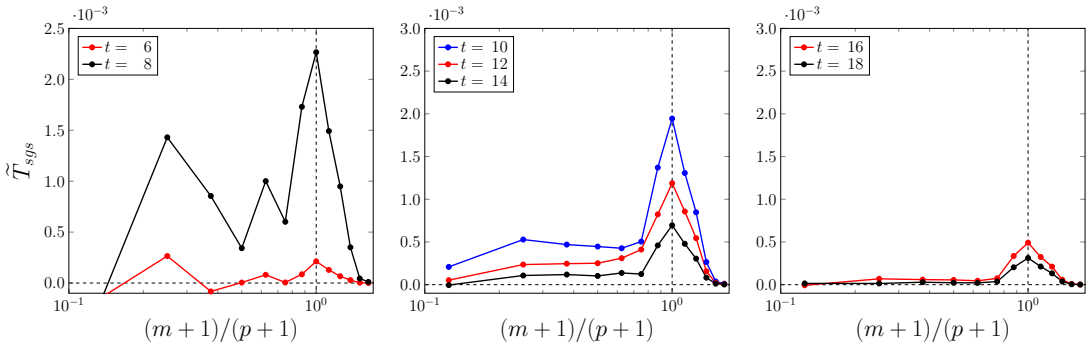

Figure 92 – TGV at Re = 20 000: Ideal modal energy transfer for the ideal SGS stress at various times for $p = 7$ and 288^3 dofs.

the energy transfer from large scales remains non negligible during the first part of the decay phase (central panel). However for $t > 14$ the resolution is sufficient such that the energy transfer from modes $m \leq 5$ is clearly negligible (right panel). Thus the ideal LES model should be able to adapt to each of these conditions by reducing the SGS model dissipation applied to large scales during the initial transition phase and late dissipation phase.

10.6.2 *Sensitivity to the polynomial degree*

In this section we investigate the generality of the obtained results by analysing discretizations corresponding to various values of the polynomial degree p. All the results here reported have been obtained from a snapshot at $t = 14$ of the TGV at Re = 20 000. The comparisons are carried out by fixing the total number of dofs to the same values employed in Sec. 10.6, that is 144^3, 288^3 and 576^3 dofs. Four values of the polynomial degree are at first considered: $p = 5, 7, 8$, and 11.

Fig. 93 presents the energy spectra of the DNS data set and the ideal DG-LES solutions for all considered discretizations. We observe that for a fixed number of dofs the energy spectra are almost identical up to k_{DG} and, as mentioned in the previous section (see Fig. 83), identical to the DNS spectrum up to $\tilde{k}_{\mathrm{DG}}$. The most notable differences appear in the tail of the spectra related to the discontinuities of the DG-LES solutions. Thus we can reasonably conclude that increasing the polynomial degree for a fixed number of dofs has a limited effect on the resolving capabilities of the DG-LES method. [2]

2. This observation only concerns the accuracy of the considered solution space in representing the DNS solution. It does not take into account the dissipation properties of the numerical fluxes as done *e. g.* by Moura *et al.* [142].

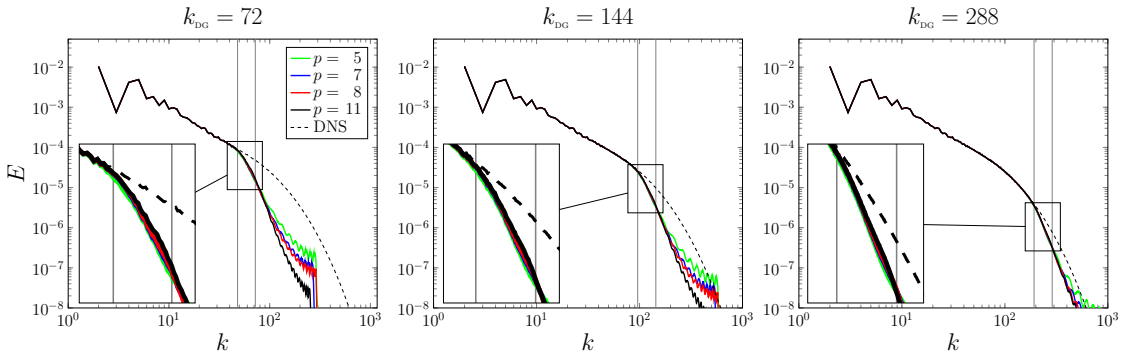

Figure 93 – TGV at Re = 20 000: Energy spectra of the DNS data and the ideal DG-LES solution for various discretizations for 144^3, 288^3 and 576^3 dofs. Close-up view at frequencies between $\tilde{k}_{DG}$ and k_{DG}.

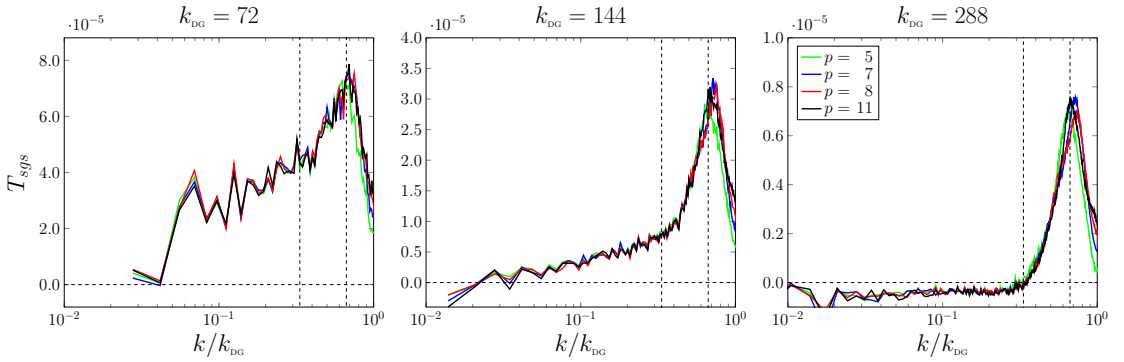

Figure 94 – TGV at Re = 20 000: Ideal SGS dissipation spectrum for various discretizations for 144^3, 288^3 and 576^3 dofs. Dashed lines mark values of $\tilde{k}_{DG}$ and $\tilde{k}_{DG}/2$.

This conclusion is also confirmed by analysing Fig. 94 which reports the SGS dissipation spectrum. Indeed the same behaviour can be observed for all polynomial degrees confirming the generality of the conclusions drawn in the previous section.

In Figs. 95 and 96 we report the modal energy transfer and eddy viscosity. The modal energy transfer levels cannot be directly compared, as a different number of modes is retained for each polynomial degree, however we can observe that the same trend seen for $p = 7$ (see Sec. 10.6.1) is obtained for the other discretizations. In particular, we remark the presence of nearly constant value for mode-numbers up to approximately $m+1 = 0.75(p+1)$ and a peak at $m = p$ for the modal energy transfer. The generality of our conclusions is further illustrated by Fig. 96 which demonstrates the close agreement of the modal eddy viscosity for all discretizations and confirms the relevance of the mode-number $m+1 = 0.75(p+1)$ in separating the two different behaviours.

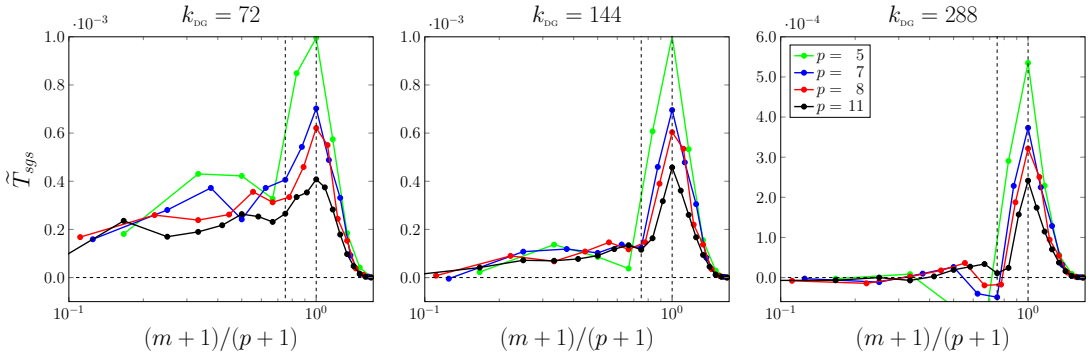

Figure 95 – TGV at Re = 20 000: Ideal modal energy transfer for various discretizations for 144^3, 288^3 and 576^3 dofs. Dashed lines indicate mode-numbers $m + 1 = 0.75(p + 1)$ and $m = p$.

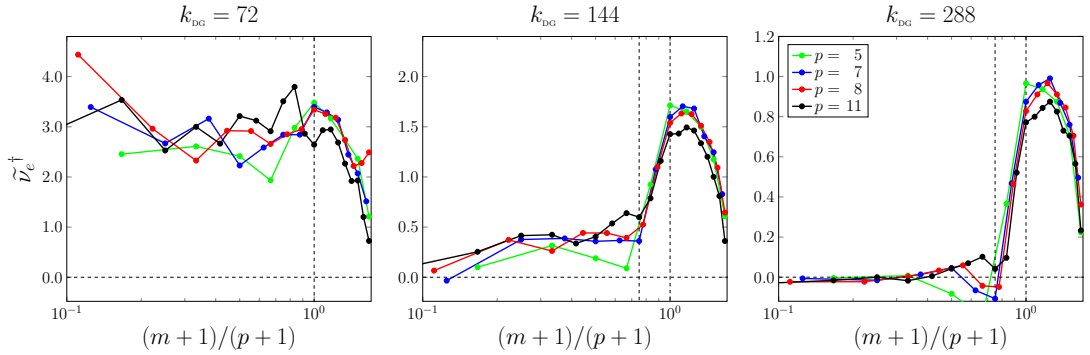

Figure 96 – TGV at Re = 20 000: Ideal modal eddy viscosity for various discretizations for 144^3, 288^3 and 576^3 dofs. Dashed lines indicate mode-numbers $m + 1 = 0.75(p + 1)$ and $m = p$.

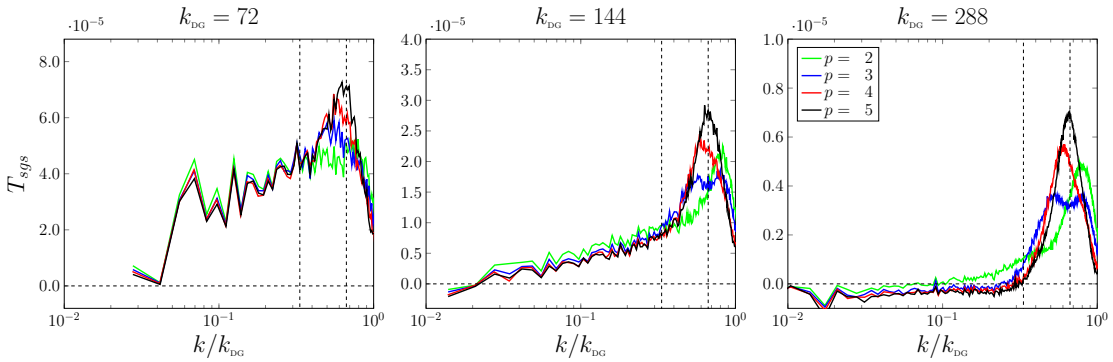

Figure 97 – TGV at Re = 20 000: Ideal SGS dissipation spectrum for various discretizations for 144^3, 288^3 and 576^3 dofs. Dashed lines mark values of $\tilde{k}_{DG}$ and $\tilde{k}_{DG}/2$.

We consider now relatively lower polynomial degree representations: $p = 2$, 3, 4 and 5. The energy spectra for all discretizations are not reported here as they lead to the same conclusions drawn from Fig. 93. More marked differences can be observed in Figs. 97 and 98 reporting the ideal SGS dissipation spectrum and modal eddy viscosity. Overall a similar behaviour can be recognized for different values of p in Fig. 97. As observed for relatively higher values of p, as the resolution is increased the SGS dissipation concentrates on the scales characterized by higher wavenumbers, and eventually the SGS dissipation acting on wavenumbers lower than $k_{DG}/3$ becomes negligible. In constrast with the results obtained for higher polynomial degrees, the presence, location and value of the peak of the SGS dissipation spectrum appear to be dependent on the polynomial degree for $p \leq 4$.

Similarly, in Fig. 98 we observe relatively marked differences in the modal eddy viscosity for different values of p. As the resolution is increased the SGS dissipation acts on the highest modenumbers. However compared to Fig. 96, no real plateau can be identified for the modal eddy viscosity at low modenumbers. For the highest resolution (right panel of Fig. 98) relatively higher values of the modal eddy viscosity are obtained for $m + 1 \geq 0.75(p + 1)$, similarly to what observed for $p \geq 5$, however, markedly negative values are obtained for the modal viscosity at low modenumbers.

10.6.3 *Effect of the DG-LES filter*

As discussed in Sec. 10.3, all the results presented have been obtained by defining the ideal DG-LES solution as the L^2-projection on the discretization space of the DNS solution filtered with a sharp spectral filter removing frequencies $\|\mathbf{k}\|_\infty \geq k_{DG}$. Other possible definitions can be considered. Among them, the L^2-projection of the DNS solution on the DG discretization space is an interesting candidate.

The effect of these two different definitions on the results obtained is therefore investigated. For this purpose we employ the snapshot at $t = 14$ of the TGV at

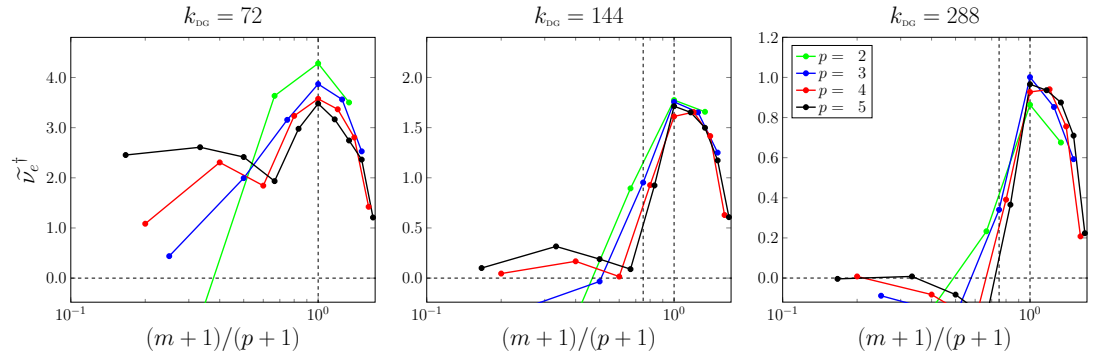

Figure 98 – TGV at Re = 20 000: Ideal modal eddy viscosity for various discretizations for 144^3, 288^3 and 576^3 dofs. Dashed lines indicate mode-numbers $m + 1 = 0.75(p + 1)$ and $m = p$.

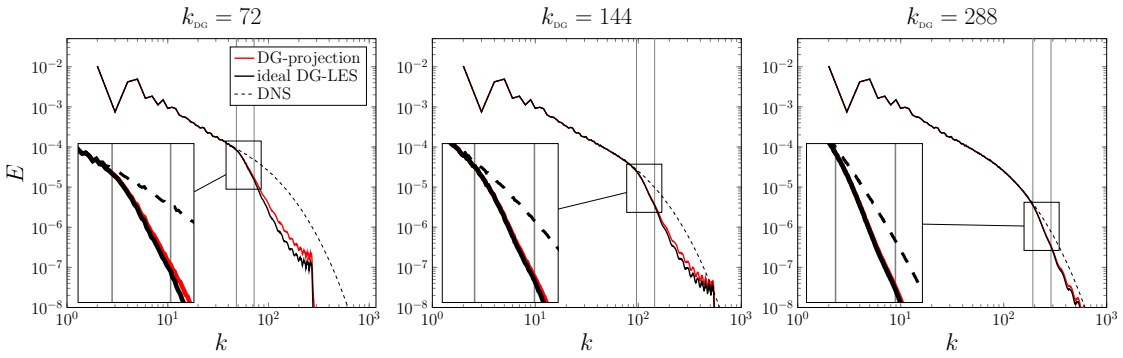

Figure 99 – TGV at Re = 20 000: Energy spectra of the DNS data, the ideal DG-LES solution, and DG-projection for three resolutions with $p = 7$. Close-up view for frequencies between $\tilde{k}_{DG}$ and k_{DG}.

Re = 20 000. In order to simplify the notation we will refer to the L^2-projection of the DNS solution on the DG space as simply the DG-projection in contrast to the employed definition of ideal DG-LES solution.

In Fig. 99 we report the energy spectra corresponding to the ideal DG-LES and the DG-projection for three resolutions. We observe that for all resolutions the energy spectra are indistinguishable for frequencies up to $\tilde{k}_{DG}$. Moreover we notice remarkably higher values of the tail of the energy spectra for the DG-projection which is especially evident in the coarsest resolution (left panel of Fig. 99). This indicates, as one would expect, that the L^2-projection of the DNS field presents stronger discontinuities than the L^2-projection of the filtered field. Nonetheless, $\tilde{k}_{DG}$ appears to be a relevant frequency identifying the resolution properties of DG using both definitions.

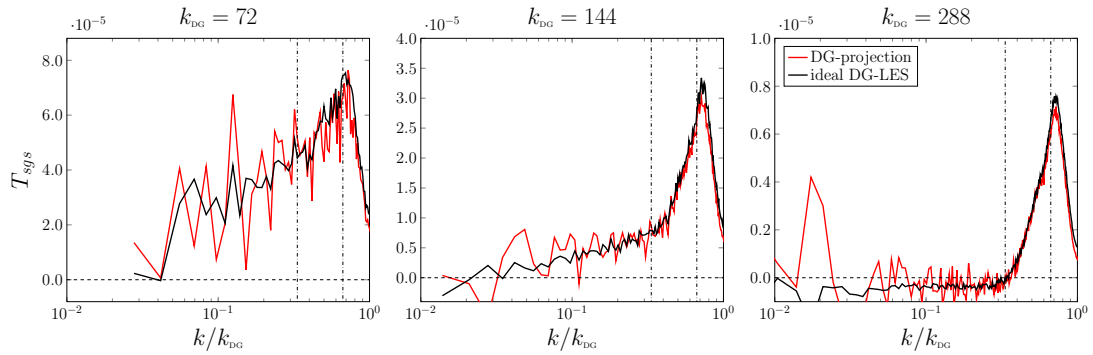

Figure 100 – TGV at Re = 20 000: Ideal SGS dissipation spectrum of the ideal DG-LES solution and the DG-projection for three discretizations with $p = 7$. Dashed lines mark values of $\tilde{k}_{DG}$ and $\tilde{k}_{DG}/2$.

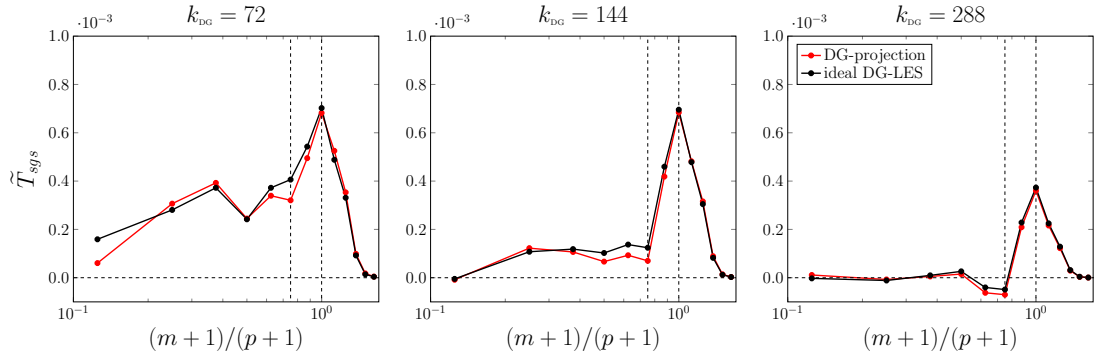

Figure 101 – TGV at Re = 20 000: Ideal modal energy transfer of the ideal DG-LES solution and the DG-projection for three discretizations with $p = 7$. Dashed lines indicate mode-numbers $m + 1 = 0.75(p + 1)$ and $m = p$.

In Fig. 100 and 101 we present the spectral and modal energy transfer for the same resolutions. These figures illustrate a fair agreement between results obtained with the two definitions. The most remarkable differences appear in Fig. 100 for the relatively low frequencies. Indeed the DG-projection leads to a more erratic behaviour of the spectral energy transfer which could be explained by the presence of aliasing errors as described in Sec. 10.3.

Slightly more significant differences can be observed in Fig. 102 which reports the modal eddy viscosity employing the BR1 scheme. In this figure we can identify lower values of the modal eddy viscosity at relatively high mode-numbers. These can be explained by the presence of stronger discontinuities and higher values of the lifting coefficients used for the BR1 scheme and therefore, higher values of the diffusive term in the denominator of Eq. (150) at high mode-numbers.

Overall the results obtained demonstrate that, with the exception of small differences, the definition of the reference DG-LES solution as the L^2-projection of the DNS

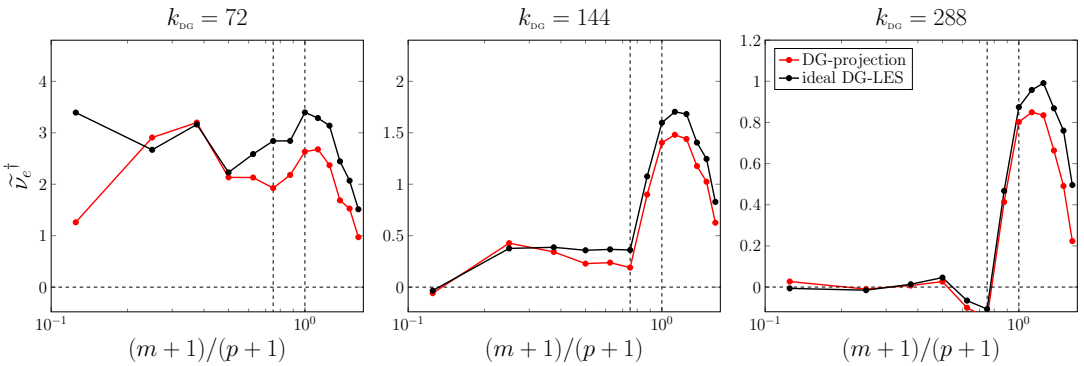

Figure 102 – TGV at Re = 20 000: Ideal modal eddy viscosity of the ideal DG-LES solution and the DG-projection for three dirscretizations with $p = 7$. Dashed lines indicate mode-numbers $m + 1 = 0.75(p + 1)$ and $m = p$.

field leads to the same conclusions drawn by employing the current definition of the ideal DG-LES solution.

10.7 A-PRIORI ANALYSIS OF THE DG-VMS APPROACH

In this section, we perform an *a-priori* analysis of the DG-VMS model based on the three variants described in Sec. 10.5. For this purpose, we evaluate the DG-VMS model from the ideal DG-LES solution corresponding to Re = 20 000 and $t = 14$ for $p = 7$ and $n_{el} = 72$. As described in the previous section, for this Reynolds number and discretization considered the resolution limit, $\tilde{k}_{DG} = 192$, falls within the dissipation range. Under these conditions the interaction between large-resolved and unresolved scales is negligible (see Fig. 86) and we expect the DG-VMS approach to recover the ideal SGS dissipation.

The three variants of the DG-VMS model are therefore evaluated from this solution for different values of the scale fraction parameter β. For all three variants we do not consider the calibration of the model coefficients, as described *e. g.* by Meyers *et al.* [138], as a function of β. One reason for not employing such calibration is that it is derived for convolution filters. As we have observed in Sec. 10.3, this is not the case for the DG-projection and additional care is required to derive a consistent calibration procedure. Additionally it has been shown by Meyers *et al.* [138] that the model constant is dependent on the ratio Δ/η, where η is the Kolmogorov scale, when $\Delta/\eta \leqslant 100$. This is the case when the DG-LES resolution falls at the beginning of the dissipation range as considered here. Thus we also make no attempt at providing a general calibration of the model coefficient from the employed DNS/LES data as the results would be dependent on this parameter in the range of validity of the DG-VMS approach. In order to facilitate the analysis, all the results are presented with the model constant selected such that the modelled dissipation spectrum presents the

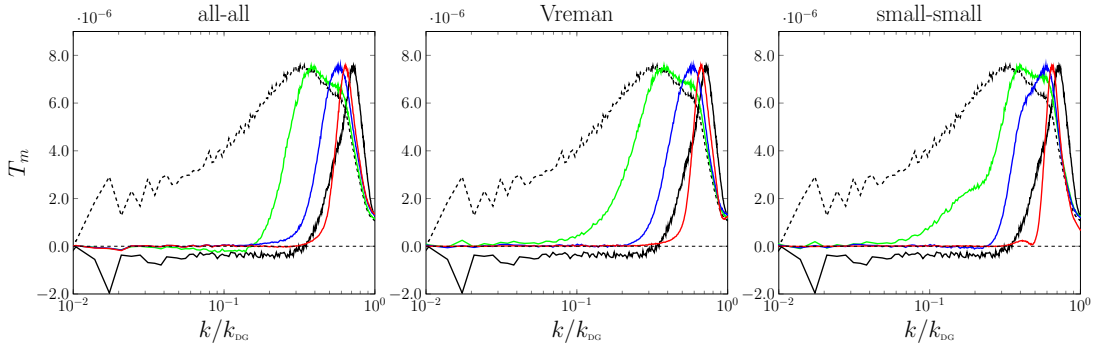

Figure 103 – TGV at Re = 20 000, $p = 7$, $k_{DG} = 288$: Ideal SGS energy transfer (black solid), SGS model dissipation spectrum provided by the Smagorinsky model (dashed) and three variants of the DG-VMS approach for: $\beta = 0.25$ (green), $\beta = 0.5$ (blue), and $\beta = 0.75$ (red) using the BR1 scheme.

same maximum value as that of the ideal SGS dissipation spectrum. The employed values of the model coefficient are reported in Table 7.

	BR1			BR2 $\eta_{br2} = 2$		
	$\beta = 0.25$	$\beta = 0.5$	$\beta = 0.75$	$\beta = 0.25$	$\beta = 0.5$	$\beta = 0.75$
all-all	0.093	0.103	0.122	0.094	0.096	0.098
Vreman	0.099	0.120	0.181	0.099	0.117	0.162
small-small	0.102	0.122	0.156	0.103	0.112	0.139
Smagorinsky		0.090			0.090	

Table 7 – TGV at Re = 20 000, $p = 7$, $k_{DG} = 288$: Model coefficients selected for the Smagorinsky and DG-VMS model using the BR1 and BR2 schemes.

In Fig. 103 we report the ideal and model SGS dissipation spectrum corresponding to the Smagorinsky model and the three variants of the DG-VMS approach using the BR1 discretization scheme.

It is obvious from this figure that, as already shown by other authors, the Smagorinsky model provides excessive dissipation at low wavenumbers. This effect is drastically reduced by employing all the considered variants of the DG-VMS approach. As expected, increasing the value of β restricts the action of the SGS model on progressively finer scales and, for a fixed model constant, reduces the total SGS dissipation.

In particular for $\beta = 0.75$ the SGS model acts only on the range of scales $[k_{DG}/3, k_{DG}]$. For lower values of β however the distribution of the modelled SGS dissipation does not correspond to the ideal SGS dissipation for any of the considered discretizations.

This effect is particularly marked for $\beta < 0.5$ and has also been observed by employing the DG-LES solution at the intermediate resolution $k_{\mathrm{DG}} = 144$ (not reported here).

We further remark that the SGS dissipation spectrum decays smoothly for low wavenumbers for all variants of the DG-VMS approach. This is expected as the high-pass projection filter is not sharp in Fourier space. As Sagaut and Levasseur [169] have shown that a smooth decay of the SGS dissipation spectrum leads to improved results in *a-posteriori* tests, this result demonstrates an advantage of using a modal decomposition as opposed to an orthogonal spectral filter.

Among the three variants, the all-all approach presents the smoothest behaviour at low wavenumbers and the small-small approach presents the sharpest behaviour. Moreover we identify the presence of bumps in the SGS dissipation spectrum of the small-small variant, clearly visible for $\beta = 0.25$ in Fig. 103. These results indicate an advantage of the Vreman variant with respect to the small-small approach. Indeed, we recall that the eddy viscosity and the strain rate are evaluated in the same way for the two variants and the obtained results show that removing the outer projection operation leads to a smoother SGS dissipation spectrum for a lower computational cost.

Comparing the all-all and the Vreman approaches is not as straightforward. Indeed we observe that the all-all variant presents a marginally better agreement with the ideal SGS dissipation spectrum and we recall that the it presents a much lower computational cost for modal DG methods. However, in contrast to the all-all variant, for the Vreman approach the SGS model is computed from the filtered gradients. For this reason the SGS stress is aligned with the small-scale gradients and tends to zero when the flow is well resolved and the solution is represented entirely by the large-scale component. An analysis of the alignment between the ideal SGS stress and the modelled one could therefore be employed in order to draw more definitive conclusions.

Further analysing Fig. 103 we observe that, despite presenting a smooth decrease of the dissipation spectrum towards the low wavenumbers, all VMS approaches present a negligible amount of SGS dissipation acting on the large resolved scales. This confirms that the DG-VMS approach is not able to replicate the viscous-type behaviour observed at low wavenumbers when the resolution limit falls within the inertial range. Additionally we observe that the modelled energy transfer presents a small region with negative values for the all-all approach with $\beta = 0.25$. A similar result has been observed also for the small-small variant for other resolutions when low values of β are considered (not shown here). This effect has not been observed for the Vreman variant and is thus possibly caused by the outer high-pass L^2-projection filter. These regions of negative energy transfer can therefore be considered as numerical artefact of the high-pass filter used in the DG-VMS approach and should not be interpreted as modelling backscatter.

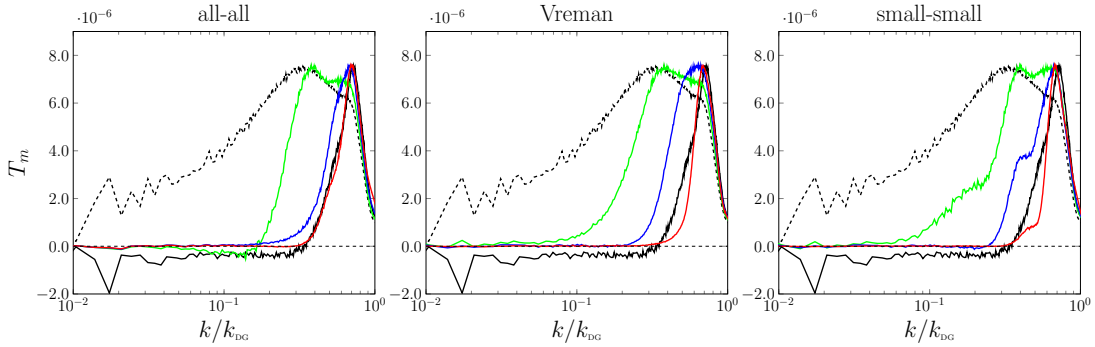

Figure 104 – TGV at Re = 20 000, $p = 7$, $k_{\mathrm{DG}} = 288$: Ideal SGS energy transfer (black solid), SGS model dissipation spectrum provided by the Smagorinsky model (dashed) and three variants of the DG-VMS approach for: $\beta = 0.25$ (green), $\beta = 0.5$ (blue), and $\beta = 0.75$ (red) using the BR2 scheme ($\eta_{br2} = 2$).

Finally we note that for all VMS approaches with $\beta = 0.75$ the peak of the SGS dissipation spectrum is located at a relatively lower frequency compared to the ideal SGS dissipation spectrum. This effect is partially explained by the use of the BR1 scheme in Fig. 103. Indeed, it is well known that the BR1 scheme presents very low and less than exact dissipation at frequencies close to k_{DG} [7]. A possible remedy is therefore to employ a different discretization for the SGS model term, *e. g.* the BR2 method.

In Fig. 104 we compare the ideal SGS dissipation spectrum and modelled energy transfer obtained with the BR2 scheme for $\eta_{br2} = 2$. As expected, the presence of the additional dissipation in the BR2 scheme leads to a shift and increase of the model dissipation toward higher wavenumbers. However we remark that the optimal value of η_{br2} has been observed to depend on the employed discretization. Additionally for sufficiently high values of η_{br2} the dissipation provided by the SGS model might be overwhelmed by that introduced by the numerical dissipation. A similar effect could be provided by the upwind dissipation associated to the discretization of the convective flux.

The conclusions drawn above are confirmed by analysing the modal energy transfer and eddy viscosity corresponding to the configuration considered in this section and the two discretization schemes BR1 and BR2. These are presented from Figs. 105 to 108.

It is clear from these figures that for the all-all approach a value of $\beta = 0.75$ must be employed in order to mimic the negligible ideal energy transfer at low mode-numbers. Additionally, we observe that when employing the BR2 scheme with $\eta_{br2} = 2$ a remarkably good agreement is obtained with both the modal energy transfer and eddy viscosity, confirming the conclusion drawn from the spectral energy transfer analysis.

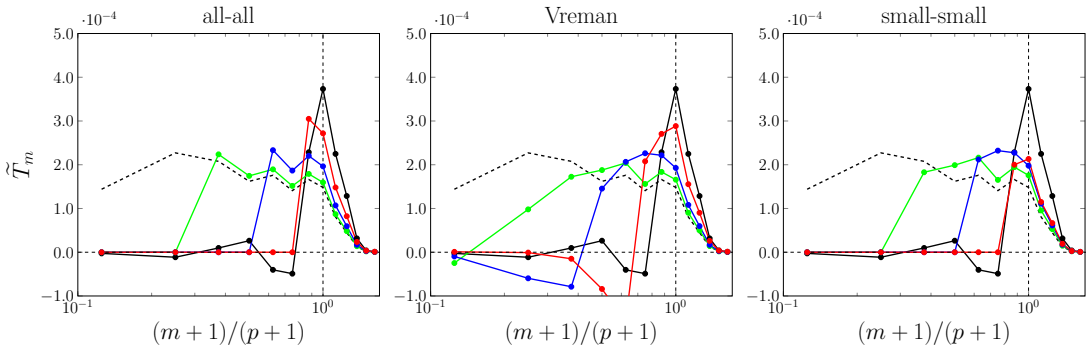

Figure 105 – TGV at Re = 20 000, $p = 7$, $k_{\mathrm{DG}} = 288$: Ideal modal energy transfer (black solid) and modelled modal energy transfer provided by the Smagorinsky model (dashed) and three variants of the DG-VMS approach for: $\beta = 0.25$ (green), $\beta = 0.5$ (blue), and $\beta = 0.75$ (red) using the BR1 scheme.

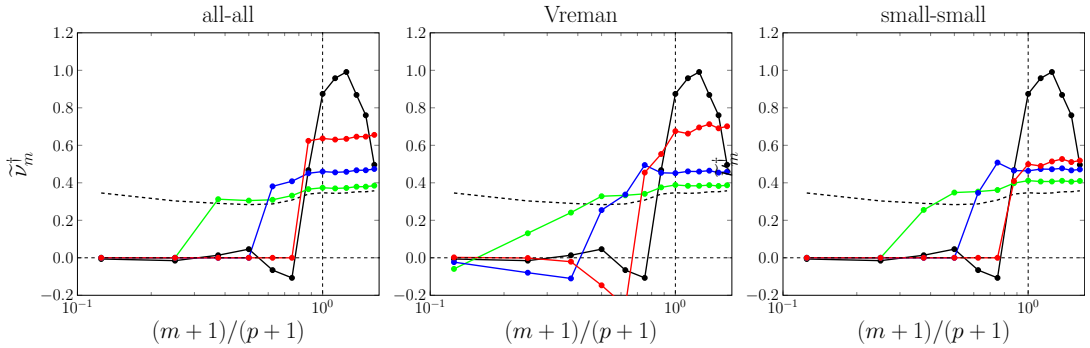

Figure 106 – TGV at Re = 20 000, $p = 7$, $k_{\mathrm{DG}} = 288$: Ideal modal eddy viscosity (black solid) and modelled modal eddy viscosity provided by the Smagorinsky model (dashed) and three variants of the DG-VMS approach for: $\beta = 0.25$ (green), $\beta = 0.5$ (blue), and $\beta = 0.75$ (red) using the BR1 scheme.

Considering now the Vreman and small-small approaches we observe that the outer filter operation does not appear necessary to limit the effect of the modelled dissipation on the highest-order modes. However we observe that while for the small-small variant $\widetilde{T}_m = 0$ for $(m+1)/(p+1) = \beta$, in the case of the Vreman approach it is positive and becomes negative for lower values of m. The combination of this positive and negative contribution leads to the smooth distribution of the modelled dissipation spectrum in Fig. 103 and 104.

In order to assess the generality of our remarks, we have repeated the presented analysis for different values of the polynomial degree p. Similar conclusions have been obtained with regards to the comparison of the three variants and the effect of variations of β on the model dissipation spectrum (not reported here). However, the optimal value of β appears to be dependent on p when $p \leq 4$. This result is expected

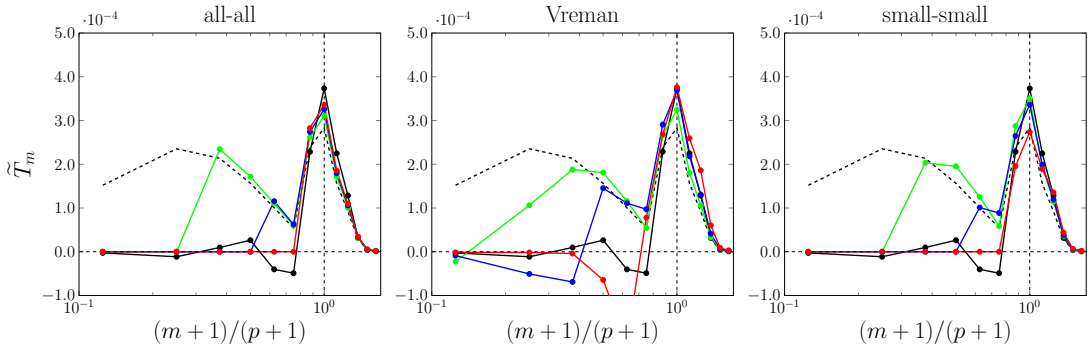

Figure 107 – TGV at Re = 20 000, $p = 7$, $k_{\mathrm{DG}} = 288$: Ideal modal energy transfer (black solid) and modelled modal energy transfer provided by the Smagorinsky model (dashed) and three variants of the DG-VMS approach for: $\beta = 0.25$ (green), $\beta = 0.5$ (blue), and $\beta = 0.75$ (red) using the BR2 scheme ($\eta_{br2} = 2$).

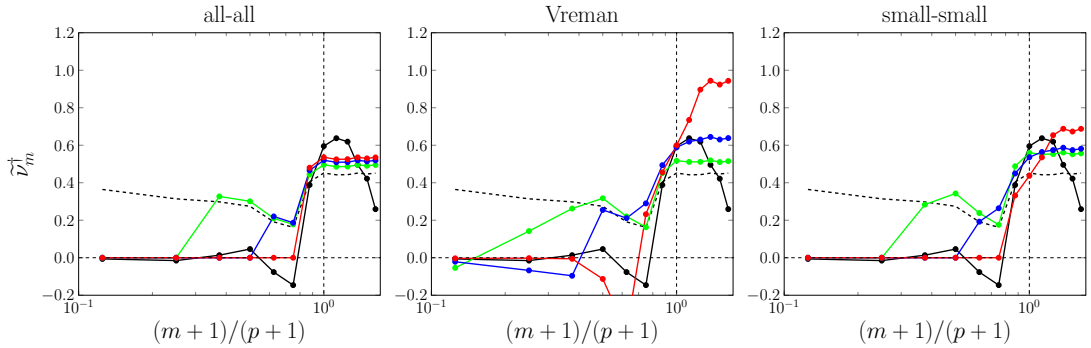

Figure 108 – TGV at Re = 20 000, $p = 7$, $k_{\mathrm{DG}} = 288$: Ideal modal eddy viscosity (black solid) and modelled modal eddy viscosity provided by the Smagorinsky model (dashed) and three variants of the DG-VMS approach for: $\beta = 0.25$ (green), $\beta = 0.5$ (blue), and $\beta = 0.75$ (red) using the BR2 scheme ($\eta_{br2} = 2$).

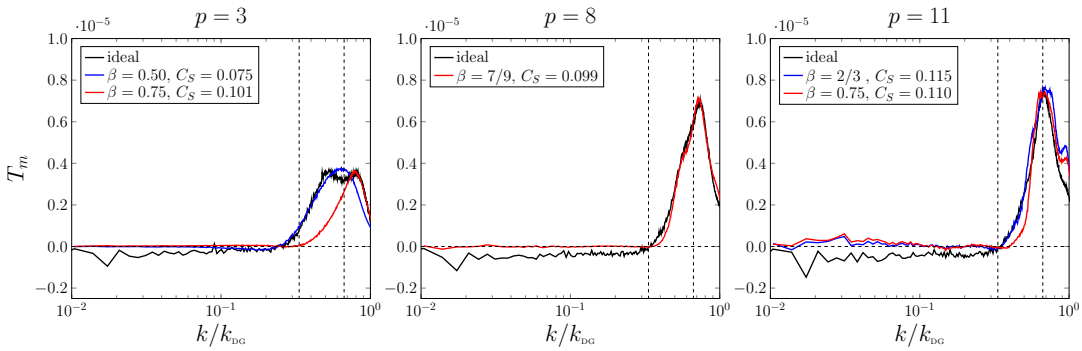

Figure 109 – TGV Re = 20 000: ideal SGS dissipation spectrum and model dissipation spectrum using the all-all DG-VMS approach using the BR2 scheme with $\eta_{BR2} = 2$ for $k_{DG} = 288$ and $p = 3$ (left), $p = 8$ (center) and $p = 11$(right).

from the *a-priori* analysis carried out in Sec. 10.6.2. To illustrate this, we report in Fig. 109 the ideal SGS dissipation spectrum and the model energy transfer for $p = 3$, 8 and 11 using the DG-VMS all-all approach and the BR2 scheme ($\eta_{br2} = 2$).

We can observe that for $p = 8$ and 11 the value $\beta \approx 0.75$ leads to the modelled dissipation acting on the scales of wavenumbers in the range $[k_{DG}/3, k_{DG}]$ similarly to the ideal SGS dissipation spectrum. For $p = 3$, however, we observe that the ideal SGS dissipation spectrum does not present a peak at $\tilde{k}_{DG}$ and the model dissipation presents a peak at a higher frequency. In this case the ideal SGS dissipation is in between that provided by the DG-VMS model for $\beta = 0.5$ and $\beta = 0.75$. This result indicates that for $p \leq 4$ the DG-VMS approach might not be able to replicate the distribution of the ideal SGS dissipation.

The analysis presented up to this point has focused on the ability of the DG-VMS approach to replicate the ideal energy transfer mechanism when the resolution limit falls within the dissipation range and the SGS dissipation acting on large-resolved scales is negligible.

We have observed in Sec. 10.6 that when the resolution limit falls within the inertial range a viscous-type behaviour can be observed and is dominant at frequencies below $k_{DG}/3$. It appears from these analyses that the DG-VMS approach is not able to replicate this mechanism.

Modifying or adapting β does not lead to a better representation of the SGS dissipation spectrum. However as we have observed in Fig. 103 this parameter allows to control the set of scales on which the SGS dissipation acts and the total amount of SGS dissipation. Thus the DG-VMS approach can nonetheless lead to improved results with respect to the standard or dynamic Smagorinsky model which might introduce in some cases excessive dissipation on the large resolved scales. This also explains the promising results observed for the local VMS approach proposed by

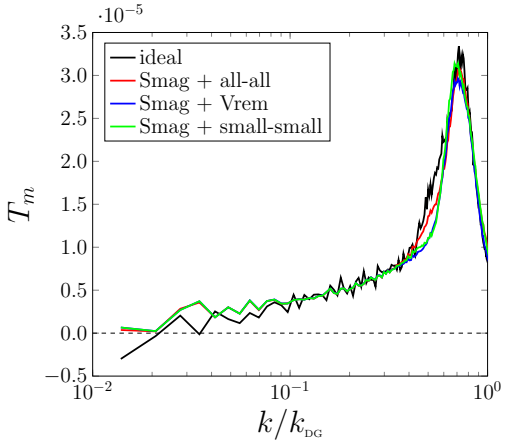

Figure 110 – TGV Re = 20 000, $p = 7$, $k_{DG} = 144$: Ideal SGS dissipation spectrum and modelled dissipation spectrum for mixed Smagorinsky and DG-VMS models.

Ramakrishnan and Collis [158] and for the dynamic partition selection algorithm for the DG-VMS approach by Naddei *et al.* [143].

The *a-priori* tests performed in this work indicate thus that the main limitation of the DG-VMS approach is its inability to mimic the energy transfer mechanism at low wavenumbers encountered at high Reynolds and typical LES resolutions. This corresponds to a viscous-type behaviour which can be modelled by an eddy-viscosity model such as the Smagorinsky model. The ideal SGS dissipation spectrum could be therefore approximated by employing a mixed Smagorinsky and DG-VMS model where the Smagorinsky model acts on all scales and the VMS approach with $\beta = 0.75$ replicates the hyperviscous behaviour dominant on frequencies $k > k_{DG}/3$. The two model coefficients however should be dynamically adapted (*e. g.* using Germano's procedure) as the relative contribution to the total SGS dissipation will depend on the resolution.

As an example, in Fig. 110 we consider the ideal SGS dissipation spectrum for a snapshot at $t = 14$ of the TGV at Re = 20 000, $p = 7$ and 288^3 dofs. The ideal SGS dissipation spectrum is compared to the three variants of the mixed model with constant coefficients, for the Smagorinsky contribution $C_{s,smag} = 0.057$ and $C_{s,a-a} = 0.063$ for the all-all variant, $C_{s,vrem} = 0.095$ for the Vreman variant and $C_{s,s-s} = 0.087$ for the small-small variant. This figure illustrates that a dynamic mixed model even with global model coefficients has the potential to provide a very accurate agreement with the ideal SGS-dissipation. Similar approaches have already been proposed, e. g. the Smagorinsky and residual-based-VMS approach by Wang and Oberai [197], or the enhanced field model by Jeanmart and Winckelmans [98]. However this is the first work that demonstrates the potential of such methodology

by *a-priori* analyses which include details of the numerical discretization and the effect of the DG-projection filter in the VMS approach.

CHAPTER 11

CONCLUSIONS AND PERSPECTIVES

RÉSUMÉ DU CHAPITRE EN FRANÇAIS

Dans ce chapitre, nous présentons une synthèse des principaux résultats obtenus dans cette thèse. Les réalisations obtenues dans le développement des techniques de résolution spatiale et dans l'analyse des modèles de turbulence pour la simulation des écoulements turbulents par LES sont présentées. Dans ce travail, nous avons démontré l'intérêt de l'adaptation p pour améliorer efficacement la précision des simulations d'écoulements turbulents tout en réduisant le coût de calcul par rapport à un raffinement uniforme. De plus, nous avons montré que les modèles LES doivent être spécifiquement adaptés aux méthodes d'ordre élevé, en tenant compte des propriétés des méthodes de discrétisation Galerkine discontinue. Dans la deuxième partie de ce chapitre, nous décrivons les perspectives de recherche future. Cela concerne notamment de nouveaux développements d'algorithmes adaptatifs d'ordre élevé pour la modélisation LES.

11.1 CONCLUSIONS

The objective of this work was to improve the accuracy and the computational efficiency of Large Eddy Simulations (LES) based on discontinuous Galerkin (DG) methods.

To this end, we have at first investigated the development of spatial resolution adaptation strategies. An overview of adaptation techniques and strategies for the DG method has been presented in Chap. 4. After introducing the adaptive algorithm for steady flows, we have highlighted several challenges encountered in the development of adaptation strategies for unsteady flows and, in particular, for scale-resolving simulations of turbulent flows.

One of the most important factors determining the accuracy and efficiency of the adaptation process is the choice of the error estimation technique. We have therefore presented in Chap. 5 an extensive comparison of different error estimation strategies proposed in the literature for the development of a p-adaptive algorithm. Both

discretization-error and residual-error based indicators have been analysed by performing p-adaptive simulations of inviscid and laminar steady and unsteady flows. It has been shown that, for a prescribed level of accuracy, all the employed refinement indicators allow for a reduction between 50% and 75% of the number of degrees of freedom compared to simulations using uniform polynomial degree. This analysis has led to the identification of the *small-scale energy density* (SSED) indicator as a suitable candidate for scale-resolving simulations of turbulent flows. It has provided accurate results, can be easily implemented as a post-processing operation, and presents a negligible computational overhead if hierarchical orthonormal basis functions are employed.

This comparison has been extended in Chap. 6 to h-adaptive simulations based on element splitting. It has been shown that all the conclusions drawn for p-adaptation are applicable to h-adaptation, confirming the suitability of the SSED indicator for h/p-adaptive scale-resolving simulations.

In order to obtain high parallel efficiency for such simulations, however, the mesh partitioning strategy must take into account the uneven distribution of the computational load across mesh elements. We have illustrated in Chap. 7 that the weights required for the mesh partitioning problem should be derived from direct measurements of the performance of the employed solver. It has also been shown that the graph partitioning algorithm based on this derivation of the computational weights can provide well-balanced partitionings and allows us to achieve high parallel efficiency on adapted h/p-discretizations.

The extension of the proposed adaptive algorithm to the simulation of unsteady flows has then been investigated. Two different strategies have been considered: dynamic and static adaptation.

At first, a dynamically p-adaptive algorithm has been presented and demonstrated in Chap. 8. The proposed strategy can provide a significant reduction of the total computational time required for the simulation of unsteady transient flows compared to simulations employing a uniform polynomial degree. The dynamically p-adaptive algorithm has been tested on two two-dimensional unsteady flow configurations, the transport of a vortex in a uniform inviscid flow and the collision of a dipole with a no-slip boundary, and a three-dimensional unsteady flow configuration, the DNS of the Taylor-Green Vortex at Re = 500. In particular, a reduction of 42% and 75% of the total computational time has been obtained respectively for the first two configurations. As regards the simulation of the Taylor-Green Vortex, a reduction of 33% of the total computational time has been obtained. This is despite the fact that dynamic load balancing is not currently available and high load imbalance is obtained for this simulation, which makes this outcome particularly promising.

Secondly, in Chap. 9 we have then presented a static p-adaptation approach which allows for a significant reduction the computational cost of the simulation of statistically steady flows. Different strategies have been considered to extend the SSED

indicator to obtain a refinement indicator for the static adaptation of unsteady flows. The most accurate results have been obtained by employing the L^∞-norm of the SSED indicator computed from the instantaneous solution. These conclusions have been drawn by analysing the performance of such strategies on static p-adaptive simulations of the periodic laminar flow past a cylinder and the Direct Numerical Simulation (DNS) of the turbulent flow over periodic hills.

Based on the experience gained from the previous studies, a novel error estimator, called *small-scale lifted* (SSL) indicator, has been proposed. Its formulation has been presented in Sec. 4.4.6. This refinement indicator has been shown in Chap. 9 to provide improved results compared to the SSED indicator, by performing statically p-adaptive LES of the transitional flow past a NACA0012 airfoil. The results obtained have demonstrated that the developed approach and the proposed error estimator can be effectively employed to improve the accuracy of DG-LES.

The analysis carried out in Chap. 9 on the NACA0012 configuration has demonstrated that, despite the increased accuracy provided by the adaptive algorithm, the LES solutions are strongly affected by the chosen LES model. Further research is therefore required for the improvement of DG-LES models, especially due to their interaction with the variable resolution properties in h/p-adaptive simulations. For this purpose, we have proposed in Chap. 10 a framework for the *a-priori* analysis of DG-LES models based on DNS databases. This framework is consistent with the employed discretization and allows for the analysis of the influence of the DG-filter in defining the ideal energy transfer mechanism between resolved and unresolved scales. Additionally, we have introduced the concept of modal eddy viscosity, which can be used for the *a-priori* analysis of the DG-VMS model or spectral vanishing viscosity approaches.

The proposed methodology has been applied to the *a-priori* analysis of the DG-VMS approach. It has been shown that when the DG-LES resolution limit falls at the beginning of the dissipation range the assumption of large-scales free of interaction with the unresolved scales is valid and the DG-VMS approach can replicate the ideal subgrid-scale dissipation. For coarser resolutions, typical of LES at high Reynolds numbers, the DG-VMS approach is unable to replicate the ideal energy transfer mechanism at the large-resolved scales. In this configuration, a more accurate agreement could be obtained by employing a mixed Smagorinsky and DG-VMS approach.

11.2 PERSPECTIVES

We believe that the results and the experience gained in this study represent a starting point for further improving the accuracy and efficiency of DG-LES in the context of scale-resolving simulations. Various research directions for further improvement are briefly outlined.

HP-ADAPTIVE DG-LES Over the course of this work, we have separately analysed *h*- and *p*-adaptation strategies. In particular, *p*-adaptive scale-resolving simulations have been carried out. Nonetheless, as discussed in Chap. 4, the most efficient approach would consist in the use of *hp*-adaptation strategies combining the advantages of both techniques. These require the use of an *hp*-decision strategy, usually based on regularity estimates, to decide between *h*- or *p*-adaptation. Several strategies have been investigated for elliptic equations by Houston and Süli [91] and have already been employed for adaptive RANS simulations, *e. g.* by Ceze [40]. Nonetheless, their application to scale-resolving simulations remains still an open research topic. In particular, the influence of *h*- and *p*-adaptation in modifying locally the DG-filtered solution and their interaction with the DG-LES model should be investigated.

IMPROVEMENT OF MARKING STRATEGIES The choice of the marking strategy can present a significant effect on the accuracy and efficiency of the adaptive algorithm. In Sec. 4.5, we have presented an overview of different techniques employed in the literature and in the present work. Nonetheless, we have not performed an extensive comparison of these techniques. This topic deserves specific attention in the context of scale-resolving simulations. In particular, optimal strategies should be devised for the definition of the coarsening and refinement thresholds.

We have also illustrated in Sec. 4.5 that some constraints are imposed on the variation of refinement level between neighbouring elements. While the 2:1 rule enforced for *h*-adaptation is a commonly accepted guideline, there is no agreement in the literature on the constraint to impose to the jump of the polynomial degree between neighbouring elements. Different constraints might be required when employing *hp*-adaptive approaches and therefore variations of the *h*- and *p*-refinement level might appear at the same time. An analysis of the influence of different types of constraints on the accuracy and dispersion errors of DG simulations should therefore provide useful guidelines.

DYNAMIC LOAD BALANCING As demonstrated in Chap. 8, a significant reduction of the computational cost of unsteady flow simulations can be obtained by employing the dynamic *p*-adaptation strategy presented in this work. In the framework of parallel computations however, this requires the development of dynamic load balancing algorithms to obtain well-balanced partitionings and achieve high parallel efficiency throughout the full simulations. The implementation of efficient dynamic load balancing techniques is nonetheless a complex task and can require extensive modifications of the solver at hand.

DEVELOPMENT AND IMPROVEMENT OF DG-LES MODELS The analysis described in Chap. 10 presents a deep insight into the ideal behaviour that DG-LES models should replicate. In particular the proposed framework can be applied for the anal-

ysis and the development of DG-LES models taking into account the details of the *hp*-discretization. As an example, we have observed in Sec. 10.7 that for relatively coarse discretizations a mixed Smagorinsky and DG-VMS model could in principle reproduce the ideal energy transfer mechanism provided that the model coefficients take appropriate values. For this purpose, suitable dynamic strategies, possibly based on the Germano procedure, should therefore be developed. We remark that while similar approaches, *e. g.* the dynamic Smagorinsky model, have already been proposed and applied to DG-LES, these strategies usually neglect the presence of jumps in the DG-LES solution. However, the proposed framework has demonstrated that this assumption is not valid and the presence of jumps has a significant effect on the ideal and modelled energy transfer. This property should be taken into account in future works.

Finally, we point out that the presented framework lends itself to the analysis of implicit LES (ILES) approaches and can provide useful insights regarding the accuracy of ILES and its range of applicability.

Part I

APPENDIX

APPENDIX A

GEOMETRICAL ORDER ESTIMATION FOR HIGH-ORDER MESHES

As described in Sec. 3.4, the evaluation of the volume and surface integrals appearing in Eq. (32) is performed by numerical integration.

It is common in the framework of high-order FE-type methods to use quadrature formulas which are exact for the integration of polynomials of maximum partial degree $2p+1$. The choice of a Gauss-Legendre quadrature implies the use of $q = p+1$ quadrature points per space direction. This quadrature formula would lead to the exact evaluation of the integrals for linear PDEs with constant coefficients.

In the most general case, however, with non-linear PDEs and the use of curvilinear meshes the quadrature formula is not exact and aliasing errors appear. Two sources of aliasing errors can be distinguished

- PDEs non-linearities,
- geometrical aliasing.

A detailed discussion on the effect of PDEs non-linearities and a description of dealiasing techniques is presented in the work of Mengaldo et al. [133] and works cited therein. In the present chapter, we focus on the generation of geometrical aliasing due to the use of high-order meshes. The reduction of aliasing errors is achieved throughout this work using a number of quadrature points per space direction larger than $p+1$. This technique is commonly referred to as *overintegration*, also called *polynomial dealiasing*. Nonetheless, the use of a large number of quadrature points causes an increase of the overall computational cost of simulations. This effect can be limited by locally adapting the number of quadrature points depending on the local distortion of each element.

In the following Sec. A.1, we therefore analyse the origin of geometrical aliasing errors. It is shown that the use of elements with non-affine mapping leads to the increase of the number of quadrature points required for the exact integration of a function. The required number of integration points is controlled by the effective mapping and Jacobian order. Knowledge of these quantities can be employed to adapt the number of quadrature points thereby reducing geometrical aliasing errors at a limited computational cost. In Sec. A.2 we illustrate a methodology to measure

the effective Jacobian order, which is employed in the present work to control the local order of quadrature formulae. The proposed approach is then demonstrated on curvilinear high-order meshes.

While the presented discussion is concerned with meshes composed of curvilinear hexahedral elements, the conclusions drawn can be extended to the analysis of any other element type.

A.1 GEOMETRICAL ALIASING

Aliasing errors are introduced when considering linear or curvilinear meshes for which the generic element is mapped to a reference element K_{ref} through a non-affine mapping.

In order to illustrate this effect let us consider the integral on element K of a polynomial function f of maximum partial degree P, that is $f \in \mathcal{P}^P(K)$. As seen in Sec. 3.4, this integral can be evaluated in the reference element as

$$\int_K f(\mathbf{x})\mathrm{d}\mathbf{x} = \int_{K_{ref}} (f \circ \Psi_K(\boldsymbol{\xi}))J_K(\boldsymbol{\xi})\mathrm{d}\boldsymbol{\xi} \ . \tag{158}$$

For a mesh of order m, with mapping function $\Psi_K \in [\mathcal{P}^m(K_{ref})]^d$, with d number of space directions, it can be shown [17, 29] that $f \circ \Psi_K(\boldsymbol{\xi}) \in \mathcal{P}^{dmP}(K_{ref})$ and $J_K(\boldsymbol{\xi}) \in \mathcal{P}^{dm-1}(K_{ref})$. Thus, in order to evaluate exactly Eq. (158), an integration formula that is exact for polynomial functions of maximum partial degree $dmP + dm - 1$ is required.

In practice, a prohibitive number of quadrature points would be required to evaluate the integrals in Eq. (32). As an example, the evaluation of the mass matrix components in Eq. (49) requires the computation of the integral

$$M_{ij}^K = \int_K \phi_K^i \phi_K^j \mathrm{d}\mathbf{x} = \int_{K_{ref}} (\phi_K^i \circ \Psi_K(\boldsymbol{\xi}))(\phi_K^j \circ \Psi_K(\boldsymbol{\xi}))J_K(\boldsymbol{\xi})\mathrm{d}\boldsymbol{\xi} \ , \tag{159}$$

where $\phi_K^i, \phi_K^j \in \mathcal{P}^p(K)$. As an example, if we assume $d = 3$, that we have a 4-th order mesh and that $p = 4$, the exact evaluation of Eq. (159) would require 54 quadrature points per space direction. This implies 157 464 quadrature points per element. It is clear that in the most general case the exact evaluation of all the integrals in Eq. (32) is unfeasible.

We remark, however, that in typically employed high-order meshes, only a limited number of elements are distorted. As an example, the high-order mesh generators *Nekmesh*, part of the *Nektar++* framework [35], and *Gmsh* [79] generate effectively high-order curved elements only in boundary layer meshes and near curved boundaries [1].

1. A larger albeit limited number of curved elements might be generated by the optimization of the mesh.

To identify the level of distortion of each element we could employ the concept of the effective mapping order μ_K introduced by Botti et al. [29]. This quantity is defined as the minimum integer such that

$$\Psi_K \in [\mathcal{P}^{\mu_K}(K_{ref})]^d \subseteq [\mathcal{P}^m(K_{ref})]^d \ . \tag{160}$$

In this work, we define analogously the effective order of the determinant of the Jacobian for each element as the minimum integer $\mu_{J,K}$ such that

$$J_K \in \mathcal{P}^{\mu_{J,K}}(K_{ref}) \subseteq \mathcal{P}^{dm-1}(K_{ref}) \ .$$

To simplify the notation, we refer to $\mu_{J,K}$ as the effective Jacobian order.

The order of the quadrature formula employed in each element can therefore be locally adapted depending on the local mapping or Jacobian order. This allows for a more accurate evaluation of integrals on curved elements/faces while using a lower order quadrature on linear elements, thereby reducing the overall computational cost of simulations.

In the present work, the local effective Jacobian order $\mu_{J,K}$ is used to adapt the local number of quadrature points per space direction.

A.2 EVALUATION OF THE EFFECTIVE JACOBIAN ORDER

Since the value of the local effective Jacobian order is not directly available from the mesh, it must be estimated during the preprocessing phase. To this end, we express $J_K(\boldsymbol{\xi})$ as

$$J_K(\boldsymbol{\xi}) = \sum_{i=1}^{(dm)^d} \widetilde{J}_K^i L_i(\boldsymbol{\xi}) \ , \tag{161}$$

where $\{L_1, L_2, \dots, L_{(dm)^d}\}$ is the hierarchical basis obtained by the tensor product of the normalized Legendre polynomials of maximum partial degree $dm-1$ and $\widetilde{J}_K^i = \int_{K_{ref}} J_K L_i \mathrm{d}\boldsymbol{\xi}$. The modal energy of J_K is then defined as

$$E_J(k) = \sum_{i=k^d+1}^{(k+1)^d} (\widetilde{J}_K^i)^2 \quad \text{, for} \quad k = 0, \dots, dm-1 \ . \tag{162}$$

The effective Jacobian order can therefore be estimated as the minimum value that satisfies the condition:

$$\frac{\|J_K - \mathbb{P}_{\mathcal{P}^{\mu_{J,K}}}[J_K]\|^2_{L^2(K_{ref})}}{\|J_K\|^2_{L^2(K_{ref})}} = \frac{\sum_{k=\mu_{J,K}+1}^{dm-1} E_J(k)}{\sum_{k=0}^{dm-1} E_J(k)} < \omega \ , \tag{163}$$

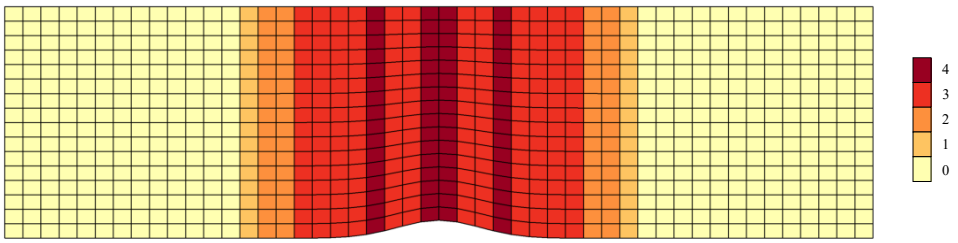

Figure 111 – Distribution of the local effective Jacobian order for the 4-th order mesh for the flow over a Gaussian bump employed in Sec. 5.3.

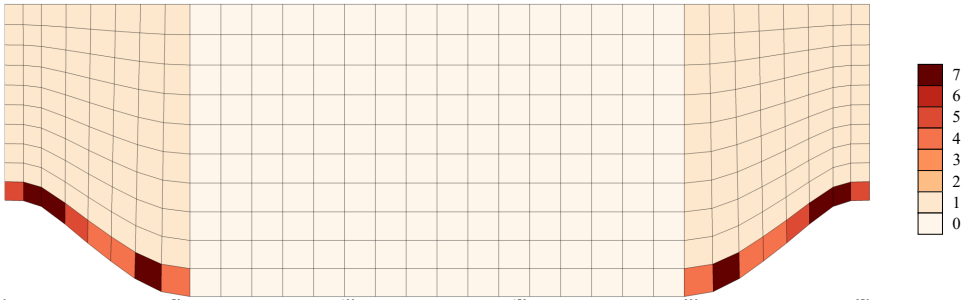

Figure 112 – Distribution of the local effective Jacobian order for the 4-th order mesh for the flow over periodic hills.

where $\mathbb{P}_{\mathcal{P}^k}[\cdot]$ indicates the projection onto the polynomial space $\mathcal{P}^k$ and ω is a suitable threshold here set to 10^{-12}.

The estimated effective Jacobian order is presented here for three configurations. In Fig. 111 we report the value of $\mu_{J,K}$ obtained for the 4-th order mesh used in Sec. 5.3 for the simulation of the inviscid flow over a Gaussian bump. This mesh can be found on the *HiOCFD* workshop website [196] and represents an example of a mesh where the effective non-linear region is not limited to the boundary layer mesh. However, regions characterized by high distortion and high values of $\mu_{J,K}$ are limited to those in the area where the Gaussian bump is located. Elsewhere, a large number of elements is characterized by an affine mapping.

In Fig. 112 we report the effective Jacobian order evaluated for the 4-th order mesh of the configuration described in Sec. 9.4 for the simulation of the turbulent flow over periodic hills. This mesh has been generated by means of the high-order mesh generation tool *Gmsh* [79]. It is possible to observe that the only region characterized by high-order elements is the first layer of the mesh elements over the hills. The mesh is thus composed mostly by elements characterized by $\mu_{J,K} = 1$ (linear) and $\mu_{J,K} = 0$ (affine mapping).

As a final example, we consider in Fig. 113 a 4-th order C-type mesh around a NACA0012 airfoil generated using *Gmsh*. The described procedure allows to identify that the largest portion of the mesh is again composed by linear elements whereas

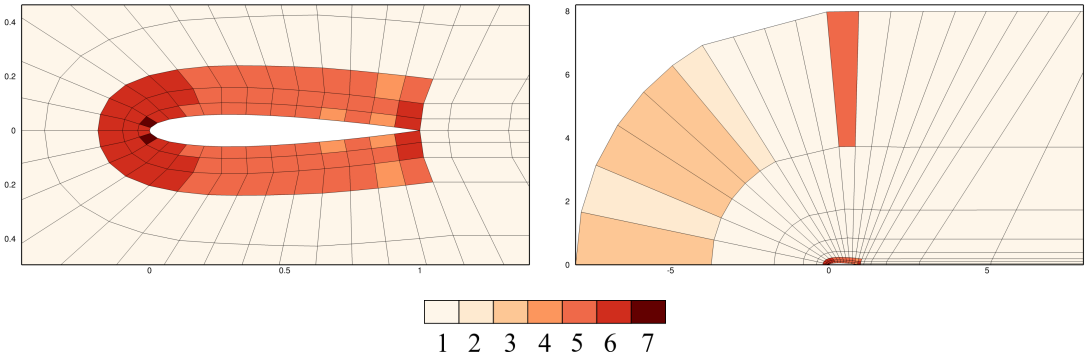

Figure 113 – Distribution of the local effective Jacobian order for a 4-th order C-type mesh around a NACA0012 airfoil.

elements characterized by high values of $\mu_{J,K}$ are located only in the boundary layer mesh near the airfoil and in proximity of the curved outer boundaries. We remark that the presence of high distortion near outer boundaries might be an undesirable feature of high-order mesh generators. Indeed, it might not be necessary to have a high-order representation of the far-field boundary and the curvilinear representation might lead to the generation of aliasing errors.

APPENDIX B

EVALUATION OF THE SSED AND SPECTRAL DECAY INDICATORS FOR HIERARCHICAL ORTHONORMAL BASES

We report here the calculation of the SSED and spectral decay indicators, introduced in Sec. 4.4.1 and 4.4.2, under the assumption that hierarchical orthonormal basis functions are employed. The recall that SSED indicator takes the form

$$\eta_K^{SSED} := \frac{\left\| (\rho \mathbf{v})_{h,p} - (\rho \mathbf{v})_{h,p-1} \right\|_{L^2(K)}}{|K|^{\frac{1}{2}}} \ . \tag{53}$$

If the solution is expressed as a linear combination of hierarchical basis functions, each component of the momentum density $(\rho U_i)_{h,p}$ and its projection on the reduced solution space S_h^{p-1} can be immediately obtained $\forall \mathbf{x} \in K$ as

$$(\rho U_j)_{h,p}(\mathbf{x}) = \sum_{j=1}^{N_p} (\rho U_i)_K^j \, \phi_K^j(\mathbf{x}) \quad \text{, and} \quad (\rho U_j)_{h,p-1}(\mathbf{x}) = \sum_{j=1}^{N_{p-1}} (\rho U_i)_K^j \, \phi_K^j(\mathbf{x}) \ .$$

The term at the numerator of Eq. (53) can therefore be evaluated as

$$\begin{aligned}
\left\| (\rho \mathbf{v})_{h,p} - (\rho \mathbf{v})_{h,p-1} \right\|_{L^2(K)} &= \left(\int_K \sum_{i=1}^{d} \left(\sum_{j=1}^{N_p} (\rho U_i)_K^j \, \phi_K^j - \sum_{j=1}^{N_{p-1}} (\rho U_i)_K^j \, \phi_K^j \right)^2 \mathrm{d}V \right)^{\frac{1}{2}} \\
&= \left(\int_K \sum_{i=1}^{d} \left(\sum_{j=N_{p-1}+1}^{N_p} (\rho U_i)_K^j \, \phi_K^j \right)^2 \mathrm{d}V \right)^{\frac{1}{2}} \\
&= \left(\sum_{i=1}^{d} \sum_{j=N_{p-1}+1}^{N_p} \sum_{l=N_{p-1}+1}^{N_p} (\rho U_i)_K^j \, (\rho U_i)_K^l \int_K \phi_K^j \phi_K^l \, \mathrm{d}V \right)^{\frac{1}{2}} \\
&= \left(\sum_{i=1}^{d} \sum_{j=N_{p-1}+1}^{N_p} \sum_{l=N_{p-1}+1}^{N_p} (\rho U_i)_K^j \, (\rho U_i)_K^l \, M_{jl}^K \right)^{\frac{1}{2}} \ .
\end{aligned} \tag{164}$$

If the basis is also orthonormal, the computation of the SSED indicator simply reduces to

$$\eta_K^{SSED} = \frac{\left(\sum_{i=1}^{d} \sum_{j=N_{p-1}+1}^{N_p} \left((\rho U_i)_K^j \right)^2 \right)^{\frac{1}{2}}}{|K|^{\frac{1}{2}}} \quad . \tag{165}$$

Following the same process, in the case of orthonormal basis functions the spectral decay indicator Eq. (55) can be evaluated as

$$\eta_K^{SD} = \left(\frac{\sum_{i=1}^{d} \sum_{j=N_{p-1}+1}^{N_p} \left((\rho U_i)_K^j \right)^2}{\sum_{i=1}^{d} \sum_{j=1}^{N_p} \left((\rho U_i)_K^j \right)^2} \right)^{\frac{1}{2}} \quad . \tag{166}$$

APPENDIX C

ENERGY AND DISSIPATION SPECTRA COMPUTATION

For the computation of the energy and dissipation spectra, presented in Chap. 10, we need to evaluate the Fourier transform of the velocity field, SGS residual, and SGS model term. For this purpose we employ the Fast Fourier Transform (FFT) algorithm as implemented in the *FFTW-3.3.8* library [70].

The FFT algorithm requires the solution to be known on an uniform Cartesian grid. The variable of which we want to compute the FFT is therefore sampled on a post-processing grid formed by the union of n_{el}^3 uniform Cartesian grids centered on each cell and composed of q_s^3 sampling points. The post-processing grid on the domain $[-\pi, \pi]^3$ is thus composed of the Cartesian product of the coordinates $(j - \frac{1}{2})\frac{2\pi}{q_s n_{el}}$ for $j = 1, \dots, N_{FFT} = q_s n_{el}$. The value of q_s must be sufficiently large to evaluate accurately the Fourier coefficients corresponding to the frequencies of interest (that is at least up to k_{DG}).

Indeed, the presence of discontinuities in the DG-LES field leads to a reduction in the order of convergence of the FFT algorithm. We remark that the FFT algorithm relies on the trapezoidal integration rule which presents an order of accuracy $\mathcal{O}({N_{FFT}}^{-1})$ in the presence of discontinuities, as opposed to the exponential convergence obtained for smooth functions. In this case the use of $n_{el}(p+1)$ points per direction, as is usually found in the literature of DG-LES, is not sufficient for the evaluation of the energy and dissipation spectra. For this reason, we employ at least $3n_{el}(p+1)$ points per direction and verify that increasing this value does not modify the energy and dissipation spectra at frequencies below $k_{\mathrm{DG}} = \frac{n_{el}(p+1)}{2}$.

In order to illustrate the need for a sufficiently high number of points for the evaluation of the FFT, we report in Fig. 114 the energy spectra of the DG-LES solution of the TGV configuration at Re = 20 000 and $t = 14$ using $p = 5$ and 7 and a total of 288 degrees of freedom for various values of q_s. It can be observed that the FFT is inaccurate for low values of q_s even at wavenumbers below k_{DG}. Slight differences can be observed for frequencies below $\tilde{k}_{\mathrm{DG}} = \frac{n_{el}(p+1)}{3}$ and in some cases marked differences can appear at frequencies close to k_{DG}. This is visible from the bump in the energy spectrum at k_{DG} for $q_s = p+1$ on the right panel of Fig. 114 corresponding to $p = 7$.

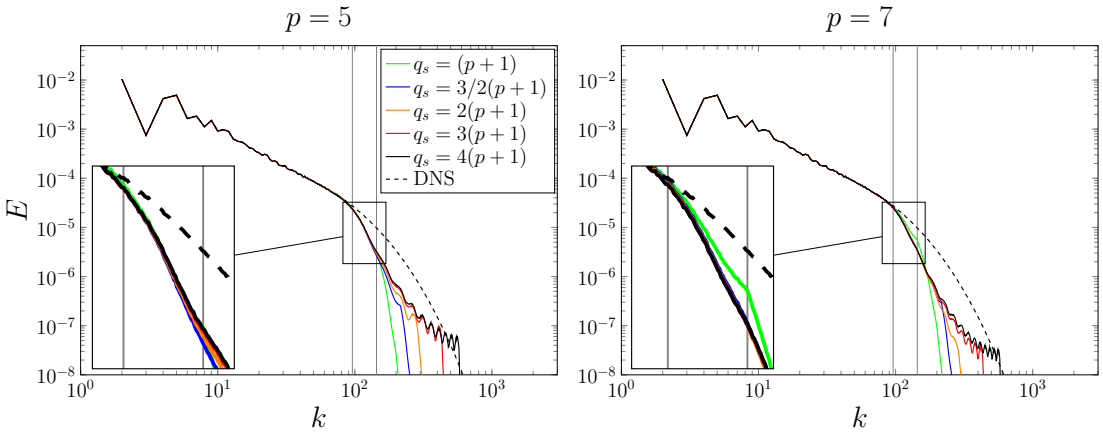

Figure 114 – TGV at Re = 20 000, $t = 14$, $k_{\mathrm{DG}} = 144$: Energy spectrum for $p = 5$ (left) and $p = 7$ (right) for various values of q_s.

Nonetheless, the spectrum converges as q_s is increased and a value of $q_s \approx 3n_{el}(p+1)$ appears sufficient to obtain the Fourier transform for frequencies up to k_{DG}. Further increasing the value of q_s leads to the slow convergence of the tail of the spectrum associated with the DG-LES discontinuities.

We note that alternative techniques can be employed to evaluate the Fourier transform avoiding the use of a large number of post-processing points. Such methodologies include the Non Uniform Fast Fourier Transform (NUFFT) [64, 118] and the Conformal Fourier Transform (CFT) [203].

APPENDIX D

CHOICE OF THE LARGE-SCALE SPACE

In Sec. 10.4 we have defined the space $W_h^m = \text{span}\{\psi_K^{\mathbf{m}}, \forall K \in \Omega_h, m - \frac{1}{2} < \|\mathbf{m}\| \leq m + \frac{1}{2}\}$. With this choice the assumption of $\tilde{T}_{sgs}(m) = 0$ for $m \leq p_L$ corresponds to the VMS approach defining the large-scale space as $V^L := \bigcup_{m \leq p_L} W_h^m$ as described in Sec. 10.5. Other definitions are possible, in particular the most common choice is to define $V^L := S_h^{p_L}$ which corresponds to assuming that $\tilde{T}^c(m) = 0$ for $m \leq p_L$ where

$$\widetilde{T}^c(m) := \mathcal{R}(\mathbf{u}, \mathbf{u}_h, \mathbb{P}_{W_h^{m,c}}[\mathbf{u}_h]) \ , \tag{167}$$

with $W_h^{m,c} = \text{span}\{\psi_K^{\mathbf{m}}, \forall K \in \Omega_h, \|\mathbf{m}\|_\infty = m\}$. It is immediate to show that $W_h^{m,c} \equiv S_h^m \setminus S_h^{m-1}$ for $m > 0$ and that $W_h^{0,c} \equiv S_h^0$.

The definition employed throughout this work Eq. (148) corresponds to analysing the modal energy transfer by grouping together modes over spherical shells characterized by $m - \frac{1}{2} < \|\mathbf{m}\| \leq m + \frac{1}{2}$, whereas Eq. (167) corresponds to grouping modes over cubic shells characterized by $\|\mathbf{m}\|_\infty = m$.

We argue that Eq. (148) allows for a more consistent description of the modal energy transfer mechanism. To justify this choice we report in Figs. 115 and 116 the contour plots of the modal eddy viscosity $\widetilde{\nu}^\dagger(\mathbf{m})$ for $p = 7$ and $p = 11$ defined as

$$\widetilde{\nu}^\dagger(\mathbf{m}) := \frac{\sum_{K \in \Omega_h} \widetilde{\mathbf{u}_h}^{\mathbf{m},K} \cdot \mathcal{R}(\mathbf{u}, \mathbf{u}_h, \psi_K^{\mathbf{m}})}{\sum_{K \in \Omega_h} \nu \widetilde{\mathbf{u}_h}^{\mathbf{m},K} \cdot \mathcal{L}(\mathbf{u}_h, \psi_K^{\mathbf{m}})} \ . \tag{168}$$

We observe that the isolevel curves for $\widetilde{\nu}^\dagger(\mathbf{m})$ are better approximated by spheres (circles in the plot) rather than by cubes centred in $(0, 0, 0)$. Therefore we assume that improved results can be obtained for LES models by modifying the modal eddy viscosity as a function of $\|\mathbf{m}\|$ rather than $\|\mathbf{m}\|_\infty$.

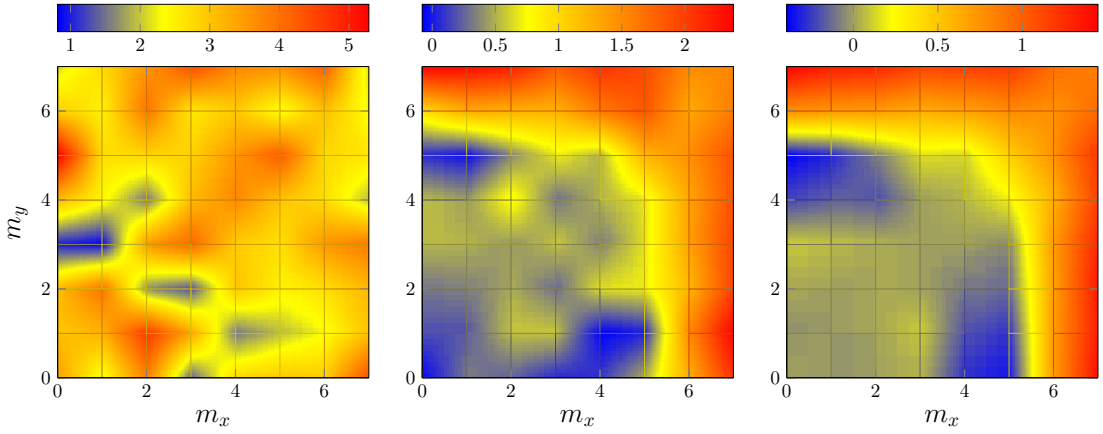

Figure 115 – TGV at Re = 20,000, $t = 14$: Contour plot of $\widetilde{\nu}^{\dagger}(\mathbf{m})$ at constant $m_z = 0$ for $p = 7$ and 144^3, 288^3 and 576^3 dofs (left to right) using the BR1 scheme.

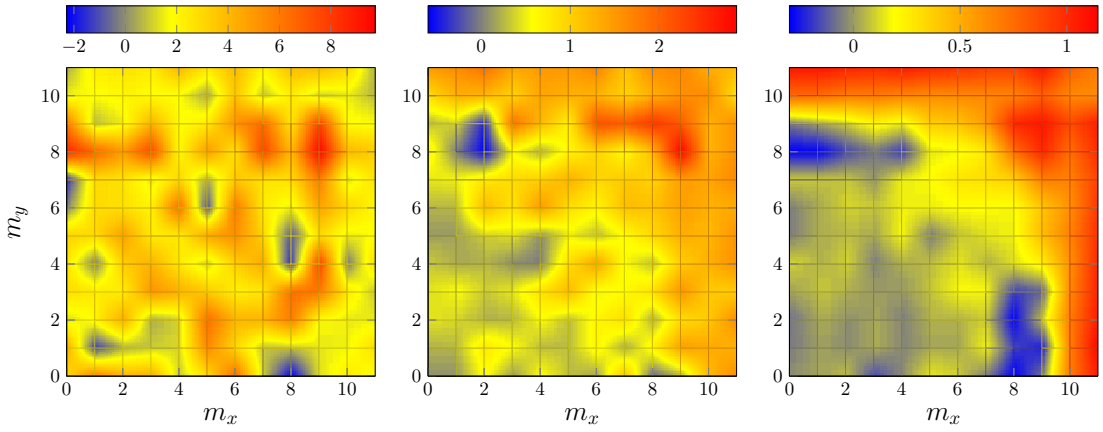

Figure 116 – TGV at Re = 20,000, $t = 14$: Contour plot of $\widetilde{\nu}^{\dagger}(\mathbf{m})$ at constant $m_z = 0$ for $p = 11$ and 144^3, 288^3 and 576^3 dofs (left to right) using the BR1 scheme.

BIBLIOGRAPHY

[1] *4th International Workshop on High-Order CFD Methods*. 2016. URL: https://how4.cenaero.be/.

[2] *5th International Workshop on High Order CFD Methods*. 2018. URL: https://how5.cenaero.be/.

[3] A. Abbà et al. « Dynamic models for Large Eddy Simulation of compressible flows with a high order DG method. » In: *Comput. Fluids* 122 (2015), pp. 209–222. URL: http://www.sciencedirect.com/science/article/pii/S0045793015002972.

[4] N. Ahmed et al. « A Review of Variational Multiscale Methods for the Simulation of Turbulent Incompressible Flows. » In: *Arch. Comput. Methods Eng.* 24 (2017), pp. 115–164.

[5] M. Ainsworth. « A posteriori error estimation for Discontinuous Galerkin finite element approximation. » In: *SIAM J. Numer. Anal.* 45.4 (2007), pp. 1777–1798.

[6] F. Alauzet et al. « 3D transient fixed point mesh adaptation for time-dependent problems: Application to CFD simulations. » In: *J. Comput. Phys.* 222.2 (2007), pp. 592–623.

[7] M. Alhawwary and Z. Wang. « On the Accuracy and Stability of Various DG Formulations for Diffusion. » In: *arXiv preprint arXiv:1810.03095* (2018).

[8] O. Antepara et al. « Parallel adaptive mesh refinement for Large-Eddy Simulations of turbulent flows. » In: *Comput. Fluids* 110 (2015), pp. 48–61.

[9] D. N. Arnold et al. « Unified analysis of discontinuous Galerkin methods for elliptic problems. » In: *SIAM J. Numer. Anal.* 39.5 (2002), pp. 1749–1779.

[10] P. Balakumar and G. I. Park. « DNS/LES Simulations of Separated Flows at High Reynolds Numbers. » In: *45th AIAA Fluid Dynamics Conference*. 2015, p. 2783.

[11] J. W. Banks et al. « Numerical error estimation for nonlinear hyperbolic PDEs via nonlinear error transport. » In: *Comput. Methods Appl. M.* 213 (2012), pp. 1–15.

[12] F. Bassi et al. « A high-order accurate discontinuous finite element method for inviscid and viscous turbomachinery flows. » In: *Proc. 2nd Eur. Conf. Turbomach. Fluid Dyn. Thermodyn.* Antwerpen, Belgium. 1997, pp. 99–109.

[13] F. Bassi et al. « Discontinuous Galerkin solution of the Reynolds-averaged Navier–Stokes and k–ω turbulence model equations. » In: *Comput. Fluids* 34.4 (2005), pp. 507–540.

[14] F. Bassi and S. Rebay. « A high-order accurate discontinuous finite element method for the numerical solution of the compressible Navier–Stokes equations. » In: *J. Comput. Phys.* 131.2 (1997), pp. 267–279.

[15] F. Bassi and S. Rebay. « A high-order accurate discontinuous finite element method for the numerical solution of the compressible Navier–Stokes equations. » In: *J. Comput. Phys.* 131.2 (1997), pp. 267–279.

[16] F. Bassi et al. « Discontinuous Galerkin solution of the Reynolds-averaged Navier–Stokes and k–ω turbulence model equations. » In: *Comput. Fluids* 34.4-5 (2005), pp. 507–540.

[17] F. Bassi et al. « On the flexibility of agglomeration based physical space discontinuous Galerkin discretizations. » In: *J. Comput. Phys.* 231.1 (2012), pp. 45–65.

[18] Y. Bazilevs et al. « Variational multiscale residual-based turbulence modeling for large eddy simulation of incompressible flows. » In: *Comput. Methods Appl. M.* 197.1-4 (2007), pp. 173–201.

[19] A. D. Beck, D. G. Flad, and C.-D. Munz. « Neural networks for data-based turbulence models. » In: *arXiv preprint arXiv:1806.04482* (2018).

[20] A. D. Beck et al. « High-order discontinuous Galerkin spectral element methods for transitional and turbulent flow simulations. » In: *Int. J. Numer. Methods Fluids* 76.8 (2014), pp. 522–548.

[21] A. Belme, A. Dervieux, and F. Alauzet. « Time accurate anisotropic goal-oriented mesh adaptation for unsteady flows. » In: *J. Comput. Phys.* 231.19 (2012), pp. 6323–6348.

[22] P. Benard et al. « Mesh adaptation for large-eddy simulations in complex geometries. » In: *Int J Numer Methods Fluids* 81.12 (2016), pp. 719–740.

[23] R. Biswas and R. C. Strawn. « A new procedure for dynamic adaption of three-dimensional unstructured grids. » In: *Appl. Numer. Math.* 13.6 (1994), pp. 437–452.

[24] S. Blaise and A. St-Cyr. « A dynamic hp-adaptive discontinuous Galerkin method for shallow-water flows on the sphere with application to a global tsunami simulation. » In: *Mon. Weather Rev.* 140.3 (2012), pp. 978–996.

[25] J. Boris et al. « New insights into large eddy simulation. » In: *Fluid Dyn. Res.* 10.4-6 (1992), p. 199.

[26] F. van der Bos and B. J. Geurts. « Computational error-analysis of a discontinuous Galerkin discretization applied to large-eddy simulation of homogeneous turbulence. » In: *Comput. Methods Appl. M.* 199.13-16 (2010), pp. 903–915.

[27] F. van der Bos, J. J. van der Vegt, and B. J. Geurts. « A multi-scale formulation for compressible turbulent flows suitable for general variational discretization techniques. » In: *Comput. Methods Appl. M.* 196.29-30 (2007), pp. 2863–2875.

[28] S. Bose. « Explicitly filtered large-eddy simulation: with application to grid adaptation and wall modeling. » PhD thesis. Stanford University, 2012.

[29] L. Botti. « Influence of reference-to-physical frame mappings on approximation properties of discontinuous piecewise polynomial spaces. » In: *J. Sci. Comput.* 52.3 (2012), pp. 675–703.

[30] M. Brachet. « Direct simulation of three-dimensional turbulence in the Taylor–Green vortex. » In: *Fluid Dyn. Res.* 8.1-4 (1991), p. 1.

[31] M. E. Brachet et al. « Small-scale structure of the Taylor–Green vortex. » In: *J. Fluid Mech.* 130 (1983), pp. 411–452.

[32] M. Breuer et al. « Flow over periodic hills–numerical and experimental study in a wide range of Reynolds numbers. » In: *Comput. Fluids* 38.2 (2009), pp. 433–457.

[33] V. Brunet et al. « Comparison of various CFD codes for les simulations of turbomachinery: from inviscid vortex convection to multi-stage compressor. » In: *ASME Turbo Expo 2018: Turbomachinery Technical Conference and Exposition*. American Society of Mechanical Engineers. 2018, V02CT42A013–V02CT42A013.

[34] C. J. Budd, W. Huang, and R. D. Russell. « Adaptivity with moving grids. » In: *Acta Numer.* 18 (2009), pp. 111–241.

[35] C. D. Cantwell et al. « Nektar++: An open-source spectral/hp element framework. » In: *Comput. Phys. Commun.* 192 (2015), pp. 205–219.

[36] C. Canuto et al. « Adaptive spectral Galerkin methods with dynamic marking. » In: *SIAM J. Numer. Anal.* 54.6 (2016), pp. 3193–3213.

[37] P. Catalano and R. Tognaccini. « RANS analysis of the low-Reynolds number flow around the SD7003 airfoil. » In: *Aerosp. Sci. Technol.* 15.8 (2011), pp. 615–626.

[38] I. Celik, Z. Cehreli, and I Yavuz. « Index of resolution quality for large eddy simulations. » In: *J. Fluids Eng.* 127.5 (2005), pp. 949–958.

[39] S. Cerutti, C. Meneveau, and O. M. Knio. « Spectral and hyper eddy viscosity in high-Reynolds-number turbulence. » In: *J. Fluid Mech.* 421 (2000), pp. 307–338.

[40] M. A.d. B. Ceze. « A Robust hp-Adaptation Method for Discontinuous Galerkin Discretizations Applied to Aerodynamic Flows. » PhD thesis. University of Michigan, 2013.

[41] J.-B. Chapelier and G. Lodato. « A spectral-element dynamic model for the Large-Eddy simulation of turbulent flows. » In: *J. Comput. Phys.* 321 (2016), pp. 279–302.

[42] J.-B. Chapelier, M. de la Llave Plata, and E. Lamballais. « Development of a multiscale LES model in the context of a modal discontinuous Galerkin method. » In: *Comput. Methods Appl. M.* 307 (2016), pp. 275–299.

[43] J.-B. Chapelier et al. « Evaluation of a high-order discontinuous Galerkin method for the DNS of turbulent flows. » In: *Comput. Fluids* 95 (2014), pp. 210–226.

[44] H. Choi and P. Moin. « Grid-point requirements for large eddy simulation: Chapman's estimates revisited. » In: *Phys Fluids* 24.1 (2012), p. 011702.

[45] H. J. Clercx and C.-H. Bruneau. « The normal and oblique collision of a dipole with a no-slip boundary. » In: *Comput. Fluids* 35.3 (2006), pp. 245–279.

[46] B. Cockburn, G. E. Karniadakis, and C.-W. Shu. *Discontinuous Galerkin methods: theory, computation and applications*. Vol. 11. Springer Science & Business Media, 2012.

[47] B. Cockburn and C.-W. Shu. « TVB Runge-Kutta local projection discontinuous Galerkin finite element method for conservation laws. II. General framework. » In: *Math. Comput.* 52.186 (1989), pp. 411–435.

[48] B. Cockburn and C.-W. Shu. « Runge–Kutta discontinuous Galerkin methods for convection-dominated problems. » In: *J. Sci. Comput.* 16.3 (2001), pp. 173–261.

[49] S. S. Collis. « Monitoring unresolved scales in multiscale turbulence modeling. » In: *Phys. Fluids* 13.6 (2001), pp. 1800–1806.

[50] S. Collis. « The DG/VMS method for unified turbulence simulation. » In: *32nd AIAA Fluid Dynamics Conference and Exhibit*. 2002, p. 3124.

[51] G.-H. Cottet, P. Koumoutsakos, and M. L. O. Salihi. « Vortex methods with spatially varying cores. » In: *J. Comput. Phys.* 162.1 (2000), pp. 164–185.

[52] E. Creusé and S. Nicaise. « A posteriori error estimator based on gradient recovery by averaging for convection–diffusion–reaction problems approximated by discontinuous Galerkin methods. » In: *IMA J. Numer. Anal.* 33.1 (2013), pp. 212–241.

[53] C. Dapogny, C. Dobrzynski, and P. Frey. « Three-dimensional adaptive domain remeshing, implicit domain meshing, and applications to free and moving boundary problems. » In: *J. Comput. Phys.* 262 (2014), pp. 358–378.

[54] L. Davidson et al. *LESFOIL: Large Eddy Simulation of Flow Around a High Lift Airfoil: Results of the Project LESFOIL Supported by the European Union 1998–2001*. Vol. 83. Springer Science & Business Media, 2012.

[55] V. Dolejší. « A design of residual error estimates for a high order BDF-DGFE method applied to compressible flows. » In: *Int. J. Numer. Methods Fluids* 73.6 (2013), pp. 523–559.

[56] V. Dolejší. « hp-DGFEM for nonlinear convection-diffusion problems. » In: *Math. Comput. Simul.* 87 (2013), pp. 87–118.

[57] V. Dolejší and M. Feistauer. *Discontinuous galerkin method - Analysis and Applications to Compressible Flow*. Vol. 48. Springer, 2015.

[58] V. Dolejší, F. Roskovec, and M. Vlasák. « Residual based error estimates for the space–time discontinuous Galerkin method applied to the compressible flows. » In: *Comput. Fluids* 117 (2015), pp. 304–324.

[59] V. Dolejší and P. Solin. « hp-discontinuous Galerkin method based on local higher order reconstruction. » In: *Appl. Math. Comput.* 279 (2016), pp. 219–235.

[60] J. A. Domaradzki, W. Liu, and M. E. Brachet. « An analysis of subgrid-scale interactions in numerically simulated isotropic turbulence. » In: *Phys. Fluids A* 5 (1993), pp. 1747–1759.

[61] *ERCOFTAC QNET-CFD Website*. URL: http://www.kbwiki.ercoftac.org/w/index.php/Main_Page.

[62] D. Ekelschot, J. Peiró, and S. Sherwin. « Mesh adaptation strategies for compressible flows using a high-order spectral/hp element discretisation. » PhD thesis. Imperial College London, 2016.

[63] G. Falcone et al. « The IPACS-Project at Glance–IPACS Benchmark Suite, Performance Modeling and Prediction Methods, Benchmarking Environment–. » In: *International Workshop on Networks for Grid Applications* (Oct. 2005).

[64] G.-X. Fan and Q. H. Liu. « Fast Fourier transform for discontinuous functions. » In: *IEEE T Antenn Propag* 52.2 (2004), pp. 461–465.

[65] A. Ferrero, F. Larocca, and G. Puppo. « A robust and adaptive recovery-based discontinuous Galerkin method for the numerical solution of convection-diffusion equations. » In: *Int. J. Numer. Methods Fluids* 77.2 (2015), pp. 63–91.

[66] K. J. Fidkowski and D. L. Darmofal. « Review of output-based error estimation and mesh adaptation in computational fluid dynamics. » In: *AIAA J.* 49.4 (2011), pp. 673–694.

[67] K. Fidkowski and D. Darmofal. « An adaptive simplex cut-cell method for discontinuous Galerkin discretizations of the Navier-Stokes equations. » In: *18th AIAA Computational Fluid Dynamics Conference*. 2007, p. 3941.

[68] D. Flad and G. Gassner. « On the use of kinetic energy preserving DG-schemes for large eddy simulation. » In: *J. Comput. Phys.* 350 (2017), pp. 782–795.

[69] P.-J. Frey and F. Alauzet. « Anisotropic mesh adaptation for CFD computations. » In: *Comput. Methods Appl. M.* 194.48-49 (2005), pp. 5068–5082.

[70] M. Frigo and S. G. Johnson. « The Design and Implementation of FFTW3. » In: *Proceedings of the IEEE* 93.2 (2005). Special issue on "Program Generation, Optimization, and Platform Adaptation", pp. 216–231.

[71] M. Galbraith and M. Visbal. « Implicit large eddy simulation of low Reynolds number flow past the SD7003 airfoil. » In: *46th AIAA Aerospace Sciences Meeting and Exhibit*. 2008, p. 225.

[72] E. Garnier, N. Adams, and P. Sagaut. *Large eddy simulation for compressible flows*. Springer Science & Business Media, 2009.

[73] G Gassner et al. « Explicit discontinuous Galerkin schemes with adaptation in space and time. » In: *36th CFD/ADIGMA course hp-adaptive hp-multigrid methods, VKI LS* (2009).

[74] G. J. Gassner and A. D. Beck. « On the accuracy of high-order discretizations for underresolved turbulence simulations. » In: *Theor. Comput. Fluid Dyn.* 27.3-4 (2013), pp. 221–237.

[75] R. Gautier, D. Biau, and E. Lamballais. « A reference solution of the flow over a circular cylinder at Re= 40. » In: *Comput. Fluids* 75 (2013), pp. 103–111.

[76] M. Germano et al. « A dynamic subgrid-scale eddy viscosity model. » In: *Phys. Fluids A* 3.7 (1991), pp. 1760–1765.

[77] B. J. Geurts and J. Fröhlich. « A framework for predicting accuracy limitations in large-eddy simulation. » In: *Phys Fluids* 14.6 (2002), pp. L41–L44.

[78] B. J. Geurts, A. Rouhi, and U. Piomelli. « Recent progress on reliability assessment of large-eddy simulation. » In: *J. Fluids Struct.* (2019).

[79] C. Geuzaine and J.-F. Remacle. « Gmsh: A 3-D finite element mesh generator with built-in pre-and post-processing facilities. » In: *Int. J. Numer. Methods Eng.* 79.11 (2009), pp. 1309–1331.

[80] D. Gottlieb and S. A. Orszag. *Numerical analysis of spectral methods: theory and applications*. Vol. 26. Siam, 1977.

[81] V. Gravemeier. « The variational multiscale method for laminar and turbulent flow. » In: *Arch. Comput. Methods Eng.* 13.2 (2006), p. 249.

[82] A. Harten and J. M. Hyman. « Self adjusting grid methods for one-dimensional hyperbolic conservation laws. » In: *J. Comput. Phys.* 50.2 (1983), pp. 235–269.

[83] R. Hartmann. « Multitarget error estimation and adaptivity in aerodynamic flow simulations. » In: *SIAM J. Sci. Comput.* 31.1 (2008), pp. 708–731.

[84] R. Hartmann and P. Houston. « Adaptive discontinuous Galerkin finite element methods for the compressible Euler equations. » In: *J. Comput. Phys.* 183.2 (2002), pp. 508–532.

[85] R. Hartmann and P. Houston. « An optimal order interior penalty discontinuous Galerkin discretization of the compressible Navier–Stokes equations. » In: *J. Comput. Phys.* 227.22 (2008), pp. 9670–9685.

[86] R. Hartmann et al. « Error estimation and adaptive mesh refinement for aerodynamic flows. » In: *ADIGMA-A Eur. Initiat. Dev. Adapt. Higher-Order Var. Methods Aerosp. Appl.* Springer, 2010, pp. 339–353.

[87] W Heisenberg. « On the theory of statistical and isotropic turbulence. » In: *P. Roy. Soc. Lond. A Mat.* 195.1042 (1948), pp. 402–406.

[88] B. Hendrickson. « Graph partitioning and parallel solvers: Has the emperor no clothes? » In: *International Symposium on Solving Irregularly Structured Problems in Parallel*. Springer. 1998, pp. 218–225.

[89] J. S. Hesthaven and T. Warburton. *Nodal discontinuous Galerkin methods: algorithms, analysis, and applications*. Springer Science & Business Media, 2007.

[90] J. Holmen et al. « Sensitivity of the scale partition for variational multiscale large-eddy simulation of channel flow. » In: *Phys. Fluids* 16.3 (2004), pp. 824–827.

[91] P. Houston and E. Süli. « A note on the design of hp-adaptive finite element methods for elliptic partial differential equations. » In: *Comput. Methods Appl. M.* 194.2 (2005), pp. 229–243.

[92] W. Huang and R. D. Russell. *Adaptive moving mesh methods*. Vol. 174. Springer Science & Business Media, 2010.

[93] T. J. R. Hughes, L. Mazzei, and K. E. Jansen. « Large eddy simulation and the variational multiscale method. » In: *Computing and Visualization in Science* 3 (2000), pp. 47–59.

[94] T. J. R. Hughes, G. N. Wells, and A. A Wray. « Energy transfers and spectral eddy viscosity in large-eddy simulations of homogeneous isotropic turbulence: Comparison of dynamic Smagorinsky and multiscale models over a range of discretizations. » In: *Phys. Fluids* 16.11 (2004), pp. 4044–4052.

[95] T. J. Hughes et al. « The multiscale formulation of large eddy simulation: Decay of homogeneous isotropic turbulence. » In: *Phys. Fluids* 13.2 (2001), pp. 505–512.

[96] J. C. Hunt, A. A. Wray, and P. Moin. « Eddies, streams, and convergence zones in turbulent flows. » In: *Proceeding8 of the Summer Program 1988*. 1988.

[97] H. T. Huynh. « A flux reconstruction approach to high-order schemes including discontinuous Galerkin methods. » In: *18th AIAA Computational Fluid Dynamics Conference*. 2007, p. 4079.

[98] H. Jeanmart and G. Winckelmans. « Investigation of eddy-viscosity models modified using discrete filters: A simplified "regularized variational multi-scale model" and an "enhanced field model". » In: *Phys. Fluids* 19.5 (2007), p. 055110.

[99] L. Jones, R. Sandberg, and N. Sandham. « Direct numerical simulations of forced and unforced separation bubbles on an airfoil at incidence. » In: *J. Fluid Mech.* 602 (2008), pp. 175–207.

[100] G. Karamanos and G. E. Karniadakis. « A spectral vanishing viscosity method for large-eddy simulations. » In: *J. Comput. Phys.* 163.1 (2000), pp. 22–50.

[101] G. Karniadakis and S. Sherwin. *Spectral/hp element methods for computational fluid dynamics*. Oxford University Press, 2013.

[102] G. Karypis. « METIS and ParMETIS. » In: *Encyclopedia of parallel computing* (2011), pp. 1117–1124.

[103] W. M. Kays. « Turbulent Prandtl number—where are we? » In: *J. Heat Transfer* 116.2 (1994), pp. 284–295.

[104] G. H. Keetels et al. « Fourier spectral and wavelet solvers for the incompressible Navier–Stokes equations with volume-penalization: Convergence of a dipole–wall collision. » In: *J. Comput. Phys.* 227.2 (2007), pp. 919–945.

[105] M. Kompenhans et al. « Adaptation strategies for high order discontinuous Galerkin methods based on Tau-estimation. » In: *J. Comput. Phys.* 306 (2016), pp. 216–236.

[106] R. H. Kraichnan. « Eddy viscosity in two and three dimensions. » In: *J. Atmos. Sci.* 33 (1976), pp. 1521–1536.

[107] A. Kravchenko, P. Moin, and R. Moser. « Zonal embedded grids for numerical simulations of wall-bounded turbulent flows. » In: *J. Comput. Phys.* 127.2 (1996), pp. 412–423.

[108] L. Krivodonova and J. E. Flaherty. « Error estimation for discontinuous Galerkin solutions of two-dimensional hyperbolic problems. » In: *Adv. Comput. Math.* 19.1-3 (2003), pp. 57–71.

[109] L. Krivodonova et al. « Shock detection and limiting with discontinuous Galerkin methods for hyperbolic conservation laws. » In: *Appl. Numer. Math.* 48.3-4 (2004), pp. 323–338.

[110] N. Kroll et al. *ADIGMA–A European Initiative on the development of adaptive higher-order variational methods for aerospace applications: results of a collaborative research project funded by the European Union, 2006-2009*. Vol. 113. Springer Science & Business Media, 2010.

[111] N. Kroll et al. *IDIHOM: Industrialization of High-Order Methods-A Top-Down Approach: Results of a Collaborative Research Project Funded by the European Union, 2010-2014*. Vol. 128. Springer, 2015.

[112] E. J. Kubatko et al. « Dynamic p-adaptive Runge–Kutta discontinuous Galerkin methods for the shallow water equations. » In: *Comput. Methods Appl. M.* 198.21-26 (2009), pp. 1766–1774.

[113] G. Kuru et al. « An adaptive Variational Multiscale Discontinuous Galerkin Method For Large Eddy Simulation. » In: *54th AIAA Aerosp. Sci. Meet. San Diego, Calif.* AIAA. 2016. URL: http://dx.doi.org.sci-hub.bz/10.2514/6.2016-0584.

[114] S. Laizet and E. Lamballais. « High-order compact schemes for incompressible flows: A simple and efficient method with quasi-spectral accuracy. » In: *J. Comput. Phys.* 228.16 (2009), pp. 5989–6015.

[115] E Lamballais et al. « Implicit/Explicit Spectral Viscosity and Large-Scale SGS Effects. » In: *Direct and Large-Eddy Simulation XI*. Springer, 2019, pp. 107–113.

[116] D. J. Lea, M. R. Allen, and T. W. Haine. « Sensitivity analysis of the climate of a chaotic system. » In: *Tellus A: Dynamic Meteorology and Oceanography* 52.5 (2000), pp. 523–532.

[117] D. J. Lea et al. « Sensitivity analysis of the climate of a chaotic ocean circulation model. » In: *Quart. J. Roy. Meteor. Soc.* 128.586 (2002), pp. 2587–2605.

[118] J.-Y. Lee and L. Greengard. « The type 3 nonuniform FFT and its applications. » In: *J. Comput. Phys.* 206.1 (2005), pp. 1–5.

[119] O. Lehmkuhl et al. « On the large-eddy simulations for the flow around aerodynamic profiles using unstructured grids. » In: *Comput. Fluids* 84 (2013), pp. 176–189.

[120] M. Lesieur, O. Métais, and P. Comte. *Large-eddy simulations of turbulence*. Cambridge university press, 2005.

[121] D. Leslie and G. Quarini. « The application of turbulence theory to the formulation of subgrid modelling procedures. » In: *J. Fluid Mech.* 91.1 (1979), pp. 65–91.

[122] D. K. Lilly. « The representation of small-scale turbulence in numerical simulation experiments. » In: *IBM Scientific Computing Symposium on Environmental Sciences*. 1966.

[123] Y. Liu, M. Vinokur, and Z. J. Wang. « Spectral difference method for unstructured grids I: basic formulation. » In: *J. Comput. Phys.* 216.2 (2006), pp. 780–801.

[124] M. Lorteau and E. Martin. *Stratégie load-balancing pour ordre variable*, Livrable 2.4.6 of the ELCI project (PIA DGE/Atos, BPI-France, 2015-2017). ONERA, 2017.

[125] M. Lorteau, M. De La Llave Plata, and V. Couaillier. « Turbulent jet simulation using high-order DG methods for aeroacoustic analysis. » In: *Int. J. Heat Fluid Flow* 70 (2018), pp. 380–390.

[126] *MPI Performance Snapshot User's Guide*. Intel. 2014-2015.

[127] J. Marcon et al. « A variational approach to high-order r-adaptation. » In: *26th International Meshing Roundtable, IMR26*. 2019.

[128] C. Mavriplis. « Nonconforming discretizations and a posteriori error estimators for adaptive spectral element techniques. » PhD thesis. Massachusetts Institute of Technology, 1989.

[129] C. Mavriplis. « A posteriori error estimators for adaptive spectral element techniques. » In: *Proc. Eighth GAMM-Conference Numer. Methods Fluid Mech.* Springer. 1990, pp. 333–342.

[130] C. Mavriplis. « Adaptive mesh strategies for the spectral element method. » In: *Comput. Methods Appl. M.* 116.1 (1994), pp. 77–86.

[131] D. McComb and A. Young. « Explict-scales projections of the partitioned nonlinear term in direct numerical simulation of the Navier-Stokes equation. » In: *Second Monte Verita Colloquium on Fundamental Problematic Issues in Fluid Turbulence*. 1998.

[132] C. Mellen, J. Frolich, and W. Rodi. « Large-Eddy simulation of the flow over periodic hills. » In: *Proceedings of the 16th IMACS world congress*. 2000.

[133] G. Mengaldo et al. « Dealiasing techniques for high-order spectral element methods on regular and irregular grids. » In: *J. Comput. Phys.* 299 (2015), pp. 56–81.

[134] O. Métais and M. Lesieur. « Spectral large-eddy simulation of isotropic and stably stratified turbulence. » In: *J. Fluid Mech.* 239 (1992), pp. 157–194.

[135] J. Meyers, B. J. Geurts, and M. Baelmans. « Database analysis of errors in large-eddy simulation. » In: *Phys. Fluids* 15.9 (2003), pp. 2740–2755.

[136] J. Meyers and P. Sagaut. « On the model coefficients for the standard and the variational multi-scale Smagorinsky model. » In: *J. Fluid Mech.* 569 (2006), pp. 287–319.

[137] J. Meyers and P. Sagaut. « Evaluation of Smagorinsky variants in large-eddy simulations of wall-resolved plane channel flows. » In: *Phys. Fluids* 19.9 (2007), p. 095105.

[138] J. Meyers, P. Sagaut, and B. J. Geurts. « Optimal model parameters for multi-objective large-eddy simulations. » In: *Phys. Fluids* 18.9 (2006), p. 095103.

[139] W. F. Mitchell and M. A. McClain. « A comparison of hp-adaptive strategies for elliptic partial differential equations. » In: *ACM Trans. Math. Softw.* 41.1 (2014), p. 2.

[140] S. M. Mitran. *A comparison of adaptive mesh refinement approaches for Large-Eddy Simulation*. Tech. rep. DTIC Document, 2001.

[141] P. Morin, R. H. Nochetto, and K. G. Siebert. « Convergence of adaptive finite element methods. » In: *SIAM Rev.* 44.4 (2002), pp. 631–658.

[142] R. C. Moura et al. « On the eddy-resolving capability of high-order discontinuous Galerkin approaches to implicit LES/under-resolved DNS of Euler turbulence. » In: *J. Comput. Phys.* 330 (2017), pp. 615–623.

[143] F. Naddei et al. « Large-scale space definition for the DG-VMS method based on energy transfer analyses. » In: *Proceedings of the 2018 Summer Program*. Center for Turbulence Research, Stanford. 2018.

[144] A. Ni et al. « Sensitivity analysis on chaotic dynamical systems by finite difference non-intrusive least squares shadowing (FD-NILSS). » In: *J. Comput. Phys.* (2019).

[145] F. Nicoud and F. Ducros. « Subgrid-scale stress modelling based on the square of the velocity gradient tensor. » In: *Flow Turbul. Combust.* 62.3 (1999), pp. 183–200.

[146] C. Norberg. « An experimental investigation of the flow around a circular cylinder: influence of aspect ratio. » In: *J. Fluid Mech.* 258 (1994), pp. 287–316.

[147] A. A. Oberai, V. Gravemeier, and G. C. Burton. « Transfer of Energy in the variational multiscale formulation of LES. » In: *Proceedings of the 2004 Summer Program*. 2004.

[148] J. T. Oden, W. Wu, and V. Legat. « An hp adaptive strategy for finite element approximations of the Navier-Stokes equations. » In: *Int. J. Numer. Methods Fluids* 20.8-9 (1995), pp. 831–851.

[149] P. Orlandi. « Vortex dipole rebound from a wall. » In: *Phys. Fluids A-Fluid* 2.8 (1990), pp. 1429–1436.

[150] M. L. Ould-Salihi, G.-H. Cottet, and M. El Hamraoui. « Blending finite-difference and vortex methods for incompressible flow computations. » In: *SIAM J. Sci. Comput.* 22.5 (2001), pp. 1655–1674.

[151] P.-O. Persson and J. Peraire. « Sub-cell shock capturing for discontinuous Galerkin methods. » In: *44th AIAA Aerosp. Sci. Meet. Exhib.* 2006, p. 112.

[152] U. Piomelli, A. Rouhi, and B. J. Geurts. « A grid-independent length scale for large-eddy simulations. » In: *J. Fluid Mech.* 766 (2015), pp. 499–527.

[153] S. B. Pope. « Large-eddy simulation using projection onto local basis functions. » In: *Lect. Notes Phys.* Springer, 2001, pp. 239–265.

[154] S. B. Pope. « Ten questions concerning the large-eddy simulation of turbulent flows. » In: *New J. Phys.* 6.1 (2004), p. 35.

[155] O. Posdziech and R. Grundmann. « A systematic approach to the numerical calculation of fundamental quantities of the two-dimensional flow over a circular cylinder. » In: *J. Fluids Struct.* 23.3 (2007), pp. 479–499.

[156] L. Qu et al. « Quantitative numerical analysis of flow past a circular cylinder at Reynolds number between 50 and 200. » In: *J. Fluids Struct.* 39 (2013), pp. 347–370.

[157] B. N. Rajani, A Kandasamy, and S. Majumdar. « Numerical simulation of laminar flow past a circular cylinder. » In: *Appl. Math. Model.* 33.3 (2009), pp. 1228–1247.

[158] S. Ramakrishnan and S. S. Collis. « Partition selection in multiscale turbulence modeling. » In: *Phys. Fluids* 18 (2006), p. 075105.

[159] U. Rasthofer and V. Gravemeier. « Recent Developments in Variational Multiscale Methods for Large-Eddy Simulation of Turbulent Flow. » In: *Arch. Comput. Methods Eng.* (2017), pp. 1–44.

[160] W. H. Reed and T. R. Hill. « Triangular mesh methods for the neutron transport equation. » In: *Los Alamos Rep. LA-UR-73-479* (1973).

[161] J.-F. Remacle et al. « Anisotropic adaptive simulation of transient flows using discontinuous Galerkin methods. » In: *Int. J. Numer. Methods Eng.* 62.7 (2005), pp. 899–923.

[162] F. Renac et al. « Aghora: a high-order DG solver for turbulent flow simulations. » In: *IDIHOM Ind. High-Order Methods-A Top-Down Approach*. Springer, 2015, pp. 315–335.

[163] W. Rodi, J. C. Bonnin, and T. Buchal. « ERCOFTAC workshop on data bases and testing of calculation methods for turbulent flows. » In: *Proceedings of the 4th ERCOFTAC/IAHR Workshop on Refined Flow Modelling*. University of Karsruhe. 1995.

[164] P. L. Roe. « Approximate Riemann solvers, parameter vectors, and difference schemes. » In: *J. Comput. Phys.* 43.2 (1981), pp. 357–372.

[165] C. Roy. « Review of discretization error estimators in scientific computing. » In: *48th AIAA Aerospace Sciences Meeting Including the New Horizons Forum and Aerospace Exposition*. 2010, p. 126.

[166] A. M. Rueda-Ramírez et al. « A p-multigrid strategy with anisotropic p-adaptation based on truncation errors for high-order discontinuous Galerkin methods. » In: *J. Comput. Phys.* 378 (2019), pp. 209–233.

[167] A. M. Rueda-Ramírez et al. « Truncation Error Estimation in the p-Anisotropic Discontinuous Galerkin Spectral Element Method. » In: *J. Sci. Comput.* 78.1 (2019), pp. 433–466.

[168] *SSEMID - Stability and Sensitivity Methods for Industrial Design*. URL: https://www.ssemid-itn.eu/.

[169] P. Sagaut and V. Levasseur. « Sensitivity of spectral variational multiscale methods for large-eddy simulation of isotropic turbulence. » In: *Phys. Fluids* 17 (2005), p. 035113.

[170] P. Sagaut. *Large eddy simulation for incompressible flows: an introduction*. Springer Science & Business Media, 2006.

[171] A. M. Salva. « A comparison of refinement indicators for h-adaptive discontinuous Galerkin methods for the Euler and Navier-Stokes equations. » MA thesis. Universitat Politècnica de Catalunya, 2018.

[172] K. Schneider and O. V. Vasilyev. « Wavelet methods in computational fluid dynamics. » In: *Annu. Rev. Fluid Mech.* 42 (2010), pp. 473–503.

[173] H. Shan, L. Jiang, and C. Liu. « Direct numerical simulation of flow separation around a NACA 0012 airfoil. » In: *Comput. Fluids* 34.9 (2005), pp. 1096–1114.

[174] J. Smagorinsky. « General circulation experiments with the primitive equations: I. The basic experiment. » In: *Mon. Weather Rev.* 91.3 (1963), pp. 99–164.

[175] R. J. Spiteri and S. J. Ruuth. « A new class of optimal high-order strong-stability-preserving time discretization methods. » In: *SIAM J. Numer. Anal.* 40.2 (2002), pp. 469–491.

[176] S. Stolz, P. Schlatter, and L. Kleiser. « High-pass filtered eddy-viscosity models for large-eddy simulations of transitional and turbulent flow. » In: *Phys. Fluids* 17.6 (2005), p. 065103.

[177] S. Sun and M. F. Wheeler. « Anisotropic and dynamic mesh adaptation for discontinuous Galerkin methods applied to reactive transport. » In: *Comput. Methods Appl. M.* 195.25-28 (2006), pp. 3382–3405.

[178] A. Syrakos et al. « Numerical experiments on the efficiency of local grid refinement based on truncation error estimates. » In: *J. Comput. Phys.* 231.20 (2012), pp. 6725–6753.

[179] L. Tang. « RANS simulation of low-Reynolds-number airfoil aerodynamics. » In: *44th AIAA Aerospace Sciences Meeting and Exhibit*. 2006, p. 249.

[180] G. I. Taylor and A. E. Green. « Mechanism of the production of small eddies from large ones. » In: *Proceedings of the Royal Society of London. Series A-Mathematical and Physical Sciences* 158.895 (1937), pp. 499–521.

[181] N. Thomareis and G. Papadakis. « Effect of trailing edge shape on the separated flow characteristics around an airfoil at low Reynolds number: A numerical study. » In: *Phys. Fluids* 29.1 (2017), p. 014101.

[182] V. Tikhomirov. « Equations of turbulent motion in an incompressible fluid. » In: *Selected Works of AN Kolmogorov*. Springer, 1991, pp. 328–330.

[183] S. Toosi and J. Larsson. « Anisotropic grid-adaptation in large eddy simulations. » In: *Comput. Fluids* 156 (2017), pp. 146–161.

[184] D. J. Tritton. « Experiments on the flow past a circular cylinder at low Reynolds numbers. » In: *J. Fluid Mech.* 6.4 (1959), pp. 547–567.

[185] M. Tugnoli et al. « A locally p-adaptive approach for Large Eddy Simulation of compressible flows in a DG framework. » In: *J. Comput. Phys.* 349 (2017), pp. 33–58. URL: https://arxiv.org/abs/1610.03319.

[186] G. Tumolo and L. Bonaventura. « A semi-implicit, semi-Lagrangian discontinuous Galerkin framework for adaptive numerical weather prediction. » In: *Q. J. R. Meteorol. Soc.* 141.692 (2015), pp. 2582–2601.

[187] G. Tumolo, L. Bonaventura, and M. Restelli. « A semi-implicit, semi-Lagrangian, p-adaptive discontinuous Galerkin method for the shallow water equations. » In: *J. Comput. Phys.* 232.1 (2013), pp. 46–67. URL: http://www.sciencedirect.com/science/article/pii/S0021999112003105.

[188] A. Uranga et al. « Implicit large eddy simulation of transition to turbulence at low Reynolds numbers using a discontinuous Galerkin method. » In: *Int. J. Numer. Methods Eng.* 87.1-5 (2011), pp. 232–261.

[189] A. Vreman. « The filtering analog of the variational multiscale method in large-eddy simulation. » In: *Phys. Fluids* 15.8 (2003), pp. L61–L64.

[190] A. Vreman. « An eddy-viscosity subgrid-scale model for turbulent shear flow: Algebraic theory and applications. » In: *Phys. Fluids* 16.10 (2004), pp. 3670–3681.

[191] A. Vreman. « The adjoint filter operator in large-eddy simulation of turbulent flow. » In: *Phys. Fluids* 16.6 (2004), pp. 2012–2022.

[192] B. Vreman, B. Geurts, and H. Kuerten. « Subgrid-modelling in LES of compressible flow. » In: *Appl. Sci. Res.* 54.3 (1995), pp. 191–203.

[193] B. Vreman, B. Geurts, and H. Kuerten. « Comparison of numerical schemes in Large-Eddy Simulation of the temporal mixing layer. » In: *Int. J. Numer. Methods Fluids* 22.4 (1996), pp. 297–311.

[194] J. Wackers et al. « Combined refinement criteria for anisotropic grid refinement in free-surface flow simulation. » In: *Comput. Fluids* 92 (2014), pp. 209–222.

[195] Q. Wang, R. Hu, and P. Blonigan. « Least squares shadowing sensitivity analysis of chaotic limit cycle oscillations. » In: *J. Comput. Phys.* 267 (2014), pp. 210–224.

[196] Z. J. Wang et al. « High-order CFD methods: current status and perspective. » In: *Int. J. Numer. Methods Fluids* 72.8 (2013), pp. 811–845.

[197] Z. Wang and A. Oberai. « A mixed large eddy simulation model based on the residual-based variational multiscale formulation. » In: *Phys. Fluids* 22.7 (2010), p. 075107.

[198] C. von Wieselsberger. « Neuere Feststellungen über die Gesetze des Flussigkeits- und Luftwiderstands. » In: *Phys. Z.* 22 (1921), p. 321.

[199] C. H. K. Williamson. « Oblique and parallel modes of vortex shedding in the wake of a circular cylinder at low Reynolds numbers. » In: *J. Fluid Mech.* 206 (1989), pp. 579–627.

[200] H. C. Yee, N. D. Sandham, and M. J. Djomehri. « Low-dissipative high-order shock-capturing methods using characteristic-based filters. » In: *J. Comput. Phys.* 150.1 (1999), pp. 199–238.

[201] M. J. Zahr and P.-O. Persson. « An optimization-based approach for high-order accurate discretization of conservation laws with discontinuous solutions. » In: *J. Comput. Phys.* 365 (2018), pp. 105–134.

[202] W. Zhang and R. Samtaney. « Assessment of spanwise domain size effect on the transitional flow past an airfoil. » In: *Comput. Fluids* 124 (2016), pp. 39–53.

[203] C.-H. Zhu et al. « A high accuracy conformal method for evaluating the discontinuous Fourier transform. » In: *Prog Electromagn Res* 109 (2010), pp. 425–440.

[204] M. de la Llave Plata, V. Couaillier, and E. Lamballais. « A discontinuous Galerkin variational multiscale approach to LES of turbulent flows. » In: *Elev. Int. ERCOFTAC Work. Direct Large-Eddy Simualtion*. Pisa, 2017.

[205] M. de la Llave Plata, V. Couaillier, and M.-C. le Pape. « On the use of a high-order discontinuous Galerkin method for DNS and LES of wall-bounded turbulence. » In: *Comput. Fluids* 176 (2018), pp. 320–337.

université PARIS-SACLAY | École doctorale de mathématiques Hadamard (EDMH)

Titre : Simulation adaptative des grandes échelles d'écoulements turbulents fondée sur une méthode Galerkine discontinue

Mots clés : Méthode Galerkine discontinue, Adaption-*h/p*, Estimation d'erreur, Simulation des grandes échelles

Résumé : L'objectif principal de ce travail est d'améliorer la précision et l'efficacité des modèles LES au moyen des méthodes Galerkine discontinues (DG). Deux thématiques principales ont été étudiées: les stratégies d'adaptation spatiale et les modèles LES pour les méthodes d'ordre élevé.
Concernant le premier thème, dans le cadre des méthodes DG la résolution spatiale peut être efficacement adaptée en modifiant localement soit le maillage (adaptation-*h*) soit le degré polynômial de la solution (adaptation-*p*). L'adaptation automatique de la résolution nécessite l'estimation des erreurs pour analyser la qualité de la solution locale et les exigences de résolution.
L'efficacité de différentes stratégies de la littérature est comparée en effectuant des simulations *h*- et *p*-adaptatives. Sur la base de cette étude comparative, des algorithmes dynamiques et statiques *p*-adaptatifs pour la simulation des écoulements instationnaires sont ensuite développés et analysés. Les simulations numériques réalisées montrent que les algorithmes proposés peuvent réduire le coût de calcul des simulations des écoulements transitoires et statistiquement stationnaires.
Un nouvel estimateur d'erreur est ensuite proposé. Il est local, car n'exige que des informations de l'élément et de ses voisins directs, et peut être calculé en cours de simulation pour un coût limité. Il est démontré que l'algorithme statique *p*-adaptatif basé sur cet estimateur d'erreur peut être utilisé pour améliorer la précision des simulations LES sur des écoulements turbulents statistiquement stationnaires.
Concernant le second thème, une nouvelle méthode, consistante avec la discrétisation DG, est développée pour l'analyse *a-priori* des modèles DG-LES à partir des données DNS. Elle permet d'identifier le transfert d'énergie idéal entre les échelles résolues et non résolues. Cette méthode est appliquée à l'analyse de l'approche Variational Multiscale (VMS). Il est démontré que pour les résolutions fines, l'approche DG-VMS est capable de reproduire le transfert d'énergie idéal. Cependant, pour les résolutions grossières, typique de la LES à nombres de Reynolds élevés, un meilleur accord peut être obtenu en utilisant un modèle mixte Smagorinsky-VMS.

Title : Adaptive Large Eddy Simulations based on discontinuous Galerkin methods

Keywords : Discontinuous Galerkin, *h*/*p*-adaptation, Error estimation, Large Eddy Simulation

Abstract : The main goal of this work is to improve the accuracy and computational efficiency of Large Eddy Simulations (LES) by means of discontinuous Galerkin (DG) methods. To this end, two main research topics have been investigated: resolution adaptation strategies and LES models for high-order methods.
As regards the first topic, in the framework of DG methods the spatial resolution can be efficiently adapted by modifying either the local mesh size (*h*-adaptation) or the degree of the polynomial representation of the solution (*p*-adaptation). The automatic resolution adaptation requires the definition of an error estimation strategy to analyse the local solution quality and resolution requirements. The efficiency of several strategies derived from the literature are compared by performing *p*- and *h*-adaptive simulations. Based on this comparative study a suitable error indicator for the adaptive scale-resolving simulations is selected.
Both static and dynamic *p*-adaptive algorithms for the simulation of unsteady flows are then developed and analysed. It is demonstrated by numerical simulations that the proposed algorithms can provide a reduction of the computational cost for the simulation of both transient and statistically steady flows.
A novel error estimation strategy is then introduced. It is local, requiring only information from the element and direct neighbours, and can be computed at run-time with limited overhead. It is shown that the static *p*-adaptive algorithm based on this error estimator can be employed to improve the accuracy for LES of statistically steady turbulent flows.
As regards the second topic, a novel framework consistent with the DG discretization is developed for the *a-priori* analysis of DG-LES models from DNS databases. It allows to identify the ideal energy transfer mechanism between resolved and unresolved scales. This approach is applied for the analysis of the DG Variational Multiscale (VMS) approach. It is shown that, for fine resolutions, the DG-VMS approach is able to replicate the ideal energy transfer mechanism. However, for coarse resolutions, typical of LES at high Reynolds numbers, a more accurate agreement is obtained by a mixed Smagorinsky-VMS model.

Université Paris-Saclay
Espace Technologique / Immeuble Discovery
Route de l'Orme aux Merisiers RD 128 / 91190 Saint-Aubin, France